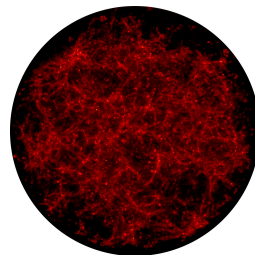
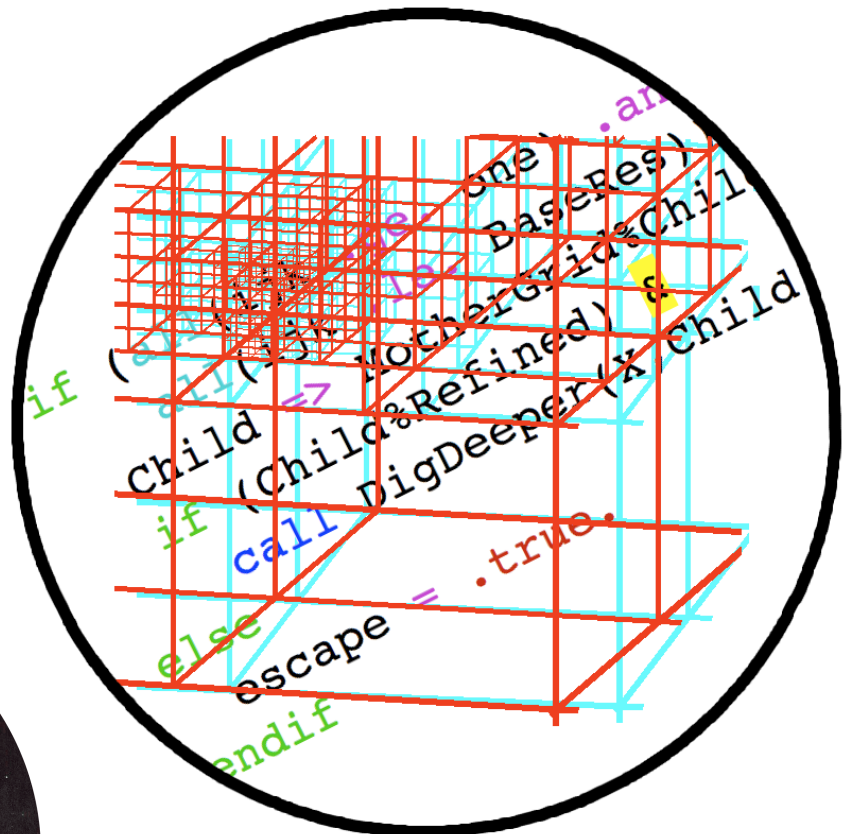


Interpreting Lyman α radiation from young, dusty galaxies



Dissertation submitted for the degree of

Philosophiæ Doctor

on June 14, 2010, by

Peter Laursen

**Supervisors: Anja C. Andersen
& Jesper Sommer-Larsen**

Dark Cosmology Centre, Niels Bohr Institute
Faculty of Science, University of Copenhagen

Cover art:

The front page illustrates the essence of this work, under the directives given by the University Design Guidelines, which seem to be very preoccupied with bubbles.

The *lower bubble* displays a snapshot from a cosmological simulation at the time when the Universe was two and a half billion years old. The region is some 13 million lightyears across. Roughly one thousand galaxies float around in this volume, organized in beautiful filamentary structures, separated by huge voids of nothingness.

Zooming in on one of the little dots, the *middle bubble* shows a pencil drawing of a few galaxies, slightly smeared out with my finger to create the effect of gaseous nebulae, and subsequently color-inverted.

The *upper bubble* shows the closest zoom-in, symbolizing the fact that this work is predominantly numerical. In the simulations, the physical properties of the galaxies are represented by millions of numbers arranged in a three-dimensional irregular matrix of cells. Two different projections of this matrix are shown in **red** and **cyan**, respectively, generating an anaglyph image which can be viewed with a pair of 3D glasses (although in the printed version the cyan may come out a bit too dark). In between the cells is seen a few lines from the computer code.

Abstract

The significance of the Ly α emission line as a probe of the high-redshift Universe has long been established. Originating mainly in the vicinity of young, massive stars and in association with accretion of large bulks of matter, it is ideal for detecting young galaxies, the fundamental building blocks of our Universe. Since many different processes shape the spectrum and the spatial distribution of the Ly α photons in various ways, a multitude of physical properties of galaxies can be unveiled.

However, this also makes the interpretation of Ly α observations notoriously difficult. Because Ly α is a resonant line, it scatters on neutral hydrogen, having its path length from the source to our telescopes vastly increased, and taking it through regions of unknown physical conditions.

In this work, a numerical code capable of calculating realistically the radiative transfer of Ly α is presented. The code is capable of performing the radiative transfer in an arbitrary and adaptively refined distribution of Ly α source emission, temperature and velocity field of the interstellar and intergalactic medium, as well as density of neutral and ionized hydrogen, and, particularly important, dust.

Accordingly, it is applied to galaxies simulated at high resolution, yielding a number of novel and interesting results, most notably the escape fractions of Ly α photons, the effect of dust, and the impact of the transfer through the intergalactic medium.

Furthermore, the remarkable detection of Ly α emission from a so-called “damped Ly α absorber” — a special type of objects thought to be the progenitor of present-day’s galaxies — is presented, and the potential of the code for interpreting observations is demonstrated.

“It would seem that large digital computers could be applied very profitably to this problem.”

Donald E. Osterbrock (1962), on the complications of Ly α radiative transfer.

Acknowledgments

I am very appreciative of having had the opportunity to work at the Dark Cosmology Centre, with its inspiring atmosphere. Although all my colleagues have contributed to making my days joyous, some have played a more direct part in accomplishing my research:

Obviously, this thesis would not have been possible without the aid and support from my supervisors Anja and Jesper. Your faith in my abilities have been overwhelming, verging on the irrational. The same must be said about Johan, who has also been very eager to include me in various projects. Steen has always been prompt to help me with numerical and statistical issues. Giorgos was very patient with me during reduction of data, and was a great traveling partner and art co-investor. I have benefited considerably from Bo's knowledge on various observational aspects of Ly α , and from Brian's perpetual sysadmin support. It is a pleasure to thank all of you.

Last, but not least, in fact most, I am grateful to Frk. Lehmann for your truly invaluable support and for taking care of everything, in particular through the past couple of months, and to Sigurd Sinus, for making me remember the essential stuff in life, such as watching excavators and throwing rocks in the water.

Contents

I	Theoretical background	1
1	Introduction	3
1.1	A brief history of Lyman α	4
1.2	Motivation	5
1.3	Structure	7
2	Galaxies in the early Universe	9
2.1	Ly α emitters	11
2.1.1	Sources of emission	11
2.1.2	Physical characteristics	13
2.2	Lyman-break galaxies	15
2.3	Damped Ly α absorbers	16
3	Resonant scattering	19
3.1	Atomic cross section	19
3.1.1	Thermal broadening of the line profile	20
3.2	Scattering	22
3.2.1	Frequency shift	22
3.2.2	Phase function	23
3.2.3	Recoil effect	25
3.2.4	Atom velocity	25
3.3	Radiative transfer	27
3.3.1	Optical depth	27
3.3.2	Photon peregrination	27
4	Cosmic dust	33
4.1	Effect on radiative transfer	34
4.1.1	Ly α escape fraction	35
4.2	What characterizes cosmic dust?	36
4.2.1	Cross section	37
4.2.2	Number density	39
4.2.3	Albedo	42
4.2.4	Phase function	42
5	The intergalactic medium	45
5.1	The Ly α forest	45
5.2	The Epoch of Reionization	46
5.2.1	The cosmic microwave background	48

5.2.2	The 21 cm line	48
II	Numerical radiative transfer	51
6	Numerical background	53
6.1	Monte Carlo RT	53
6.1.1	Random numbers	54
6.2	Smoothed particle hydrodynamics	55
6.3	Underlying cosmological simulations	56
6.3.1	Ionizing UV radiative transfer	58
7	MoCALATA	61
7.1	Emission of photons	62
7.2	Propagation of the radiation	63
7.2.1	Optical depth	63
7.2.2	Gas and dust cross section	63
7.2.3	Spatial displacement	64
7.2.4	Lorentz transformation between adjacent cells	65
7.3	Scattering	65
7.3.1	Atom velocity	66
7.3.2	Re-emission	69
7.3.3	Interaction with dust	69
7.4	Simulating observations	70
7.4.1	Surface brightness maps and spectra	70
7.5	Acceleration schemes	71
7.5.1	Core-skipping scheme	71
7.5.2	Semi-analytical scheme	75
7.5.3	Luminosity-boosting scheme	79
8	Tests	81
8.1	Testing against analytical solutions	81
8.1.1	Individual scatterings	81
8.1.2	Neufeld solution	81
8.1.3	Maximum of the emergent spectrum	82
8.1.4	Average number of scatterings	83
8.1.5	Gas bulk motion	83
8.1.6	Escape fraction	87
8.2	Convergence tests	87
8.2.1	Resolution and interpolation scheme	87
8.2.2	AMR structure	88
8.2.3	UV RT scheme	90
8.3	Dust parameter study	90
9	Intergalactic radiative transfer	95
9.1	Preparations	97
9.1.1	Cosmological models	97
9.1.2	Galaxy selection criteria	97
9.2	IGMTRANSFER	98

III	Scientific achievements	103
10	On the consequences of resonant scattering	105
10.1	Extended surface brightness	105
10.2	Broadened spectrum	107
10.3	Anisotropic escape	109
11	On the effects of dust	113
11.1	The need for adaptive resolution	113
11.2	Where are the photons absorbed?	114
11.3	Effect on the emergent spectrum	116
11.4	Escape fraction	117
11.5	General results	118
11.5.1	Anisotropic escape of Ly α	118
11.5.2	Correlation of f_{esc} with galactic mass	119
11.5.3	Narrowing of the spectrum	120
11.5.4	Extended surface brightness profile	120
11.6	Temporal fluctuations	120
11.7	Discussion	121
12	On the impact of the intergalactic medium	125
12.1	Results	126
12.1.1	The Ly α transmission function	126
12.1.2	Effect on the spectrum and escape fraction	128
12.1.3	Probing the Epoch of Reionization	131
12.2	Convergence test	133
12.3	Discussion	134
12.3.1	The origin of the dip	134
12.3.2	Galactic outflows	136
12.3.3	Transmitted fraction of Ly α photons	137
12.3.4	The significance of dust	137
12.3.5	“Early” vs. “late” reionization	138
13	On the Lyα emission from damped Lyα absorbers	141
13.1	Q2348-011	142
13.1.1	Observations	143
13.1.2	Data reduction	144
13.1.3	Results	144
13.1.4	Follow-up observations	146
13.2	Q2222-0946	146
13.2.1	Galaxy counterpart	148
13.2.2	The Ly α emission line profile	149
14	Postscript	153
14.1	Summary	154
14.1.1	Extended surface brightness	154
14.1.2	Anisotropic escape	154
14.1.3	Narrowing of the Ly α line profile by dust	154
14.1.4	Correlation of Ly α escape fraction with galaxy size	155
14.1.5	Absorption in the intergalactic medium	155

14.1.6	Constraints on the Epoch of Reionization	156
14.1.7	Identification of a DLA galaxy counterpart	156
14.2	Outlook	156
14.2.1	$\text{Ly}\alpha$ radiative transfer in a multi-phase medium	156
14.2.2	$\text{Ly}\alpha$ polarization	157
14.2.3	Probing the very first galaxies	158
IV	Appendix	161
A	Quantum mechanical derivation of the $\text{Ly}\alpha$ cross section	163
A.1	The Hamiltonian	163
A.1.1	Total Hamiltonian	163
A.1.2	The Hamiltonian of the perturbation	164
A.2	Absorption	165
A.3	Natural broadening of the line profile	167
A.4	Transition rate	167
B	Paper I	171
C	Paper II	175
D	Paper III	179
E	Paper IV	183
	Bibliography	187
	Index	203

Part I

Theoretical background

Chapter 1

Introduction



INCE THE EMERGENCE OF a deeper consciousness, mankind has strived to understand and explain the place we inhabit in the cosmos, along with the numerous enchanting phenomena that surround us. The magnificent and eternal sky, occasionally strewn with transient events, cannot help but mesmerize and impose a spirit of inquiry on the beholder.

Possessing only pure reason and the eye, it is not surprising that our ancestors ascribed most natural phenomena to the will of divine beings whenever something seemed *too* fantastic. Without in any way denying the existence of such creatures, perhaps the most stunning fact about Nature is that, at least to a very large degree, it is comprehensible within the realm of known physical laws. With the advent of modern telescopes and sensitive detectors we began to grasp the vastness of the Universe, with our Milky Way only being one among at least billions, and most likely an infinite amount of galaxies, organized in beautiful filamentary structures throughout the cosmos. Galaxies are thus the building blocks of our Universe, and to understand the physics governing the formation, structure, and evolution of these enigmatic conglomerations of stars, gas, and dust, as well as more exotic components such as black holes and dark matter, is a magnificent challenge of astronomy, revealing ultimately the necessary conditions for the genesis of life itself.

Astronomers, unlike other physicists, do not have the privilege of being able to perform experiments in a lab. Instead we either have to stick with whatever experiment Nature performs for us, and then simply *observe*, applying our knowledge of physics in order to interpret our observations. Thanks to the finite speed of light, however, a privilege that we *do* have is our ability to look back in time, and thus by observing different cosmic epochs gain a picture of the evolution of the Universe and its contents. Nevertheless, since most cosmological phenomena happen on timescales much longer than the human lifetime, we are always confined to “snapshots” of the observed objects.

To actually learn in much greater detail how things happen, we have another possibility, namely to *simulate* on a computer how we think Nature might operate. Although in principle a computer cannot do anything humans are not also able to, they do it a billion times faster. Over the years, many elaborate numerical codes have been constructed that reproduce and predict the Universe on all scales, from dust agglomeration, over planetary and stellar formation, to

simulations of cosmological volumes¹. Although these codes include an steadily increasing number of physical processes, numerical resolution, etc., and although they are able to predict various observables, many of them fail to account for the fact that the observed light may be rather different from the light that was emitted.

Except for meteorites and dust grains in the neighborhood of Earth, the only means of gaining information from the Universe is by observations of light², be it cooling radiation from huge collapsing gas reservoirs forming galaxies, spectral lines from planetary nebulae, or thermal radiation from heated dust. However, once radiation leaves its origins, it may still be subject to various physical processes altering its intensity, direction, and spectral distribution. If we do not understand these processes, we may severely misinterpret the predictions of the models, when comparing to observations.

This is particularly true in the case of *resonantly scattered* photons, i.e. photons that are absorbed and emitted in another direction with more or less almost the same frequency. In this case, the photons will follow a complicated path from it is emitted to it is detected, taking it through regions of space that may be physically quite different from the those lying between its point of emission and the observer.

1.1 A brief history of Lyman α

The most “famous” resonant line is Ly α , the energy of which corresponds to the energy difference between the ground state and the first excited state of neutral hydrogen. Because this is the most frequent transition, and because hydrogen constitutes more than 90% of all elements in the Universe by number, the Ly α line is often the most prominent line emerging from astrophysical objects. In Sec. 2.1.1, the various physical processes that may result in emission of Ly α are discussed in detail, but in anticipation of events we note that they are mainly produced by gas surrounding young, massive stars, and, to a lesser extent, by the cooling of collapsing gas. In their classic paper, Partridge & Peebles (1967) suggested how detection of young galaxies would be feasible, using the Ly α line. Nevertheless, for almost three decades only a few such Ly α emitters (LAEs, i.e. galaxies detected from their emission in Ly α , either by narrowband photometry or spectroscopy, see also Sec. 2.1) were discovered (see, e.g., Djorgovski & Thompson, 1992). Several theories were proposed to explain the high amount of null-results, e.g. suppression of the Ly α line due to metals (Meier & Terlevich, 1981), absorption by dust (Hartmann et al., 1988) and lower-than-expected formation of massive stars (Valls-Gabaud, 1993).

However, as surveys eventually were able to go deeper, and as searching wide regions on the sky became feasible, large numbers of high-redshift, star-forming galaxies were discovered. Notable surveys include the Large Area Lyman Alpha survey (LALA; e.g., Rhoads et al., 2000) and the Subaru Deep Field survey (e.g., Taniguchi et al., 2005), and together with more recent surveys, gradually a census of the nature of LAEs at a wide range of redshifts has been provided (e.g. Guaita et al. (2010) at $z = 2.1$, Nilsson et al. (2009) at $z = 2.3$, Wang et al. (2009) at $z = 4.5$, Ouchi et al. (2010) at $z = 6.6$, and for small, spectroscopically

¹That is, volumes that are more or less representative of the Universe as a whole.

²At least until we manage to detect gravitational waves.

unconfirmed samples even farther, with [Hibon et al. \(2010\)](#) and [Tilvi et al. \(2010\)](#)). The current LAE redshift record holder ($z = 6.96$; [Iye et al., 2006](#)) is now five years “old”, demonstrating the arduousness of detecting galaxies thus distant. Galaxies up to $z \sim 8$ ([Bouwens et al., 2004](#)) has been detected via the Lyman-break technique (see [Sec. 2.2](#)), but have not been spectroscopically confirmed³ (both of these techniques are discussed in the next chapter), but in time deeper observations will be realized with, e.g., the Ultra-VISTA project (launched this spring, reaching $z = 8.8$; PIs Dunlop, Le Fevre, Franx, & Fynbo) and the James Webb Space Telescope (to be launched in 2013; e.g., [Gardner, 2006](#)).

For this reason, Ly α has become one of the most important diagnostic tools for exploring the high-redshift Universe. Since it is an ultraviolet (UV) wavelength, the atmosphere is opaque to Ly α emitted at redshifts smaller than ~ 1.5 , but hereafter it is often easily detectable, and at $z \gtrsim 2.1$, it becomes the strongest emission line in the optical-NIR window.

Since it is often the only line visible, it is crucial for determining redshifts (e.g., [Hu et al., 2002a,b](#); [Kodaira et al., 2003](#)). From the shape of the line profile, equivalent width and offset from other emission and absorption lines, information about morphology, kinematics and underlying stellar population of the host galaxy can be gained; [Kunth et al. \(1998\)](#) used P Cygni features in the Ly α line to infer the presence of strong, galactic outflows, while the equivalent width has been used as evidence for an unusually strong ionizing continuum, possibly caused by first generation (Pop III) stars ([Malhotra & Rhoads, 2002](#)). Also, strong Ly α emission from distant quasars are used to map the cosmic web of sheets and filaments in the intervening Universe through Ly α *absorption*, resulting in the so-called Ly α forest (e.g., [Weinberg et al., 2003](#), see also [Sec. 5.1](#)).

1.2 Motivation

Through the past years it has become possible to actually resolve observationally these young Ly α emitting galaxies. In several cases, the galaxies have been found to be significantly more extended on the sky when observed in Ly α as opposed to optical bands (e.g., [Møller & Warren, 1998](#); [Fynbo et al., 2001, 2003](#); [Saito et al., 2006](#)). Specifically, [Fig. 1.1](#) displays surface brightness (SB) maps of the LAE LEGO2138_29 ([Fynbo et al., 2003](#)), observed in Ly α and in the *R*-band, as well as their SB profiles, i.e. the SB of the objects averaged over the azimuthal angle. Because the galaxies are still in a proto-phase, they should be surrounded by an envelope of accreting and partially neutral gas, and thus this phenomenon may be the result of the photons having to scatter their way out of the galaxies.

Spectroscopically, LAEs also exhibit an interesting feature: As will be discussed in (much!) further detail in [Chap. 3](#), due to the high opacity of neutral hydrogen for a photon in the line center, in general the radiation will have to diffuse in frequency to either the red or the blue side of the line center, and should thus escape in a double-peaked profile. Although this has indeed been observed in several cases (e.g. [Yee & De Robertis, 1991](#); [Venemans et al., 2005](#); [Tapken et al., 2007](#)), more often the Ly α profile are characterized by an asymmetric profile

³Since the submission of this thesis the record has broken, with a spectroscopically confirmed LAE at $z = 8.55$ [Lehnert et al. \(2010\)](#).

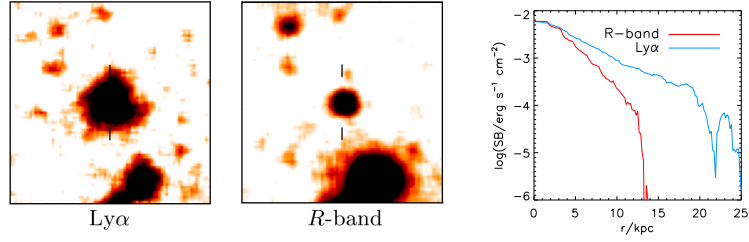


Figure 1.1: The Ly α emitter LEGO2138_29 (redshift $z = 2.86$) observed in Ly α *left* and in the R-band *middle*. *Right* panel shows the azimuthally averaged SB profiles, where the SB of the R-band *red* is normalized such that its maximum coincides with the maximum of the Ly α SB *blue*. The source is clearly much more spatially extended in Ly α than in the R-band. Courtesy of Fynbo et al. (2003).

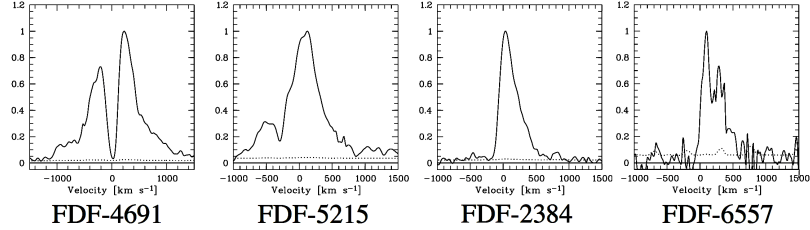


Figure 1.2: Four examples of Ly α line profiles, obtained with a resolution of $R \simeq 2000$. *Panel 1* shows a beautiful double-peaked profile. In *panel 2*, the blue peak is diminished, but still clearly visible. *Panel 3* is an archetypical Ly α profile, with the blue peak completely gone. Its asymmetry is a clear signature of resonant scattering processes. The profile in *panel 4* is more noisy, and it is difficult to say whether we see one peak, as in panel 3, or two peaks blended by insufficient resolution. From Tapken et al. (2007).

resembling the red peak of the anticipated double-peak profile (e.g Nilsson et al., 2007; Grove et al., 2009). Figure 1.2 shows some typical LAE line profiles. In some cases this may simply be an issue of insufficient spectral resolution, but galactic outflows or absorption in the intergalactic medium (IGM) could also be the cause.

To cast light upon the physical mechanisms that might govern these phenomena and thus learn more about the LAEs themselves, the complex problem of Ly α RT needs to be solved. The puzzle is further complicated by the possible presence of dust in the galaxies, the effect of which is yet quite poorly constrained. Since photons are only observed from the location where their last scattering took place, it is difficult to say exactly where it was produced, how long a distance it has been traveling, as well as through which sort of regions. The problem of Ly α RT under various astrophysical circumstances has already been dealt with, both analytically (e.g., Osterbrock, 1962; Adams, 1972; Harrington, 1973; Neufeld, 1990; Loeb & Rybicki, 1999) and numerically (e.g. Ahn et al., 2000, 2001; Zheng & Miralda-Escudé, 2002; Cantalupo et al., 2005; Ta-

sitsiomi, 2006a; Dijkstra et al., 2006a; Hansen & Oh, 2006; Verhamme et al., 2006). Unfortunately, due to analytical and computational limitations, most of the works have had to consider only very simplified constellations of gas, not capturing the full intricacy of realistic astrophysical situations. A number of studies have used cosmological simulations to predict the appearance and emergent spectrum from LAEs (e.g., Fardal et al., 2001; Furlanetto et al., 2003, 2005; Barton et al., 2004; Gnedin & Prada, 2004; Cantalupo et al., 2005; Le Delliou et al., 2005, 2006). However, with a few important exceptions (Cantalupo et al., 2005; Tasitsiomi, 2006a; Laursen & Sommer-Larsen, 2007; Kollmeier et al., 2010; Faucher-Giguère et al., 2010), traditionally the radiative transfer (RT) of Ly α radiation has been treated as absorption instead of scattering, simply modifying the observed intensity by a factor of $e^{-\tau}$, where τ is the optical depth of neutral hydrogen lying between the emitter and the observer. For moderately thin media, this may be an acceptable approximation, since the radiation is scattered out of the direction to the observer, but in the dense regions in the vicinity of the emitter, radiation that is initially emitted in a different direction may be scattered *into* the direction of the observer.

1.3 Structure

Toward these ends, a numerical code, capable of predicting the diffusion of Ly α radiation in real and frequency space, as well as the effects of dust, is constructed and applied to simulated galaxies resulting from a fully cosmological simulation. An early, more primitive version of the code has already addressed the question of the extendedness of LAEs (Laursen & Sommer-Larsen, 2007), and the present code expands on this work. The dissertation is structured as follows:

In the remainder of Part **I** the project is put into context by describing in sufficient detail the theoretical background and the equations necessary for understanding the requirement for, and the development of, the numerical RT code that is the mainstay of this work. The different types of galaxies that will be investigated are described, the basic theory of resonant scattering and dust, and a brief account of the IGM.

Part **II** presents first the underlying cosmological simulations to which the RT code is applied, and subsequently the details of code itself are explained. In Chapter **8** the code is extensively tested against a numbers of situations for which analytical solutions exist. Also in this chapter, various convergence tests and parameter studies are discussed, which are probably better understood after having seen the results. Finally, the scheme for performing RT in the IGM is described.

Each of the first four chapters of Part **III** elaborate on the tangible fruit of three years' labor — three papers written (Paper **I**; Paper **II**; Paper **III**), and one co-written (Paper **IV**), by the author of this thesis. Longer sections of these chapters are taken directly from the papers, but much is rearticulated, expanded, and/or reshuffled to create a coherent presentation. Three of the chapters represent theoretical results obtained from numerical simulations, while the fourth report on related observational achievements. The main conclusions are summarized and discussed in Chapter **14**, where also future prospects are considered.

The appendices in Part **IV** features a quantum mechanical derivation of the hydrogen cross section, illuminating under which circumstances it is valid. Subsequently, the abstracts of each of the four papers are provided.

If you are currently reading the .pdf version of the thesis, the references in the bibliography are hyperlinks taking you to the online NASA ADS database. A version including the full papers can be downloaded from the URL www.dark-cosmology.dk/~pela/PhD/PhD.html.

Chapter 2

Galaxies in the early Universe



THE GRACEFUL, REVOLVING ARMS of spiral galaxies, the symmetry, the beautiful colors and patterns, the colossal masses and sizes, impels the astronomer to unveil their origin. How did such marvelous objects come into existence? How did they evolve? What are they made of? In order to answer these questions, physical theories and observational data must be united to construct a comprehensive picture.

The formation of a galaxy can be outlined as follows: primordial quantum fluctuations existing immediately after the creation of the Universe — the Big Bang — and being blown up to astronomical sizes by the inflation, grow in amplitude with time, due to the gravitational attraction of matter. Since dark matter outbalances baryonic matter by a factor of five, the dynamics and structure formation of both are initially governed by dark matter. Eventually, some 400 Myr after the Big Bang, the gas falling into the huge potential wells created by the dark matter becomes dense enough that it may collapse further, giving birth to stars. The very first stars — “Pop III” — are thought to be extremely massive and luminous, since the pristine, metal-free gas is not able to ignite fusion before several hundreds of solar masses of gas have accreted. The massive amount of radiation, and the feedback imposed by the exploding stars generate galactic superwinds that blow out from the proto-galaxy with speeds of thousands of km s^{-1} . At this time, the gas in the Universe is largely neutral, and the hard UV radiation from the stars cannot travel far before ionizing the hydrogen. At first the high density of the gas means that it quickly recombines, making it virtually impossible for any radiation with an energy higher than that of the hydrogen ionization potential to escape. This era in the history of the Universe is referred to as *the Dark Ages*. Eventually, the continuous emission of ionizing radiation, together with the expansion of the Universe diluting the gas, makes it possible to create “bubbles” of ionized hydrogen around the galaxies that grow in size and ultimately overlap, making the Universe largely ionized. This “Epoch of Reionization”, described further in Sec. 5.2 marks the end of the Dark Ages (e.g. Ferrara, 2003), and is thought to take place during a relatively short period of time, cosmologically speaking. The exact course, however, is still quite far from

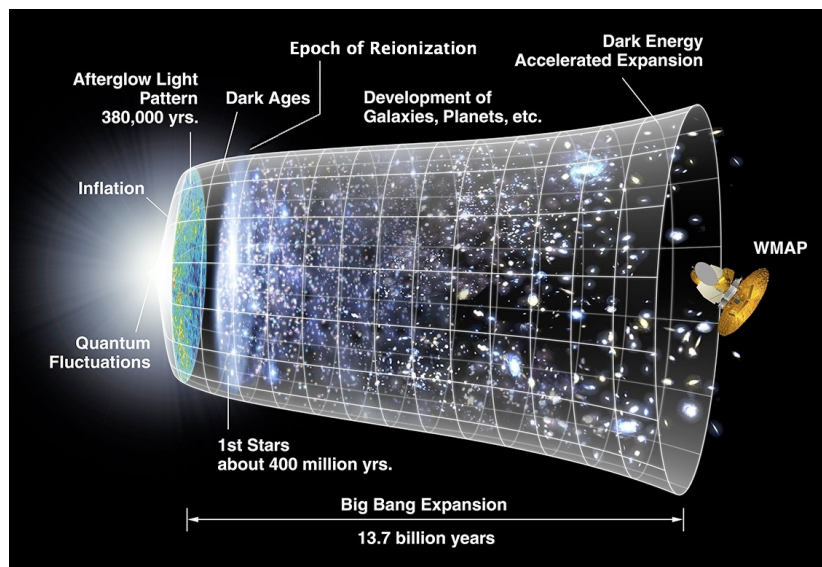


Figure 2.1: Timeline of the Universe: Two spatial dimensions, plus time increasing from left to right. The Universe was born 13.7 Gyr ago, and has expanded ever since. From the recombination of hydrogen 380 000 years after the Big Bang, to its reionization approximately half a Gyr later, the Universe was opaque to UV radiation, and since the first stars emit primarily in this wavelength region, observing the very first galaxies is a challenging task. Credit: NASA/WMAP Science Team.

being well understood. Figure 2.1 summarizes the above discussion in graphics.

Observing galaxies in their infancy is a challenging task: apart from the opacity of the IGM, their mere distance makes them so faint that they easily drown in the diffuse background radiation of star light. Moreover, at redshifts $z \gtrsim 1.5$, the angular diameter of an object begins to *increase*, thus lowering its SB, making it even fainter.

Looking for such faint blobs in an image, making sure that it is not only noise, or irrelevant foreground objects, clearly requires special techniques. Whereas distant galaxies were once only spotted in visible wavelengths on photographic plates imaging everything along the line of sight, modern filters, CCDs, and spectrographs now make it possible to confine the search to specific regions in space, time, and wavelength.

Obviously the physical properties of galaxies do not depend on the means by which they are observed, but different techniques impose different selection criteria on the observed galaxy population. If one searches for galaxies in a particular wavelength region, one will tend to find a special kind of galaxies, namely those that are bright in this region. Merging various galaxy populations is a major goal of galaxyology. In the present work we will be studying three distinct populations, viz. the already introduced LAEs, along with the so-called *Lyman-break galaxies*, and *damped Ly α absorbers*. To get a notion of their individual selection criteria and their overall physical properties, the following three sections

describe these three populations.

2.1 Ly α emitters

Ly α emitters (LAEs) are simply galaxies observed in Ly α , achieved either through spectroscopy or through narrowband imaging. Since a redshift of ~ 1.5 is needed to shift the ultraviolet wavelength of Ly α into the optical atmospheric window, ground-based observations generally yield high-redshift LAEs (e.g. Cowie & Hu, 1998; Fynbo et al., 2001; Venemans et al., 2005; Iye et al., 2006; Nilsson et al., 2009). Nearby LAEs are only observable from space, with the International Ultraviolet Explorer satellite (IUE; e.g. Meier & Terlevich, 1981; Terlevich et al., 1993), the Galaxy Evolution Explorer (GALEX; e.g. Deharveng et al., 2008), and the Hubble Space Telescope (HST; e.g. Hayes et al., 2007; Atek et al., 2008; Östlin et al., 2009). Narrowband imaging has the advantage that many LAE candidates can be found simultaneously, but to investigate a non-vanishing volume of space the width of the filter cannot be too small, and thus the redshift determination is not very accurate. Spectroscopically confirmed LAEs cannot only pinpoint their redshift precisely, but also make sure that an object is in fact an LAE and not an interloper emitting strongly at another wavelength. Common contaminants are H α / β and [OII/III] emitters located at lower redshifts. On the other hand spectroscopy is very time-consuming, usually requiring each object to be targeted individually for several hours.

2.1.1 Sources of emission

A Ly α photon is emitted from a hydrogen atom in the first excited state. Several physical processes may result in the atoms being in this state, but can in most cases be divided into recombinations following the ionization of the hydrogen, or collisions with other atoms. In the context of galaxies, three distinct processes are the main contributors to Ly α . These are described below, along with a fourth agent that may in some cases outshine the others — a quasar.

Stellar sources

The most significant source to Ly α radiation in young galaxies is recombining hydrogen following ionization by the hard UV radiation from massive stars. At the onset of star formation, UV radiation from young, hot, massive stars will ionize the surrounding neutral hydrogen (HI). When the protons and electrons recombine, a fraction of the recombinations will result in the emission of a Ly α photon. Spitzer (1978) found that, at $T = 10^4$ K, a typical temperature of the HII/HII regions, approximately 38% of the recombinations go directly to the ground state. The result is then just another ionizing UV photon. Eventually, a recombination will go to a higher state, subsequently cascading down the various states, generating one or more photons with insufficient energy to ionize hydrogen. If the result is a photon with more energy than the Ly α photon, it may excite a hydrogen atom. In the end, the effect will be an atom excited to the first state. However, if this state is the $2S$ state, the most probable decay is via an intermediate state, resulting in the emission of two photons, each with less energy than a Ly α photon. Only in the $2P$ state can the atom decay

directly to the ground state, emitting a Ly α photon (see Sec. A.4). Spitzer (1978) found that, at $T = 10^4$ K, ultimately 68% of the recombinations are accompanied by the emission of a Ly α photon. This fraction is only mildly sensitive to temperature; for 5×10^3 K (2×10^4 K) the fraction is 70% (64%). This is the scenario described by Partridge & Peebles (1967), who argued that as much as 10% of the total luminosity of the galaxy may be emitted as Ly α .

Gravitational cooling

Galaxies are formed from gas falling from the IGM into the deep potential wells created by mostly dark matter, collapsing under its own gravity. As the gas becomes more dense, atomic collisions become more frequent, heating the gas to several million degrees, which cools and emits Ly α , i.e. the potential energy of the gas is released as cooling radiation. Fardal et al. (2001) find that, at high redshifts, most of this radiation is emitted by gas with $T < 20\,000$ K, and consequently $\sim 50\%$ in Ly α alone.

UV background radiation

UV radiation that is not absorbed in the interstellar medium (ISM) escapes its host galaxy. Whether emanating from massive stars or from quasars, in this way the Universe was reionized at a redshift around $z \sim 6\text{--}11$, and the IGM was filled up with a ubiquitous, *metagalactic* UV background (UVB). This field pierces through some or all of the neutral hydrogen in the young galaxies. For column densities N_{HI} less than about $10^{17.2} \text{ cm}^{-2}$, the optical depth for a UV photon is of the order unity, meaning that the whole system can be penetrated. In most galactic systems, however, N_{HI} is so large that the inner regions become self-shielded from the UV field. Systems with $10^{17.2} \text{ cm}^{-2} < N_{\text{HI}} < 10^{20.3} \text{ cm}^{-2}$ are referred to as Lyman limit systems (LLSs), while systems with $N_{\text{HI}} > 10^{20.3} \text{ cm}^{-2}$ are called damped Ly α absorbers (DLAs), since for column densities higher than this the damping wings of the absorption line profile become apparent. Although the Ly α photons resulting from the UVB are only about 1% of those resulting from massive stars, the mechanism is the same — the neutral gas is photo-ionized, recombines, and produces Ly α radiation. Moreover, the UV field can also photo-heat non-self-shielded gas, which subsequently cools, radiating Ly α (Furlanetto et al., 2005).

Quasars and superwinds

A particular class of Ly α emitting objects, known as “Ly α blobs” (LABs) has been known now for a decade (Fynbo et al., 1999; Steidel et al., 2000; Matsuda et al., 2004; Nilsson et al., 2006). Although LABs are extremely large (a few tens to >150 kpc) and very Ly α -luminous (up to $5 \times 10^{43} \text{ erg s}^{-1}$), they exhibit little or no continuum radiation. Hence, a probable mechanism behind these objects could be cooling radiation (Haiman et al., 2000; Fardal et al., 2001; Dijkstra et al., 2006a,b), although the phenomenon has also been attributed to hidden quasars and superwinds:

Many, if not all, galaxies go through a phase in their early life in which gas accreting onto a central, supermassive black hole results in an active galactic nucleus (AGN), ejecting tremendous amounts of energy in two jets along the

axis of rotation. A sub-class of AGNs are the quasars, or QSOs. The jets may then ionize surrounding gas, possibly producing Ly α radiation (Haiman & Rees, 2001; Weidinger et al., 2004, 2005)

Even if no quasar is present, superwinds from starbursts and supernovae (SNe) sweeping up surrounding material may have the same effect (Taniguchi & Shioya, 2000; Taniguchi et al., 2001; Mori et al., 2004; Wilman et al., 2005).

2.1.2 Physical characteristics

As with many other galaxy “types”, the term “LAEs” represents a selection method, not a physically distinct category of galaxies. Nevertheless, one may speak of a *typical* LAE as a fairly small, quite young, relatively highly star-forming galaxy or proto-galaxy, of rather low metallicity and dust contents. However, large deviations from this exist.

Ages

The ages of LAEs, i.e. the time that has passed since the onset of star formation, has typically been found to be of the order 100 Myr (Lai et al., 2007, 2008), but ages of ~ 10 Myr (Gawiser et al., 2007; Pirzkal et al., 2007; Finkelstein et al., 2008) and ~ 1 Gyr (Nilsson et al. 2007, and Lai et al. 2008, when including objects also detected with IRAC) have also been found.

Stellar masses

LAEs are generally small systems. Their stellar masses can be obtained, or at least constrained, through spectral energy distribution (SED) fitting. Such fitting have found typical masses of $M_*/M_\odot \sim 10^8$ - 10^9 (Gawiser et al., 2006a; Lai et al., 2007; Finkelstein et al., 2007; Nilsson et al., 2007).

Star formation rates

One of the essential characteristics of a galaxy is its star formation rate (SFR), i.e. the amount of gas mass converted into stars per unit time. Typical LAE SFRs lie in the range 1 - $10 M_\odot \text{ yr}^{-1}$ (Cowie & Hu, 1998; Hu et al., 1998; Gronwall et al., 2007; Nilsson et al., 2007). This may be compared to the Milky Way SFR of around $1 M_\odot \text{ yr}^{-1}$ (e.g. Robitaille & Whitney, 2010)), but taking into account their low masses reveals that LAEs have the highest *specific* SFR (sSFR; the SFR divided by stellar mass) of any type of galaxy, a signature of their young ages (Castro Cerón et al., 2006).

Metallicities and dust contents

Perhaps the most debated attribute of LAEs is their dust contents and its influence on their observability. Due to the resonant scattering of the Ly α photons increasing the path out of the galaxies by a large and unknown factor, Ly α may be much more vulnerable to dust than continuum radiation. Accordingly, LAEs have been thought to be relatively free of dust. The color excess $E(B - V)$, defined as the difference between the extinction in the B band and the V band, is a measure of the amount of dust in a galaxy, since it quantifies the reddening of the continuum. At $z \sim 3$, Gronwall et al. (2007) find $E(B - V)$'s lying

approximately in the range 0.01 to 0.1. Verhamme et al. (2008) find similar values by fitting line profiles using a radiative transfer model similar to the one developed in this work.

At somewhat higher redshifts, $z \sim 5$, marginal evidence for slightly higher extinction have been reported (Lai et al., 2007; Finkelstein et al., 2007), although also similar values are found (Pirzkal et al., 2007).

Since dust is made of metals, the amounts of dust must in some way be correlated with metallicity. In general, approximately half of the produced metal deplete onto dust, with only marginal evidence for a redshift evolution (see, e.g., Fig. 1 of Pei, Fall, & Hauser, 1999).

Clustering properties

Galaxies are thought in some way to trace the underlying dark matter distribution (e.g. Kaiser, 1984; Bardeen et al., 1986). This distribution is of course inherently impossible to observe, but one way to learn about the enigmatic dark matter is by studying the clustering properties of galaxies, usually quantified through the two-point correlation function. However, due to the complexities involved in both the formation and the radiative transfer of Ly α , no consensus has yet been reached on whether or not LAEs are a good tracer. To substantiate this issue, probably much larger volumes needs to be surveyed (Orsi et al., 2008).

As LAEs are, in general, smaller systems than other high-redshift populations such as Lyman-break galaxies (see next section), sub-mm galaxies (SMGs), and distant red galaxies (DRGs), they provide an opportunity of probing the faint end of the bolometric luminosity function (LF). Other populations are heavily biased toward having strong continua, thus implying very massive galaxies, in turn implying that they probe preferentially the overpopulated regions of the Universe like galaxy clusters.

Evolution

Looking at the LF of LAEs, no significant evolution seems to occur from $z \sim 6$ to $z \sim 3$ (Ouchi et al. 2003; Maier et al. 2003; Malhotra & Rhoads 2004; van Breukelen 2005; Shimasaku et al. 2006, but see also Kashikawa et al. 2006)

Comparing $z = 2.25$ LAEs in the COSMOS field with LAEs at $z \sim 3$, corresponding to a time interval of roughly one Gyr, Nilsson et al. (2009) studied the evolution of LAEs. They found that the sample at the lower redshift appears to be characterized by redder objects as well as an increase in the ratio between SFRs inferred from UV and those inferred from Ly α . Both of these factors are a signature of the LAEs becoming more dusty, which is in accord with what may be expected (more on this in Chap. 4). Moreover, the distribution of equivalent widths (EWs) becomes narrower with time. This is consistent with the higher UV-to-Ly α SFRs, since the EW is proportional to the ratio of the Ly α flux to UV flux, similar to the SFRs.

Finally, the fraction of LAEs containing AGN was found to increase. This is also expected, since $z \sim 2$ corresponds to the peak of the AGN number density distribution (e.g. Wolf et al., 2003b).

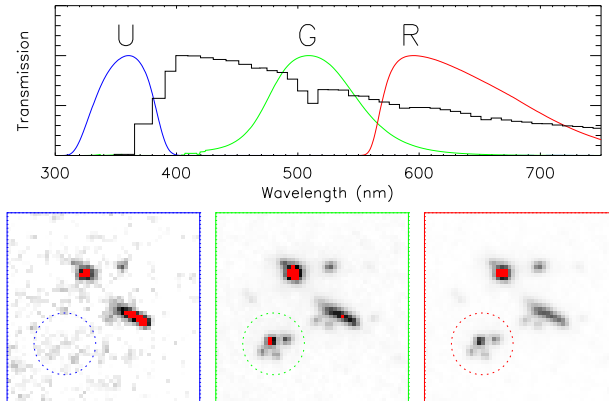


Figure 2.2: Demonstration of the LBG technique. *Top:* Due to the presence of neutral hydrogen, the spectrum of a galaxy exhibits a “break” at a rest wavelengths of 912 Å, in this case redshifted to around 400 Å, i.e. corresponding to a redshift of ~ 3.4 . Almost no flux hence enters the *U*-filter (central wavelength 3600 Å), whereas the galaxy is easily detected in the *G*-filter (central wavelength 5100 Å). The actual images are seen in the *bottom* plot. The redshift of the galaxy can in this case be constrained to lie between $z_{lo} \sim 3600/900 - 1 = 3$ and $z_{hi} \sim 5100/900 - 1 \sim 4.5$. To further constrain the redshift, spectroscopic follow-up is needed. *Credit:* J. P. U. Fynbo.

2.2 Lyman-break galaxies

The *Lyman-break* is the sharp drop in intensity in the spectrum of a galaxy, located at a (rest) wavelength of 912 Å. This wavelength matches the ionization potential of neutral hydrogen, so photons of shorter wavelengths will have a high probability of being absorbed before escaping the galaxy. Observing a region of the sky in several filters may thus reveal an image of a galaxy in the “redder” filters, whereas the sky seems empty in the “bluer” filters. Figure 2.2 shows an example of this.

Since large areas can be surveyed for many galaxies simultaneously, this technique significantly moved forward the frontier of galaxy surveys. While first mentioned by Meier (1976), it was not employed to detect high-redshift galaxies until almost two decades later, the first being Steidel & Hamilton (1993) (although it was used to put constraints on the abundances of galaxies at $z > 3$ a few years earlier (Guhathakurta et al., 1990; Songaila et al., 1990)). By now, the total sample a galaxies detected in this way — appropriately dubbed Lyman-break galaxies (LBGs), or drop-out galaxies — probably approaches 10 000 (Steidel et al., 2003; Madau et al., 1996; Pettini et al., 2001; Bunker et al., 2004; Stanway et al., 2004; Ouchi et al., 2004a,b; Wadadekar et al., 2006). LBGs tend to be somewhat older and more massive than LAEs, with stellar masses lying in the range 10^9 to $10^{11} M_{\odot}$. Their SFRs are typically higher, reaching several hundred $M_{\odot} \text{ yr}^{-1}$ (e.g. Rigopoulou et al., 2006; Shapley et al., 2001). Considerable amounts of dust are observed to reside in the LBGs (e.g. Sawicki & Yee, 1998; Calzetti, 2001; Takeuchi & Ishii, 2004; Rigopoulou et al., 2006), with extinction from $A_V \simeq 0.3\text{--}0.5$ (Shapley et al., 2001; Verma et al.,

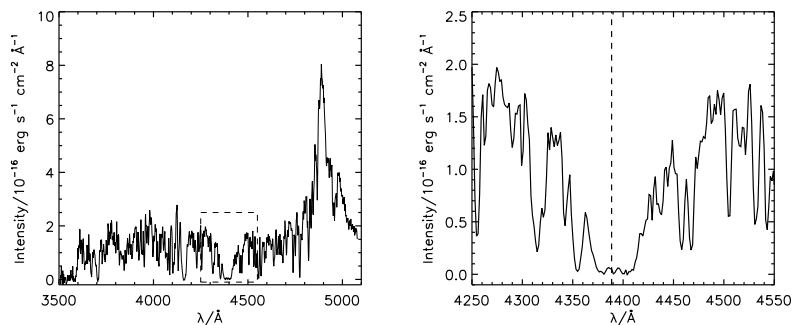


Figure 2.3: Full spectrum of the quasar Q2348-011 at $z = 3.0$ (*left*) and a zoom-in on the region around a DLA situated at $z = 2.6$. This spectrum was acquired at the Nordic Optical Telescope by the author and collaborators, and will be discussed further in Chap. 13.

2007) to $A_V \simeq 1-2$ (Papovich et al., 2001). Their clustering properties appear to be similar to those of LAEs (Steidel et al., 1998; Giavalisco et al., 1998; Ouchi et al., 2004b).

2.3 Damped Ly α absorbers

The LAEs and LBGs described above, together with other populations such as SMGs and DRGs, all have in common that they are selected by virtue of their emission. Damped Ly α absorbers (DLAs), in contrast, are identified by their ability to cause broad absorption lines in the spectra of bright background sources. The “bright background source” will usually be a quasar, but may also be more transient sources such as a SN or gamma-ray burst (GRB).

As will be discussed in further detail in Sec. 5.1, the IGM consists of diffuse clouds of neutral hydrogen of various column densities. As the intense light from a source travels through the IGM, it suffers a cosmological redshift by the expansion of the Universe. If a sufficient amount of neutral hydrogen happens to be located at the place where a given wavelength region initially with a wavelength bluer than that of Ly α has been redshifted to 1216 \AA , the spectrum will be subjected to an absorption line. For clouds of column densities $N_{\text{HI}} \gtrsim 10^{20.3} \text{ cm}^{-2}$, the absorption feature becomes so broad that the damping wings of line profile, i.e. the part of the profile caused by natural broadening as opposed to thermal broadening, becomes visible. An example of such a system, the DLA, is seen in Fig. 2.3. Sometimes the absorption feature itself is labelled “DLA”, but usually the term refers to the system responsible of the absorption.

At $z \sim 3$, most of the neutral gas in the Universe is contained within DLAs (O’Meara et al., 2007). The fact that DLAs are in their very nature self-shielded against the ionizing UVB implies that the gas is able to cool sufficiently to initiate star formation. This makes them obvious candidates for present-day galaxies (Wolfe et al., 1986).

Due to the high luminosity of the background quasars, detecting galaxies associated with DLAs is, in general, a strenuous task. Both the scarce number of

observations (e.g. Paper IV) and numerical simulations (e.g. Pontzen et al., 2008) indicate that a characteristic impact parameter for the line of sight through the hydrogen cloud responsible for the absorption is, at most, ~ 10 kpc, corresponding at a redshift of $z \sim 3$ to the order of an arcsecond. Consequently, even under very good seeing conditions, detection of a galaxy against a bright quasar will be extremely difficult. For this reason, not much is known about the underlying galaxy population resulting in DLAs, if at all there is such a “population”. The number of known DLAs now exceeds one thousand (Prochaska et al., 2005; Noterdaeme et al., 2009). By selection they are very gas rich. Since DLAs are always accompanied by narrow metal lines at the same redshift, at least some star formation is expected to have been occurring for a while (Vladilo, 1999; Wolf et al., 2003a). However, inferred metallicities are usually quite low ($[X/H]^1 \sim -1$ (Vladilo, 2002; Savaglio et al., 2000), and even down to -2 (Pettini et al., 1997, 1999), indicating that the systems must be very young.

¹Here, X denotes a generic term for various metals, and the metallicity $[X/Y]$ is a convenient way of writing $\log(X/Y) - \log(X_{\odot}/Y_{\odot})$. Usually metals that are believed not to deplete significantly to dust are used, e.g. Zn (Roth & Blades, 1995).

Chapter 3

Resonant scattering



IT HAS BEEN STATED THAT “*galaxies are to astronomy what atoms are to physics*” (Sandage, 1961). However, whereas the physics of atoms can easily be studied with no knowledge of galaxies, the converse is certainly not true. To gain more intuition about the concept of resonant scattering and the conditions under which the derived atomic cross section — crucial to the developed code — is valid, the proper quantum mechanical derivation of the cross section will now be reviewed. For a more thorough derivation, see, e.g., Bransden & Joachain (2003).

We will then proceed to go deeper into the actual scattering process and finally discuss the spatial motion of the photons, establishing how radiative transfer is a journey, or diffusion, in both real and frequency space.

3.1 Atomic cross section

The cross sectional area of the scattering hydrogen atom is dependent on the frequency ν of the photon. Only if its energy matches closely the energy difference $E_f - E_i$ between the initial state ψ_i and final state ψ_f of the hydrogen atom — if it is in *resonance* — does it have a large probability of exciting the electron. Traditionally, this cross section is expressed as

$$\sigma_\nu = \frac{\pi e^2}{m_e c} f_{if} \phi_{if}(\nu), \quad (3.1)$$

where $-e$ and m_e is the charge and the mass of the electron, respectively, f_{if} is the *oscillator strength*, and $\phi_{if}(\nu)$ is the normalized line profile of the corresponding transition, giving the probability of interaction as a function of frequency. For the Ly α transition, $i = 1$ and $f = 2$.

Historically, the electron-proton system was viewed as an oscillating spring, and the oscillator strength was introduced as an empirically determined quantity for optical transitions with bound electrons. However, it can also be derived analytically by considering the Hamiltonian of the interaction of the atom with a photon. This is done in App. A, yielding the absorption cross section for the

Ly α transition to be

$$\sigma_\nu = f_{12} \frac{\pi e^2}{m_e c} \frac{\Delta\nu_L/2\pi}{(\nu - \nu_0)^2 + (\Delta\nu_L/2)^2}, \quad (3.2)$$

where

$$f_{12} = 0.4162 \quad (3.3)$$

is the oscillator strength,

$$\nu_0 = 2.466 \times 10^{15} \text{ s}^{-1} \quad (3.4)$$

is the line center frequency, and

$$\Delta\nu_L = 9.936 \times 10^7 \text{ s}^{-1} \quad (3.5)$$

the natural line width.

It is of conceptual importance to understand that the cross section — contingent on the assumption that an ensemble of non-interacting particles is incident upon the scatterer — must be interpreted in a statistical sense, whether described classically or quantum mechanically. In the classical limit, each incident particle can be assigned an impact parameter, i.e. a distance to the axis parallel to which it approaches the scatterer. It is the essence of scattering cross section measurements that no effort be made to determine the actual path of an individual particle.

3.1.1 Thermal broadening of the line profile

The result obtained in Eq. 3.2 gives the probability distribution function (PDF) for a hydrogen atom absorbing a photon of frequency ν . However, so far it was assumed that the scattering atom is at rest. If the atom is moving with (non-relativistic) velocity \mathbf{v}_{atom} , the frequency of the photon will be Doppler shifted in the reference frame of the atom. To first order, a Lorentz transformation yields

$$\nu' = \nu \left(1 - \frac{\hat{\mathbf{n}}_i \cdot \mathbf{v}_{\text{atom}}}{c} \right), \quad (3.6)$$

where $\hat{\mathbf{n}}_i$ is a unit vector representing the direction of the incident photon.

The total velocity of the atoms is a sum of several contributions, which can be divided into two categories; macroscopic and microscopic. Macroscopic velocity is the total bulk motion of the gas, e.g. the turbulent motion of the fluid elements and/or an overall expansion of a gas cloud. This is most easily taken into account by a Lorentz transformation between reference frames (numerically between adjacent cells of the simulation, see Sec. 7.2.4) using Eq. 3.6. Microscopic velocities can be due to pressure, i.e. atom collisions. This was verified in Sec. A.4 to be insignificant in the environments studied in the present work. However, it could easily be implemented in the model, since collisions give rise to a Lorentzian profile (e.g., Emerson, 1996). Equation 3.5 would then be replaced by

$$\Delta\nu_{L,\text{nat.}+\text{coll.}} = \frac{E_{2,\text{nat.}+\text{coll.}}}{h_{\text{Pl}}} = 2\pi \left(\frac{1}{t_{1/2}} + \frac{1}{t_{1/2,\text{coll.}}} \right), \quad (3.7)$$

where h_{Pl} is Planck's constant,

$$t_{1/2} = 1.60 \times 10^{-9} \text{ s} \quad (3.8)$$

is the natural half-life of the excited state (compare with Sec. A.4) and $t_{1/2, \text{coll}}$ is the half-life of the excited state due to the possibility of the electron being de-excited by collisions.

The second microscopic effect is the random thermal velocity of the gas. For a gas at some temperature T , these velocities follow a Maxwellian distribution, i.e. a Gaussian distribution in three mutually perpendicular directions. Equating the kinetic energy of the individual particles to their thermal energy, the thermal velocity dispersion (times $\sqrt{2}$) is

$$v_{\text{th}} = \left(\frac{2k_B T}{m_H} \right)^{1/2} \quad (3.9)$$

$$= 12.85 T_4^{1/2} \text{ km s}^{-1}, \quad (3.10)$$

where k_B is Boltzmann's constant, m_H is the mass of the hydrogen atom, and $T_4 = T/(10^4 \text{ K})$. From Eqs. 3.6 and 3.9 the associated Doppler frequency shift $\Delta\nu_D$ of the frequency distribution is then

$$\Delta\nu_D = \frac{v_{\text{th}}}{c} \nu_0 \quad (3.11)$$

$$= 1.057 \times 10^{11} T_4^{1/2} \text{ s}^{-1}. \quad (3.12)$$

To simplify notation, frequency will be parametrized through

$$x \equiv \frac{\nu - \nu_0}{\Delta\nu_D}. \quad (3.13)$$

In terms of these quantities, with $\phi(\nu)d\nu = \phi(x)dx$, the thermal line profile is then

$$\mathcal{G}(x) = \frac{1}{\sqrt{\pi}} e^{-x^2}, \quad (3.14)$$

while the natural line profile is

$$\mathcal{L}(x) = \frac{a}{\pi} \frac{1}{x^2 + a^2}, \quad (3.15)$$

where

$$a \equiv \frac{\Delta\nu_L}{2\Delta\nu_D} \quad (3.16)$$

is (half) the relative line width, or the ‘‘damping parameter’’.

The resultant line profile in the reference frame in which the gas is on average in rest (the Lagrangian frame of the fluid element) is a Voigt profile, i.e. a convolution of the Lorentzian and the Gaussian:

$$\begin{aligned} \mathcal{V}(x) &= \int_{-\infty}^{\infty} \mathcal{L}(x-y) \mathcal{G}(y) dy \\ &= \frac{1}{\sqrt{\pi} \Delta\nu_D} H(a, x), \end{aligned} \quad (3.17)$$

where

$$H(a, x) = \frac{a}{\pi} \int_{-\infty}^{\infty} \frac{e^{-y^2}}{(x-y)^2 + a^2} dy \quad (3.18)$$

is the Voigt function, and $\int_{-\infty}^{\infty} \mathcal{V}(x) dx = 1$, since the same is true for \mathcal{L} and \mathcal{G} , and convolution conserves normalization.

Thus, we may write the final cross section of the hydrogen atom as

$$\sigma_x = f_{12} \frac{\sqrt{\pi} e^2}{m_e c \Delta \nu_D} H(a, x). \quad (3.19)$$

To get a notion of the magnitude of the cross section, for a temperature of 10^4 K it evaluates in the line center to

$$\sigma_0 = 5.898 \times 10^{-14} \text{ cm}^2, \quad (3.20)$$

four orders of magnitude larger than the HI cross section at the Lyman limit.

3.2 Scattering

3.2.1 Frequency shift

It must be emphasized that the discussed broadening of the line and the corresponding uncertainty in energy does *not* imply that a photon of a given energy can be absorbed, and subsequently re-emitted with a different energy. Indeed, this would be possible had the energy of the ground state been associated with an uncertainty in energy as well. However, since the lifetime of this state is effectively infinite, its energy is well-defined. Except for a very small recoil effect, which will be discussed in Sec. 3.2.3, the scattering is coherent in the reference frame of the atom. However, to an external observer, any motion of the atom will, in general, add a Doppler shift to the photon.

Measuring the velocity of the atom in terms of the thermal velocity,

$$\mathbf{u} = \frac{\mathbf{v}_{\text{atom}}}{v_{\text{th}}}, \quad (3.21)$$

allows us to compare directly frequency and velocity, so that Eq. 3.6 reads

$$x' = x - \mathbf{u} \cdot \hat{\mathbf{n}}_i, \quad (3.22)$$

where x' is the frequency as measured in the reference frame of the atom. Figure 3.1 shows a qualitative interpretation of how the Doppler shift arises.

Consequently, to track the photons in both real and frequency space, it is important to know both the direction in which the photon is scattered *and* the exact velocity of the scattering atom.

One may ask if it makes sense to refer to the photon as being the same before and after the scattering event, since in fact it ceases to exist (for about 10^{-9} seconds), and since, to the external observer, its energy has changed. However, even though it does not exist for a short while, in the reference frame of the atom — which is just as good as any other reference frame — the photon retains a “memory” of its energy before the event. Its state of existence is thus not independent of its former being, and the fact that its intrinsic properties seem

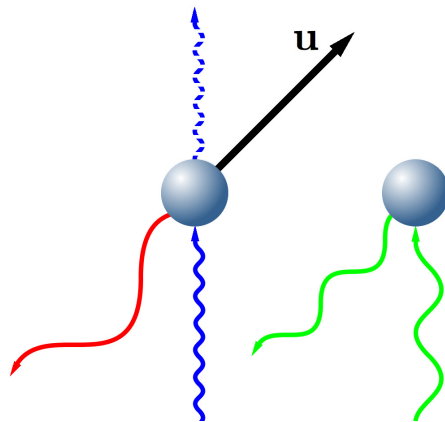


Figure 3.1: Illustration of the mechanism responsible for the frequency shift of a scattered photon. In the reference frame of an external observer (*left*), a photon blueward of the line center (*blue*) is scattered by an atom receding in such manner that the component of its velocity \mathbf{u} along the direction of the photon matches closely the frequency x . In the reference frame of the atom (*right*), the photon then seems close to the line center (*green*). Except for a minute recoil effect, the photon leaves the atom with the same frequency. However, to the external observer, if the photon is scattered in a direction opposite the atom's motion (*red*), it will be redshifted. Only if by chance it is scattered in the exact same direction (*dashed blue*), its frequency remains unaltered. For $|x| \gg 1$, the number of atoms with sufficiently high velocities is so small that the photon is most likely to be scattered by a low-velocity atom. In this case, no matter in which direction the photon is scattered the motion of the atom will not shift the frequency significantly.

to change is just a consequence of us not moving along with the atom. Hence, from any philosophical and, in particular, pragmatic point of view, we propose that a photon be one and the same photon, until it is destroyed by some other physical process.

3.2.2 Phase function

When light is scattered, it may be polarized. A full discussion of the concept of polarization is beyond the scope of this thesis (albeit it would certainly be interesting — and feasible — to numerically probe the polarization of the scattered light from young galaxies). However, we note that polarization is strongly connected with the direction of scattering, in that the radiation will be more polarized, the closer to 90° the scattering is (e.g., Chandrasekhar, 1950). Thus, isotropic scattering will on average result in unpolarized light.

Core scattering

The probability distribution of the directions of scattering is given by the *phase function* $W(\theta)$, where θ is the angle between the direction vectors $\hat{\mathbf{n}}_i$ and $\hat{\mathbf{n}}_f$ of the incident and outgoing photon, respectively (for reasons of symmetry,

the scattering must always be isotropic in the azimuthal direction and hence independent of ϕ). [Hamilton \(1940\)](#) found that $W(\theta)$ is determined by the multipole order of the emitted radiation and the difference in total angular momenta J of the three involved states, i.e. the initial, intermediate and final state. Specifically, in the dipole approximation (see [Sec. A.2](#)) the phase function is,

$$W(\theta) \propto 1 + \frac{R}{Q} \cos^2 \theta, \quad (3.23)$$

where R/Q is the degree of polarization for 90° scattering.

For resonant scattering, the initial and final state are the same, while the intermediate state corresponds to the excited state. For one-electron atoms, the spin quantum number is $s = \pm 1/2$. Since ℓ can assume values up to $n - 1$, the total angular momentum $J = \ell + s$ for the ground state is always $1/2$, while the first excited state can have $J = 1/2$ or $J = 3/2$. Thus, the involved states are the ground state $1S_{1/2}$ and the three excited states $2S_{1/2}$, $2P_{1/2}$ and $2P_{3/2}$. As discussed in [App. A](#), we ignore the possibility of being excited to the $2S_{1/2}$ state. It is then found ([Hamilton, 1940](#)) that for the $2P_{1/2}$ transition, with $J = 1/2$ and $\Delta J_{if} = \Delta J_{fi} = 1$,

$$\begin{aligned} \frac{R}{Q} &= \frac{(2J - 1)(2J + 3)}{12J^2 + 12J + 1} \\ &= 0, \end{aligned} \quad (3.24)$$

while for the $2P_{3/2}$ transition, with $J = 3/2$, $\Delta J_{if} = 1$ and $\Delta J_{fi} = -1$

$$\begin{aligned} \frac{R}{Q} &= \frac{(J + 1)(2J + 3)}{26J^2 - 15J - 1} \\ &= \frac{3}{7}. \end{aligned} \quad (3.25)$$

The spin multiplicity of each state is $2J + 1$, so the probability of being excited to the $2P_{3/2}$ state is twice that of the $2P_{1/2}$ state. Thus, changing variable to $\mu = \cos \theta$ so that $\mu \in [-1, 1]$, with a probability of $1/3$ the photon is scattered according to

$$\boxed{W_{\text{core},1/2}(\mu) = \frac{1}{2}}, \quad (3.26)$$

i.e. isotropically, while with a probability of $2/3$ according to

$$\boxed{W_{\text{core},3/2}(\mu) = \frac{7}{16} \left(1 + \frac{3}{7} \mu^2 \right)}. \quad (3.27)$$

Note that [Eqs. 3.26](#) and [3.27](#) are normalized to unity, not to $1/4\pi$.

Wing scattering

As indicated by the subscript in [Eqs. 3.26](#) and [3.27](#), the derived probability distributions are only valid in the ‘‘core’’ of the line profile, i.e. close to the line center. Investigating polarization of scattered light from the Sun, [Stenflo \(1980\)](#) found that in the ‘‘wings’’, the two lines of $2P_{1/2}$ and $2P_{3/2}$ interfere quantum

mechanically, making the scattering behave like that of a classical oscillator, i.e. pure Rayleigh scattering. In this case the direction follows a dipole distribution, with 100% polarization at 90° scattering. Thus, the normalized phase function is

$$W_{\text{wing}}(\mu) = \frac{3}{8} (1 + \mu^2). \quad (3.28)$$

The transition x_{cw} from core to wing scattering is not well-defined, but can be taken to be the value of x where the Gaussian and the Lorentzian contributes about equally much to the profile, i.e. where

$$\frac{1}{\sqrt{\pi}} e^{-x_{\text{cw}}^2} \sim \frac{a}{\pi x_{\text{cw}}^2} \quad (3.29)$$

The solution to this equation can be approximated as

$$x_{\text{cw}}(a) = 1.59 - 0.60 \log a - 0.03 \log^2 a. \quad (3.30)$$

The difference in the phase functions is not very important (this is verified by tests), but since the value of x_{cw} is calculated anyway in the process of determining the velocity of the scattering atom (Sec. 7.3.1) and in the acceleration scheme described in Sec. 7.5.1, the exact value is used.

3.2.3 Recoil effect

By conservation of momentum, except for the case when the photon is scattered in the same direction as the incident photon, at each scattering the photon must transfer some energy to the atom. Field (1959) found that, on average, the photon loses a fractional energy of

$$g = \frac{h\Delta\nu_D}{2k_B T}. \quad (3.31)$$

Except for very low temperatures, compared to the Doppler shift this effect is negligible, at least for a single scattering. However, as a photon easily undergoes millions or even hundreds of millions of scatterings, one might suspect that the cumulative energy loss would eventually shift all photons to the red side of the line. This was suggested by Kahn (1962). But as will be discussed in Sec. 3.3, when a photon is in the wing, there is a bias toward being scattered back toward the center, so that any systematic redshift will be counteracted. In this way, Eq. 3.31 can be understood as reflecting the thermalization of photons around the frequency ν_0 . Still, even though Adams (1971) argues that the effect of recoil *is* negligible (at least in the case of a homogeneous, static medium of uniform temperature), since the calculation is quite rapid it is not omitted in the developed code.

3.2.4 Atom velocity

As mentioned earlier, the velocities of the atoms follow a Gaussian probability distribution in three directions. However, due to the frequency dependency of the scattering cross section, the velocity distribution f of the atoms responsible

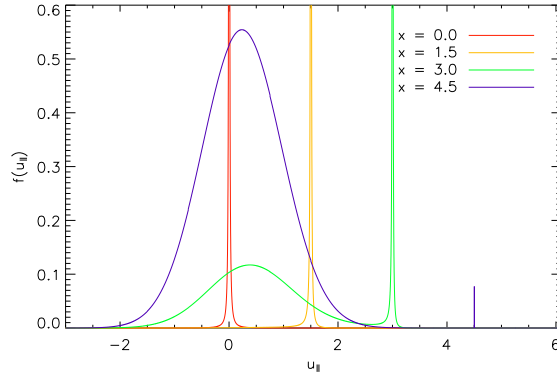


Figure 3.2: Probability function as given by Eq. 3.34 for a number of different frequencies. For $x = 0$, $f(u_{\parallel})$ simply resembles a normal Lorentz profile, but for larger values of x , the Gaussian part becomes increasingly significant.

for the scattering of a particular photon is quite different. Since motion perpendicular to $\hat{\mathbf{n}}_i$ does not contribute to any Doppler shift, a natural basis for \mathbf{u} is

$$\mathbf{u} = \begin{pmatrix} u_{\parallel} \\ u_{\perp,1} \\ u_{\perp,2} \end{pmatrix}, \quad (3.32)$$

where u_{\parallel} is the velocity parallel to $\hat{\mathbf{n}}_i$ and $u_{\perp,i}$, with $i = 1, 2$, are the — mutually orthogonal — velocities perpendicular to $\hat{\mathbf{n}}_i$. In this basis, $u_{\perp,i}$ still follow a Gaussian distribution, i.e.

$$\mathcal{G}(u_{\perp,i}) = \frac{1}{\sqrt{\pi}} e^{-u_{\perp,i}^2}. \quad (3.33)$$

In the direction parallel to $\hat{\mathbf{n}}_i$, the PDF $\mathcal{G}(u_{\parallel})$ must be convolved with the probability $\mathcal{L}(x - u_{\parallel})$ of the atom being able to scatter the photon. The resulting, normalized probability distribution

$$f(u_{\parallel}) = \frac{a}{\pi H(a, x)} \frac{e^{-u_{\parallel}^2}}{(x - u_{\parallel})^2 + a^2} \quad (3.34)$$

can be seen in Fig. 3.2 for a number of incident frequencies. This distribution reflects the fact that for a photon of frequency x , being scattered by an atom with $u_{\parallel} = x$ is highly favored, so that in the reference frame of the atom the photon appears to be exactly at resonance. Since for large values of $|x|$ the number of such atoms reduces as e^{-x^2} , in this case the photon is more likely to be scattered by an atom to which it appears to be far in the wing.

From Eqs. 3.22 and 7.23 and with $\hat{\mathbf{n}}_f$ given by the proper phase function, for a frequency x_i of the incident photon, the frequency x_f of the scattered photon is then

$$x_f = x_i - u_{\parallel} + \hat{\mathbf{n}}_f \cdot \mathbf{u} + g(\hat{\mathbf{n}}_i \cdot \hat{\mathbf{n}}_f - 1). \quad (3.35)$$

3.3 Radiative transfer

3.3.1 Optical depth

We will now look deeper into the spatial transfer of radiation. Consider first a beam of radiation of initial intensity I_0 , traveling through an isothermal hydrogen cloud of homogeneous density $n_{\text{H I}}$. For a small distance dr , effectively the atoms are covering a fractional area $n_{\text{H I}}\sigma_x$, so the change dI in intensity is

$$dI = -I_0 d\tau, \quad (3.36)$$

where

$$d\tau \equiv n_{\text{H I}}\sigma_x dr \quad (3.37)$$

is the optical depth covered by the beam. If the gas is mixed with dust of density n_{d} and cross section σ_{d} , Eq. 3.37 is replaced by

$$\boxed{d\tau \equiv (n_{\text{H I}}\sigma_x + n_{\text{d}}\sigma_{\text{d}})dr.} \quad (3.38)$$

Integrating Eq. 3.36 along the path of the beam, covering a total optical depth τ reduces the intensity to

$$I(\tau) = I_0 e^{-\tau}. \quad (3.39)$$

from which we see that the optical depth traversed by a single photon is governed by the probability distribution

$$\boxed{P(\tau) = e^{-\tau},} \quad (3.40)$$

which is properly normalized in the interval $[0, \infty[$. This distribution has an average of $\langle \tau \rangle = 1$.

3.3.2 Photon peregrination

The first attempts to predict the diffusion of Ly α was made under the assumption of coherent scattering in the observers frame (Ambarzumian, 1932; Chandrasekhar, 1935). Several physical quantities which may or may not be directly observable have been subject to interest, e.g. the average number N_{scat} of scatterings required to escape the medium (to determine the possibility of the photon being destroyed by collisions or dust) and the shape of the emergent spectrum. Due to the complexity of the problem, the physical configurations investigated have traditionally been photons emitted from the center of a homogeneous, isothermal cloud of either spherical symmetry or, in particular, of infinite extension in two directions and finite extension in one (a plane-parallel ‘‘slab’’). Denoting by τ_0 the optical depth for a photon in the line center from the initial point of emission to the edge of the gaseous cloud, from pure random walk considerations N_{scat} would be expected to be of the order τ_0^2 . Accordingly, the medium would not have to be very optically thick for destruction processes of Ly α to become significant.

Henyey (1940) and Spitzer (1944) acknowledged the fact that scattered photons undergo a change in frequency due to thermal Doppler broadening of the scattering atoms. Relying on these considerations, Zanstra (1949, 1951) argued that, in each scattering, the frequency of the Ly α photon would undergo

complete redistribution over the Doppler line profile, i.e. there is no correlation between x_i and x_f , and the probability that $x < x_f < x + dx$ is $\phi(x_f)dx$. In this picture, the photon still executes a random walk, but at each scattering there is a small possibility that it will be redistributed so far into the wing as to render the medium optically thin and thus allow escape. This reduces N_{scat} significantly, and the result was later verified numerically for intermediate optical depths ($\tau_0 \sim 10^4$) by Koelbloed (1956).

Still based on the assumption of isotropic scattering, Unno (1952a,b) calculated an “exact redistribution” formula $q(x_i, x_f)$, giving the probability distribution of x_f as a function of x_i . With this result, Osterbrock (1962) found that in the wings, the rms frequency shift $(\Delta x)_{\text{rms}}$ per scattering is

$$\boxed{(\Delta x)_{\text{rms}} = 1}, \quad (3.41)$$

and the mean shift $\langle \Delta x \rangle$ per scattering is

$$\boxed{\langle \Delta x \rangle = -1/|x|}, \quad (3.42)$$

i.e. the photon has a tendency to drift toward the line center. Thus, a photon at frequency $x \gg 1$ will execute a nearly random walk in frequency, returning to the core in $N_{\text{scat,ret.}} \sim x^2$ scatterings. Simultaneously, the photon is undergoing a random walk in real space, but barely diffuses spatially. Only when eventually it is shifted to $x \geq x_1$, where x_1 is the frequency that renders the optical depth unity, the photon will escape in a *single longest flight*. The probability $w(x_1)$ of escape per scattering is

$$w(x_1) \sim \int_{x_1}^{\infty} q(x_i, x_f) dx_f, \quad (3.43)$$

from which he found that $N_{\text{scat}} \propto \tau_0$ for moderate optical depths. However, he argued that for some limiting large optical depth — which he was not able to calculate due to the lack of “sufficiently large digital computers” — x_f is so large that the photon will execute a random walk also in real space, whence in this case $N_{\text{scat}} \propto \tau_0^2$.

Nonetheless, applying the method of Feautrier (1964), Adams (1972) found numerically that also for extremely large optical depths (τ_0 up to 10^8), $N_{\text{scat}} \propto \tau_0$. Although he could not prove it rigorously, he was able to give a heuristic argument on physical grounds for this behavior. The essential point in Osterbrock’s argument was that during each excursion to the wing, the photon would travel a distance in space much smaller than the size of the medium. But since $\phi(x)$ varies quite slowly in the wings, the mean free path τ_{mfp} , measured in line center optical depths, is

$$\begin{aligned} \tau_{\text{mfp}} &\sim \frac{1}{\phi(x)} \\ &\sim \frac{x^2}{a}. \end{aligned} \quad (3.44)$$

Since

$$N_{\text{scat}} = \frac{1}{w(x_1)}, \quad (3.45)$$

the rms distance τ_{rms} traversed before returning to the core is

$$\begin{aligned}\tau_{\text{rms}} &\sim \tau_{\text{mfp}}\sqrt{N_{\text{scat,ret.}}} \\ &\sim \frac{x^3}{a}.\end{aligned}\tag{3.46}$$

Now, if the photon escapes in a *single longest excursion*, then the frequency x_m where the average photon escapes must satisfy $\tau_{\text{rms}} \sim \tau_0$, so that

$$x_m \sim (a\tau_0)^{1/3},\tag{3.47}$$

which is in fact the frequency where the emergent spectrum takes its maximum value. Assuming for simplicity complete redistribution, so that x_f is given by $\phi(x) \sim e^{-x^2}$, Adams (1972) realized the important fact that $\phi(x)dx$ does not, as previously assumed, give the probability for a *given photon* to be scattered into the interval $[x, x + dx]$, since the photon will scatter there $\sim x^2$ times before returning to the core. This implies that the probability that a given photon scatter into this frequency interval for the first time is $[\phi(x)/x^2]dx$. Hence, from Eq. 3.43, the probability of escape is

$$\begin{aligned}w(x_m) &\sim \int_{x_m}^{\infty} \frac{\phi(x)}{x^2} dx \\ &\sim \frac{a}{x_m^3},\end{aligned}\tag{3.48}$$

so that, from Eqs. 3.45 and 3.48,

$$N_{\text{scat}} \sim \tau_0.\tag{3.49}$$

Inspired by Unno (1955), utilizing the Eddington approximation — which implies that the radiation field is everywhere nearly isotropic, but with a small net outward flow — and expanding the redistribution function as formulated by Hummer (1962) to second order, Harrington (1973) obtained a diffusion equation for the angular averaged intensity $J(\tau, x)$ within a (non-absorbing) slab of extremely large optical depths (defined¹ as $a\tau_0 \geq 10^3/\sqrt{\pi}$, or $\tau_0 \geq 1.2 \times 10^6$ for $T = 10^4$ K). For the sake of completeness we here give the equation, which may be written as

$$\frac{\partial^2 J}{\partial \tau^2} + \frac{\partial^2 J}{\partial \varsigma^2} = -3\phi(x)\frac{E(\tau, x)}{4\pi},\tag{3.50}$$

where $E(\tau, x)$ is the rate of photon generation per unit mean optical depth, per unit area, per unit Doppler width, and $\varsigma \equiv \sqrt{2/3} \int_0^x [1/\phi(x')]dx'$. With the photons emitted isotropically from a central source emitting 1 photon per unit time, i.e. $1/4\pi$ photons per unit time per steradian, such that $E(\tau, x) = (3/2)^{1/2}\delta(\tau)\delta(\varsigma)$, an initial frequency $x_{\text{inj}} = 0$, and scatterings assumed to be dominated by isotropic wing scatterings, he was able to solve Eq. 3.50 and obtain an expression for the emergent spectrum. Neufeld (1990) gave a more general solution to the problem, allowing for the destruction of photons and the

¹Note that in Harrington's papers, as well as most coeval authors', the optical depth at frequency x is defined as $\tau_x = \tau_0\phi(x)$, whereas in our definition $\tau_x = \tau_0H(a, x)$. Since $H(a, x) = \sqrt{\pi}\phi(x)$, this implies that $\tau_{\text{Harrington}} = \sqrt{\pi}\tau_{\text{us}}$. This definition has been chosen to follow more recent studies.

injection at any initial optical depth in the slab, with arbitrary initial frequency. For centrally² emitted radiation in a non-absorbing medium, the solution to Eq. 3.50 at the surface, i.e. at $\tau = \pm\tau_0$, is

$$J(\pm\tau_0, x) = \frac{\sqrt{6}}{24} \frac{x^2}{\sqrt{\pi} a \tau_0} \frac{1}{\cosh \left[\sqrt{\pi^3/54} (x^3 - x_{\text{inj}}^3)/a\tau_0 \right]}. \quad (3.51)$$

With perhaps some injustice, we will refer to Eq. 3.51 as the ‘‘Neufeld solution’’, even when $x_{\text{inj}} = 0$, in which case it reduces to the result of Harrington (1973). The profile is normalized to $1/4\pi$ and exhibits two bumps, symmetrically centered on $x = 0$ and drifting further apart for increasing $a\tau_0$. Note that it solely depends on the product $a\tau_0$, and that the physical size of the gaseous system does not enter the equation. A higher optical depth is compensated for by a lower value of a , i.e. a higher temperature since $a \propto \Delta\nu_D^{-1} \propto T^{-1/2}$. The physical explanation for this is that the more dense the medium is, the further into the wing the photons have to drift, while a higher temperature will make the medium less opaque to radiation, since in the wings $\phi(x) \propto a$. Setting $\partial J/\partial x = 0$, we obtain a transcendental equation for the maximum of the profile with the solution (Harrington, 1973)

$$x_m = \pm 1.066(a\tau_0)^{1/3}. \quad (3.52)$$

Moreover, the average number of scatterings can be shown from Eq. 3.51 to be (Harrington, 1973)

$$N_{\text{scat}} = 1.612\tau_0. \quad (3.53)$$

Notice the close agreement between these results for x_m and N_{scat} , and the results obtained by Adams (1972) given by Eqs. 3.47 and 3.49.

Dijkstra et al. (2006a) derived an expression similar to Eq. 3.51, but for spherical symmetry. In this case the emergent spectrum is³

$$J_{\text{sph}}(\pm\tau_0, x) = \frac{\sqrt{\pi}}{4\sqrt{6}} \frac{x^2}{a\tau_0} \frac{1}{1 + \cosh \left[\sqrt{2\pi^3/27} x^3/a\tau_0 \right]}, \quad (3.54)$$

with the maximum occurring at

$$x_{m,\text{sph}} = \pm 0.92(a\tau_0)^{1/3}. \quad (3.55)$$

and an average number of scatterings approximately one-half of that of the slab. Furthermore, the spectrum for an homologously expanding (as in Hubble flow) or contracting (as in a gravitational collapse) medium, but with no thermal motion, was examined analytically by Loeb & Rybicki (1999).

Evidently, all of the configurations considered so far are highly idealized compared to realistic, astrophysical situations, but for more general geometries and

²Neufeld assumed that the photons are emitted from a thin layer inside the slab, parallel to the surface. However, for reasons of symmetry, we may as well assume that they are emitted from a single point.

³Note that Eq. 3.54 differs from the result given by Dijkstra et al. (2006a) by a factor of $1/2$, since their profile is normalized to $1/2\pi$ instead of $1/4\pi$. This convention was chosen to be able compare more easily with the Neufeld solution.

velocities analytic solutions are not obtainable. Nevertheless, they provide valuable and at least qualitative insight into the characteristics of young galaxies, HI envelopes surrounding hot stars, etc. Moreover, they offer direct means of testing numerical methods, and with the analytical approximations obtained in this section, we have a firm basis for testing the developed code.

Chapter 4

Cosmic dust



NCE SOLELY AN OBSCURING NUISANCE to astronomers, infrared (IR) astronomy revealed cosmic dust to be not only interesting in itself, but also to play an important role in many astrophysical processes. For example, to form molecular hydrogen, a third agent is needed to carry away the released energy. Since the probability for three hydrogen atoms to meet simultaneously is extremely small, the most efficient way is by first sticking to a dust grain, crawl stochastically across its surface, and finally meet another atom and form H_2 , transferring the excess energy to the dust grain (Gould & Salpeter, 1963). Many other molecules, especially organic, are believed to be catalyzed by grain surface chemistry (e.g. Turner, 1990; Ceccarelli et al., 2001; Bisschop et al., 2007).

In the final stages of the life of a star, radiation pressure drives out large amounts of gas from the surface of the star. In this process the dust aids the mass loss by absorbing the radiation, being accelerated, and sweeping up gas on its way away from the star (see, e.g., Höfner, 2009).

Dust absorbs light and converts it to IR radiation. Since such long wavelengths are only little affected by other absorption processes, observing astrophysical objects in IR is sometimes easier, or even the only possibility. This is the underlying mechanism of the SMG selection method.

Moreover, dust grains stick together to form rocks which, in turn, form planets which are probably needed to form life.

From dust samples from air- and spaceborn plate collectors, the physical properties of *local* dust is reasonably well-constrained. However, extrapolating this to the rest of the Universe is most likely a bit too bold. One of the incentives for implementing dust in the numerical simulations of $\text{Ly}\alpha$ RT was to learn about the dust itself. Unfortunately it turned out that in the context of $\text{Ly}\alpha$, different types of dust give rise to virtually identical observables. However, since this means that the outcome is not very sensitive to the exact nature of the modeled dust, the *effect* of dust in the early Universe can thus be ascertained with relatively high confidence.

The remainder of this chapter discusses the basic theory of dust, necessary for understanding the constructed scheme for the effects of dust in the numerical code.

4.1 Effect on radiative transfer

Whereas absorption processes in gas in many cases are well-known, the effect of dust on the RT is still an intensely debated subject. In contrast to gas, laboratory experiments with dust are extremely complex, partly due to the complications involved in replicating the physical environments of the ISM, partly due to our limited knowledge vis-à-vis what actually constitutes cosmic dust.

In the present-day Universe, most dust is formed in the atmospheres of stars on the asymptotic giant branch (AGB) of the Hertzsprung-Russel diagram; the dying phase of stars less massive than $\sim 8 M_{\odot}$ (e.g. Höfner & Andersen, 2007; Mattsson et al., 2008; Gail, 2009). In these environments the gas is sufficiently cool, yet sufficiently dense that molecules may form and stick together to form dust grains.

However, there is observational evidence that dust is also abundantly present in the early Universe (e.g. Smail et al., 1997; Bertoldi et al., 2001; Stratta et al., 2007; Coppin et al., 2009). Since the time to reach the AGB phase is of the order of 1 Gyr, something else may have provided the ISM with dust at these epochs. A promising candidate is SNe, the ejecta of which are believed to exhibit favorable conditions for the formation of dust for a short period of time, approximately 600 days after the explosion (e.g. Kotak et al., 2009).

For the Milky Way (MW), as well as the Small and Large Magellanic Clouds (SMC; LMC), the dust extinction curves, i.e. the extinction of light as a function of wavelength, are fairly well established (e.g. Bianchi et al., 1996; Nandy et al., 1981; Prevot et al., 1984; Pei, 1992), and from the observed color excess $E(B - V)$ one may then derive the total extinction. The term “extinction” refers to removal of light from the line of sight, be it due to absorption or scattering, and may be characterized by the number A_{λ} of magnitudes by which the observed light from an object is diminished. For more distant galaxies one is usually obliged to assume similar extinction curves. Since the stellar population of the SMC is younger than that of the LMC, an SMC extinction curve might be expected to describe better the dust in high-redshift galaxies, and has indeed proved to be a good fit in GRB host galaxies (e.g. Jakobsson et al., 2004) and quasar host galaxies (e.g. Richards et al., 2003; Hopkins, 2003). Note, however, that the prominent feature at 2175 Å, characteristic of the LMC and MW extinction but the SMC, has been detected in a few cases also at high redshift (Junkkarinen et al., 2004; Ellison et al., 2006; Srianand et al., 2008; Elíasdóttir et al., 2009).

Extinction curves are obtained by comparing the flux received from a pair of identical (i.e. same spectral class) stars — one obscured by dust and the other unobscured. Measuring at a range of wavelengths, one gets the shape of the curve. The overall normalization of extinction curves comes from the observed property that the extinction is found to be very close to proportional with the column density N_{H} of hydrogen (e.g. Bohlin et al., 1978). Typically, one combines measurements of N_{HI} (and N_{H_2}) with the extinction in the V band, A_V . In this way, one then knows how much light is extinguished when traveling a given physical distance in space.

However, for light that does not travel directly from the source to the observer, as is the case for resonantly scattered lines like $\text{Ly}\alpha$, the situation becomes more complicated. Not only does the total distance covered by the photons increase by a large and a priori unknown factor, but the photons received from a given point

on the sky may also have traveled through physically different environments, in turn implying an unknown and possibly highly increased probability of being absorbed by dust.¹

4.1.1 Ly α escape fraction

For this reason, the observed fact that Ly α radiation nonetheless *does* escape has long puzzled astronomers. Many astrophysical and cosmological key questions depend upon precise measurements of the luminosities of distant galaxies; in particular, SFRs and SFR histories, as well as LFs, are crucially contingent on the amount of assumed luminosities. A fundamental problem in this context is naturally the question of how large a fraction of the emitted light actually escapes the galaxy. If an unknown fraction of the emitted light is absorbed, either by gas or by dust, the inferred quantity of interest clearly will be subject to large uncertainties or, at best, a lower limit.

The fact that Ly α line profiles are often seen to exhibit a P Cygni-like profile has led to the suggestion that high-velocity outflows of gas are needed to enable escape (Kunth et al., 1998; Östlin et al., 2009; Atek et al., 2008), and in fact Dijkstra & Loeb (2009) showed that the pressure exerted on the ISM by Ly α itself can drive large gas masses out of the galaxies. However, at high redshifts many galaxies are still accreting matter, which should result in an increased *blue* peak. Since this is rarely observed, the shape could be caused by other mechanisms, e.g. IGM absorption.

The angle under which a galaxy is viewed may also affect the amount of observed radiation. Ionizing UV radiation could create “cones” of low neutral hydrogen density emanating from the star-forming regions through which the Ly α can escape (Tenorio-Tagle et al., 1999; Mas-Hesse et al., 2003). Even without these ionized cones, scattering effects alone may cause an anisotropic escape of the Ly α ; tentative evidence for this was found with the early version of the code (Laursen & Sommer-Larsen, 2007).

Another commonly repeated scenario is a multi-phase medium, where the dust is locked up in cold clouds so that the photons primarily travel in an ionized, dustless medium (Neufeld, 1991; Hansen & Oh, 2006). Since continuum radiation travels through the cloud, it would be attenuated more by the dust. This could explain the high Ly α equivalent widths occasionally observed in LAEs (e.g. Malhotra & Rhoads, 2002; Rhoads et al., 2003; Shimasaku et al., 2006). Previous attempts to determine Ly α escape fractions from high-redshift galaxies have mainly been trying to match observed Ly α luminosities with expected, and different methods obtain quite different results. In fact, as is evident from the following discussion, there seems to be no general consensus on the value, the scatter, or even the order of magnitude of f_{esc} .

Le Delliou et al. (2005, 2006) found very good agreement between galaxies simulated with the galaxy formation model GALFORM and observational data at $z = 3\text{--}6$, using a constant escape fraction of $f_{\text{esc}} = 0.02$ and assuming no IGM absorption. Davé et al. (2006) obtained similar results by matching the Ly α

¹In principle the Ly α photon may also be destroyed by other mechanisms, e.g. by collisionally induced transition of the excited atom from the $2P$ state to the $2S$ state and subsequent two-photon emission, or pumping of the nearby $B\text{--}X$ 1-2 $P(5)$ and 1-2 $R(6)$ electronic transition of H₂ (Neufeld, 1990). However, under almost all conditions encountered in the ISM, these processes can be safely ignored (see also App. A).

LF of galaxies from their cosmological smoothed particle hydrodynamics simulation to the data of Santos et al. (2004), although Nagamine et al. (2008) argued that the data are based on a small sample and that the simulation box size is too small. Matching the simulated Ly α LF to the observed one by Ouchi et al. (2008), Nagamine et al. (2008) themselves obtain $f_{\text{esc}} \simeq 0.1$, although the preferred scenario is not that a certain fraction of the Ly α radiation escapes, but rather that a certain fraction of LAEs are “turned on” at a given time (the so-called “duty cycle scenario”). In a similar way, Dayal et al. (2009) find somewhat higher escape fractions at $z \sim 5.7$ and ~ 6.5 ($f_{\text{esc}} \sim 0.3$), which they use for predicting the LF of LAEs at $z \sim 7.6$.

Verhamme et al. (2008), using the Monte Carlo Ly α radiative transfer code MCLYA (Verhamme et al., 2006) and assuming a shell-like structure of gas, found a large range of escape fractions by fitting calculated spectra to observed ones of $z \sim 3$ LBGs, with f_{esc} ranging from ~ 0 to ~ 1 .

Gronwall et al. (2007) compared inferred Ly α and rest-frame UV continuum SFRs of a large sample of LAEs from the MUSYC (Gawiser et al., 2006a) survey and argue that an escape fraction of $\sim 1/3$ is needed to explain the discrepancy, although Nilsson et al. (2009) pointed out that a missing $(1+z)$ -factor probably explains the difference. Matching Ly α -inferred SFRs to SED modeling of observed LAEs, Gawiser et al. (2006b) found an f_{esc} of ~ 0.8 , with a lower limit of 0.2. While SED fitting may not be the most accurate way of estimating SFRs, aiming to match these observations, Kobayashi et al. (2007) obtain similar results theoretically by incorporating the effects of galactic outflows.

To calculate the SFR from Ly α , case B recombination is assumed, i.e. that the recombinations take place in optically thick regions. In this case Osterbrock (1989) showed that the ratio between emitted Ly α and H α radiation is 8.7. Additionally assuming solar element abundances, a Salpeter (1955) initial mass function (IMF) with mass limits 0.1 and $100 M_{\odot}$, and that star formation has been going on for $\sim 10^8$ yr, the calculated H α luminosity can be converted to a SFR using the relation (Kennicutt, 1998)

$$\frac{\text{SFR}}{M_{\odot} \text{ yr}^{-1}} = \frac{L_{\text{H}\alpha}}{1.3 \times 10^{41} \text{ erg s}^{-1}}. \quad (4.1)$$

This relation is widely used, even though obviously the assumption may be far from valid.

If available, Ly α may also be compared directly to H α . Usually, both lines are not obtained simultaneously, however. Instead one may compare the average luminosities of two samples of galaxies observed in each line, i.e. compare the LFs. The problem is obviously that a sample of LAEs will usually be biased against objects emitting strongly in Ly α , and similarly for H α emitters. Hayes et al. (2010b) overcome this issue by performing a double-blind survey targeting the GOODS-S field (Giavalisco et al., 2004). They find that a Ly α escape fraction of $(5.3 \pm 3.8)\%$ is needed to make the two obtained LFs match.

4.2 What characterizes cosmic dust?

Four quantities characterize what impact the dust grains will have on the propagating Ly α photons: the *density*; the (wavelength-dependent) *cross section* of interaction; the *albedo* giving the probability that a photon incident on a dust

grain will be scattered rather than absorbed; and finally the *phase function* defining the direction into which a non-absorbed photon is scattered. To understand how this is implemented in the code, these quantities will be discussed below.

Dust grains are built up from metals, and thus the dust density is expected to scale with gas metallicity in some fashion. Metals are created in dying stars, i.e. in AGB stars and SNe. For sufficiently dense and cold environments, the neutral metals form molecules which eventually stick together to form dust. No formal definition of the distinction between large molecules and dust grains exists, but may be taken to be of the order of ~ 500 atoms or so.

Depending on the abundances of the individual metals, as well as the physical conditions, a variety of different types of dust may be produced, with regards to both composition and structure, and hence with different scattering properties. Much effort has been put into unraveling the nature of cosmic dust, in particular in explaining the 2175 Å bump. This feature is generally attributed to carbonaceous materials, e.g. graphite, diamonds, and/or polycyclic aromatic hydrocarbons, but still the precise nature remains unknown.

For grain sizes much smaller than the wavelength λ of the light, the exact shape of the particle is not significant and the scattering can be calculated as Rayleigh scattering. For grains larger than λ , Mie theory provides a solution assuming spherical geometry. However, a significant fraction of interstellar dust is expected to be comprised by particles of sizes comparable to the wavelength of $\text{Ly}\alpha$. In principle, the result of a photon interacting with a dust grain may be calculated analytically by solving Maxwell's equations, on the basis of the geometry of the particle and its optical properties, i.e. the dielectric functions. This is possible in the case of simple geometries such as spheres and spheroidals (Mie, 1908; van de Hulst, 1957; Bohren & Huffman, 1983). More general shapes and composites can be modeled by discretizing the grain into a large number of dipoles; the so-called *discrete dipole approximation* (Purcell & Pennypacker, 1973; Draine, 1988), but for the complex and, more importantly, uncertain or unknown shape of realistic grains, this is not feasible.

Had we full knowledge of the relevant properties of dust, a distribution of the various species could be calculated in simulated galaxies, and the radiative transfer could then be realized by computing the total optical depth of the ISM as a sum of all contributors, and determining for each scattering the kind of particle responsible for the scattering. However, lacking a sound theory of the formation of dust grains, in particular in the high-redshift Universe, we take a different approach: although the exact nature of cosmic dust is not known, the average extinction — and hence the cross-sectional area — of dust as a function of wavelength is known for many different sightlines through the SMC and the LMC (e.g. Gordon et al., 2003). Since the metallicity of the Magellanic Clouds is fairly well known, the extinction curve of the SMC (or LMC) can be scaled to the metallicity of the gas at each point in the simulated galaxies, thus yielding the extinction in the simulations.

4.2.1 Cross section

Observationally, the extinction A_V in the V band is found to have a surprisingly constant proportionality with the column density of hydrogen from sightline to sightline within the MW (e.g. Bohlin et al., 1978). Similar results, but with

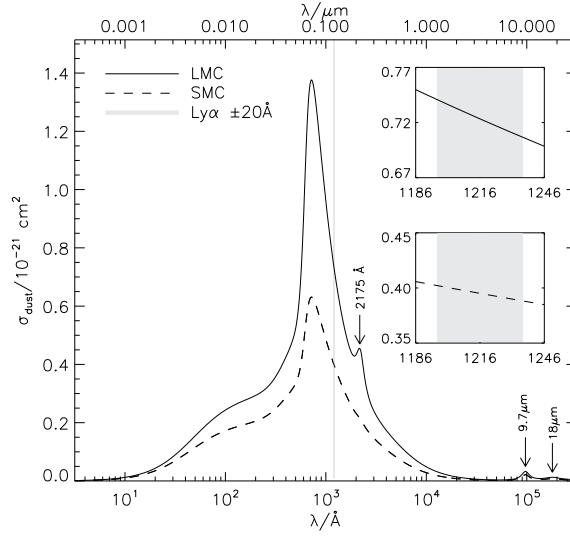


Figure 4.1: Dust cross section fits to the observed extinction curves of the LMC (*solid*) and the SMC (*dashed*). The difference in amplitude is mainly due to the SMC being less metal-rich than the LMC. The vertical, gray-shaded area is the region inside which the (rest-frame) Ly α line is expected to fall. The two insets show a zoom-in of this region on the extinction curves (*top*: LMC, *bottom*: SMC), demonstrating the linearity across the Ly α line.

different normalizations, are found for the SMC and the LMC (Gordon et al., 2003). Accordingly, the cross section $\sigma_d(\lambda)$ of dust may be conveniently expressed as an effective cross section *per hydrogen atom*, thus eliminating any assumptions about the size distribution, shape, composition, etc., and merely relying on observed extinction curves. The optical depth τ_d of dust when traveling a distance r through a region of hydrogen density n_H is then

$$\tau_d = n_H r \sigma_d = N_H \sigma_d. \quad (4.2)$$

The quantity usually measured is A_λ/N_H , and the cross section is then

$$\sigma_d = \frac{\ln 10}{2.5} \frac{A_\lambda}{N_H} \quad (4.3)$$

We use the fit to the SMC or LMC extinction curves proposed by Pei (1992), which is an extension of the Mathis, Rumpl, & Nordsieck (1977)-model. The fit is a sum of six terms (Drude profiles) representing a background, a far-ultraviolet (FUV), and a far-infrared (FIR) extinction, as well as the 2175 Å, the 9.7 μm , and the 18 μm extinction features. Based on newer data from Weingartner & Draine (2001), Gnedin et al. (2008) adjusted the fit and added a seventh term to account for the narrow, asymmetric FUV peak in the dust extinction.

Figure 4.1 shows these fits. The two insets show that the extinction curves are very close to being linear in the vicinity of the Ly α line. In fact, in this region it is an excellent approximation to write the cross section as

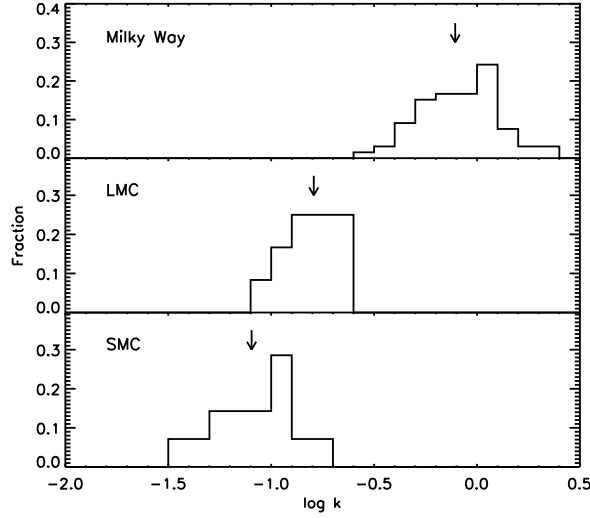


Figure 4.2: Distributions of dust-to-gas ratio along individual lines of sight within the MW (*top*), LMC (*middle*), and SMC (*bottom*). Here, k is defined as $k = 10^{21}(\tau_B/N_{\text{H I}}) \text{ cm}^{-2}$, where τ_B is the extinction optical depth in the B band. The arrows indicate the mean dust-to-gas ratio in each galaxy. Although the three histograms differ substantially in the means, they have similar logarithmic dispersion. The plot is taken from Pei (1992).

$$\sigma_d/10^{-21} \text{ cm}^2 = \begin{cases} 0.395 + 1.82 \times 10^{-5} T_4^{1/2} x & \text{for the SMC} \\ 0.723 + 4.46 \times 10^{-5} T_4^{1/2} x & \text{for the LMC.} \end{cases} \quad (4.4)$$

where as usual $x \equiv (\nu - \nu_0)/\Delta\nu_D$, and $T_4 \equiv T/10^4 \text{ K}$. Note that T only enters Eq. 4.4 to account for the temperature dependency of x ; σ_d itself is independent of T .

4.2.2 Number density

The reason for the variability of extinction with galaxy, and the non-variability with sightline, is to a large degree the different overall metallicities of the galaxies. Although differences do exist within the galaxies, as seen in Fig. 4.2 the differences in dust-to-gas ratio are larger from galaxy to galaxy (Pei, 1992).

In most of the calculations we will use an SMC curve, but as shown in Sec. 8.3 the result are not very different if an LMC curve is used.

Because the cross section is expressed as a cross section per hydrogen atom, the relevant quantity is not dust density, but hydrogen density. However, since in general the metallicity at a given location in a simulated galaxy differs from that of the Magellanic Clouds, the amplitude of the extinction will also differ. Assuming that extinction scales with metallicity, a corresponding pseudo number

density n_d of dust at a given location of hydrogen density n_H and metallicity Z_i of element i can then be calculated as

$$n_d \sim n_H \frac{\sum_i Z_i}{\sum_i Z_{i,0}}, \quad (4.5)$$

where $Z_{i,0}$ is the average metallicity of element i in the galaxy the extinction curve of which is applied. Obviously, n_d is not a true dust number density, but merely a rescaled hydrogen number density.

On average, the SMC metallicities of the different elements are deficient relative to Solar values by 0.6 dex (e.g. [Welty et al., 1997](#)), while the LMC is deficit by 0.3 dex (e.g. [Welty et al., 1999](#)). Small metal-to-metal deviations from this exist, but, as will be shown in [Sec. 8.3](#), scaling Z_i to the metallicity of the individual metals, using values from [Russell & Dopita \(1992\)](#), does not change the outcome significantly.

The reason that [Eq. 4.5](#) is not expressed as a strict equality is that we have so far neglected to differentiate between neutral and ionized hydrogen. Dust grains may be destroyed in a number of ways, e.g. through collisions with other grains, sputtering due to collisions with ions, sublimation or evaporation, or even explosions due to UV radiation (e.g. [Greenberg, 1976](#)). These scenarios are all expected to become increasingly important for hotter environments. Accordingly, studies of the interstellar abundances of dust have usually assumed that ionized regions contribute negligibly to the dust density, and merely concerned themselves with measuring column densities of neutral hydrogen, i.e. $\text{HI} + \text{H}_2$. Moreover, many metallicity measurements are derived from low-resolution spectra not capable of resolving and characterizing various components of the ISM. As discussed in [Sec. 4.2.2](#), dust is also observed in regions that are primarily ionized, and since the bulk of the $\text{Ly}\alpha$ photons is produced in the proximity of hot stars with a large intensity of ionizing UV radiation, even a little dust associated with the ionized gas might affect the results.

Hence, we assume that the amount of dust scales with the total amount of neutral hydrogen *plus* some fraction f_{ion} of the ionized hydrogen, and [Eq. 4.5](#) should then be

$$n_d = (n_{\text{HI}} + f_{\text{ion}} n_{\text{HII}}) \frac{\sum_i Z_i}{\sum_i Z_{i,0}} \quad (4.6)$$

Again it is emphasized that this is not a physical number density of dust grains but with this expression, the total optical depth of gas and dust as seen by a photon traveling a distance r is

$$\tau_{\text{tot}} = r(n_{\text{HI}}\sigma_x + n_d\sigma_d). \quad (4.7)$$

In principle, the summation term in [Eq. 4.6](#) should also include a term accounting for the fact that the dust-to-metal ratio f_{dm} in a given cell may be different from that for which the empirical data exist. In the Milky Way and the Magellanic Clouds, $f_{\text{dm}} \simeq 1$ for most metals, i.e. roughly 1/2 of the metals is condensed to dust grains. The depletion patterns in high-redshift galaxies are not well constrained, but no measurements suggest that it should be substantially different from the local Universe. In fact [Pei, Fall, & Hauser \(1999\)](#) interpret the depletion patterns of Cr and Zn measured in DLAs by [Pettini et al. \(1997\)](#) as giving $f_{\text{dm}} \simeq 1$ out to $z \lesssim 3$. Similarly, fitting depletion patterns

of eight elements in GRB host galaxies, Savaglio et al. (2003) find $f_{\text{dm}} \simeq 1$. To recap, we make no assumptions about how metals deplete to dust other than it is not appreciably different from the present epoch.

Dust in ionized gas

Ionized gas is found in a number of physically distinct locations throughout the Universe. Compact HII regions, or Strömgren spheres, surround young, hot stars, while more diffuse HII is a part of the ISM. Larger HII “bubbles” are formed around regions of massive star formation due not only to ionizing radiation from the stars but also to the energy deposited in the ISM from supernova feedback. Outside the galaxies, the IGM is predominantly ionized out to redshifts of at least $z \sim 5$ –6. Observations show or indicate the presence of dust in all of these media. While generally lower than in the neutral gas, inferred dust-to-gas mass ratios (f_{dg}) in ionized gas span a range from roughly equal to the typically assumed MW ISM value of ~ 0.01 , to upper limits of $\sim 10^{-4}$ times lower than this.

Based on 45–180 μm (FIR) spectroscopy, Aannestad & Emery (2001) found the Galactic HII region S125 to be strongly depleted of dust, with a dust-to-gas ratio of $f_{\text{dg}} \leq 10^{-6}$, while Smith et al. (1999), using mid-infrared (MIR) imaging and spectroscopy, inferred a dust-to-gas ratio of the Galactic HII region RCW 38 of 10^{-5} to 10^{-4} . On the other hand, using FIR spectroscopy Chini et al. (1986) found 12 HII regions to be dust-depleted by “only” a factor of 10 relative to the MW ISM (i.e. $f_{\text{dg}} \sim 10^{-3}$), while from FIR photometry, Harper & Low (1971) found the median dust-to-ionized-gas ratio of seven HII regions to be close to 0.01.

For the more diffuse HII gas that constitutes part of the ISM, most obtained extinction curves in a sense already include the contribution of HII to n_{d} , although its quantity is not revealed when measuring HI column densities. Hence, any value of f_{ion} for the diffuse ISM larger than 0 would account twice for the ionized gas.

The dominant destruction mechanism of dust is probably shock waves, associated with, e.g., high-velocity clouds and SN winds (Draine & Salpeter, 1979a,b). However, since SNe are thought to be the prime creator of dust at high redshifts, the HII bubbles in the vicinity of massive star-forming regions cannot be entirely devoid of dust, and observational evidence of dust related to SN remnants (SNR) and starburst regions does indeed exist. Using MIR imaging, Bouchet et al. (2006) determined the dust-to-gas ratio of SN 1987A to be $\sim 5 \times 10^{-3}$. Somewhat lower results are found in Kes 75 ($\sim 10^{-3}$ from FIR and X-ray, Morton et al., 2007) and in Kepler’s SN ($\sim 10^{-3}$ from IR and bremsstrahlung, Contini, 2004). On larger scales, the hostile environments imposed by the SNe and ionizing radiation will reduce the dust density in starburst regions. Fitting continuum SEDs, Contini & Contini (2004) found that $10^{-4} \lesssim f_{\text{dg}} \lesssim 10^{-2}$ in various starburst regions in a sample of seven luminous infrared galaxies. However, such regions are not ionized to the same level as compact HII regions and SNRs, and as argued in the case of the diffuse HII, the scaling of dust with HI to some extent already accounts for the HII.

Various feedback processes are also responsible for expelling a non-vanishing amount of metals and dust into the IGM, although inferred dust-to-gas ratios tend to be small: from IR-to-X-ray luminosities, Giard et al. (2008) inferred a

dust-to-gas ratio of a few to 5 times 10^{-4} , as did [Chelouche et al. \(2007\)](#) by comparing photometric and spectroscopic properties of quasars behind SDSS clusters. Higher values (dust-to-HI ~ 0.05 in the M81 Group, [Xilouris et al., 2006](#)) — possibly expelled from the starburst galaxy M82 — and lower values ($f_{\text{dg}} \sim 10^{-6}$ in the Coma cluster and even less in five other Abell clusters, [Stickel et al., 2002](#)) are also found. Additionally, sputtering by the hot halo gas may tend to destroy primarily small grains, leading to a flattening of the extinction curve in the UV; at the Ly α wavelength, this may reduce the average cross section by a factor of 4–5 ([Aguirre et al., 2001](#)).

In summary, the factor f_{ion} is a practical way of modeling the destruction of dust in physically “hostile” environments. For simplicity, in the RT code we will not distinguish between HII in various regions but merely settle on an average dust-to-gas ratio of ionized gas of $\sim 10^{-4}$; that is we set $f_{\text{ion}} = 0.01$. In [Sec. 8.3](#), other values of f_{ion} are investigated and it is found that using 0.01, the resulting escape fractions lie approximately midway between those found when using $f_{\text{ion}} = 0$ (corresponding to the *complete* destruction of dust in regions where hydrogen is ionized) and $f_{\text{ion}} = 1$ (corresponding to no destruction of dust at all). Moreover, these extreme values do not seem to change f_{esc} by more than $\sim 25\%$.

4.2.3 Albedo

When a photon interacts with a dust grain, it may be either absorbed or scattered. The efficiency with which the dust grain scatters radiation is dependent on the composition (material, shape, etc.) of the dust and on the wavelength of the incident photon. If the photon is not scattered (i.e. emitted with the same wavelength as the incident photon), it is absorbed. In this case it is converted into heat and re-emitted at a later time as IR radiation. Expressing the total cross section as a sum of a scattering cross section σ_{s} and an absorbing cross section σ_{a} , such that $\sigma_{\text{d}} = \sigma_{\text{s}} + \sigma_{\text{a}}$, the albedo A of the dust is defined as

$$A = \frac{\sigma_{\text{s}}}{\sigma_{\text{d}}}. \quad (4.8)$$

The albedo of dust has been investigated observationally from reflection nebulae (e.g. [Calzetti et al., 1995](#)) and diffuse galactic light (e.g. [Lillie & Witt, 1976](#)). At the Ly α wavelength, A lies approximately between 0.3 and 0.4 for various size distributions fitted to the LMC and SMC, assuming that the dust is made mainly of graphite and silicates ([Pei, 1992](#); [Weingartner & Draine, 2001](#)). We adopt the model-derived value of $A = 0.32$ (from [Li & Draine, 2001](#)). The albedo of this model matches observed values over a wide range of wavelengths. In [Sec. 8.3](#), the impact of using other values is investigated.

4.2.4 Phase function

If a photon is not absorbed, it is scattered. As with scattering on hydrogen, the probability distribution of deflection angles θ from its original path is given by the phase function. For reasons of symmetry, the scattering must be symmetric in the azimuthal angle ϕ (unless the grains are collectively oriented in some preferred direction due to, e.g., magnetic field lines), but in general this is not the case in θ . In fact, dust is often observed to be considerably forward scattering [e.g. in reflection nebulae ([Burgh et al., 2002](#)), diffuse galactic light

(Schiminovich et al., 2001), and interstellar clouds (Witt & Oliveri, 1990)]. This asymmetric scattering may be described by the Henyey-Greenstein (1941) phase function

$$P_{\text{HG}}(\mu) = \frac{1}{2} \frac{1 - g^2}{(1 + g^2 - 2g\mu)^{3/2}}, \quad (4.9)$$

where $\mu = \cos \theta$, and $g = \langle \mu \rangle$ is the asymmetry parameter. For $g = 0$, Eq. 4.9 reduces to Eq. 3.26 (isotropic scattering), while $g = 1$ (-1) implies complete forward (backward) scattering. g is a function of wavelength, but for λ close to that of Ly α , Li & Draine (2001) found that $g = 0.73$. Again, other values are investigated in Sec. 8.3.

Chapter 5

The intergalactic medium



ALBEIT EXTREMELY DILUTE, space between galaxies is not entirely empty. In the *intracluster* medium (ICM), i.e. the space between galaxies bound together in a cluster, number densities are typically of the order 10^{-3} to 10^{-4} cm^{-3} (e.g. Fabian, 1994). For comparison, the density in the ISM is roughly equal to one hydrogen atom per cm^3 , while star-forming regions exceed 10^2 , and even up to 10^6 atoms per cm^3 in the densest molecular clouds (e.g. Ferrière, 2001). The clusters are not randomly dispersed in the IGM, but are connected via huge sheets and filaments of gas of \sim ten times lower densities. However, this is still much denser than the average of the Universe, the bulk of the gas lying in the immense voids of densities of 10^{-7} to 10^{-6} cm^{-3} , stretching several tens to hundreds of Mpc across. To put things into perspective, a sphere the size of the Earth-Moon system in the IGM would contain an amount of matter suitable to fill up a cup.

Whereas the temperature of the ISM is generally of the order 10^4 K, and one or two orders of magnitude lower in molecular clouds, the rarefied IGM is easily heated to much higher temperatures. When gas falls from the voids onto the filaments it heats up, reaching temperatures of 10^5 to 10^7 K. Even higher temperatures of $\sim 10^8$ K are reached as it falls into the clusters. The filaments are themselves connected in “knots”, where the largest of all clusters are found. In this thesis, the IGM is taken to mean everything outside the galaxies, although sometimes the term is used only for the ICM.

5.1 The Ly α forest

The physical state of the IGM can be probed by looking at absorption lines in the spectrum of a bright source whose intrinsic spectrum is well-known. Since hydrogen constitutes the vast majority of the elements, a particularly popular line is obviously the Ly α line. As light travels through the expanding Universe, it gets redshifted, implying that wavelengths blueward of the Ly α line center are eventually shifted into resonance. If for a given wavelength this happens in the vicinity of a sufficient amount of neutral hydrogen, the spectrum experiences an absorption line (although strictly speaking the photons are not absorbed, but rather scattered out of the line of sight). This results in the so-called Ly α forest

(LAF; Lynds, 1971; Sargent et al., 1980).

The different absorption features in the LAF should not be thought of as arising from a number of individual clouds of neutral hydrogen along the line of sight, as was originally thought. Rather, as has been substantiated observationally (e.g. Bechtold et al., 1994; Dinshaw et al., 1994; Fang et al., 1996), theoretically (e.g. Rauch & Haehnelt, 1995; Bi & Davidsen, 1997; Hu et al., 1997), and numerically (e.g. Zhang et al., 1995; Hernquist et al., 1996; Miralda-Escudé et al., 1996), the features are mostly due to continuously distributed, relatively smooth, low-density gas regions, with the line widths dictated by the Hubble flow across them, smoothed further by thermal broadening.

As the transmission of radiation is sensitive to the ionization state of the IGM, the LAF has been used observationally to put constraints on the so-called Epoch of Reionization, described in the following section. However, many other interesting problems can be constrained by looking at the LAF. For instance, the primordial fluctuations will leave an imprint in the LAF of later epochs (Croft et al., 1998). Prior to decoupling at $z \sim 1100$, acoustic waves in the photon/baryon plasma — the so-called *baryon acoustic oscillations* (BAOs) — shape the power spectrum on scales of ~ 150 Mpc. In principle these should also be observable in the LAF, thereby probing the expansion history of the Universe and thus providing information about dark energy (Eisenstein, 2005). Constraints can also be put on the maximum amount of hot dark matter (HDM) allowed, since too much HDM erases structure on small scales. Additionally, the abundance of deuterium can be measured, and as the absorbing systems are generally of low metallicity, this will probably be “unprocessed” deuterium, thus gauging nucleosynthesis.

5.2 The Epoch of Reionization

Inspecting the spectra of quasars at successively higher redshift, one notices that the Ly α absorption lines become increasingly copious, eventually overlapping, until at a redshift of $z \sim 6$ the spectrum is rendered completely black blueward of the Ly α line. This missing flux is the *Gunn-Peterson trough*, predicted theoretically by Gunn & Peterson (1965), but only observed more than three decades later (Becker et al., 2001). Figure 5.1 shows this evolution in quasar spectra.

Observations of a large number of quasars show that the Universe was largely opaque to radiation blueward of Ly α at $z \gtrsim 6$ (Songaila, 2004; Fan et al., 2006). Around this redshift, the Universe underwent its second major change of state, the first being the “recombination” at $z \sim 1100$ where the cosmic microwave background (CMB) was released. Since the recombination, the Universe had been largely neutral and thus opaque to all wavelengths blueward of Ly α . Accordingly, this era is referred to as the *dark ages*.¹ Somewhen relatively shortly before $z \sim 6$, during the *Epoch of Reionization* (EoR), the Universe became transparent, and a paramount puzzle in modern cosmology is the question of when and how the hydrogen, and later helium, of the Universe was reionized.

¹Sometimes the era *before* recombination is denoted the dark ages. At this time the Universe was even more opaque since light scattered on free electrons, the cross section of which is independent of wavelength. However, at this time the Universe was 3000 K and above, so in fact it was not dark, but filled with a yellowish glow.

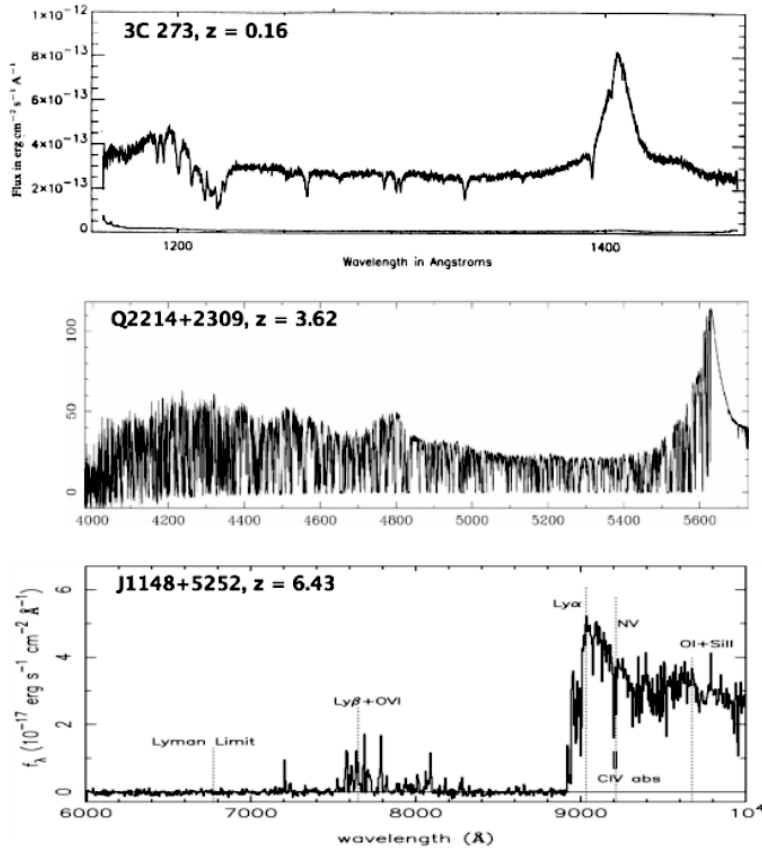


Figure 5.1: Spectra of quasars at three different epochs. The present-day Universe is almost completely ionized, transmitting essentially the full spectrum (*upper panel*). While the Universe at $z \sim 3.6$ is largely ionized, many diffuse H I region still persists, resulting in the Ly α forest (*middle panel*). At even higher redshift, close to the Epoch of Reionization, all radiation blueward of the Ly α line is absorbed, leading to the Gunn-Peterson trough (*lower panel*). The spectra are taken from Brandt et al. (1993), Rauch (1998), and Goto (2006), respectively.

The EoR marks a comprehensive change of the physical state of the gaseous Universe, and to understand the cause, as well as the course, of this phenomenon is a challenging task. Besides being a compelling event in itself, it also has profound implications for the interpretation of observations and theoretical cosmological models, not only due to the increased transparency of the IGM, but also because of the accompanying rise in IGM temperature. While reionization is in one way or another directly caused by the appearance of the earliest luminous sources, it also in turn affects subsequent structure formation (Choudhury & Ferrara, 2006).

The very first stars that formed, Pop III, are now thought to be too few and too ephemeral to produce enough ionizing photons to sustain reionization (Meiksin, 2005). Quasars provide a massive amount of photons, but tend to appear too

late for ionization of hydrogen (although they may be important for the reionization of helium). It is generally believed that the main source for the reionization of hydrogen is massive star formation in galaxies, and much effort is being put into ascertaining how easily ionizing photons can escape their host galaxies in order to be able to ionize the IGM (Razoumov & Sommer-Larsen, 2007; Gnedin et al., 2008; Razoumov & Sommer-Larsen, 2009). A plausible scenario is that galaxies gradually ionize their immediate surroundings such that they are encompassed in large “bubbles” of ionized gas, thus resulting in a highly inhomogeneous ionization structure of the IGM. Eventually these bubbles percolate and overlap, until ultimately almost all of the IGM is ionized (e.g. Gnedin, 2000).

Different probes exist for scrutinizing the EoR, yielding different and not readily mergable results. Regardless of the physical mechanism responsible for the reionization, it is likely that it did not happen at a specific moment in time, but rather over an extended period, the EoR, although this period may have been quite brief. In addition to measuring the evolution of quasar spectra, two promising methods exist:

5.2.1 The cosmic microwave background

After the CMB was released at the “surface of last scattering”, it traveled freely through the neutral Universe. However, when electrons were released by the reionization a small fraction of the CMB photons Thomson scattered on these free electrons, introducing small anisotropies in their polarization. These anisotropies has been studied with the WMAP satellite, allowing the total optical depth τ_e of electrons to be deduced. In a short interval dt of time, a photon travels a distance $c dt$, through which the optical depth is

$$\begin{aligned} d\tau_e &= n_e(z) \sigma_T c dt \\ &= n_e(z) \sigma_T c \frac{1}{(1+z)H(z)} dz, \end{aligned} \quad (5.1)$$

where $\sigma_T = 6.65 \times 10^{-25} \text{ cm}^2$ is the Thomson scattering cross section, and $H(z)$ is the Hubble parameter at redshift z , given by Eq. 7.41. That is, given an electron density history, the resulting total τ_e can be calculated by integrating Eq. 5.1. In reality, the situation is the converse, however. A total optical depth is measured, or at least inferred from the CMB polarization maps, and to convert this to an EoR, an *instant* reionization is typically assumed, i.e. that the neutral fraction x_{neu} of the Universe went from 1 to 0 at a given redshift, z_{reion} ². The latest measured value of τ_e is 0.088, in this way corresponding to $z_{\text{reion}} = 10.5$ (Jarosik et al., 2010).

5.2.2 The 21 cm line

The other method relies on the temperature dependence of the forbidden hydrogen 21 cm line. When the first sources of light appeared and a Ly α background was established, the spin temperature T_S of the gas coupled to the kinetic temperature T_k through the Wouthuysen-Field effect (Wouthuysen, 1952; Field,

²The term “ z_{reion} ” thus refers to a characteristic redshift for the EoR, whereas the term “ z_{re} ” in the present work is used for the redshift at which the UVB initiates is the cosmological simulations, the EoR occurring slightly later.

1958). A small fraction of the Ly α photons exchanged energy with the hydrogen atoms through the scattering, causing a spin flip between the two hyperfine levels $F = 0$ and $F = 1$. If the IGM has expanded adiabatically since it was thermally decoupled from the CMB at $z \sim 200$, then $T_k < T_{\text{CMB}}$ implying that this mechanism is supposed to manifest itself as absorption at $21(1+z)$ cm. If X-rays have heated the neutral IGM efficiently, however, it will be observable as an emission signal (Madau et al., 1997). Either way, the signal will thus be a signature of the first sources of light, and hence of the EoR.

While this probe of the high-redshift IGM has been considered for many years (e.g. Hogan & Rees, 1979; Scott & Rees, 1990) no observations have yet confirmed its efficiency, although this will hopefully change in the near future with the new generation of radio telescopes such as the Low Frequency Array (LOFAR)³, the Primeval Structure Telescope (PaST)⁴, and the Square Kilometre Array (SKA)⁵.

³<http://www.lofar.org>

⁴<http://web.phys.cmu.edu/~past>

⁵<http://www.skatelescope.org>

Part II

Numerical radiative
transfer

Chapter 6

Numerical background



CHAPTER 3 DEALT WITH the theoretical aspects of resonant line RT, and various analytical solutions. An entirely different approach to the problems of RT is the so-called Monte Carlo method. The principal achievement of the present work is the development and application of a numerical code, relying on this technique, capable of performing Ly α RT in the most realistic way possible. This chapter describes the algorithms and numerical simulations anterior to the RT, while the developed Ly α RT code is described in the following chapters.

6.1 Monte Carlo RT

The Monte Carlo (MC) technique is a class of computational algorithms, suitable for simulating the behavior of various physical and mathematical systems. It distinguishes itself from other simulation methods (such as cosmological simulations) by being stochastic, i.e. in some manner nondeterministic, as opposed to deterministic algorithms. Being especially useful in studying systems with a large number of coupled degrees of freedom, the basic idea of this technique is that every time the fate of some process — be it physical, mathematical, financial, or whatever — is governed by a probability distribution, the outcome is determined randomly by using a random number (or, more often, a pseudo-random number supplied by a random number generator).

MC methods were originally practiced under more generic names such as “statistical sampling”. The first to apply such methods, at least in the literature, was [Georges-Louis Leclerc, Comte de Buffon \(1733\)](#), calculating π from the number of randomly thrown needles falling inside some area. [Lord Kelvin \(1901\)](#) used numbers written on pieces of papers, drawn from a bowl, to numerically evaluate certain integrals, and in the 1930s Enrico Fermi, though never publishing anything on the subject, used numerical experiments that would now be called MC calculations to study the behavior of the newly discovered neutron.

[Metropolis & Ulam \(1949\)](#) published the first paper on the MC technique, dubbing it so after the famous casino in Monaco to honor Stanisław Ulam’s uncle, a passionate gambler ([Ulam, 1991](#)). It has been used for solving RT problems since the early 1960s ([Fleck, 1963](#)) and for resonant scattering RT a few years

later (Auer, 1965). In essence, a large number of photons are followed as they diffuse randomly in real and frequency space from their locations of emission until they escape the medium. The optical depth that a photon reaches before being scattered, the velocity of the scatterer, the direction into which the photon is scattered, and several other physical quantities are determined from the various probability distributions by which they are governed.

Nevertheless, though conceptually simple, the demand for strong computer power until quite recently restricted this technique to deal with more or less the same idealized configurations that had already been dealt with analytically. Thus, the majority of previous attempts to model RT in astrophysical situations have been based on strongly simplified configurations.

By far, the most work on the subject has been concerned with the emerging spectrum from an isothermal, homogeneous medium of plane-parallel or spherical symmetry (e.g. Auer, 1965; Avery & House, 1968; Panangia & Ranieri, 1973; Ahn et al., 2001, 2002; Zheng & Miralda-Escudé, 2002). Some allow for isotropic velocities (e.g. Caroff et al., 1972; Natta & Beckwith, 1986; Loeb & Rybicki, 1999; Dijkstra et al., 2006a) and for a density gradient (Barnes & Haehnelt, 2010), and some include simple models for dust (e.g. Bonilha et al., 1979; Ahn et al., 2000; Hansen & Oh, 2006; Verhamme et al., 2006). However, even though the results of this work have improved our knowledge tremendously on many physical processes, they do not capture the complexity and diversity of realistic, astrophysical situations where velocities can be quite chaotic, and densities and temperatures can vary by many orders of magnitude over relatively small distances.

A few codes have been constructed and applied to arbitrary distributions of physical parameters resulting from cosmological simulations (Cantalupo et al., 2005; Tasitsiomi, 2006a; Laursen & Sommer-Larsen, 2007; Kollmeier et al., 2010; Faucher-Giguère et al., 2010). The next chapter describe the construction a similar code — MOCALATA¹. Although the work carried out in this thesis is largely inspired by the above discussed, it distinguishes itself in several ways from earlier works: the two most important features of MOCALATA are its adaptive grid and its realistic treatment of dust. The adaptive mesh refinement (AMR) allows for investigation of arbitrarily detailed systems, the resolution only being limited by the underlying cosmological simulation (or, in extreme cases, by computer memory), while the dust is absolutely necessary to rely on the resulting spectra and images, for instance allowing us to compute escape fractions. Furthermore, in addition to studying the emergent spectrum and SB distribution, the effect of viewing the system from different angles is investigated. Also, the wavelength and redshift dependent RT through the IGM is treated.

6.1.1 Random numbers

Evidently, a key concept of an MC code is the generation of *random numbers*. Since the output of any deterministic computation is inherently predictable, truly random numbers cannot be generated by a computer, but several algorithms exist that for virtually any purpose come sufficiently close to. Most

¹In a somewhat pathetic attempt to come up with a cool acronym, MOCALATA stands for **Monte Carlo Lyman alpha Transfer with AMR**.

such pseudorandom number generators provide a series of numbers randomly distributed in the interval $[0, 1]$. Such a number is called a univariate. The developed code makes use of the pseudorandom number generator `ran1` (Press et al., 1992), providing a series of numbers that does not repeat itself before at least 2×10^{18} callings.

The general technique for generating random numbers with an arbitrary PDF that is analytically integrable, *and* the integral of which is invertible, is as follows:

As a case in point, we will explicate how to generate a random value of an optical depth τ , governed by the PDF found in Eq. 3.40:

$$P(\tau) = e^{-\tau}. \quad (6.1)$$

Since Eq. 6.1 is properly normalized in the interval $[0, \infty[$, finding a τ randomly distributed under this function corresponds to integrating Eq. 6.1 from 0 to τ until the area under the function is equal to some univariate \mathcal{R} :

$$\mathcal{R} = \int_0^{\tau} e^{-\tau'} d\tau' \quad (6.2)$$

$$= -e^{-\tau} + 1. \quad (6.3)$$

If the PDF is not normalized, it should be so before integrating. Next, this expression for \mathcal{R} is inverted to give us $\tau = \tau(\mathcal{R})$:

$$\tau(\mathcal{R}) = -\ln(1 - \mathcal{R}), \quad (6.4)$$

or, equivalently,

$$\boxed{\tau(\mathcal{R}) = -\ln \mathcal{R}.} \quad (6.5)$$

If the PDF is not analytically integrable, it can be integrated numerically, split up into bins. The appropriate bin is then found by cumulating the values in the bins until the univariate is reached.

6.2 Smoothed particle hydrodynamics

Smoothed particle hydrodynamics (SPH) is a class of computational algorithms used for simulating the flow of fluids. Introduced over three decades ago (Lucy, 1977; Gingold & Monaghan, 1977), it is now applied in a wide range of fields of physics, including astrophysics, aerodynamics, oceanography, and volcanology. The basic principle of SPH is to represent a fluid by N_{par} discrete particles containing the physical parameters of interest. In contrast to mesh-based, or Eulerian, methods where derivatives are evaluated at fixed points in space, SPH is a Lagrangian technique, i.e. the coordinates move with the fluid. Hence, compared to regularly spaced gridding, SPH allows for a huge dynamical range in density, since little computational power is spent in regions of low density.

The parameters of a particle are “smeared out” over a finite spatial distance by a kernel function W that decreases monotonically away from the particle, out to some distance where it vanishes. This distance is given by (twice) the *smoothing length* h_{SPH} of the particle, and is usually dependent on the local density such that h_{SPH} is small in dense regions and large in rarefied regions.

The kernel could for instance be a Gaussian. More commonly, however, a cubic spline is used. The value $A(\mathbf{r})$ of any given quantity A in any given point \mathbf{r} is then

$$A(\mathbf{r}) = \sum_j \frac{A_j}{\rho_j} m_j W(|\mathbf{r} - \mathbf{r}_j|, h_{\text{SPH}}), \quad (6.6)$$

where the summation is over the nearest N_{nb} neighbors, and A_j , ρ_j , m_j , and \mathbf{r}_j are the quantity of interest, the associated density, the mass, and the position of the j 'th particle, respectively. The optimal choice for N_{nb} is somewhat controversial (and dependent on the specific simulation); in the present simulation, $N_{\text{nb}} = 50$ is used. When h_{SPH} varies in time and space, the choice of which particle's h_{SPH} to use in Eq. 6.6 becomes ambiguous; in the *scatter* interpretation h_{SPH} refers to the j 'th particle, whereas in the *gather* interpretation h_{SPH} refers to particle closest to \mathbf{r} . There is no a priori reason to favor one over another; a compromise may be to use the mean of the two smoothing lengths, or, even better, to use the mean of the two kernels (Hernquist et al., 1989).

The motion of the particles is found by solving the Euler equation including the appropriate forces between them (or the Navier-Stokes equation, if viscosity is included); in pure N-body simulations, e.g. DM-only simulations, the only relevant force is gravity. The large scale structure of the Universe is dominated by dark matter, but on galactic scales, hydrodynamics needs to be taken into account, resulting in pressure forces between particles. Thus, in SPH simulations two different types of particles are used: collisionless dark matter particles and collisional gas particles. Since each of the N_{par} particles influence the other $N_{\text{par}} - 1$, brute force calculations of their mutual attraction results in $\mathcal{O}(N_{\text{par}}^2)$ coupled differential equations. Interpolating particles onto a mesh and Fourier transforming the gravitational potential converts the partial differential equations to multiplications with Green's functions, making the number of operations scale like $\mathcal{O}(N_{\text{par}} \log N_{\text{par}})$ instead; this scheme is called the Particle-Mesh (PM) method (e.g. Efstathiou et al., 1985). An alternative way, requiring also only $\mathcal{O}(N_{\text{par}} \log N_{\text{par}})$, is a hierarchical tree where forces between nearby particles are calculated as a direct sum, but particles increasingly farther away are treated in increasingly larger collective groups (Barnes & Hut, 1986).

To avoid numerical singularities, the gravitational force F between two particles of masses m_i and m_j , separated by a distance r_{ij} , is calculated as $F = Gm_i m_j / (r_{ij}^2 + \epsilon^2)$, where G is the gravitational constant and ϵ is the (small) *gravity softening length*.

A plethora of additional physical processes may then be implemented, such as viscosity, thermal conduction, star formation (converting gas particles into collisionless star particles), chemical evolution, stellar feedback (converting the stars back to gas and injecting energy into the surrounding medium), RT of ionizing radiation, etc.

6.3 Underlying cosmological simulations

The cosmologic simulations used in this study are conducted using an N-body/hydrodynamical TreeSPH code. The simulations are first carried out at low resolution, but in a large spherical volume of space with open boundary conditions. Subsequently, interesting galaxy-forming regions are resimulated at high resolution.

Typically, resimulations are performed at $8\times$ higher mass resolution, but also ultrahigh resolution ($64\times$) simulations are executed.

The spherical hydrosimulations are themselves resimulations at $8\times$ the resolution of DM-only simulations, run with 128^3 DM particles with periodic boundary conditions. In the hydrosimulations, all of the original DM particles are then split into a DM particle and a gas (SPH) particle according to an adopted universal baryon fraction of $f_b = 0.15$, in line with recent estimates.

The simulations are started at an initial redshift $z_i = 39$, at which time there is only DM and gas particles. The latter eventually evolves partly into star particles, while, in turn, star particles can become gas particles again. Both a [Salpeter \(1955\)](#) and a [Kroupa \(1998\)](#) IMF has been considered. A standard, flat Λ CDM cosmology is assumed, with $\Omega_m = 0.3$, $\Omega_\Lambda = 0.7$, and $h = H_0/100 \text{ km}^{-1} \text{ Mpc}^{-1} = 0.7$. Two models with different values of the rms linear density fluctuation σ_8 on scales of $8h^{-1} \text{ Mpc}$ are examined: one with $\sigma_8 = 0.74$ and one with $\sigma_8 = 0.9$. These values bracket the latest WMAP-inferred value of ~ 0.8 ([Jarosik et al., 2010](#)). The comoving diameter of the simulated volume is $D_{\text{box}} = 10h^{-1} \text{ Mpc}$.

In addition to H and He, the code also follows the chemical evolution of C, N, O, Mg, Si, S, Ca, and Fe, using the method of [Lia et al. \(2002a,b\)](#). This algorithm invokes in a non-instantaneous fashion the effects of supernovae of type II and type Ia, and mass loss from stars of all masses. Star formation spawns feedback processes, manifesting itself in galactic superwinds. In the simulations, these winds are realized using the “conservative” entropy equation solving scheme ([Springel & Hernquist, 2002](#)) (rather than thermal energy), improving the shock resolution over classical SPH schemes.

The Ly α emission is produced by the three different processes described in [Sec. 2.1.1](#); from recombinations in photoionized regions around massive stars (responsible for $\sim 90\%$ of the total Ly α luminosity), gravitational cooling of infalling gas ($\sim 10\%$), and a metagalactic UV background (UVB) photoionizing the external parts of the galaxy ($\sim 1\%$).

The UVB field is assumed to be that given by [Haardt & Madau \(1996\)](#), where the gas is treated as optically thin to the UV radiation until the mean free path of a UV photon at the Lyman limit becomes less than 0.1 kpc , at which point the gas is treated as optically thick and the UV field is “switched off”. Motivated by the steep decline in the transmission of the IGM blueward of the Ly α line around $z \sim 6$ (discussed in [Sec. 5.1](#)), the original [Haardt & Madau](#) UVB is assumed to switch on at a redshift of $z_{\text{re}} = 6$. To comply with the results of WMAP, which predicts a somewhat earlier UVB, a different set of models was also run, in which the intensity curve was “stretched” to initiate at $z \sim 10$. When these two different versions are discussed together, the model with $z_{\text{re}} = 10$ will be referred to as “early” reionization, while $z_{\text{re}} = 6$ will be referred to as “late” reionization.

The masses of SPH, star and DM particles were $m_{\text{gas}} = m_\star = 7.3 \times 10^5$ and $m_{\text{DM}} = 4.2 \times 10^6 h^{-1} M_\odot$, and the gravity softening lengths were $\epsilon_{\text{gas}} = \epsilon_\star = 380$ and $\epsilon_{\text{DM}} = 680 h^{-1} \text{ pc}$. The gravity softening lengths were fixed in physical coordinates from $z = 6$ to $z = 0$, and in comoving coordinates at earlier times. For a more thorough description of the code, the reader is referred to [Sommer-Larsen et al. \(2003\)](#) and [Sommer-Larsen \(2006\)](#). A snapshot of one of the simulations at $z = 2.5$ is seen in [Fig. 6.1](#).

Nine individual galaxies are extracted from the cosmological simulation at red-

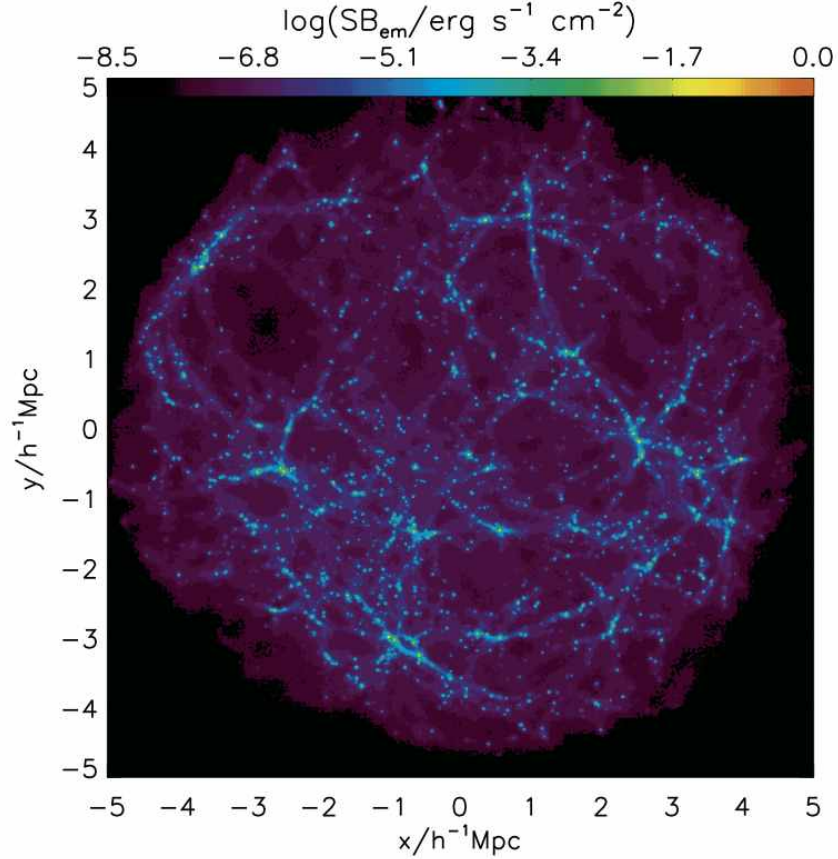


Figure 6.1: Snapshot of a cosmological simulation at a redshift of $z = 2.5$. Color coding indicates $\text{Ly}\alpha$ emissivity, and distances are given in comoving coordinates. In this particular simulation, $z_{\text{re}} = 10$ and $\sigma_8 = 0.74$ was used.

shift $z = 3.6$ — at which time the Universe was 1.8 Gyr old — to be used for the $\text{Ly}\alpha$ RT. These galaxies are representative of typical galaxies in the sense that they span three orders of magnitude in mass, the most massive eventually evolving into a disk galaxy with circular speed $V_c \simeq 300 \text{ km s}^{-1}$ at $z = 0$. The numerical and physical properties of these galaxies are listed in Tab. 6.1 and Tab. 6.2, respectively.

6.3.1 Ionizing UV radiative transfer

To model the propagation of ionization fronts realistically, Razoumov & Sommer-Larsen (2006, 2007) employed the following RT scheme to post-process the cosmological simulation: first, the physical properties of the SPH particles are interpolated from the 50 nearest neighboring particles onto an adaptively refined grid of base resolution 128^3 cells, with dense cells recursively subdivided into eight cells until no cell contains more than ten particles. *The resulting adaptively refined grid is the same that will be used for the $\text{Ly}\alpha$ RT.*

CHARACTERISTIC QUANTITIES OF THE SIMULATIONS

Galaxy	S33sc	K15	S29	K33	S115	S87	S108	S115sc	S108sc
$N_{p,tot}$	1.2×10^6	2.2×10^6	1.1×10^6	1.2×10^6	1.3×10^6	1.4×10^6	1.3×10^6	1.3×10^6	1.3×10^6
N_{SPH}	5.5×10^5	1.0×10^6	5.1×10^5	5.5×10^5	6.4×10^5	7.0×10^5	6.3×10^5	6.4×10^5	6.3×10^5
m_{SPH}, m_{star}	5.4×10^5	9.3×10^4	9.3×10^4	9.3×10^4	1.1×10^4	1.2×10^4	1.2×10^4	2.6×10^3	1.5×10^3
m_{DM}	3.0×10^6	5.2×10^5	5.2×10^5	5.2×10^5	6.6×10^4	6.5×10^4	6.5×10^4	1.4×10^4	8.1×10^3
$\epsilon_{SPH}, \epsilon_{star}$	344	191	191	191	96	96	96	58	48
ϵ_{DM}	612	340	340	340	170	170	170	102	85
l_{min}	18	10	10	10	5	5	5	3	2.5

Table 6.1: Total number of particles ($N_{p,tot}$), number of SPH particles only (N_{SPH}), masses (m), gravity softening lengths (ϵ), and minimum smoothing lengths (l_{min}) of dark matter (DM), gas (SPH), and star particles used in the simulations. Masses are measured in $h^{-1}M_{\odot}$, distances in $h^{-1}pc$

PHYSICAL PROPERTIES OF THE SIMULATED GALAXIES

Galaxy	S33sc	K15	S29	K33	S115	S87	S108	S115sc	S108sc
$SFR/M_{\odot} \text{ yr}^{-1}$	70	16	13	13	0.5	0.46	1.62	3.7×10^{-3}	1.7×10^{-3}
M_{*}/M_{\odot}	3.4×10^{10}	1.3×10^{10}	6.0×10^9	6.5×10^9	2.5×10^8	1.8×10^8	4.9×10^8	2.0×10^7	5.9×10^6
M_{vir}/M_{\odot}	7.6×10^{11}	2.8×10^{11}	1.7×10^{11}	1.3×10^{11}	2.5×10^{10}	2.1×10^{10}	2.6×10^9	4.9×10^9	3.3×10^8
r_{vir}/kpc	63	45	39	35	20	19	10	12	5
[O/H]	-0.08	-0.30	-0.28	-0.40	-1.22	-1.28	-0.51	-1.54	-1.64
$V_c(z=0)/km \text{ s}^{-1}$	300	245	205	180	125	132	131	50	35
$L_{Ly\alpha}/erg \text{ s}^{-1}$	1.6×10^{44}	4.5×10^{43}	2.9×10^{43}	2.5×10^{43}	1.3×10^{42}	1.1×10^{42}	2.6×10^{42}	4.9×10^{40}	3.2×10^{39}
$L_{\nu,UV}/erg \text{ s}^{-1}Hz^{-1}$	5.0×10^{29}	6.7×10^{28}	9.3×10^{28}	5.5×10^{28}	3.6×10^{27}	3.3×10^{27}	1.2×10^{28}	2.6×10^{25}	1.2×10^{25}

Table 6.2: Star formation rates (SFRs), stellar masses (M_{*}), virial masses (M_{vir}), virial radii (r_{vir}), metallicities ([O/H]), circular velocities (V_c), Ly α luminosities ($L_{Ly\alpha}$), and UV luminosities ($L_{\nu,UV}$) for the simulated galaxies. All quoted values correspond to a redshift of $z = 3.6$, except V_c which is given for $z = 0$.

Around each stellar source, a system of $12 \times 4^{n-1}$ radial rays ($n = 1, 2, \dots$ being the angular resolution level) is constructed that split either as one moves farther away from the source or as a refined cell is entered. Once a radial ray is refined angularly, it stays refined at larger distances from the source, even when leaving the high-resolution region. In each cell, the photoreaction number and energy rates due to photons traveling along ray segments passing through that cell are accumulated. These rates are then used to update temperature and the ionization state of hydrogen and helium, which in turn are used to calculate the Lyman continuum (LyC) opacities used in the RT. In addition to stellar photons, ionization and heating by LyC photons originating outside the computational volume is accounted for with the FTTE scheme (Razoumov & Cardall, 2005) assuming the Haardt & Madau UVB, modified to match the particular reionization model.

Since the ratios of HI, HeI, and HeII densities varies from cell to cell, the UV RT cannot be conducted monochromatically but has to be done as multi-

frequency transfer. The UV photons are separated in three bands, $[13.6, 24.6[$ eV, $[24.6, 54.4[$ eV, and $[54.4, \infty[$, assuming a mixture of stellar and quasar spectra which would provide the UVB. In each cell the angle-averaged intensity is added to the chemistry solver to compute the ionization equilibrium.

Chapter 7

MoCALATA



FIRM BASIS HAS NOW been established for understanding the development and the structure of the developed MC Ly α RT code MoCALATA. In short the structure of MoCALATA is as follows: at the heart of a simulation lies an *adaptively refined grid of cells*, with each cell containing a set of physical parameters characterizing that particular point in space. Being adaptively refined means that one may have extremely high resolution only in the places where it is required, retaining low resolution elsewhere. In this way the need for memory is tremendously reduced, compared to achieving the same resolution with a regular grid¹.

The physical parameters may be set “by hand”, as in the case of a homogeneous, isothermal sphere, or may be a “snapshot” from a cosmological simulation. If the underlying cosmological simulation is an AMR code, like AP³M (Couchman, 1991), ENZO (O’Shea et al., 2004) and ART (Kravtsov et al., 1997), the original grid is simply used for the Ly α RT. If the underlying cosmological simulation is particle based, like Gadget (Springel, 2005) and the code that we will make use of (Sommer-Larsen et al., 2003, see also Sec. 6.3), first the physical parameters of interest must be interpolated onto the mesh. Cells may be subdivided into eight subcells which, in turn, may be further refined. The refinement criterion is usually taken to be density, but can in principle be any condition, e.g. density gradient, velocity, etc.

Thus, in each cell we will have values for the temperature T , the number density $n_{\text{H I}}$ of neutral hydrogen, the number density n_{d} of dust, the three dimensional bulk velocity \mathbf{v}_{bulk} , as well as the luminosity $L_{\text{Ly}\alpha}$. n_{d} is itself calculated on the basis of the metallicity of the eight different metals and the ionization state of hydrogen in the cell.

A photon is then launched with a probability of being launched from a given cell proportional to the luminosity in that cell. Depending on the optical depth of the gas and dust lying along the path of the photon, it then travels some distance before it either scatters on a hydrogen atom or a dust grain, is absorbed by dust, or escapes the computational box. If scattered, it changes direction and continues its journey.

¹Throughout this thesis we will use the terms cell, grid point and mesh point more or less interchangeably; a mesh- or grid point can be thought of as being the center of a cell.

At each point of scattering the probability that the photon is emitted in the direction of a virtual observer *and* escapes through the intervening column of gas is calculated and added as a weight to the pixel element of a three dimensional array corresponding to the frequency and the projected position of the photon. The whole process is then repeated until the photon escapes the computational box, and subsequently repeated for the other photons until the output converges, and adding more photons does not alter the output significantly.

MoCALATA is written in the general-purpose, procedural, imperative programming language Fortran (95). Generally, to avoid numerical errors, calculations are carried out in double precision, providing approximately 16 digits of precision. To save memory, however, the large arrays storing the physical parameters are kept in single precision. Since each photon's path is independent of the others', the simulation can be distributed on several CPUs, and the code has thus been parallelized using OpenMP.

7.1 Emission of photons

The ratio of $L_{\text{Ly}\alpha}$ of a given cell to the total luminosity L_{tot} of all cells determines the probability of a photon being emitted from that particular cell. The initial position \mathbf{x}_{em} of the photon is a random location in the cell.

Irrespective of the emission being due to recombination or collisional excitation and subsequent decay, the photons are emitted isotropically. Accordingly, an initial direction vector \mathbf{n}_i can be found as

$$\mathbf{n}_i = \begin{pmatrix} 2\mathcal{R}_1 - 1 \\ 2\mathcal{R}_2 - 1 \\ 2\mathcal{R}_3 - 1 \end{pmatrix} \quad (7.1)$$

where $\mathcal{R}_1, \mathcal{R}_2, \mathcal{R}_3$ are three different univariates. In order not to favor the corners of the cube surrounding \mathbf{x}_i , if $n_i^2 > 1$ (i.e. if \mathbf{n}_i lies outside a unit sphere) it is rejected and three new univariates are drawn. Otherwise it is accepted and normalized to get the initial *unit* direction vector $\hat{\mathbf{n}}_i$.

In the reference frame of the emitting atom, the photon is injected with a frequency x_{nat} , given by the distribution $\mathcal{L}(x)$ (Eq. 3.15). The atom, in turn, has a velocity \mathbf{v}_{atom} in the reference frame of the gas element drawn from a thermal profile of Doppler width $\Delta\nu_{\text{D}}$. Measuring atom velocities in terms of Doppler widths, $\mathbf{u} = \mathbf{v}_{\text{atom}}/v_{\text{th}}$, each component u_i is then distributed according to $\mathcal{G}(u_i)$, given by Eq. 3.14.

To first order in v/c , Eq. 7.1 is valid in all relevant reference frames, and a Lorentz transformation to the reference frame of the gas element then yields the initial frequency

$$x_i = x_{\text{nat}} + \mathbf{u} \cdot \hat{\mathbf{n}}_i. \quad (7.2)$$

For photons emitted in the dense, star-forming regions, it makes no difference whether x_i is calculated in the above manner or simply set equal to zero. However, when studying large volumes of space, a nonvanishing fraction of the Ly α photons may be produced through cooling radiation, which also takes place well away from the star-forming regions of the galaxy. In these environments, whereas the probability of a photon with $x = 0$ escaping is still extremely small, being injected one or two Doppler widths away from line center may allow the photon to escape directly.

7.2 Propagation of the radiation

7.2.1 Optical depth

The optical depth τ covered by the photon before scattering is governed by the PDF given by Eq. 3.40. Thus, instead of calculating the probability of being scattered for each single atom encountered along the way, we can determine the optical depth from Eq. 3.40 and subsequently convert it into a physical distance r using Eq. 3.38. The method of generating a random value of τ was discussed in Sec. 6.1.1.

7.2.2 Gas and dust cross section

Neutral hydrogen

Recall that in the rest frame of the gas element, the scattering cross section σ_x of H I given by Eq. 3.19:

$$\sigma_x = f_{12} \frac{\sqrt{\pi} e^2}{m_e c \Delta \nu_D} H(a, x), \quad (7.3)$$

where

$$H(a, x) = \frac{a}{\pi} \int_{-\infty}^{\infty} \frac{e^{-y^2}}{(x-y)^2 + a^2} dy. \quad (7.4)$$

is the Voigt function.

Unfortunately, Eq. 7.4 is not analytically integrable. Indeed, it can be integrated numerically, but due to the broad wings of the Lorentzian this is not practical, especially since one would have to do this for a fine grid covering all the anticipated values of a and x . A common way to come around this is to simply use

$$H(a, x) \simeq \begin{cases} e^{-x^2} & \text{in the core} \\ \frac{a}{\sqrt{\pi} x^2} & \text{in the wings,} \end{cases} \quad (7.5)$$

or to expand $H(a, x)$ in a . However, [Tasitsiomi \(2006a\)](#) offers an analytical fit which is an excellent approximation for temperatures $T > 2$ K, and may be written as

$$H(a, x) = q \sqrt{\pi} + e^{-x^2}, \quad (7.6)$$

where

$$q = \begin{cases} 0 & \text{for } z \leq 0 \\ \left(1 + \frac{21}{x^2}\right) \frac{a}{\pi(x^2+1)} P(z) & \text{for } z > 0, \end{cases} \quad (7.7)$$

with

$$z = \frac{x^2 - 0.855}{x^2 + 3.42}, \quad (7.8)$$

and

$$P(z) = 5.674z^4 - 9.207z^3 + 4.421z^2 + 0.1117z. \quad (7.9)$$

In Fig. 7.1 the Voigt function as given by Eq. 7.6 is compared with the “exact” solution resulting from a 4th order numerical integration (Simpson’s method), and with the approximation given by Eq. 7.5.

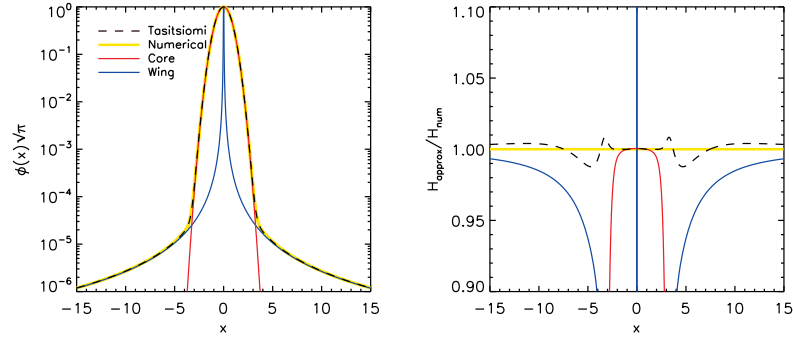


Figure 7.1: Comparison of the approximation given by Eq. 7.6 (dashed) with the numerical solution (yellow) of the Voigt function for a temperature of $T = 10000$ K. Also shown are the core (Gaussian, red) and the wing (Lorentzian, blue) approximation given by Eq. 7.5. In the right panel the discrepancy between the solutions stand out more clearly. It is clear that in the core/wing approximation, the exact transition between the two becomes crucial.

Dust

The total cross section (per hydrogen atom) of the dust grains is given by Eq. 4.4:

$$\sigma_d/10^{-21} \text{ cm}^2 = \begin{cases} 0.395 + 1.82 \times 10^{-5} T_4^{1/2} x & \text{for the SMC} \\ 0.723 + 4.46 \times 10^{-5} T_4^{1/2} x & \text{for the LMC.} \end{cases} \quad (7.10)$$

7.2.3 Spatial displacement

With τ , σ_x , and σ_d as given by Eqs. 6.5 and 7.3, and 7.10, respectively, we can now determine the physical distance r that the photon will travel before being scattered:

$$r = \frac{\tau}{n_{\text{H I}}\sigma_x + n_d\sigma_d}. \quad (7.11)$$

The new — not necessarily final, as we will see — position of the photon is then

$$\mathbf{x}_f = \mathbf{x}_i + r\hat{\mathbf{n}}_i, \quad (7.12)$$

where $\mathbf{x}_i = \mathbf{x}_{\text{em}}$.

If \mathbf{x}_f lies inside the cell, the photon is scattered. However, because in general the physical conditions vary from cell to cell, if the final location is outside the initial cell we must redo the calculations above inside the neighboring cell. Towards this end, we consecutively check whether \mathbf{x}_f is outside the six planes constituting the boundaries of the cell and, if so, determine the exact position of the intersection \mathbf{x}_{cut} of the photon's trajectory with the plane.

Specifically, let x_+ be the x -value of the plane including the face of the cell lying in the positive x -direction and define x_- , y_{\pm} and z_{\pm} accordingly. Then the distance from \mathbf{x}_i to the face is

$$\delta x = \frac{x_+ - x_{i,1}}{\hat{n}_{i,1}}, \quad (7.13)$$

where $x_{i,1}$ is the x -component of \mathbf{x}_i , etc., and should not be confused with the initial frequency x_i . If $x_{f,1} > x_+$, the photon has crossed the plane and is “pulled back” to the point of intersection

$$\mathbf{x}_{\text{cut}} = \mathbf{x}_i + \delta x \hat{\mathbf{n}}_i. \quad (7.14)$$

However, only if $y_- \leq x_{\text{cut},2} < y_+$ and $z_- \leq x_{\text{cut},3} < z_+$, the photon actually left the cell through the x_+ -face; otherwise, it must have left through one of the other faces which we then check. Whatever the case, when \mathbf{x}_{cut} has been determined, we set $\mathbf{x}_f = \mathbf{x}_{\text{cut}}$ and let the photon continue its journey, redoing the steps above, but with the physical parameters of the new cell. The optical depth of this particular part of the journey has already been determined, however, so the new optical depth τ' that will enter the equations is reduced by the amount spent in the previous cell:

$$\tau' = \tau_{\text{orig.}} - |\mathbf{x}_{\text{cut}} - \mathbf{x}_i| (n_{\text{HI}} \sigma_x)_{\text{prev.cell}}. \quad (7.15)$$

In contrast to a regular grid, in an AMR grid a given cell will not in general have a unique neighbor. The cells are structured in a nested grid, where a refined cell is the “parent” of eight “child” cells which, in turn, may or may not be refined. The new host cell of the photon is then determined by walking up and down the hierarchical tree structure.

7.2.4 Lorentz transformation between adjacent cells

Obviously, the frequency ν of the photon is not altered upon entering the neighboring cell. However, because of the temperature dependence of $\Delta\nu_D$, ν is no longer represented by the same value of x . Moreover, since x was defined relative to the gas bulk motion, we must perform a Lorentz transformation in order to express x relative to the bulk motion in the new cell.

To an external observer, the frequency of the photon is measured to be

$$x_{\text{ext}} = x + \mathbf{u}_{\text{bulk}} \cdot \hat{\mathbf{n}}_i, \quad (7.16)$$

where $\mathbf{u}_{\text{bulk}} = \mathbf{v}_{\text{bulk}}/v_{\text{th}}$. Denoting with primed and unprimed variables values in the “new” and the “old” cell, respectively, from Eq. 7.16 and the definition of x ,

$$(x' + \mathbf{u}'_{\text{bulk}} \cdot \hat{\mathbf{n}}_i) \Delta\nu'_D = (x + \mathbf{u}_{\text{bulk}} \cdot \hat{\mathbf{n}}_i) \Delta\nu_D, \quad (7.17)$$

or

$$x' = (x + \mathbf{u}_{\text{bulk}} \cdot \hat{\mathbf{n}}_i) \frac{\Delta\nu_D}{\Delta\nu'_D} - \mathbf{u}'_{\text{bulk}} \cdot \hat{\mathbf{n}}_i. \quad (7.18)$$

In this way the photon is transferred through the medium until either the initially assigned τ is “spent” and the photon is scattered/absorbed, or it escapes the computational box.

7.3 Scattering

Once the location of the scattering event has been determined, another univariate \mathcal{R} determines whether the photon hits a hydrogen atom or a dust grain by

comparing it to the ratio

$$\begin{aligned}\varrho &= \frac{n_d \sigma_d}{n_{\text{Hi}} \sigma_x + n_d \sigma_d} \\ &= \frac{\tau_d}{\tau_x + \tau_d}.\end{aligned}\tag{7.19}$$

7.3.1 Atom velocity

If $\mathcal{R} > \varrho$, the interaction is caused by hydrogen, in which case the velocity \mathbf{u} of the atom responsible is generated.

Parallel velocity

The probability distribution of velocities parallel to the incident direction of the photon is given by Eq. 3.34:

$$f(u_{\parallel}) = \frac{a}{\pi H(a, x)} \frac{e^{-u_{\parallel}^2}}{(x - u_{\parallel})^2 + a^2}\tag{7.20}$$

To pick a random parallel velocity u_{\parallel} , in principle all we have to do is to integrate Eq. 7.20 from $-\infty$ to u_{\parallel} until we reach some univariate \mathcal{R} . The problem is that Eq. 7.20 is not analytically integrable and that again numerical integration is not practical.

The solution to this problem is based on the *rejection method* (Press et al., 1992): choosing a random number with a given distribution can be interpreted geometrically as choosing a random point $P(x, y)$ in two dimensions uniformly distributed in the area under the function graphing the distribution. Since the function is not integrable, we do not have a direct way of choosing P . However, we can draw a function $g(u_{\parallel})$ that lies everywhere *above* the original function $f(u_{\parallel})$, and that *is* integrable. We will call this function the *comparison function*. If a random point chosen uniformly under this function lies under $f(u_{\parallel})$ as well, we will accept the corresponding value of u_{\parallel} ; if not, we will reject it and draw a new P (in fact, this is similar to the method we used in three dimensions to generate the initial direction vector, Eq. 7.1).

To determine whether P lies within the original probability distribution, a uniform deviate between 0 and $g(u_{\parallel})$ is drawn as the y -value of P . If this number lies also between 0 and $f(u_{\parallel})$, we keep the x -value of P as u_{\parallel} . Alternatively, we can pick the second random number between zero and one, and then accept or reject u_{\parallel} according to whether it is respectively less or greater than the ratio $f(u_{\parallel})/g(u_{\parallel})$.

For a given frequency and temperature, the factor $a/\pi H(a, x)$ in Eq. 7.20 is constant. Thus, we want to find a random value of u_{\parallel} with the distribution

$$f(u_{\parallel}) \propto \frac{e^{-u_{\parallel}^2}}{(x - u_{\parallel})^2 + a^2},\tag{7.21}$$

where a and x are given. The distribution being invariant with respect to the transformation $(x, u_{\parallel}) \rightarrow (-x, -u_{\parallel})$, we can operate with a positive x , and then multiply the result with the sign of the original x .

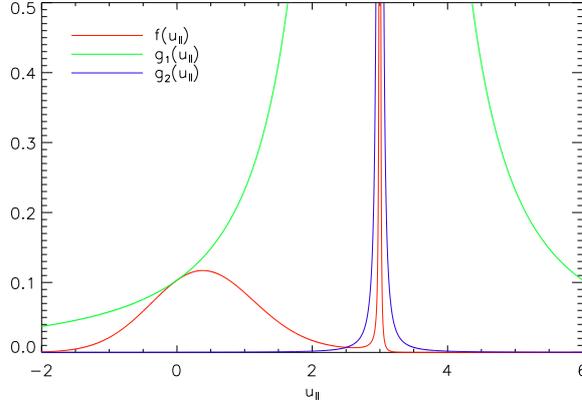


Figure 7.2: Probability distribution $f(u_{\parallel})$ of parallel velocities u_{\parallel} (red) for $x = 3$. Also shown are the two comparison functions $g_1(u_{\parallel})$ (green) and $g_2(u_{\parallel})$ (blue), with a separating parameter of $u_0 = 2.75$. A random point $P(x, y)$ under g is determined, and the corresponding value of u_{\parallel} accepted if P lies under f as well.

The comparison function can be chosen as

$$g(u_{\parallel}) \propto \frac{1}{(x - u_{\parallel})^2 + a^2}, \quad (7.22)$$

since this is integrable, invertible, and everywhere larger than $f(u_{\parallel})$ (except at $u_{\parallel} = 0$, where $g = f$). A first univariate \mathcal{R}_1 then gives us a value of u_{\parallel} , which is accepted if a second univariate \mathcal{R}_2 is smaller than $f/g = e^{-u_{\parallel}^2}$.

Unfortunately, when $x \gtrsim 2$ the fraction of rejected velocities becomes inexpediently large. To increase the fraction of acceptance, Zheng & Miralda-Escudé (2002) make use of *two* comparison functions, applying to two domains separated by some parameter u_0 :

$$g(u_{\parallel}) \propto \begin{cases} g_1(u_{\parallel}) = \frac{1}{(x - u_{\parallel})^2 + a^2} & \text{for } u_{\parallel} \leq u_0 \\ g_2(u_{\parallel}) = \frac{e^{-u_0^2}}{(x - u_{\parallel})^2 + a^2} & \text{for } u_{\parallel} > u_0 \end{cases}, \quad (7.23)$$

in which case the acceptance fractions are $e^{-u_{\parallel}^2}$ and $e^{-u_{\parallel}^2}/e^{-u_0^2}$ for g_1 and g_2 , respectively.

Defining a number p as the relative area under the first part of the comparison function

$$\begin{aligned} p &= \frac{\int_{-\infty}^{u_0} g(u_{\parallel}) du_{\parallel}}{\int_{-\infty}^{+\infty} g(u_{\parallel}) du_{\parallel}} \\ &= \frac{\int_{-\infty}^{u_0} g(u_{\parallel}) du_{\parallel}}{\int_{-\infty}^{u_0} g_1(u_{\parallel}) du_{\parallel} + \int_{u_0}^{+\infty} g_2(u_{\parallel}) du_{\parallel}} \\ &= \frac{\theta_0 + \pi/2}{(1 - e^{-u_0^2})\theta_0 + (1 + e^{-u_0^2})\pi/2}, \end{aligned} \quad (7.24)$$

where

$$\theta_0 = \tan^{-1} \left(\frac{u_0 - x}{a} \right), \quad (7.25)$$

we determine which domain to use by comparing p with a univariate \mathcal{R}_1 . Then $u_{||}$ is generated through

$$u_{||} = a \tan \theta + x, \quad (7.26)$$

where θ is a random number uniformly distributed in $[-\pi/2, \theta_0]$ and $[\theta_0, \pi/2]$ for $\mathcal{R}_1 \leq p$ and $\mathcal{R}_1 > p$, respectively.

Finally, a second univariate \mathcal{R}_2 is compared with the corresponding fraction of acceptance, thus determining whether the generated value of $u_{||}$ is accepted or rejected.

The last obstacle in determining $u_{||}$ is how to find an appropriate value of u_0 , since the number of accepted values of $u_{||}$ is highly dependent on u_0 . For the wide range of temperatures and frequencies involved we find that a satisfactory average acceptance-to-rejection ratio of order unity is achieved for

$$u_0 = \begin{cases} 0 & \text{for } 0 \leq x < 0.2 \\ x - 0.01a^{1/6}e^{1.2x} & \text{for } 0.2 \leq x < x_{\text{cw}}(a) \\ 4.5 & \text{for } x \geq x_{\text{cw}}(a) \end{cases} \quad (7.27)$$

as the value u_0 separating the two comparison functions, an x_{cw} defines the boundary between the core and the wings of the Voigt profile, given by Eq. 3.30.

Perpendicular velocity

Velocities perpendicular to $\hat{\mathbf{n}}_i$ follow a regular Gaussian which unfortunately is also not integrable. However, Box & Müller (1958) showed that *two independent* deviates can be generated simultaneously from this distribution from two univariates \mathcal{R}_1 and \mathcal{R}_2 in the following way:

$$\begin{aligned} u_{\perp,1} &= (-\ln \mathcal{R}_1)^{1/2} \cos 2\pi\mathcal{R}_2 \\ u_{\perp,2} &= (-\ln \mathcal{R}_1)^{1/2} \sin 2\pi\mathcal{R}_2. \end{aligned} \quad (7.28)$$

In this particular part it is possible to speed up the code tremendously. The acceleration scheme is described in Sec. 7.5.

Change of basis

The axes defining $u_{\perp,1}$ and $u_{\perp,2}$ can be in any directions, as long as $\hat{\mathbf{u}}_{\perp,1} \perp \hat{\mathbf{u}}_{\perp,2} \perp \hat{\mathbf{u}}_{||} \equiv \hat{\mathbf{n}}_i$. To be specific, we generate $\hat{\mathbf{u}}_{\perp,1}$ by projecting $\hat{\mathbf{n}}_i$ onto the xy -plane, re-normalizing and rotating by $\pi/2$ about the z -axis, resulting in

$$\hat{\mathbf{u}}_{\perp,1} = \frac{1}{(\hat{n}_{i,1}^2 + \hat{n}_{i,2}^2)^{1/2}} \begin{pmatrix} -\hat{n}_{i,2}\hat{\mathbf{x}} \\ \hat{n}_{i,1}\hat{\mathbf{y}} \\ 0 \end{pmatrix}, \quad (7.29)$$

where $\hat{\mathbf{x}}, \hat{\mathbf{y}}$ are the unit direction vectors of the “lab” system (the external observer), while $\hat{\mathbf{u}}_{\perp,2}$ is generated through the cross product

$$\hat{\mathbf{u}}_{\perp,2} = \hat{\mathbf{n}}_i \times \hat{\mathbf{u}}_{\perp,1} \quad (7.30)$$

With the atom velocities in the three directions given by Eqs. 7.26 and 7.52, the total velocity \mathbf{u} of the atom in the lab frame is then

$$\mathbf{u} = u_{\perp,1}\hat{\mathbf{u}}_{\perp,1} + u_{\perp,2}\hat{\mathbf{u}}_{\perp,2} + u_{\parallel}\hat{\mathbf{n}}_i. \quad (7.31)$$

7.3.2 Re-emission

The direction vector $\hat{\mathbf{n}}_f$ of the scattered photon is determined by the proper phase function; for core scatterings, according to the discussion in Sec. 4.2.4 a first univariate establishes if the intermediate state is $2P_{1/2}$ (probability: 1/3) or $2P_{3/2}$ (probability: 2/3). In the first case the photon is scattered isotropically so that, as in the case of emission, $\hat{\mathbf{n}}_f$ is given by Eq. 7.1. Otherwise it is scattered according to the distribution given by Eq. 3.27. Wing scatterings follow the distribution given by Eq. 3.28. Integrating these functions from $\mu = -1$ until a univariate \mathcal{R} is reached and inverting yields the only real solution

$$\mu = \varphi^{-1/3} - \varphi^{1/3}, \quad (7.32)$$

where

$$\varphi = \begin{cases} \frac{1}{7} (14 - 24\mathcal{R} + (245 - 672\mathcal{R} + 576\mathcal{R}^2)^{1/2}) & \text{in the core} \\ 2 - 4\mathcal{R} + (5 - 16\mathcal{R} + 16\mathcal{R}^2)^{1/2} & \text{in the wings.} \end{cases} \quad (7.33)$$

Since the scattering is azimuthally isotropic, we may draw two more variates $\tau_1, \tau_2 \in [-1, 1]$, rejecting them if $\mathfrak{s} \equiv \tau_1^2 + \tau_2^2 > 1$, and normalize them to

$$\tau'_1 = \left(\frac{1 - \mu^2}{\mathfrak{s}} \right)^{1/2} \tau_1 \quad (7.34)$$

$$\tau'_2 = \left(\frac{1 - \mu^2}{\mathfrak{s}} \right)^{1/2} \tau_2. \quad (7.35)$$

The direction of the outgoing photon can then be represented by

$$\hat{\mathbf{n}}_f = \begin{pmatrix} \tau'_1 \hat{\mathbf{u}}_{\perp,1} \\ \tau'_2 \hat{\mathbf{u}}_{\perp,2} \\ \mu \hat{\mathbf{n}}_i \end{pmatrix}. \quad (7.36)$$

7.3.3 Interaction with dust

If $\mathcal{R} \leq \varrho$, the interaction is caused by dust. In this case a second univariate is compared to the albedo of the dust grain, dictating whether the photon is absorbed, thus terminating the journey of this particular photon, or scattered, in which case it is re-emitted in a random direction given by the [Henyey-Greenstein](#) phase function (Eq. 4.9):

$$P_{\text{HG}}(\mu) = \frac{1}{2} \frac{1 - g^2}{(1 + g^2 - 2g\mu)^{3/2}}. \quad (7.37)$$

To generate a new direction from this distribution, again the rejection method described above is applied.

7.4 Simulating observations

Following the scheme described in Secs. 7.1 through 7.3, the photon is trailed as it scatters in real and frequency space, until eventually it escapes the computational box. Subsequently, this procedure is repeated for the remaining $n_{\text{ph}} - 1$ photons. Each time a photon leaves the box, we can sample its frequency and its point of last scattering, in this way yielding the spectrum and a three dimensional image of the extension of the Ly α radiation.

7.4.1 Surface brightness maps and spectra

However, since in general the morphology of a galaxy may very well cause an anisotropic luminosity, it is more interesting to see how the system would appear when observed from a given angle. Because the number of photons escaping in a particular direction is effectively zero, following Yusuf-Sadeh & Morris (1984) we calculate instead *for each scattering* and for each photon the probability of escaping the medium in the direction of the observer, or, in fact, six different observers situated in the positive and negative directions of the three principal axes, as

$$w = W(\mu)e^{-\tau_{\text{esc}}}, \quad (7.38)$$

where $W(\mu)$ is given by the proper phase function (Eqs. 3.26, 3.27 or 3.28), μ is given by the angle between $\hat{\mathbf{n}}_i$ and the direction of the observer, and τ_{esc} is the optical depth of the gas and dust lying between the scattering event and the edge of the computational box (integrated through the intervening cells). This probability is added as a weight to an array of three dimensions; two spatial and one spectral. The two spatial dimensions can be thought of as a CCD, consisting of N_{pix}^2 pixels each suspending a solid angle Ω_{pix} of the computational box. Behind each pixel element is a one-dimensional spectral array with N_{res} bins.

Since flux leaving the source diminishes as $1/d_L^2$, where d_L is the luminosity distance, the total surface brightness SB_{pix} of the area covered by the pixel, measured in energy per unit time, per unit area *at the location of the observer*, per unit solid angle suspended by the pixel is then

$$\text{SB}_{\text{pix}} = \frac{L_{\text{tot}}}{d_L^2 \Omega_{\text{pix}} n_{\text{ph}}} \sum_{\text{ph.,scat.}} W(\mu)e^{-\tau_{\text{esc}}}, \quad (7.39)$$

where the sum is over all photons and all scatterings. Note that Eq. 7.39 does not contain a factor $1/4\pi$, due to the fact that the phase functions are normalized to unity.

In a flat Universe, the luminosity distance of an object at redshift z is given by (e.g., Weinberg, 1972)

$$d_L = \frac{c}{H_0}(1+z) \int_0^z \frac{dz'}{H(z')/H_0} \quad (7.40)$$

(which must be integrated numerically), where H_0 is the present Hubble parameter, and

$$\frac{H(z)}{H_0} = \left[\Omega_m(1+z)^3 + \Omega_k(1+z)^2 + \Omega_\Lambda \right]^{1/2}, \quad (7.41)$$

with Ω_m and Ω_Λ the (dark and baryonic) matter and dark energy density parameter, respectively. For a non-zero curvature parameter $\Omega_k \equiv 1 - \Omega_m - \Omega_\Lambda$, the integral in Eq. 7.40 must be replaced by

$$\frac{1}{\sqrt{\Omega_k}} \sinh \left(\sqrt{\Omega_k} \int_0^z \frac{dz'}{H(z')/H_0} \right) \quad \text{for } \Omega_k > 0 \quad (7.42)$$

$$\frac{1}{\sqrt{|\Omega_k|}} \sin \left(\sqrt{|\Omega_k|} \int_0^z \frac{dz'}{H(z')/H_0} \right) \quad \text{for } \Omega_k < 0. \quad (7.43)$$

Equation 7.39 is the SB that an observer would measure at a distance d_L from the galaxy. Hence, this is the interesting quantity for comparing with actual observations. Theorists tend to be more concerned with the intrinsic SB, i.e. the flux measured by a hypothetical observer at the location of the source. The conversion is given by

$$\text{SB}_{\text{there}} = \frac{\Omega d_L^2}{A} \text{SB}_{\text{here}}, \quad (7.44)$$

where A is the area suspended by the solid angle Ω . The ratio between the two defines the angular diameter distance

$$d_A^2 = \frac{A}{\Omega}. \quad (7.45)$$

Since the SB of a receding object decreases as $(1+z)^4$ and the angular area as $(1+z)^2$, d_A is related to d_L by

$$d_L = (1+z)^2 d_A. \quad (7.46)$$

From Eqs. 7.45 and 7.46, Eq. 7.44 can be written

$$\text{SB}_{\text{there}} = (1+z)^4 \text{SB}_{\text{here}}, \quad (7.47)$$

or, if Ω is measured in arcsec² rather than steradians

$$\boxed{\text{SB}_{\text{there}} = 206265^2 (1+z)^4 \text{SB}_{\text{here}}.} \quad (7.48)$$

Finally, the 3D array can be collapsed along the frequential direction to give a ‘‘bolometric’’ SB map (i.e. all wavelengths in the vicinity of the Ly α line), along the two spatial directions to give the integrated spectrum, or along all directions to give the total flux received from the source. Since in fact a full spectrum is obtained for each pixel, it is also possible to simulate long-slit spectroscopy, giving frequency as a function of position of a selected part of the image.

7.5 Acceleration schemes

7.5.1 Core-skipping scheme

In very dense regions of the gas, as long as the photon is in the core, the optical depth is so enormous that each scattering is accompanied by a negligible spatial shift. Only when by chance the photon encounters an atom with a large perpendicular velocity will it be scattered out of the core, i.e. beyond

$|x| = x_{\text{cw}} \sim 3$, and be able to make a long journey. Since the probability P of this happening is

$$P \simeq \frac{2}{\sqrt{\pi}} \int_{x_{\text{cw}}}^{\infty} e^{-x^2} dx \quad (7.49)$$

$$\sim 1 - \text{erf}(3) \quad (7.50)$$

$$\sim 10^{-5}, \quad (7.51)$$

and since complete redistribution is a fair approximation in the core, it will take of the order of 10^5 scatterings before entering the wing. These scatterings are insignificant in the sense that they do not contribute to any important displacement in neither space nor frequency. Hence, we may as well skip them altogether and go directly to the first scattering that pushes the photon into the wing. This can be achieved by drawing $u_{\perp,1}$, $u_{\perp,2}$ from a *truncated* Gaussian that favors atoms with high velocities (Avery & House, 1968). The total perpendicular velocity $u_{\perp} = (u_{\perp,1}^2 + u_{\perp,2}^2)^{1/2}$ follows a two-dimensional Maxwellian $\mathcal{M}(u_{\perp})$ where the direction of \mathbf{u}_{\perp} is isotropically distributed in the plane. Replacing for Eq. 7.28 (Dijkstra et al., 2006a),

$$\begin{cases} u_{\perp,1} &= (x_{\text{crit}}^2 - \ln \mathcal{R}_1)^{1/2} \cos 2\pi \mathcal{R}_2 \\ u_{\perp,2} &= (x_{\text{crit}}^2 - \ln \mathcal{R}_1)^{1/2} \sin 2\pi \mathcal{R}_2, \end{cases} \quad (7.52)$$

corresponds to drawing u_{\perp} from the distribution

$$\mathcal{M}(u_{\perp}) = \begin{cases} 0 & \text{for } |u_{\perp}| \leq x_{\text{crit}} \\ 2u_{\perp} e^{-(u_{\perp}^2 - x_{\text{crit}}^2)} & \text{for } |u_{\perp}| > x_{\text{crit}} \end{cases} \quad (7.53)$$

where x_{crit} is the critical value of x within which scatterings can be neglected. The value x_{crit} is not simply equal to x_{cw} , since for a non-dense medium, a core scattering can in fact be associated with a considerable spatial journey, while in extremely thick clouds even scatterings in the inner part of the wing may be neglected. Moreover, the exact value of x_{crit} is actually quite important; a high value can decrease the computational execution time by *several orders of magnitude*, while a too high value will push the photons unnaturally far out in the wings, skewing the result. From the Neufeld solution we know that the important parameter is the product $a\tau_0$. Correspondingly, we expect x_{crit} to be a function of the value of $a\tau_0$ in the current cell. Indeed, from numerous tests it is found that we can use

$$x_{\text{crit}} = \begin{cases} 0 & \text{for } a\tau_0 \leq 1 \\ 0.02e^{\xi \ln^{\chi} a\tau_0} & \text{for } a\tau_0 > 1, \end{cases} \quad (7.54)$$

where $(\xi, \chi) = (0.6, 1.2)$ or $(1.4, 0.6)$ for $a\tau_0 \leq 60$ or $a\tau_0 > 60$, respectively, without affecting the final result. Of course, if the photon is already in the wing, the proper Gaussian is used.

Dust absorption in the core

With a dusty medium, we must investigate the possibility that the photon would have been destroyed, had we *not* used this acceleration scheme, i.e. the probability $P_{\text{abs}}(x_{\text{crit}})$ of absorption for a photon initially in the core, before escaping

the frequency interval $[-x_{\text{crit}}, x_{\text{crit}}]$. Ultimately, we will determine this probability numerically, but to interpret the result, we will first investigate the scenario analytically. In the following calculation, factors of order unity will be omitted. The probability per interaction that a photon with frequency x be absorbed is

$$p_{\text{abs}}(x) = \frac{\tau_{\text{a}}}{\tau_{\text{d}} + \tau_x} \sim \frac{1}{1 + \phi(x)\tau_0/\tau_{\text{a}}}, \quad (7.55)$$

since $\tau_{\text{a}} \sim \tau_{\text{d}}$ and $\tau_x \sim \phi(x)\tau_0$. Here, $\tau_{\text{a,d,x,0}}$ corresponds to the optical depth of this particular part of the journey. The number $dN(x)$ of scatterings taking place when the frequency of the photon is close to x is

$$dN(x) = N_{\text{tot}}\phi(x)dx, \quad (7.56)$$

where N_{tot} is the total number of scatterings before the photon exits $[-x_{\text{crit}}, x_{\text{crit}}]$, i.e. the total number of scatterings skipped. Here we have assumed *complete redistribution* of the frequency, i.e. there is no correlation between the frequency of the photon before and after the scattering event. This is a fair approximation in the core (Unno, 1952b; Jefferies & White, 1960). However, as discussed in Sec. 3.3.2, once the photon is in the wing it has a tendency to stay there, only slowly drifting toward the line center with a mean shift per scattering $\langle \Delta x \rangle = -1/|x|$.

For the purpose of the current calculation, the Voigt profile is approximated by a Gaussian in the core and a power law in the wing, such that

$$\phi(x) \sim \begin{cases} e^{-x^2} & \text{for } x < x_{\text{cw}} \\ \frac{a}{x^2} & \text{for } x \geq x_{\text{cw}}, \end{cases} \quad (7.57)$$

where x_{cw} marks the value of x at the transition from core to wing (Eq. 3.30). At each scattering, the probability of escaping the region confined by x_{crit} is

$$p_{\text{esc}}(x_{\text{crit}}) = 2 \int_{x_{\text{crit}}}^{\infty} \phi(x)dx \sim \begin{cases} \text{erfc } x_{\text{crit}} & \text{for } x_{\text{crit}} < x_{\text{cw}} \\ \frac{a}{x_{\text{crit}}} & \text{for } x_{\text{crit}} \geq x_{\text{cw}}, \end{cases} \quad (7.58)$$

where erfc is the complimentary error function.

Using Eq. 7.56, the total probability of being absorbed can be calculated as

$$P_{\text{abs}}(x_{\text{crit}}) = \int_0^{x_{\text{crit}}} p_{\text{abs}}(x)dN(x) = N_{\text{tot}} \int_0^{x_{\text{crit}}} p_{\text{abs}}(x)\phi(x)dx. \quad (7.59)$$

The total number of scatterings before escape if the photon is not absorbed is $N_{\text{tot}} \sim 1/p_{\text{esc}}$. For $x_{\text{crit}} < x_{\text{cw}}$, from Eqs. 7.55 and 7.58, Eq. 7.59 then evaluates to

$$P_{\text{abs}}(x_{\text{crit}}) \sim \frac{1}{\text{erfc } x_{\text{crit}}} \int_0^{x_{\text{crit}}} \frac{dx}{e^{x^2} + \tau_0/\tau_{\text{a}}}. \quad (7.60)$$

The exponential integral and the factor $1/\text{erfc } x_{\text{crit}}$ are of the same order, but since the factor $\tau_0/\tau_{\text{a}} \sim \sigma_0/\sigma_{\text{a}}$ is of the order 10^8 , Eq. 7.60 will usually be negligible.

In the case of $x_{\text{crit}} \geq x_{\text{cw}}$,

$$P_{\text{abs}}(x_{\text{crit}}) \sim \int_0^{x_{\text{crit}}} \frac{dx}{a/\phi(x) + a\tau_0/\tau_{\text{a}}}. \quad (7.61)$$

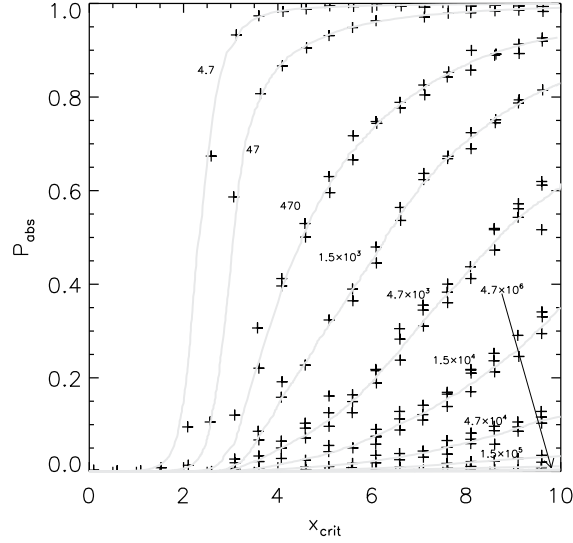


Figure 7.3: Probability of absorption P_{abs} before escaping the region of the line confined by the value x_{crit} , for a series of different values of $a\tau_0/\tau_a$ (labeled at the corresponding lines, and obtained with various combinations of a , τ_0 , and τ_a).

This integral can be evaluated separately for the intervals $[0, x_{\text{cw}}[$ and $[x_{\text{cw}}, x_{\text{crit}}]$. For the first, the result is usually negligible, as in the case with Eq. 7.60. The second integral yields

$$P_{\text{abs}}(x_{\text{crit}}) \sim \frac{1}{\mathfrak{t}} \left(\tan^{-1} \frac{x_{\text{crit}}}{\mathfrak{t}} - \tan^{-1} \frac{x_{\text{cw}}}{\mathfrak{t}} \right), \quad (7.62)$$

where

$$\mathfrak{t} \equiv (a\tau_0/\tau_a)^{1/2}. \quad (7.63)$$

For $x_{\text{crit}} \geq x_{\text{cw}}$, the assumption of complete redistribution becomes very inaccurate, as the photon spends considerably more time in the wings, with a larger probability of being destroyed. However, Eqs. 7.62 and 7.63 reveal a signature of the behavior of $P_{\text{abs}}(x_{\text{crit}})$, namely that it has a “ \tan^{-1} -ish” shape, and that it scales not with the individual parameters a , τ_0 , and τ_a , but with their interrelationship as given by the parameter \mathfrak{t} . To know exactly the probability of absorption, a series of Monte Carlo simulations were carried out for a grid of different temperatures, gas densities, and dust densities. The results, which are stored as a look-up table, are shown in Fig. 7.3. Indeed, the same fit applies approximately to different T , $n_{\text{H I}}$, and n_{d} giving equal values of \mathfrak{t} .

Whenever the acceleration scheme is applied, a bilinear interpolation over $\log \mathfrak{t}$ and x_{crit} determines the appropriate value of P_{abs} . A univariate is then drawn and compared to P_{abs} , thus determining if the photon is absorbed or allowed to continue its journey. Note that under most physically realistic conditions, only low values of P_{abs} are actually met. However, when invoking the acceleration scheme many times, the probability of absorption may become significant.

7.5.2 Semi-analytical scheme

Most of the computing time is spent in the very dense cells. Since each cell is in fact a cube of homogeneous and isothermal gas with zero velocity gradient (henceforward a “uniform cube”), if an analytical Neufeld-equivalent solution for the distribution of frequencies exists, it would be possible to skip a great number of scatterings and thus speed up the code further.

The slab solution is an alternate series which can be written in closed form. Unfortunately, this is not feasible for the cube solution, but under certain approximations, [Tasitsiomi \(2006b\)](#) found that it is still possible to write it as an alternate series. The problem is that, whereas for the slab the terms quickly die off, the same is not true for the cube. In fact she found that to achieve an accuracy better than 3%, one must exceed 30 terms.

Hence, it seems more convenient to seek a “Neufeld-based” approximation. Since for the cube, the radiation can escape from six faces rather than just two, we may expect the emergent radiation to be described by a function similar to the slab solution, but using a lower value of $a\tau_0$.

Emergent Spectrum

Toward these ends, a series of simulations is run in which photons are emitted isotropically from the centers of cubes of constant — but different — temperature and density, and zero bulk velocity. The distance from the center to each face is z_0 . We will investigate optical depths $\tau_0 = 10^5, 10^6, 10^7$, and 10^8 (measured along the shortest path from center to face). In all simulations, $n_{\text{ph}} = 10^5$, and different temperatures are tested. A Neufeld profile is then fitted to the emergent spectrum, using $\eta a\tau_0$ as the independent variable, where η is the parameter to be determined. A priori, we have no reason to believe that the same value of η , if any, should be able to describe all optical depths. However, it is found that, save for the lowest optical depth ($\tau_0 \sim 10^5$), excellent fits are obtained using

$$\boxed{\eta = 0.71.} \quad (7.64)$$

This is seen in Fig. 7.4.

Directionality of the Emergent Photons

In realistic, cosmological simulations, the direction with which the photons exit the cell is also important. Since in the limit $\tau_0 \rightarrow \infty$, any finite size step *not* perpendicular to the surface will just shift to position of the photons in the parallel direction, for extremely optically thick slabs, the photons should have a tendency to exit perpendicular to the surface. In this case, [Phillips & Mészáros \(1986\)](#) found that the directionality of the emergent radiation approaches that of Thomson scattered radiation from electrons, with intensity

$$\frac{I(\mu)}{I(0)} = \frac{1}{3} (1 + 2\mu), \quad (7.65)$$

where $\mu = \cos\theta$, with θ the angle between the outgoing direction $\hat{\mathbf{n}}_f$ of the photon and the normal to the surface.

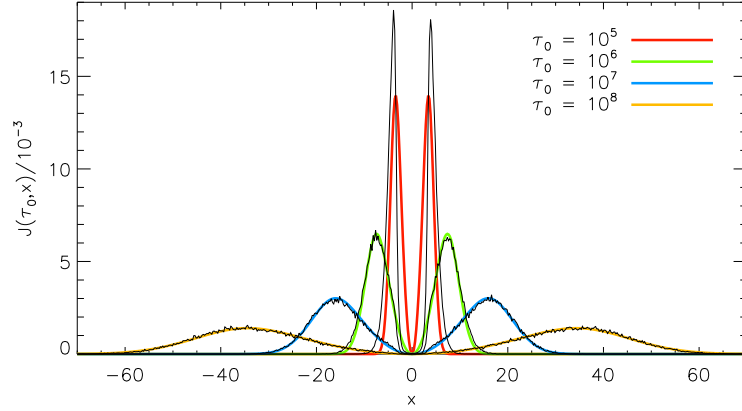


Figure 7.4: Emergent spectra of a uniform cube of different optical depths. A damping parameter of $a = 0.00047$ has been used. Neufeld profiles are fitted to the spectra using $\eta a \tau_0$, with $\eta = 0.71$ for all τ_0 .

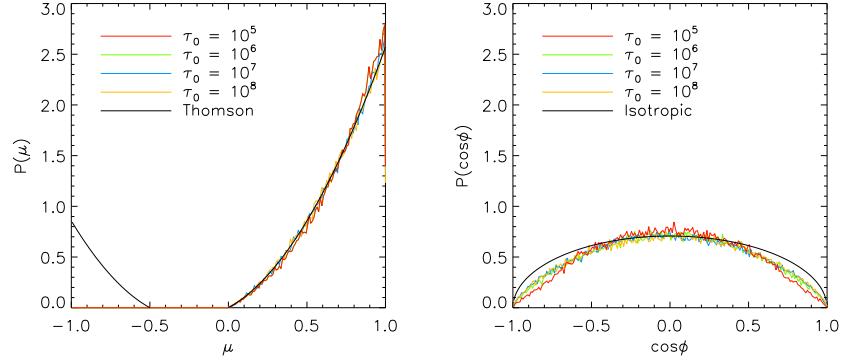


Figure 7.5: Directionality of the photons emerging from a uniform cube for different values of τ_0 . In the direction perpendicular to the face of the cube (*left*), $\hat{\mathbf{n}}_f$ follows the distribution given by Eq. 7.67, while in the azimuthal direction (*right*) there is a slight deviation from isotropy.

Since the number of photons emerging at μ is $\propto I(\mu)\mu d\mu$, the probability $P(\leq \mu)$ of exiting the slab with $\mu \leq \mu'$ is (Tasitsiomi, 2006b)

$$\begin{aligned} P(\leq \mu') &= \frac{\int_0^{\mu'} (1 + 2\mu)\mu d\mu}{\int_0^1 (1 + 2\mu)\mu d\mu} \\ &= \frac{\mu'^2}{7} (3 + 4\mu'). \end{aligned} \quad (7.66)$$

We confirm that this is also an excellent description for a cube (Fig. 7.5). The probability distribution is found by differentiating Eq. 7.66 and recognizing that μ must be positive for the photon to escape:

$$P(\mu) = \begin{cases} \frac{6}{7}(\mu + 2\mu^2) & \text{for } 0 < \mu \leq 1 \\ 0 & \text{otherwise,} \end{cases} \quad (7.67)$$

Since Eq. 7.67 is valid for all six faces of the cube, the azimuthal angle ϕ parallel

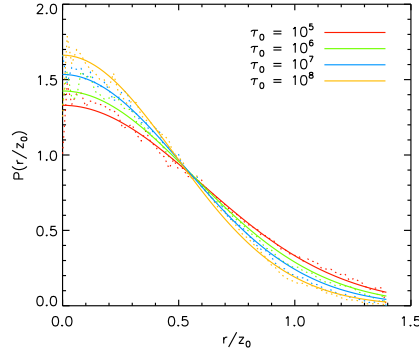


Figure 7.6: Probability distribution (solid lines) of the exiting point for photons emerging from a uniform cube of side length $2z_0$, as a function of distance r from the center of the face, normalized to z_0 , for different values of τ_0 . The distributions have been calculated as best fits to the corresponding simulated SB profiles (dotted lines), as given by Eq. 7.68.

to the face cannot, as in the case of a slab, be evenly distributed in $[0, 2\pi]$ (Tasitsiomi, 2006b). However, as can be seen from Fig. 7.5, the deviation from uniformity is quite small, and can probably be neglected. Furthermore, it seems less pronounced, the higher the optical depth.

Point of Escape

The final parameter characterizing the photons escaping the cube is the point \mathbf{x}_{esc} where it crosses the face. Figure 7.6 shows the azimuthally averaged SB profiles of the emergent radiation as a function of distance from the center of the face, for different optical depths. It is found that the SB profile is fairly well described by a truncated Gaussian

$$\text{SB}(r/z_0) = \begin{cases} \frac{2}{\sqrt{2\pi}\sigma_{\text{SB}}} e^{-(r/z_0)^2/2\sigma_{\text{SB}}^2} & \text{for } 0 \leq r \leq z_0\sqrt{2} \\ 0 & \text{for } r > z_0\sqrt{2}. \end{cases} \quad (7.68)$$

The dispersion σ_{SB} of the SB decreases very slowly with optical depth, and can be written as $\sigma_{\text{SB}} = 0.48 - 0.04 \log \tau_0/10^8$. However, in the context of a cell-based structure, one might state that it is meaningless to discuss differences in position on scales smaller than the size of a cell, and it is found that final results are not altered by simply setting $\sigma_{\text{SB}} = 0.5$.

Implementation of the Cube Solution

With the probability distributions of frequency, direction and position for the photons escaping the cell, we are now able to accelerate the code further: every time a photon finds itself in a host cell of $a\tau_0$ higher than some given threshold, which to be conservative we define as $a\tau_0 \gtrsim 2 \times 10^3$, an *effective cell* with the photon in the center is built, with “radius” z_0 equal to the distance from the photon to the nearest face of the host cell (see Fig. 7.7). Since the effective cell

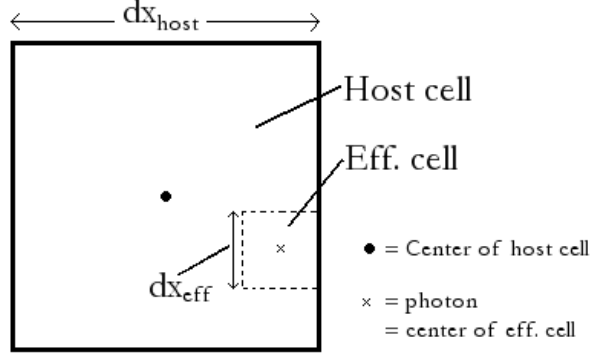


Figure 7.7: Geometry of the “effective cell inside cell”-configuration. The “radius” of the effective cell is $z_0 = dx_{\text{eff}}/2$.

is always completely circumscribed by the host cell, its physical parameters are equal to those of its host cell.

If the value of $a\tau_0$ in the effective cell, $(a\tau_0)_{\text{eff}}$, is below the threshold (i.e. if the photon is too close to the face of the host cell), the normal scheme is used. Otherwise, the photon is assigned a new frequency according to the effective Neufeld distribution: drawing a univariate \mathcal{R} and setting this equal to the Neufeld-equivalent cube solution² integrated from $-\infty$ to x yields (after some algebra)

$$\begin{aligned} \mathcal{R} &= \int_{-\infty}^{x_f} J_{\text{cube}}(\tau_0, x) dx \\ &= \frac{2}{\pi} \tan^{-1} e^{\sqrt{\pi^3/54}(x_f^3 - x_i^3)/\eta(a\tau_0)_{\text{eff}}}. \end{aligned} \quad (7.69)$$

Inverting the above expression, the frequency x of the photon then becomes

$$x_f = \left(\sqrt{\frac{54}{\pi^3}} \eta(a\tau_0)_{\text{eff}} \ln \tan \frac{\pi \mathcal{R}}{2} + x_i^3 \right)^{1/3}. \quad (7.70)$$

Finally, the direction and the position of the photon is determined from Eqs. 7.67 and 7.68 (with a probability of escaping from a given face equal to $1/6$), whereafter it continues its journey.

Dust absorption in a uniform cube

With the inclusion of dust, we must calculate the possibility of the photon being absorbed in such a cube. From the above, we might expect that replacing $a\tau_0$ by $\eta a\tau_0$ and τ_a by $\eta\tau_a$ in the slab-relevant equation for the escape fraction (Eq. 8.3) yields the relevant solution. In fact, even better fits can be achieved by simultaneously replacing the square root by an exponentiation to the power

²Of course normalized to unity instead of the usual $1/4\pi$.

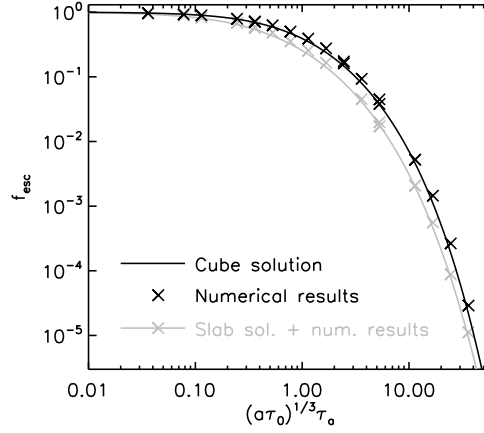


Figure 7.8: Escape fractions (*black crosses*) of photons emitted from the center of a cube of damping parameter a , line center optical depth τ_0 , and dust absorption optical depth τ_a , measured from the center to the face, compared to the analytical solution (*solid black*) given by Eq. 7.71. For comparison, the equivalent results for the slab (*gray*; the same as in Fig. 8.9) are also displayed.

of 0.55. That is, every time the semi-analytical acceleration scheme is invoked, a univariate is drawn and compared to the quantity

$$f_{\text{esc}} = \frac{1}{\cosh\left(\zeta' \left[\eta^{4/3}(a\tau_0)^{1/3}(1-A)\tau_d\right]^{0.55}\right)}, \quad (7.71)$$

determining whether or not the photon should continue its journey.

Figure 7.8 shows the calculated escape fractions from a number of cubes of different physical properties.

The tests performed in Sec. 8.1 and many of the results of Chapters 10 and 11 were performed both with and without this acceleration scheme, all agreeing to a few percent within statistical errors.

7.5.3 Luminosity-boosting scheme

Since the vast majority of the photons are emitted within a relatively small volume of the total computational domain, many photons are needed to reach good statistics in the outer regions. In order to reach convergence faster, the probability of emitting photons from low-luminosity cells can be artificially boosted by some factor $1/w > 1$, later corrected for by letting the emitted photon only contribute with a weight w to statistics (spectra, SB profiles, escape fractions). This factor is calculated for the i 'th cell as

$$w_i = \left(\frac{L_i}{L_{\text{max}}}\right)^{1/b}, \quad (7.72)$$

where L_i is the original luminosity of the cell, L_{max} is the luminosity of the most luminous cell (not to be confused with \mathcal{L}_{max}), and b is a “boost buffer” factor

that determines the magnitude of the boost; for $b = 1$, all cells will have an equal probability of emitting a photon while for $b \rightarrow \infty$ the probability approaches the original probability.

The optimal value of b depends on the quantity and physical region of interest. Since photons are absorbed primarily in the central regions, f_{esc} calculations will usually converge fastest using $b \rightarrow \infty$, and since after all most photons are received from this region as well, the same counts for the spatially integrated spectrum. If one wishes to investigate the SB or the spectrum of the outer regions, b should not simply be set equal to unity, however, since a significant fraction of the photons received from here are photons originating in the central parts and later being scattered in the direction of the observer. In this case, faster convergence can be reached with $b \sim 1.5$ and up to a few tens.

Chapter 8

Tests



BEFORE THE DEVELOPED CODE is applied to yield any scientific results, it is important to test it in several ways. The analytical solutions derived in Chap. 3 serves as a way of testing the code. Without loss of continuity, this chapter can be read at a later time. However, several of the tests are a premise for the semi-analytical acceleration scheme described in Sec. 7.5.2.

After the code has been applied, the sensitivity of the obtained results on the underlying cosmological simulations must also be tested. This is done in Sec. 8.2. Lastly, in Sec. 8.3 the model for the effects of dust is tested by varying the different parameters in the model. These two sections are probably better read *after* having read the chapters on the results.

8.1 Testing against analytical solutions

The various probability distribution generators of MOCALATA were tested against their analytical solutions (in the case such solutions exist; otherwise against numerical integration). Here, only the result for the parallel velocities u_{\parallel} (Fig. 8.1) is showed.

8.1.1 Individual scatterings

To test the individual scatterings, Fig. 8.2 shows the relation between the frequency of the incident and of the scattered photon, compared with the exact redistribution function as formulated by Hummer (1962). Furthermore, the rms and mean shift, and the average number of scattering before returning to the core for wing photons are shown. For $x \rightarrow \infty$, the values are seen to converge to the results derived by Osterbrock (1962), and given by Eqs. 3.41 and 3.42.

8.1.2 Neufeld solution

The most basic confirmation of the reliability of the code is a test of the Neufeld solution. Hence, a simulation of a slab (i.e. with the x - and y -dimension set to infinity) is run in which the bulk velocity of the elements is set to zero, while the temperature and hydrogen density are constant in such a way as to give the

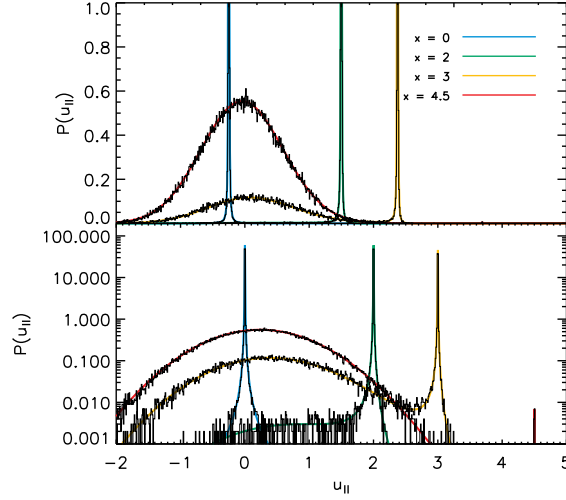


Figure 8.1: Probability distribution $P(u_{||})$ of parallel velocities $u_{||}$ of the scattering atom for four values x of the frequency of the incoming photon, as generated from Eq. 7.21. For photons in the line center ($x = 0$, *blue*), $P(u_{||})$ resembles the natural line broadening function. For successively larger, but relatively low frequencies ($x = 2$, *green*, and $x = 3$, *yellow*), the photon still has a fair chance of being scattered by an atom to which it appears close to resonance. For larger frequencies ($x = 4.5$, *red*), however, atoms with sufficiently large velocities are so rare that the distribution instead resembles a regular Gaussian, slightly shifted toward $u_{||} = x$. The method for generating $u_{||}$ is quite good at resolving the resonance peak. This is particularly visible in the logarithmic plot (bottom panel).

desired line center optical depth τ_0 from the center of the slab to the surface. Base cells are refined in arbitrary locations, to an arbitrary level of refinement. Also, $W(\theta) = \text{constant}$ is used and the recoil term in Eq. 3.35 is omitted to match the assumptions made by Neufeld. The result for different values of τ_0 is shown in Fig. 8.3, while the result of varying the initial frequency is shown in Fig. 8.4. For the lowest optical depth ($\tau_0 = 10^5$, corresponding to $a\tau_0 = 47$ at $T = 10^4$ K), the fit is not very accurate. However, this is not an artifact caused by, say, an insufficient number of photons in the simulation, but merely reflects the fact that the Neufeld solution is no longer valid when the optical depth becomes too low (at low optical depths, the transfer of photons is no longer dominated by wing scatterings, where the line profile can be approximated by a power law).

8.1.3 Maximum of the emergent spectrum

Figure 8.5 shows the values of x for which the emergent spectrum takes its maximum, compared with the analytical solution (Eq. 3.52, Harrington, 1973).

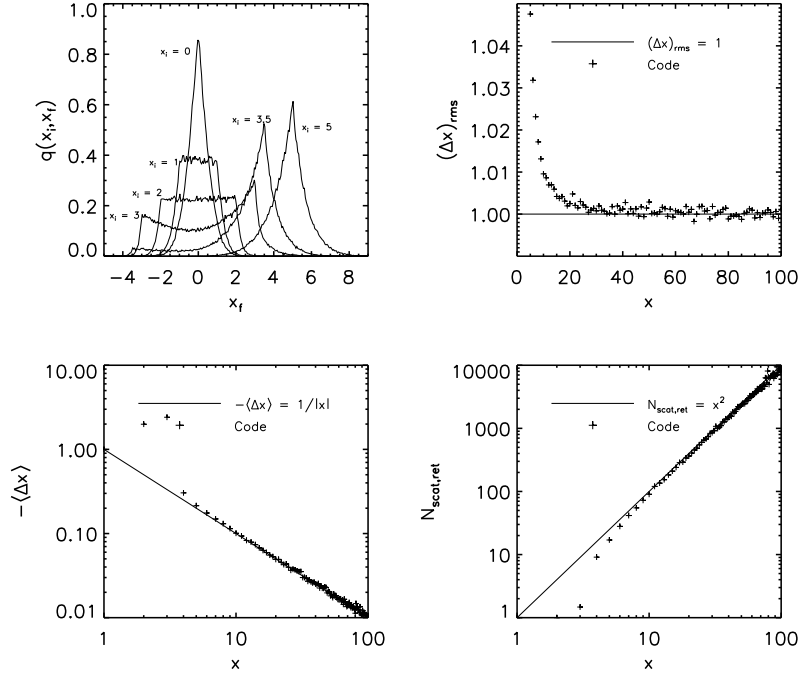


Figure 8.2: Tests of the relation between the frequency x_i of the incoming photon, and the frequency x_f of the outgoing photon (*top left*). For photons close to the line center, frequencies are distributed more or less uniformly over the line profile. For larger x , frequencies close to the incoming frequency are preferred, but also frequencies of opposite sign. The distribution follows that predicted by Hummer (1962). For even larger frequencies, photons are less likely to be scattered by atoms to which they are at resonance, and the outgoing frequency is then only a few Doppler widths away from the incoming. For sufficiently large x , the rms shift $(\Delta x)_{\text{rms}} \rightarrow 1$ (*top right*), the mean shift $\langle \Delta x \rangle \rightarrow -1/|x|$ (*bottom left*), and the average number of scattering needed to return to the core $N_{\text{scat,ret}} \rightarrow x^2$ (*bottom right*), as predicted by Osterbrock (1962).

8.1.4 Average number of scatterings

Figure 8.6 shows the average number of scatterings N_{scat} . Of course, in this case a non-accelerated version of the code (i.e. $x_{\text{crit}} = 0$) was used, since we are interested in the true number of scatterings. To get a feeling for the physical significance of the optical depths, the region of τ_0 is divided into the domains of LLSs and DLAs, characterized by limiting neutral hydrogen column densities of $N_{\text{HI}} = 10^{17.2} \text{ cm}^{-2}$ and $N_{\text{HI}} = 10^{20.3} \text{ cm}^{-2}$, respectively.

8.1.5 Gas bulk motion

To test if the implementation of the bulk velocity scheme produces reliable results, we inspect the emergent spectrum of a sphere subjected to isotropic, homologous expansion or collapse. Thus, the velocity $\mathbf{v}_{\text{bulk}}(\mathbf{r})$ of a fluid element

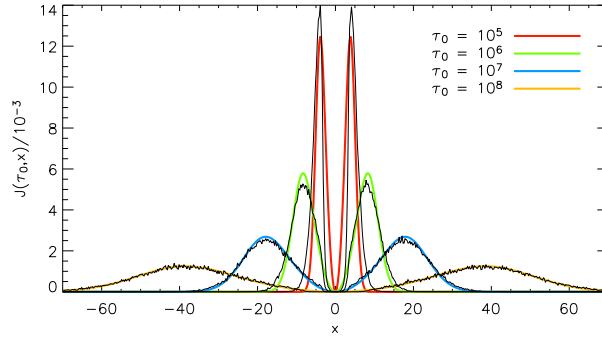


Figure 8.3: Emergent spectrum of photons injected in the line center in an isothermal and homogeneous slab of gas, for different values of line center optical depth τ_0 from the center of the slab to the surface, compared with the corresponding Neufeld solutions. For increasingly optically thick media, the photons must diffuse in frequency further and further from the line center in order to escape the medium. For all simulations, $T = 10^4$ K (corresponding to $a = 0.00047$) and $n_{\text{ph}} = 10^5$ was used. The analytical solution becomes increasingly more accurate as $\tau_0 \rightarrow \infty$.

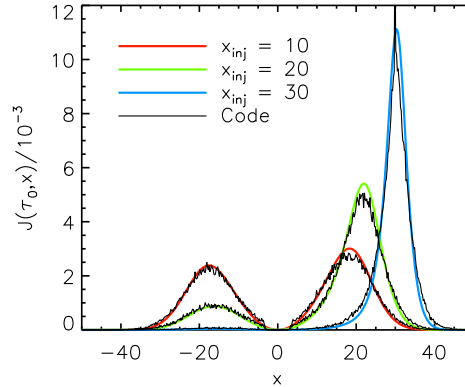


Figure 8.4: Emergent spectrum of 10^5 photons injected with different initial frequencies x_{inj} in a slab of line center optical depth $\tau_0 = 10^7$ and temperature $T = 10^4$ K (corresponding to $a\tau_0 = 4700$), compared with the corresponding Neufeld solutions.

at a distance \mathbf{r} from the center is set to

$$\mathbf{v}_{\text{bulk}}(\mathbf{r}) = \mathcal{H}\mathbf{r}, \quad (8.1)$$

where the Hubble-like parameter \mathcal{H} is fixed such that the velocity increases linearly from 0 in the center to a maximal absolute velocity v_{max} at the edge of the sphere ($r = R$):

$$\mathcal{H} = \frac{v_{\text{max}}}{R}, \quad (8.2)$$

with v_{max} positive (negative) for an expanding (collapsing) sphere.

For $T \neq 0$ K, no analytical solution for the spectrum exists. Qualitatively, we expect an expansion to cause a suppression of the blue wing and an enhancement

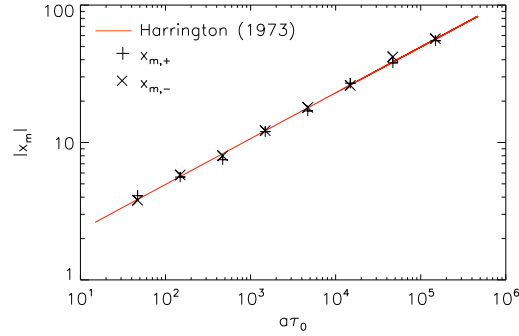


Figure 8.5: Absolute values x_m of x for which the emergent spectrum of a slab takes its maximum, as a function of $a\tau_0$ of the slab, compared with the analytical solution (red) given by Eq. 3.52. Values are shown separately for the positive (+) and the negative (\times) peak, denoted by $x_{m,+}$ and $x_{m,-}$, respectively.

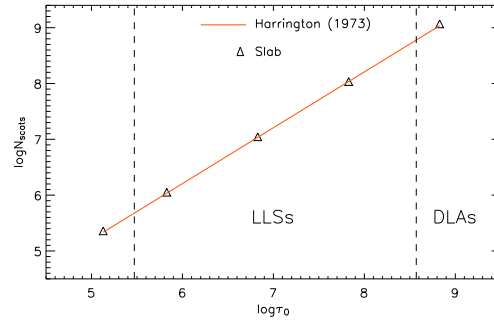


Figure 8.6: Average number of scatterings N_{scat} (triangles) for different line center optical depths τ_0 , compared with the analytical solution (red line) given by Eq. 3.53. The dashed lines indicate the regions of optical depths for LLSs and DLAs. While a temperature of $T = 10$ K was used for simulations, the number of photons varied from 10^5 to $\sim 10^3$ for the lowest and highest optical depths, respectively.

of the red wing of the spectrum. The reason for this is that photons blueward of the line center that would otherwise escape the medium, are shifted into resonance in the reference frame of atom lying closer to the edge, while red photons escape even more easily. Conversely, a collapsing sphere will exhibit an enhanced blue wing and a suppressed red wing. This is indeed seen in Fig. 8.7. Another way to interpret this effect is that photons escaping an expanding cloud are, on the average, doing work on the gas, thus losing energy, and vice versa for a collapsing cloud.

In Fig. 8.8, results for a sphere of gas expanding at different velocities are shown. For increasing v_{max} , the red peak is progressively enhanced and displaced redward of the line center. However, above a certain threshold value the velocity gradient becomes so large as to render the medium optically thin and allow less

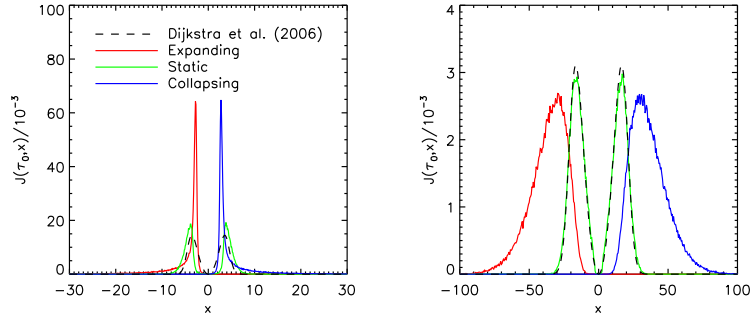


Figure 8.7: Emergent spectrum from an isothermal ($T = 10^4$ K) and homogeneous sphere of gas undergoing isotropic expansion (*red*) or contraction (*blue*) in such a way that the velocity at the edge of the sphere is $v_{\max} \pm 200$ km s $^{-1}$. Left panel shows the result for a column density N_{HI} from the center to the edge of 2×10^{18} cm $^{-2}$, corresponding to $\tau_0 = 1.2 \times 10^5$ and characteristic of a typical LLS. Right panel shows the result for $N_{\text{HI}} = 2 \times 10^{20}$ cm $^{-2}$ ($\tau_0 = 1.2 \times 10^7$), characteristic of a typical DLA. Also shown is the result from a simulation with $v_{\text{bulk}} = 0$ (*black dashed*), and the analytical solution for the static sphere (*green*) as given by Dijkstra et al. (2006a). For the LLS, τ_0 is clearly too small to give an accurate fit.

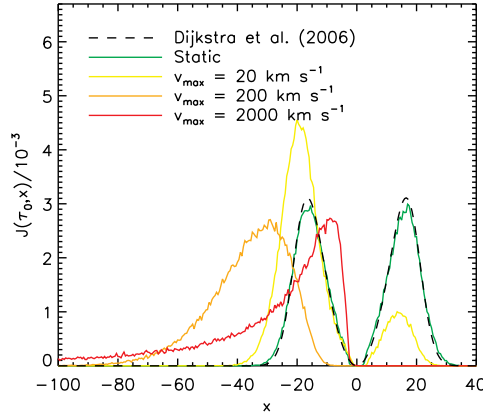


Figure 8.8: Emergent spectrum from an isothermal ($T = 10^4$ K) and homogeneous sphere of hydrogen column density $N_{\text{HI}} = 2 \times 10^{20}$ cm $^{-2}$ (a DLA) undergoing isotropic expansion with different maximal velocities v_{\max} at the edge of the sphere. For increasing v_{\max} , the peak of the profile is pushed further away from the line center. However, if v_{\max} becomes too large, the medium becomes optically thin and the peak moves back towards the center again.

redshifted photons to escape, making the peak move back toward the line center again.

The results matches closely those found by previous authors (Zheng & Miralda-Escudé, 2002; Tasitsiomi, 2006a; Verhamme et al., 2006).

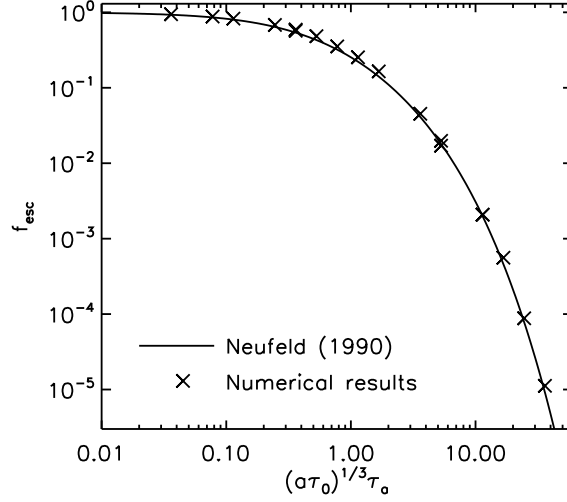


Figure 8.9: Escape fractions f_{esc} of photons emitted from the center of a semi-infinite slab of gas damping parameter a , hydrogen optical depth τ_0 , and dust absorbing optical depth τ_a , compared to the analytical solution in Eq. 8.3.

8.1.6 Escape fraction

Neufeld (1990) provided an analytical expression for the escape fraction of photons emitted from inside a slab of an absorbing medium. The solution, which is valid for very high optical depths ($a\tau_0 \gtrsim 10^3$, where τ_0 is the optical depth of neutral hydrogen from the center to the surface of the slab) and in the limit $(a\tau_0)^{1/3} \gg \tau_a$, where τ_a is the absorption optical depth of dust, is

$$f_{\text{esc}} = \frac{1}{\cosh \left[\zeta' \sqrt{(a\tau_0)^{1/3} \tau_a} \right]}, \quad (8.3)$$

where $\zeta' \equiv \sqrt{3}/\zeta\pi^{5/12}$, with $\zeta \simeq 0.525$ a fitting parameter. Figure 8.9 shows the result of a series of such simulations, compared to the analytical solution. Various AMR grid configurations were tested. Of course, the physical parameters such as n_{HI} , n_{d} , and T of a cell do not depend on the level of refinement, but the acceleration schemes discussed in Sec. 7.5 do.

8.2 Convergence tests

This section, as well as Sec. 8.3 where the dust model is tested, makes numerous references to the results obtained in Chapters 10 and 11, and may advantageously be read subsequent to those chapters.

8.2.1 Resolution and interpolation scheme

In order to check the impact of the resolution of the cosmological simulation on the results of the Ly α RT, the above RT calculations were also carried out

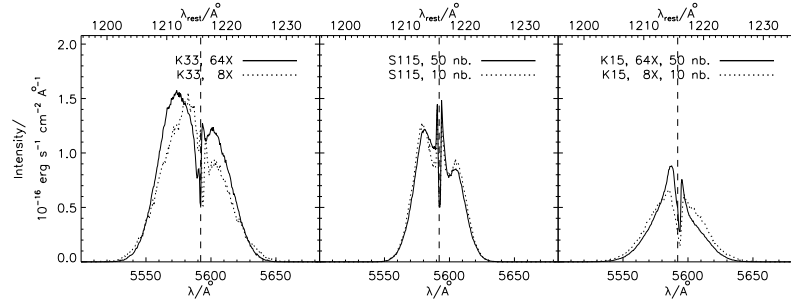


Figure 8.10: Comparison spectra for the resolution test and the interpolation test. *Left* panel shows the spectrum escaping in the negative y -direction of K33, simulated at high (*solid curve*) and intermediate (*dotted*) resolution. *Middle* panel shows the spectrum escaping in the negative x -direction of S115, simulated at ultrahigh ($64\times$) resolution, but interpolating the physical parameters onto the AMR grid using the 50 nearest neighboring particles (*solid*) and the 10 nearest neighbors (*dotted*). *Right* panel shows the spectrum escaping in the negative z -direction of K15, simulated at high resolution and interpolating from 50 neighbors (*solid*), compared with intermediate resolution/10 neighbors (*dotted*). The differences do not change the results qualitatively. Note that in the middle (right) panel, the intensity has been multiplied (divided) by a factor of 10 in order to use the same scale as for all three galaxies.

on the galaxies extracted directly from the cosmological simulations, i.e. at $8\times$ lower resolution than the resimulated galaxies. Furthermore, the procedure by which the SPH particles are interpolated onto the grid was tested by using the 10 nearest neighboring particles instead of the usual 50 particles, and running similar RT calculations on the output grids. Although in both cases the results changed somewhat, there seems to be no general trend. Due to the slightly different evolution of the lo-res galaxies (being a different simulation), the precise configuration of stars and gas clouds will not necessarily be the same, and thus luminous peaks in the SB maps cannot be expected to coincide exactly. However, the maximum SBs appear to agree to within a few tens of percents, as do the slopes and the overall amplitudes of the SB profiles. The outcome of three such simulations, performed *without* dust, can be seen in Figures 8.10 and 8.11.

The convergence proves stable also when dust is added to the calculations. The resulting SB profile and spectrum for K15 are seen in Fig. 8.12. The resulting escape fraction is a bit lower than for the hi-res simulation, but less than 5%.

8.2.2 AMR structure

To investigate the significance of the AMR structure, simulations were also carried out in which the structure was progressively desolved, level by level. In K15, K33, and S115, the maximum level \mathcal{L} of refinement is 7, where $\mathcal{L} = 0$ corresponds to the unrefined base grid of 128^3 cells. Eight cells of $\mathcal{L} = \ell$ are desolved to $\mathcal{L} = \ell - 1$ by taking the average of the physical parameters. Since temperature reflects the internal energy of a body of gas, and since the combined velocity is given by momentum, T and \mathbf{v}_{bulk} are weighted by the respective cell masses.

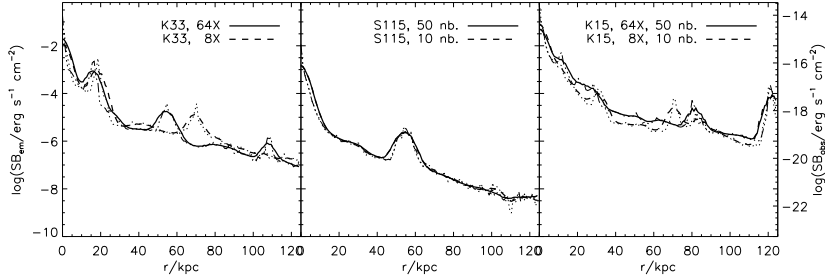


Figure 8.11: Comparison SB profiles of the six models from Fig. 8.10 at a seeing of $0''.8$ (solid and dashed curves), overplotted on the true SB profiles (dotted). While performing the simulations at different resolutions may shift some of the luminous regions somewhat spatially, the maximum SB and the overall slope remain virtually unaltered. Moreover, modifying the number of neighboring particles used for the interpolation scheme seems unimportant.

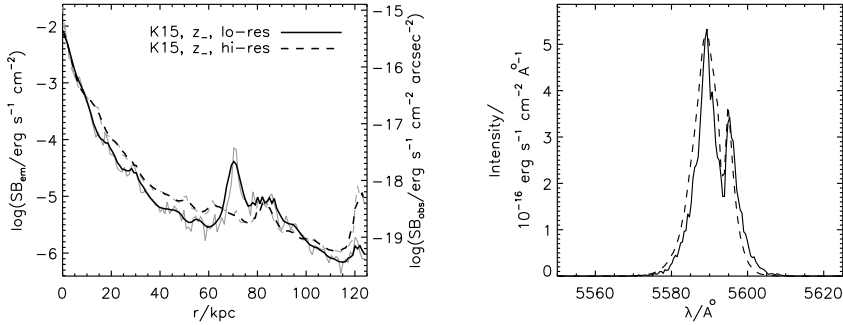


Figure 8.12: Comparison of the SB profile (left) and emergent spectrum (right) of the radiation escaping the galaxy K15 when performed on galaxies simulated at low (solid) and high (dashed) resolution. Gray lines show the true profile and black lines show the profile convolved with a seeing of $0''.5$. While the SB in the central regions appear to agree nicely, the fact that we are comparing two different simulations make luminous regions in the outskirts appear somewhat shifted.

Figure 8.13 shows the resulting escape fractions of these three galaxies. Desolving the first few levels does not alter f_{esc} notably, indicating that the galaxies are sufficiently resolved. However, eventually we see the importance of the AMR structure: with insufficient resolution, the clumpiness of the central, luminous ISM is lost, “smoothing out” the low-density paths that facilitate escape, and consequently f_{esc} decreases. When the resolution becomes even worse, the central regions are averaged with the surrounding low-density gas, so that most of the photons are being emitted from medium dense cells, resulting in a small probability of scattering on neutral hydrogen, and hence a small probability of being absorbed by dust.

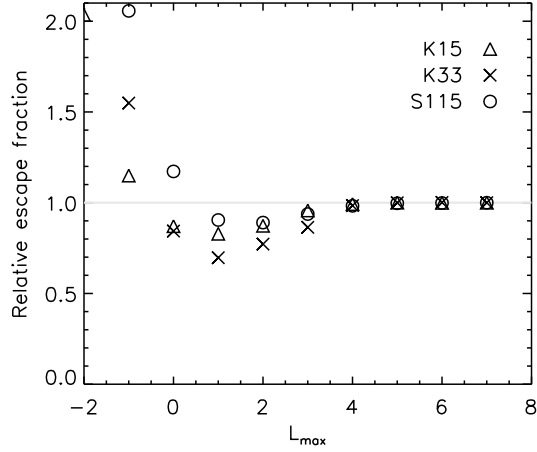


Figure 8.13: Relative escape fractions f_{esc} from the three galaxies K15, K33, and S115 as a function of the maximum level \mathcal{L}_{\max} of AMR refinement. $\mathcal{L}_{\max} = 0$ corresponds to having only the 128^3 base grid, while $\mathcal{L}_{\max} < 0$ corresponds to desolving the base grid. For increasingly lower resolution, f_{esc} drops due to the low-density paths being smeared out with high-density regions. Eventually, however, when the resolution is so coarse that the central star- and gas-rich regions are mixed with the surrounding low-density region, f_{esc} increases rapidly.

8.2.3 UV RT scheme

Finally, to see the effect of the improved UV RT scheme (Sec. 6.3.1), Fig. 8.14 shows the emergent spectrum from K15 for the different schemes (excluding the effects of dust). Both edge-on and face-on spectra are sensitive to the changes in ionization of predominantly low-density regions which is computed with LyC radiative transfer. As discussed in Sec. 8.1.2, the quantity that determines the shape of the spectrum is the product $a\tau_0 \propto n_{\text{HI}}/T$ (at a fixed physical size). Generally, a higher temperature will also imply a lower density of neutral hydrogen, and vice versa, and thus we might expect n_{HI}/T to change rapidly to higher or lower values for the improved scheme. However, for high density cells the change in the ratio n_{HI}/T is minor when invoking the improved scheme, in most cases of order unity. Only in low-density cells is this ratio considerably altered, but since $> 90\%$ of all scatterings take place in high-density cells, the overall effect is small. The only notable difference is seen in the inner part of the spectrum, which is exactly the part that is created by the low-density regions, since photons near the line center cannot escape from high-density regions.

8.3 Dust parameter study

The adopted model of dust clearly involves a multitude of assumptions, some more reasonable than others. To inspect the dependency of the outcome on the values of the parameters, a series of simulations of K15 was run, varying the below discussed values. The resulting escape fractions compared to that

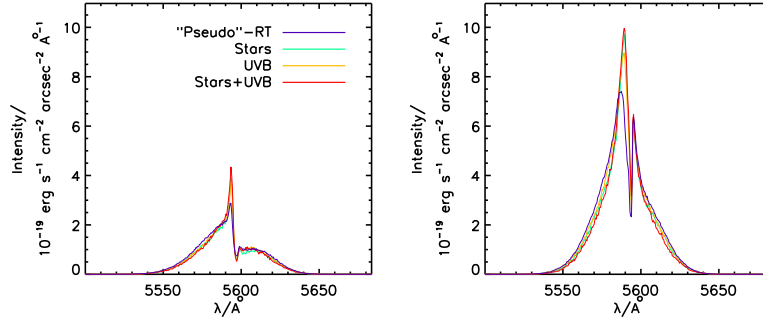


Figure 8.14: Emergent spectrum of the galaxy K15, as seen when observing the sheet-like structure in which the galaxy is embedded edge-on (*left*) and face-on (*right*). *Blue lines* show the spectrum for the model without the improved UV RT, while *green, yellow, and red lines* show the spectrum when treating the UV RT properly for the stellar sources only, the UV background only, and both, respectively. The only real difference is seen in the blue peak of the spectra, which is a bit higher for the improved models.

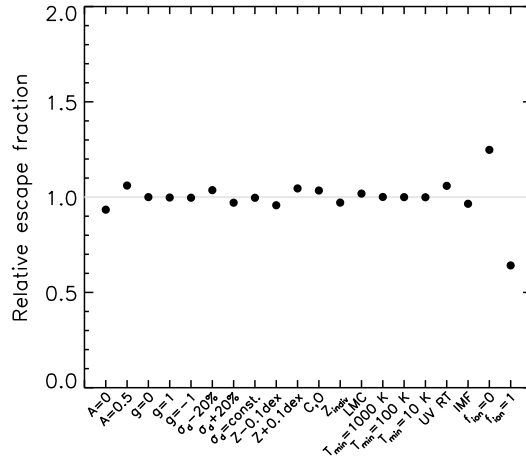


Figure 8.15: Relative escape fraction from the galaxy K15 as a “function” of model, i.e. simulation where all parameters but one are equal to that of the benchmark model used for the simulations in Chap. 11. See text for an explanation of abscissa labels. Except for the factor f_{ion} , the chosen benchmark model appears quite robust to varying other parameters.

of the “benchmark” model, used for the simulations in Chap. 11, are shown in Fig. 8.15.

The *albedo* A of the dust grains. The chosen value of 0.32 is bracketed by the values 0.5 and 0, i.e. somewhat more reflective and completely black, respectively. As expected, the higher the albedo, the higher the escape fraction, but note that even completely black dust reduces f_{esc} by less than 10%. This is

because the bulk of the photons is absorbed in the very dense environments, where scattering off of one grain in many cases just postpones the absorption to another grain.

The scattering asymmetry parameter g . The three cases $g = 0, 1, -1$ are tested, corresponding to isotropic scattering, total forward scattering, and total backscattering. The difference from the benchmark model value of 0.73 is virtually nonexistent; the fact that most of the scatterings take place in the dense environments makes the transfer be dominated by scattering on hydrogen.

The dust cross section σ_d . Fitzpatrick & Massa (2007) showed that the variance of the extinction curves (in the MW, normalized to A_V) is approximately 20% at the Ly α wavelength. Decreasing (increasing) the dust cross section by this quantity increases (decreases) the escape fraction as expected, but not by more than $\sim \pm 5\%$ percent. Also, a constant cross section with $\sigma_d = \sigma_d|_{x=0}$ was tested, but with no notable effect.

Likewise, a variance of *the reference metallicity Z* is present from sightline to sightline in the Magellanic Clouds, probably at least 0.1 dex. Using a smaller (larger) reference Z makes the metallicity in the simulations comparatively larger (smaller), with a larger (smaller) dust density as a result and hence a smaller (larger) escape fraction. Since the escaping photons represent different sightlines in the galaxies, it is fair to use the average Z (for the individual metals) in Eq. 4.6, but to investigate the sensitivity on the reference metallicity, simulations with Z_{SMC} increased (reduced) by 0.1 dex was run, resulting in a -5% ($+5\%$) change in f_{esc} .

Letting n_d scale with the metallicity of only C and O instead of the total metallicity does not alter f_{esc} much either. This model is relevant since C and O probably are the main constituents of dust.

Although the metallicity of the Magellanic Clouds is smaller than that of the MW, the *relative* abundances between the various elements are more or less equal. Small deviations do exist, however, but letting n_d scale with the metallicity of the individual metals does not change the results much (point labeled “ Z_{indiv} ” in Fig. 8.15).

Dust type. Using an LMC extinction curve instead of SMC results in a slightly (few %) larger escape fraction, since the quantity $\tau_d \propto n_d \sigma_d \propto \sigma_d / Z_0$ is roughly 10% lower for the LMC than for the SMC.

The minimum temperature T_{min} of the simulations. The cosmological simulation includes cooling of the gas to $\sim 10^4$ K. Since the temperature affects the RT of Ly α , the temperature of the cells with $T \simeq 10^4$ K was artificially lowered to 10^3 , 10^2 (approximately the temperature of the cold neutral medium), and 10 K (approximately the temperature of a molecular cloud), to see if not including sufficient cooling could affect the results. However, as is seen in Fig. 8.15, the difference is insignificant.

The ionizing UV RT scheme. As found in Sec. 8.2.3, implementing a more realistic UV RT scheme does not alter the outcome of the non-dusty Ly α RT significantly. When including dust, as seen from Fig. 8.15 the improved RT results in a slightly increased f_{esc} , although less than 10%. The reason is that this RT is more efficient than the “old” RT scheme at ionizing the neutral gas in the immediate vicinity of the stars and, accordingly, at lowering the dust density. However, in these regions the gas density is so high that ionization in most cases is followed by instantaneous recombination, and hence the physical state of the gas in the case of the improved RT is not altered significantly.

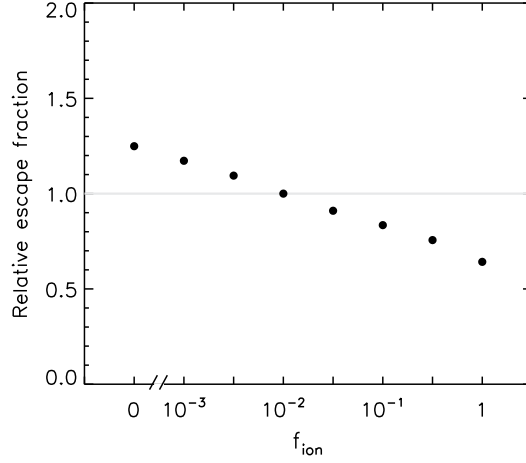


Figure 8.16: Relative variation in escape fraction f_{esc} from the galaxy K15, as a function of f_{ion} , the fraction of ionized hydrogen that contributes to the density of dust (Eq. 4.6). Note the discontinuity on the abscissa axis. Even a little dust in the ionized region can affect f_{esc} quite a lot.

The initial mass function. Since a Salpeter IMF is more top-heavy than a Kroupa IMF, i.e. produces relatively more massive stars per stellar mass, it also yields a higher metallicity and hence a higher absorption by dust. However, the increased feedback from the massive stars serves as to counteract star formation, and these two effects more or less balance each other. The ratio of the Kroupa-to-Salpeter feedback energy is 0.617, while for the yield the ratio is 0.575 (for oxygen). The result, as is seen from Fig. 8.15, is only a slightly smaller escape fraction.

The fraction of ionized hydrogen f_{ion} contributing to the dust density. Insufficient knowledge about the dust contents of ionized gas is by far the greatest source of uncertainty in f_{esc} , as is seen in the figure. This effect is further investigated in Fig. 8.16, where the relative escape fraction from K15 for different values of f_{ion} is shown.

From the figure, it is seen that even a small amount of dust associated with the ionized hydrogen can affect the escape fraction quite a lot. The reason is that most of the scatterings and the absorption take place in the dense region where also the star formation is high. In these regions supernova feedback shockwaves will recurrently sweep through the ISM, heating and ionizing the medium without significantly lowering the density. For $f_{\text{ion}} = 1$, the calculated dust density of these regions is not affected, while for $f_{\text{ion}} = 0$, this effect renders the gas virtually dustless, resulting in highly porous medium with multiple possibilities for the photons of scattering their way out of the dense regions.

The resulting escape fraction of the benchmark model lies approximately midway between the two extrema and if nothing else, f_{esc} can be regarded as having an uncertainty given by the result of these extrema, i.e. $\sim 20\%$. Nevertheless, $f_{\text{ion}} = 0.01$ seems a realistic value, cf. the discussion in Sec. 4.2.2.

Chapter 9

Intergalactic radiative transfer



THE $\text{Ly}\alpha$ RT DESCRIBED IN THE previous chapters in principle only predicts the spectrum of radiation that one would observe if located in the vicinity of the galaxies. Obviously, in reality the radiation has to travel through the IGM afterwards. At a redshift of ~ 3.6 , the IGM is largely ionized, and the spectra escaping the galaxies are, in general, not very different from what would be observed at Earth. However, even a very small amount of neutral hydrogen may influence the observations. To investigate just *how* large an impact the IGM exerts on the radiation, full IGM RT has to be computed. Furthermore, at higher redshifts where the IGM is generally more neutral and more dense, neglecting the effect would lead to severely erroneous results.

In principle this could be achieved by performing first the “galactic” RT in the high-resolution resimulations and subsequently continuing the RT in the low-resolution cosmological volume from the location of the individual galaxies. However, although the physics of scattering in galaxies and that of scattering in the IGM is not inherently different, the different physical conditions imposes a natural division of the two schemes: in the dense gas of galaxies, photons are continuously scattered in and out of the line of sight, whereas in the IGM, once a photon is scattered out of the line of sight, it is “lost”, becoming part of the background radiation. The probability of a background photon being scattered *into* the line of sight, on the other hand, is vanishingly small.

In order to disentangle galactic from intergalactic effects, and, more importantly, to investigate the general effect of the IGM instead of merely the IGM lying between us and the nine resimulated galaxies, we take a different approach: the transmission properties of the IGM are studied by calculating the normalized spectrum $F(\lambda)$ — the *transmission function* — in the vicinity of the $\text{Ly}\alpha$ line, as an average of a large number of sightlines cast through the cosmological volume, and originating just outside a large number of galaxies.

As the red part of the spectrum is only shifted farther away from resonance, IGM absorption tends to skew the line and not simply diminish it by some factor. In most earlier studies of the line profiles of high-redshift galaxies, the IGM has either been ignored (e.g. Verhamme et al., 2006, 2008), taken to transmit the

red half and remove the blue part (e.g. Finkelstein et al., 2008), or to influence the line uniformly by a factor $e^{-\langle\tau\rangle}$, where $\langle\tau\rangle$ is the average optical depth of the Universe (e.g. Bruscoli et al., 2003; Meiksin, 2005; Faucher-Giguère et al., 2008; Rykoff et al., 2009).

Consider a source emitting the normalized spectrum $F_{\text{em}}(\lambda) \equiv 1$ for all λ . In an idealized, completely homogeneous universe undergoing completely homologous expansion (“ideal Hubble flow”) and with the absorption profiles having a negligible width, the observed spectrum would simply be a step function, with $F(\lambda) = F_{\text{red}} = 1$ for $\lambda > \lambda_0$, and $F(\lambda) = F_{\text{blue}} < 1$ for $\lambda \leq \lambda_0$. Three factors contribute to make F differ from a step function:

Firstly, the Ly α line is not a delta function, but has a finite width. For high densities of neutral hydrogen, the damping wing of the profile may even extend significantly into the red part of the spectrum, such that in the vicinity of the line center also part of F_{red} is less than one.

Secondly, the IGM is highly inhomogeneous, leading to large variations in F blueward of λ_0 . This is the reason for the LAF seen at intermediate to high redshifts. However, when we consider the average effect of the IGM and let F be the average of many sightlines F_{blue} should still be a constant function of wavelength. Nevertheless, in the proximity of galaxies the gas density is higher than far from the galaxies; on the other hand, in these regions the stellar ionizing UV radiation may reduce the neutral hydrogen density. Consequently, wavelengths just blueward of the line center may not on average be subject to the same absorption as farther away from the line. Regardless of which of these two effects is more important, the correlation of the IGM with the source cannot be neglected.

Finally the expansion is not exactly homologous, since peculiar velocities of the gas elements will cause fluctuations around the pure Hubble flow. Considering again not individual sightlines but the average effect of the IGM, these fluctuations are random and cancel out; on average, for every gas element that recedes from a galaxy faster than the Hubble flow and thus causes an absorption line at a slightly bluer wavelength, another gas element does the opposite. Hence, the average transmission in a “realistic” universe is the same as in a universe where there are no peculiar velocities. However, in the proximity of overdensities, the extra mass results in a “retarded” expansion of the local IGM. When expansion around a source is somewhat slower than that of the rest of the Universe, on average matter in a larger region will be capable of causing absorption, since the slower the expansion, the farther the photons will have to travel before shifting out of resonance.

This chapter focuses on two different aspects of the intergalactic transmission. First, to see how the Ly α line is affected by the IGM, we calculate a “transmission function” given by the average, normalized flux $F(\lambda)$. Specifically, F is calculated by taking the median value in each wavelength bin of many sightlines, originating just outside a large number of galaxies (where “just outside” will be defined later). The standard deviation is defined by the 16 and 84 percentiles. From the above discussion we may expect that F be characterized by a red part $F_{\text{red}} \simeq 1$, and a blue part $F_{\text{blue}} < 1$, but with a non-trivial shape just blueward of the line center, since the IGM in the vicinity of the sources is different than far from the sources. We will also examine the average transmission $\mathcal{T} = \mathcal{T}(z)$ of the IGM, defined by first calculating for each individual sightline the fraction of photons that are transmitted through the IGM in a relatively large wave-

length interval well away from the line center, and then taking the median of all sightlines (again with the 16 and 84 percentiles defining the standard deviation). This quantity is sensitive to the overall ionization state of the IGM, and has therefore been used observationally to put constraints on the EoR (Becker et al., 2001; Djorgovski et al., 2001).

9.1 Preparations

9.1.1 Cosmological models

The basics of the cosmological simulation were described in Sec. 6.3. For the IGM RT, three different models will be investigated: Model 1 has the Haardt & Madau UVB field initiating at $z_{\text{re}} = 10$, and has density fluctuations given by $\sigma_8 = 0.74$; Model 2 has $z_{\text{re}} = 10$ and $\sigma_8 = 0.9$; Model 3 has $z_{\text{re}} = 6$ and $\sigma_8 = 0.74$. In all cases, the improved UV RT is applied afterwards (Sec. 6.3.1).

9.1.2 Galaxy selection criteria

Galaxies are located in the simulations as described in Sommer-Larsen et al. (2005). To make sure that a given identified structure is a real galaxy, the following selection criteria are imposed on the sample:

1. To ensure that a given structure “ i ” is not just a substructure of a larger structure “ j ”, if the center of structure i is situated within the virial radius of j , it must have more stars than j .
2. The minimum number of star particles must be at least $N_{\star, \text{min}} = 15$. This corresponds to a minimum stellar mass of $\log(M_{\star, \text{min}}/M_{\odot}) = 7.2$.
3. The circular velocity, given by $V_c = \sqrt{GM_{\text{vir}}/r_{\text{vir}}}$ must be $V_c \geq 35 \text{ km s}^{-1}$.

The IGM in the vicinity of large galaxies is to some extent different from the IGM around small galaxies. The more mass gives rise to a deeper gravitational potential, enhancing the retarded Hubble flow. On the other hand, the larger star formation may cause a larger bubble of ionized gas around it. To investigate the difference in transmission, the sample of accepted galaxies is divided into three subsamples, denoted “small”, “intermediate”, and “large”. To use the same separating criteria at all redshifts, instead of separating by mass — which increases with time due to merging and accretion — the galaxies are separated according to their circular velocity, which does not change significantly over time. The thresholds are defined somewhat arbitrarily as $V_1 = 55 \text{ km s}^{-1}$ (between small and intermediate galaxies) and $V_2 = 80 \text{ km s}^{-1}$ (between intermediate and large galaxies).

The final sample of galaxies is seen in Figure 9.1, which shows the relation between stellar and virial mass, and the distribution of circular velocities.

The exact number of galaxies in the three models studied in this work is seen in Tab. 9.1.

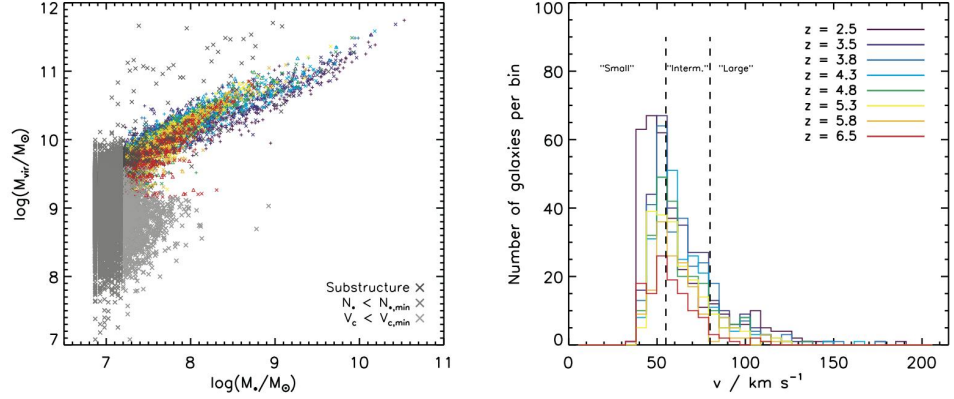


Figure 9.1: *Left:* Scatter plot of virial masses M_{vir} vs. stellar masses M_* for the full, unfiltered sample of galaxies. The colors signify redshift, with more red meaning higher redshift (exact values are seen in the right plot’s legend). The data points of Model 1, 2, and 3 are shown with *triangles*, *plus signs*, and *crosses*, respectively. The galaxies that are rejected are overplotted with *gray crosses*, with *dark*, *medium*, and *light gray* corresponding to rejection criterion 1, 2, and 3, respectively. *Right:* Distribution of circular velocities V_c for the accepted galaxies in Model 1. The distributions for Model 2 and 3 look similar, although Model 2 has more galaxies (see Tab. 9.1).

9.2 IGMTRANSFER

For the IGM RT the same nested grid is used as for the ionizing UV RT. The transmission properties of the IGM are studied by calculating the normalized spectrum $F(\lambda)$ in the vicinity of the Ly α line, as an average of a high number of sightlines cast through the simulated cosmological volume. The code used for these calculations — dubbed IGMTRANSFER — has been made publically available (Laursen et al., 2010b) and can be downloaded from the URL www.dark-cosmology.dk/~pela/IGMtransfer.html.

The resulting value of $F(\lambda)$ at wavelength λ for a given sightline is

$$F(\lambda) = e^{-\tau(\lambda)}. \quad (9.1)$$

The optical depth τ is the sum of contributions from all the cells encountered along the line of sight:

$$\tau(\lambda) = \sum_i^{\text{cells}} n_{\text{HI},i} r_i \sigma(\lambda + \lambda v_{\parallel,i}/c). \quad (9.2)$$

Here, $n_{\text{HI},i}$ is the density of neutral hydrogen in the i ’th cell, r_i is the distance covered in that particular cell, $v_{\parallel,i}$ is the velocity component of the cell along the line of sight, and $\sigma(\lambda)$ is the cross section of neutral hydrogen. Due to the resonant nature of the transition, the largest contribution at a given wavelength will arise from the cells the velocity of which corresponds to shifting the wavelength close to resonance.

NUMBER OF GALAXIES IN THE SIMULATIONS

Model	z_{re}	σ_8	z	Total	Small	Intermediate	Large
1.	10	0.74	2.5	343	207	80	56
			3.5	309	138	127	44
			3.8	283	125	119	39
			4.3	252	102	115	35
			4.8	225	111	86	28
			5.3	201	98	85	18
			5.8	154	75	62	17
2.	10	0.9	3.5	405	207	128	70
			4.3	384	165	150	69
			4.8	341	150	129	62
			5.3	324	145	125	54
			5.8	277	121	106	50
			6.5	252	126	92	34
3.	6	0.74	3.5	325	162	122	41
			3.8	318	165	117	36
			4.3	293	150	110	33
			4.8	250	138	84	28
			5.3	204	101	85	18
			5.8	160	75	67	18
			6.5	126	69	50	7

Table 9.1: “Small”, “intermediate”, and “large” galaxies are defined as having circular velocities $V_c < 55 \text{ km s}^{-1}$, $55 \text{ km s}^{-1} \leq V_c < 80 \text{ km s}^{-1}$, and $V_c \geq 80 \text{ km s}^{-1}$, respectively.

Although no formal definition of the transition from a galaxy to the IGM exists, we have to settle on a definition of where to begin the sightlines, i.e. the distance r_0 from the center of a galaxy. Observed Ly α profiles result from scattering processes in first the galaxy and subsequently the IGM, and regardless of the chosen value of r_0 , for consistency galactic Ly α RT should be terminated at the same value when coupling the two RT schemes. In view of the above discussion on scattering in and out of the line of sight, the sightlines should begin where photons are mainly scattered out of the line of sight, and only a small fraction is scattered into the line of sight (see Fig. 9.2).

Since more neutral gas is associated with larger galaxies, as well as with higher redshift, clearly r_0 depends on the galaxy and the epoch, but measuring r_0 in units of the virial radius r_{vir} helps to compare the physical conditions around different galaxies. In Sec. 12.1.1 it is argued that a reasonable value of r_0 is $1.5r_{\text{vir}}$, and showed that the final results are only mildly sensitive to the actual chosen value of r_0 .

At a given redshift, $F(\lambda)$ is calculated as the median of in each wavelength bin of 10^3 sightlines from each galaxy in the sample (using 10^4 sightlines produces virtually identical results). The number of galaxies amounts to several hundreds,

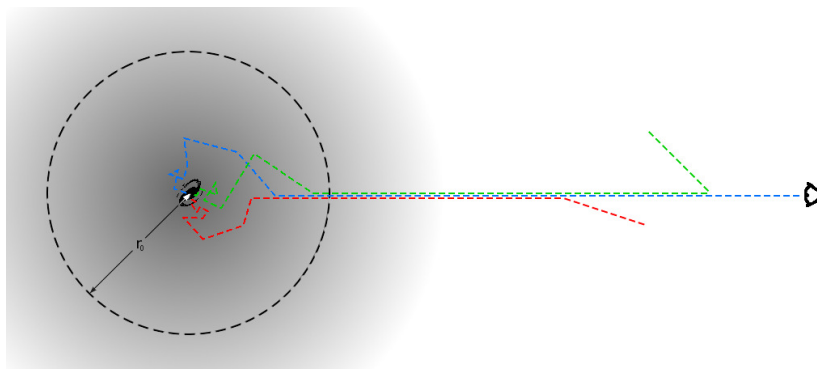


Figure 9.2: Illustration of the difference between the galactic RT and the IGM RT. Close to the galaxy, photons are scattered both in and out of the line of sight. In the rarefied IGM, photons are mainly scattered out of the line of sight, obviating the need for a full MC RT. The exact value of r_0 is somewhat arbitrary, but is of the order of the virial radius of the galaxy.

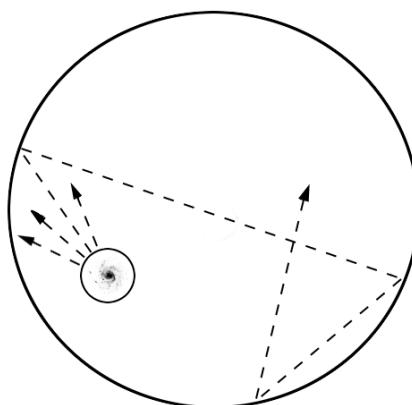


Figure 9.3: Illustration of how the sightlines are cast through the cosmological volume. To sample sufficiently the full solid angle of 4π around the individual galaxies, 10^4 sightlines are cast from each galaxy (of which four are shown here). Each sightline is started at a distance r_0 from the center of a galaxy and followed until the bluest wavelength of the emitted spectrum has been redshifted into resonance. When the edge of the spherical volume reached, the ray “bounces” back, i.e. continues in a random inward angle.

and increases with time. To avoid any spuriousities at the edge of the spherical volume only a $0.9D_{\text{box}}$ sphere is used. Due to the limited size of the volume, in order to perform the RT until a sufficiently short wavelength is redshifted into resonance the sightlines are allowed to “bounce” within the sphere, such that a ray reaching the edge of the sphere is re-“emitted” back in a random angle in such a way that the total volume is equally well sampled (see Fig. 9.3). Note however that in general the wavelength region close to the line that is affected

by the correlation of the IGM with the source is reached well before the the first bouncing.

The normalized spectrum is emitted at rest wavelength in the reference frame of the center of mass of a galaxy, which in turn may have a peculiar velocity relative to the cell at which it is centered. This spectrum is then Lorentz transformed between the reference frames of the cells encountered along the line of sight. Since the expansion of space is approximately homologous, each cell can be perceived as lying in the center of the simulation, and hence this bouncing scheme does not introduce any bias, apart from reusing the same volume several times for a given sightline. However, since the sightlines scatter around stochastically and thus pierce a given region from various directions, no periodicities arise in the calculated spectrum.

To probe the average transmission, the sightlines are propagated until the wavelength 1080 \AA has been redshifted into resonance, corresponding to $\Delta z \simeq 0.1$. In this case the sightlines bounce roughly 30 (20) times at $z = 2.5$ (6.5).

Part III

Scientific achievements

Chapter 10

On the consequences of resonant scattering¹



THE ORIGINAL MOTIVATION for the development of MOCALATA was to test whether resonant scattering of Ly α photons could explain the frequent observations that LAEs, when observed in Ly α , seem to be more extended on the sky compared to continuum band observations. This was mentioned in Sec. 1.2, and Fig. 1.1 showed an example of such an observation.

In most of the following sections, we will mainly focus on a particular galaxy, namely the one poetically dubbed “K15”, at a fiducial redshift of $z = 3.6$, but other galaxies, as well as other epochs, will also be considered. The numerical and physical properties of all galaxies was showed in Tab. 6.1 and Tab. 6.2, respectively.

The galaxy K15 is rather large, and would show up in surveys as both an LBG and an LAE. It evolves into a Milky Way/M31-like disk galaxy at $z = 0$. K15 consists of two small, star-forming, disk-like structures separated by a few kpc, on one of which the computational box is centered, and a third more extended disk, but of lower SFR, located about 15 kpc from the center. We will refer to the two small disks as the principal emitter, and to the more extended disk as the secondary emitter. Additionally, the star-forming regions are embedded in a significant amount of more diffuse, non-star-forming, HI gas in a ~ 10 –15 kpc thick, sheet-like structure, taken to constitute the xy -plane.

To separate the effects of dust from the effects of pure resonant scattering, the simulations in this chapter were performed without the effects of dust. In Chap. 11 we proceed to include dust in the calculations and discuss the extend to which extend the conclusions of this chapter are valid.

10.1 Extended surface brightness

Fig. 10.1 shows how K15 would look, viewed from two different directions — from the negative x - and z -direction, corresponding to an “edge-on” and a “face-on” view of the sheet-like structure, respectively. To emphasize the result

¹This chapter is based on Paper I (App. B).

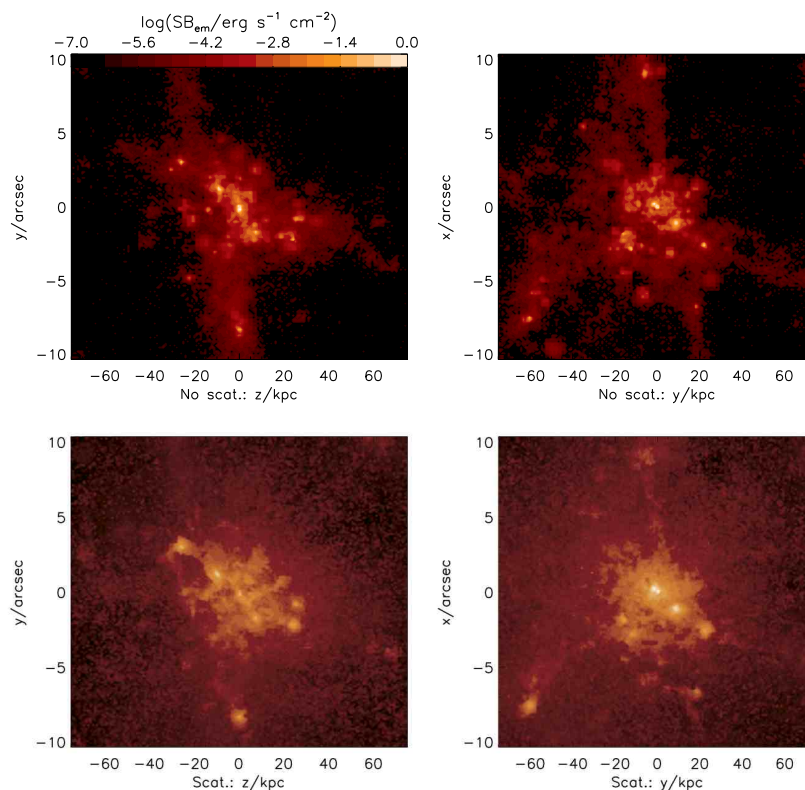


Figure 10.1: SB map of the simulated galaxy K15, lying at a redshift of $z = 3.6$. Left and right column show the system when viewed edge-on and face-on, respectively. The top panels display the galaxy as if the Ly α radiation was able to escape directly, without scattering. The bottom panel shows the effect of the scattering. For this simulation, $\sim 10^7$ photons was used, a good deal more than needed for acceptable convergence.

of treating resonant scattering properly, the galaxy is also shown as if the gas were optically thin to the Ly α radiation.

The effect of the scattering is incontestable: although the original constellation of the dominant emitters is still visible, the SB distribution is clearly much more extended. Certain regions can be quite bright in Ly α even though they have no intrinsic emission. This astonishing result establishes the importance of treating the scattering processes properly.

Figure 10.2 shows the azimuthally averaged SB profiles. To allow for a more direct comparison with observations, the profiles are shown smoothed with a point spread function corresponding to a seeing of $0''.8$ and excluding the luminosity of the secondary emitter.

The profiles in Fig. 10.2 match the observed Ly α SB of the galaxy LEGO2138.29 (Fynbo et al., 2003) beautifully. It is worth noting that the two galaxies — the simulated and the observed — were not chosen to match each other, although LEGO2138.29 was chosen due its superior extendedness in Ly α .

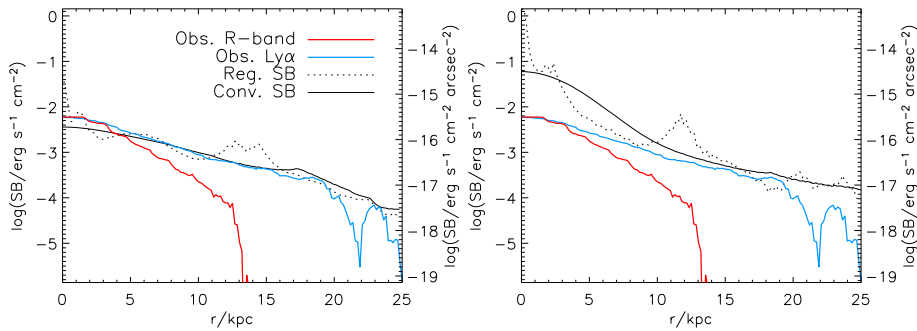


Figure 10.2: SB profiles of the simulated galaxy K15 when viewed edge-on (*left*) and face-on (*right*). *Dotted* lines show the true SB profiles, while *solid* lines show the SB profiles of the images convolved with a seeing of $0''.8$ and omitting the luminosity of the remote emitters. Also shown are the SB profiles of the galaxy LEGO2138.29 (Fynbo et al., 2003) in $\text{Ly}\alpha$ (*blue*) and in the R -band (*red*, normalized to the maximum observed $\text{Ly}\alpha$ SB). In particular the SB of the yz -plane nicely reproduces the observed SB. Left axes measure the SB at the source, while right axes measure the SB observed at $z = 0$.

10.2 Broadened spectrum

Not only the SB profile is smeared out, but also the spectrum is broadened by resonant scattering. Figure 10.3 shows the general effect of the scattering on the spectrum: while the only broadening of the input spectrum visible is due to the bulk motion of the gas elements emitting the photons (both the natural and usually also the thermal broadening being much smaller), the scattered spectrum is severely broadened, diminished by an order of magnitude, and split up into two peaks.

The double-peak profile seen in Fig. 10.3 is characteristic of $\text{Ly}\alpha$ emission lines; the high opacity for photons near the line center makes diffusion to the either side necessary in order to escape the galaxy. Nonetheless, unlike in previous simple models, the intensity in the line center is not zero. The photons that contribute to this intensity are those produced mainly by gravitational cooling, in the outskirts of the systems.

Figures 10.4 and 10.5 display the spectra emerging from galaxies K33 and S115 at $z = 3.6$, in six different directions. The exact shape varies quite a lot, but all spectra appear to exhibit the double-peak profile. Moreover, they are broadened by several 1000 km s^{-1} . Although such broad LAE line profiles are indeed observed, somewhat narrower profiles of several hundreds to $\sim 1000 \text{ km s}^{-1}$ are more typical. In Chap. 11 we will see how this can be explained by the presence of dust.

Double-peaks have been observed on several occasions (e.g., Yee & De Robertis, 1991; Venemans et al., 2005). Tapken et al. (2007), using a resolution of $R \sim 2000$, found three out of 16 LAEs at redshifts $z \sim 3-4$ to exhibit a double-peaked profile, while Yamada et al. (priv. comm.), using $R \sim 1500$ found that 26 of 94 LAEs at redshift 3.1 have double-peaked profiles. The difference in magnitude of the two peaks can be a signature of infalling/outflowing gas, cf. Sec. 8.1.5.

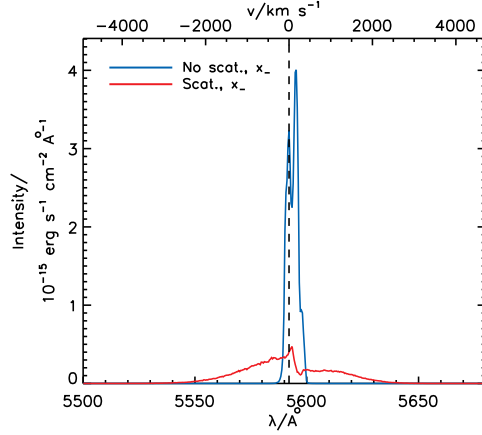


Figure 10.3: Spectrum of the galaxy K15 as if the radiation were able to escape directly (*blue*), and the realistic spectrum of the scattered photons (*red*). Scattering broadens the spectrum by many Ångströms. Moreover, due to the fact that the hydrogen cross section is so large for photons in the line center, the spectrum is split up into two peaks.

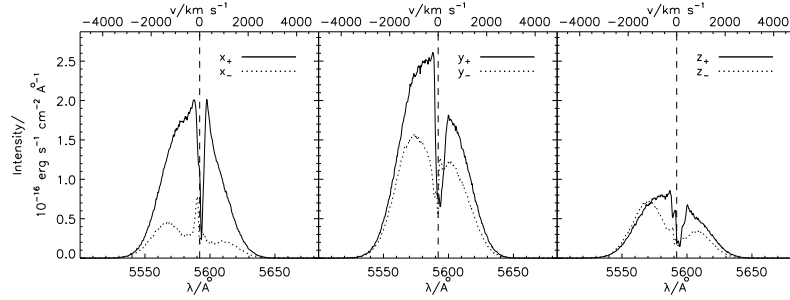


Figure 10.4: Spectral distribution of the photons escaping the galaxy K33 in six different directions; along the positive (+) and negative (-) x -, y -, and z -direction. The dashed line in the middle of each plot indicates the line center. The lower abscissa gives the redshifted wavelength of the photons while on the upper abscissa, the wavelength distance from the line center is translated into recessional velocity. The resonant scattering of Ly α is seen to broaden the line by several thousands of km s $^{-1}$.

In principle, this difference may be used as a probe of the gas dynamics, and has indeed been used to infer the presence of galactic superwinds. However, as shown in Chap. 12, the removal or diminishing of the blue peak might also be caused by IGM resonant scattering.

Even if the double-peak survives intergalactic transmission, fairly high resolution is required to be able to resolve them. With a typical separation $\Delta\lambda$ of the peaks of the simulated spectra from a few to $\simeq 10$ Å (at $z \sim 3.6$), the resolution must be $R = 5600/\Delta\lambda \simeq 500\text{--}2000$.

It is interesting that while the Ly α profile of K15 also shows a moderate gas

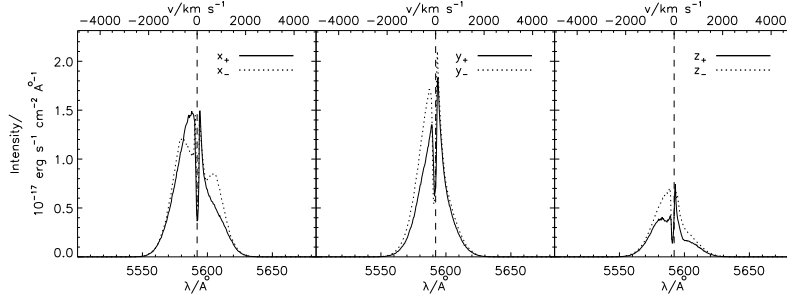


Figure 10.5: Same as Fig. 10.4, but for the galaxy S115.

infall, we see some outflow signatures in the spectrum of the lower-mass galaxy S115 from negative x - and y -directions. Fitting a Neufeld, or Dijkstra, profile to the observed spectra can give us an idea of the intrinsic properties of the system. Unfortunately, due to the degeneracy between column density and temperature, one would have to gain knowledge either of the parameters by other means to constrain the other (e.g. by inferring column density from the spectrum of a coincident background quasar, or by assuming a temperature of, say, 10^4 K, representative of most of the Ly α emitting gas).

10.3 Anisotropic escape

The SB profiles and the spectra presented in the previous sections reveal another interesting property of LAEs, namely that the radiation in general does not escape isotropically. Qualitatively, we expect the photons to escape more easily in directions where the column density of neutral gas is lower. As mentioned already, K15 is embedded in a sheet-like structure, lying at the intersection of three filaments of gas. Since the bulk of the photons are produced in the central, star-forming regions, the total optical depth is larger in the direction parallel to the sheet than perpendicular to it, and hence we would expect the photons to escape more easily in the face-on direction. Similarly, K33 is situated in a filament of gas, taken to lie along the z -axis. Here, we would expect the photons to escape more easily in the x - and y -directions.

Here this anticipation is quantified. Averaging the SB in the azimuthal direction, the SB profiles of the three galaxies, each as viewed from two different directions, are shown in Fig. 10.6, while Tab. 10.1 summarizes the observed maximum surface brightnesses, SB_{\max} . In fact, regarding K33, SB_{\max,x_-} turns out to be smaller than both SB_{\max,z_-} and SB_{\max,z_+} , due to the presence in the line of sight of hydrogen clouds with little star formation causing a shadowing effect. As seen in Tab. 10.1, the observed SB of a given galaxy varies with viewing angle by approximately an order of magnitude.

This result is intriguing in relation to the classification of galaxies. As discussed in Chap. 2, galaxies are commonly annotated according to the method by which they are selected, and one of the mysteries in the context of galaxy formation and evolution is the connection between the different types. As already mentioned, sufficiently high column densities of neutral hydrogen in the line of sight toward a bright background source give rise to broad absorption lines in their spectra,

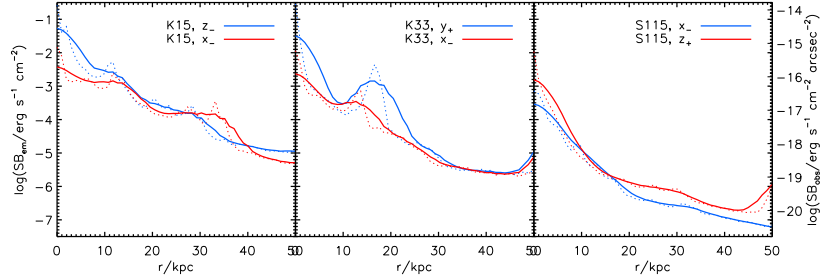


Figure 10.6: SB profiles for the inner 50 kpc of the three galaxies K15 (*right*), K33 (*middle*), and S115 (*left*). For each galaxy, the SB is showed as observed from two different angles (*blue* and *red*, respectively). Both the “true” SB profiles (*dotted*) and the profiles of the SB convolved with a seeing of $0''.8$ (*solid*) are shown. Left *y*-axis gives the SB that would be seen by an observer at the location of the galaxies, while right *y*-axis gives the SB as observed from Earth.

MAXIMUM OBSERVED SURFACE BRIGHTNESSES
FROM DIFFERENT DIRECTIONS

Galaxy	K15	K33	S115
$\log \text{SB}_{\max, x_+}$	8.6×10^{-3}	6.2×10^{-3}	1.3×10^{-3}
$\log \text{SB}_{\max, x_-}$	3.7×10^{-3}	2.3×10^{-3}	1.5×10^{-3}
$\log \text{SB}_{\max, y_+}$	9.9×10^{-3}	3.2×10^{-2}	7.6×10^{-4}
$\log \text{SB}_{\max, y_-}$	1.2×10^{-2}	2.1×10^{-2}	1.2×10^{-3}
$\log \text{SB}_{\max, z_+}$	4.9×10^{-2}	3.4×10^{-3}	2.9×10^{-4}
$\log \text{SB}_{\max, z_-}$	5.3×10^{-2}	4.7×10^{-3}	4.0×10^{-4}
Max/min	14.3	13.6	5.3

Table 10.1: SBs are calculated from the images convolved with a seeing of $0''.8$ and are measured in $\text{erg s}^{-1} \text{cm}^{-2}$ at the location of the galaxies. The maximally and the minimally observed SB_{\max} ’s for a given galaxy are written in boldface and italics, respectively, and the ratios between these are given in the lower row.

and may be detected as the DLAs. On the other hand, galaxies with high enough SFRs may be detected in narrowband searches by an excess of their narrowband to continuum flux as LAEs.

Both K15, K33, and S115 contain enough neutral hydrogen to make them detectable as DLAs in the spectra of hypothetical quasars. More interestingly, the present results show that while their relatively high SFRs may make at least K15 and K33 detectable as LAEs when viewed from a given direction, it may not be possible to see them in $\text{Ly}\alpha$ from another direction; instead, it may be possible to observe them as LBGs. This effect demonstrates how galaxies selected by different means may be connected to each other.

Overlaps in the properties of LAEs and LBGs have also been inferred observationally; Gawiser et al. (2006b) found that more than 80% of a sample of emission line-selected LAEs have the right *UVB*-colors to be selected as LBGs. The primary difference between the two populations is the selection criteria, as only $\sim 10\%$ are also brighter than the $R_{\text{AB}} < 25.5$ “spectroscopic” LBG

magnitude cut. Also, when correcting for dust, Gronwall et al. (2007) found comparable SFRs for the two populations.

For high-redshift LAEs, SFRs are inferred almost exclusively from Ly α flux measurements, assuming isotropic luminosity. However, as is evident from the above discussion, in general the complex morphology of a galaxy may very well cause a preferred direction of photon escape. For the three galaxies of the present study, the angular variation in flux can be as high as a factor of 3.4, 6.2, and 3.3, for K15, K33, and S115, respectively (here the flux is calculated by integrating the SB maps over a region of radius $r = 25$ kpc, centered at $r = 0$). Although not as pronounced as in the case of SB_{max}, this introduces a considerable source of uncertainty, which may propagate into estimates of SFRs or into calculations of the content of dust residing in galaxies.

Chapter 11

On the effects of dust¹



WHEN DUST IS INCLUDED in the calculations, the adaptive resolution of MOCALATA really comes into its own. In general, any clumpiness of the gas elements will lower the effective optical depth. That this is true can be seen from the following argument: taking the average over all lines of sight, for a heterogeneous medium the effective optical depth is

$$\tau_{\text{het}} = -\ln\langle e^{-\tau} \rangle, \quad (11.1)$$

while for a homogeneous medium $\tau_{\text{hom}} = \langle \tau \rangle = \text{constant}$. Since from the standard triangle inequality

$$e^{-\langle \tau \rangle} \leq \langle e^{-\tau} \rangle, \quad (11.2)$$

it is seen that $\tau_{\text{het}} \leq \tau_{\text{hom}}$. This is true for any wavelength. For Ly α , in the absence of dust, increasing τ , or decreasing clumpiness, does not increase absorption but instead broadens the spectrum further. *With* dust, however, the situation becomes more complicated. Although the resonant scattering increases the path length of the photons, in an inhomogeneous medium more low-density paths exist through which the radiation can escape.

11.1 The need for adaptive resolution

Consequently, in simulations of Ly α RT with dust, high resolution is rather crucial to accurately determine the escape of the photons. As is evident from Fig. 11.1, the bulk of the photons is produced in regions of very high column densities, exceeding $N_{\text{H I}} = 10^{23} \text{ cm}^{-2}$. Even for metallicities of only 1/100 Z_{\odot} , Eq. 8.3 implies an escape fraction of $\sim 10^{-5}$ (for $T \sim 10^4 \text{ K}$). However, Eq. 8.3 assumes a *homogeneous* medium. As was argued by Neufeld (1991) and investigated numerically by Hansen & Oh (2006), in a multi-phase medium, the Ly α photons may escape more easily. In the (academic) case of all the dust residing in cool, dense clouds of neutral hydrogen which, in turn, are dispersed in a hot, empty medium, the Ly α escape fraction may approach unity. The reason is that the photons will scatter off of the surface before penetrating substantially

¹This chapter is based on Paper II (App. C).

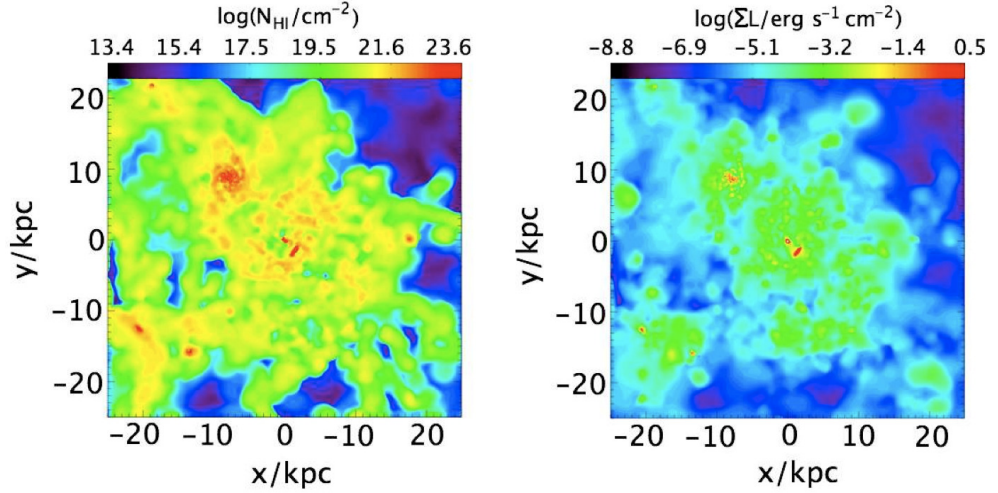


Figure 11.1: Neutral hydrogen column density (N_{HI}) map (*left*) and integrated source Ly α emissivity (Σ_L) map (*right*) of the simulated galaxy K15. The vast majority of the photons are seen to be emitted in the very dense environments. According to the analytical solution for the Ly α escape fraction provided by Neufeld (1990, Eq. 8.3 in this paper), virtually all photons should be absorbed by dust, but taking into account the clumpiness of the ISM allows for much higher escape fractions.

into the clouds, thus effectively confining their journey to the dustless intercloud medium.

Although this scenario is obviously very idealized, the presence of an inhomogeneous medium undoubtedly reduces the effective optical depth, and has indeed been invoked to explain unusually large Ly α equivalent widths (e.g. Finkelstein et al., 2008). Nevertheless, it is not clear to which degree the escape fraction of Ly α will actually be affected. Other scenarios have been proposed to explain the apparent paradoxical escape of Ly α , e.g. galactic superwinds, as discussed in Sec. 4.1.1. Generally, whether large or small a more or less universal escape fraction is assumed. This work presents the first calculations of f_{esc} , based on fully cosmological, numerical galaxy formation models, demonstrating that a wide range of escape fractions are possible, and that a significant fraction may escape the galaxies at redshifts $z \sim 3-4$, even if no particularly strong winds are present.

Again, in the following we will first focus on K15, choosing the observer placed toward negative values on the z -axis (the z_- -direction), the direction in which most radiation escapes. In Sec. 11.5 we proceed to discuss the extend to which the results are representative for other galaxies and directions.

11.2 Where are the photons absorbed?

Figure 11.2 shows the SB maps of the galaxy K15. The left panel shows how the galaxy would look if the gas were dust-free, while the right panel displays

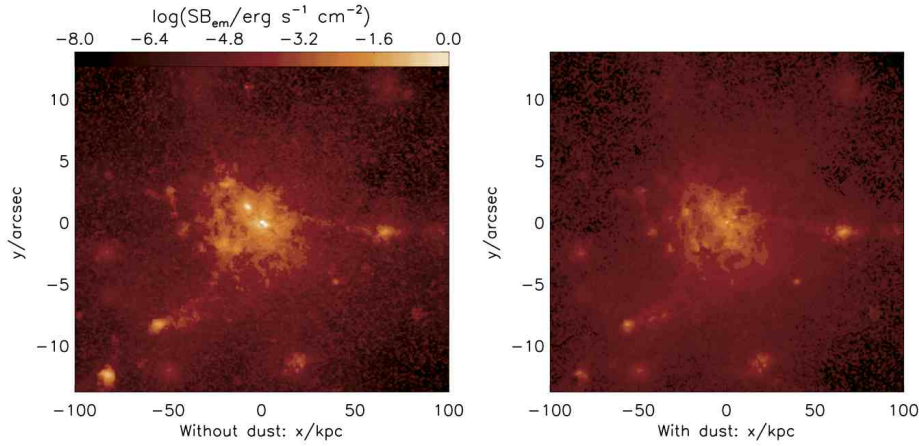


Figure 11.2: SB maps of the galaxy K15, as viewed from the negative z -direction, without dust (*left*) and with dust (*right*). Including dust in the radiative transfer affects primarily the most luminous regions.

the more realistic case of a dusty medium. Comparing the two images, it is seen that the regions that are affected the most by dust are the most luminous regions. This is even more evident in Fig. 11.3, where the azimuthally averaged profiles of the SB maps are shown.

The reason for this is two-fold: the most luminous regions are the regions where the stars reside. Because dust is produced by stars, this is also where most of the dust is. Since the stars, in turn, are born in regions of high hydrogen density, the RT is here associated with numerous scatterings, severely increasing the path length of the photons, and consequently increasing further the probability of being absorbed.

The SB in the less luminous regions also decreases. Although dust also resides here, having been expelled by the feedback of starbursts, only little absorption actually takes place here because both gas and dust densities are rather small. The decrease in luminosity is mainly due to the photons being absorbed in the high-density regions that would otherwise have escaped the inner regions and subsequently been scattered by the circumambient neutral gas into the direction of the observer. This is also discernible from Fig. 11.4 that displays an image of the absorbed photons.

Figure 11.5 shows the *source* Ly α emissivity of the photons that are eventually absorbed, compared to that of the photons that eventually escape. Here it becomes evident that virtually all the absorbed photons are emitted from the central parts, while photons that escape are emitted from everywhere. In particular, the radiation produced through gravitational cooling escapes more or less freely.

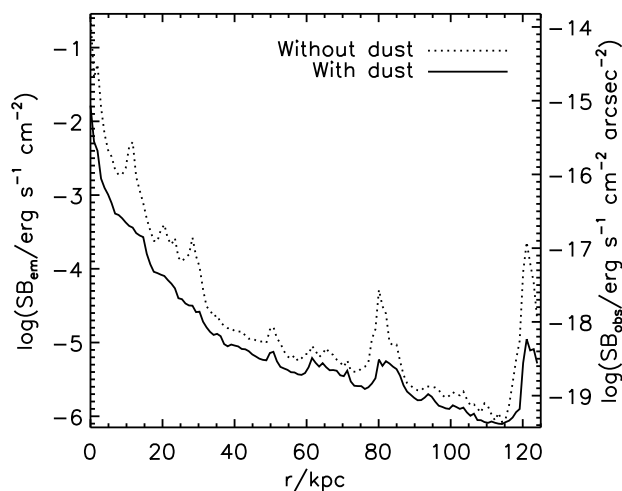


Figure 11.3: SB profile of the galaxy K15, again without dust (*dotted*) and with dust (*solid*). Left ordinate axis gives the SB as measured at the source while right ordinate gives the values measured by an observer at a distance given by the luminosity distance of the galaxy. The decrease in SB in the less luminous regions is noticeable. However, this decrease is for the most part *not* due to photons being absorbed in the hot and tenuous circumgalactic medium but rather reflects a lack of photons that in the case of no dust would have escaped the luminous regions and subsequently scattered on neutral hydrogen in the direction of the observer.

11.3 Effect on the emergent spectrum

Due to the high opacity of the gas for a Ly α photon at the line center, photons generally diffuse in frequency to either the red or the blue side in order to escape. Consequently, the spectrum of the radiation escaping a dustless medium is characterized by a double-peaked profile. The broadening of the wings is dictated by the product $a\tau_0$ (Eq. 3.51), i.e. low temperatures and, in particular, high densities force the photons to diffuse far from line center. Since such conditions are typical of the regions where the bulk of the photons is absorbed, the emergent spectrum of a dusty medium is severely narrowed, although the double-peaked feature persists. Figure 11.6 displays the spatially integrated spectra of the dustless and the dusty version of K15.

This interesting result shows that even though the dust is effectively gray (the small wavelength dependence of Eq. 4.4) does not produce substantially different results from using a completely wavelength *independent* cross section), the emergent spectrum is affected in a highly “non-gray” fashion: whereas the escape fraction of the inner part of the spectrum is of the order 50%, it rapidly drops when moving away from the line center.

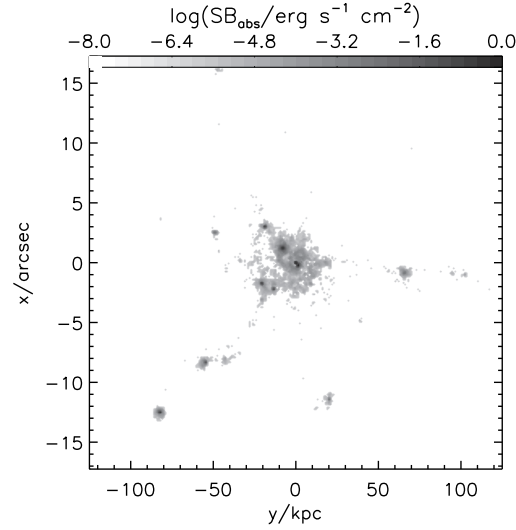


Figure 11.4: Image of the locations of absorption of the Ly α radiation. This image corresponds roughly to the column density of dust, although dusty HII regions may not show up as clearly as dust-deficient HI regions.

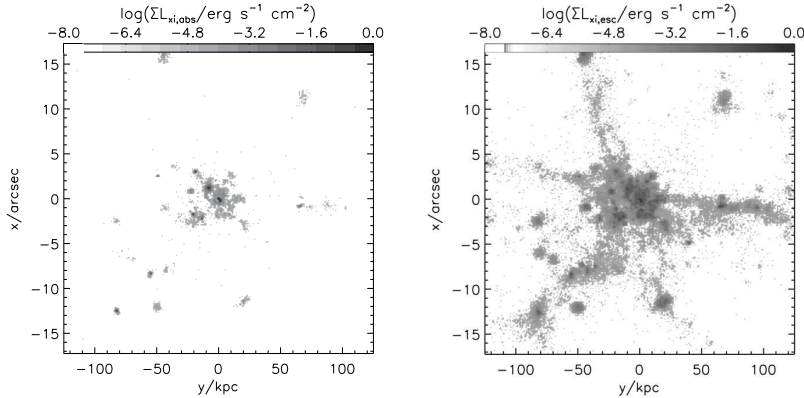


Figure 11.5: Surface density maps of the source Ly α emissivity, of the photons that are eventually absorbed (*left*), and the photons that eventually escape (*right*). These images clearly show that absorbed and escaping photons do not in general probe the same physical domains.

11.4 Escape fraction

In the z_- -direction of K15, the fraction of Ly α photons escaping is 0.14, when comparing to the dustless version of K15. As mentioned earlier, the z_- -direction is the direction into which most radiation escapes — without dust, this direction is ~ 3 times as luminous as the x_- -direction, which is where the least radiation is emitted. Including dust, because the brightest regions are affected the most, the ratio between the luminosity in the least and the most luminous directions

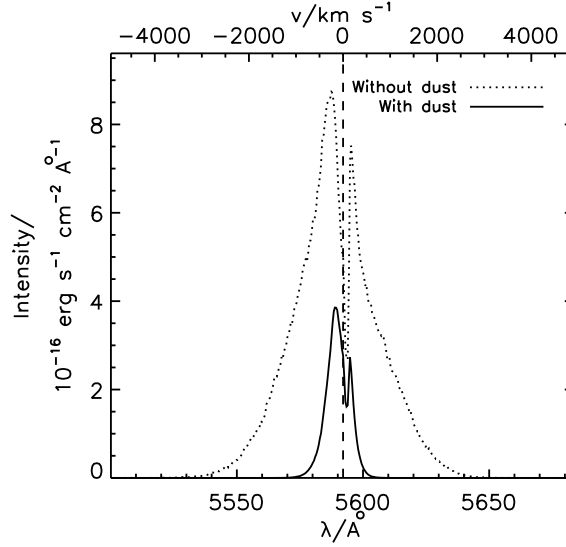


Figure 11.6: Observed spectral distribution of the radiation escaping the galaxy K15 in the negative z -direction, with (*solid*) and without (*dotted*) dust. The vertical, dashed line marks the $\text{Ly}\alpha$ line center. Although the dust is close to being gray, the spectrum is not affected in the same way at all wavelengths; the inner parts are only diminished by a factor of ~ 2 , while the wings are severely reduced. The reason is that the photons in the wings are the ones produced in the dense and dusty regions of the galaxy, so these photons have a higher probability of being absorbed.

is somewhat reduced, although z_- is still more than twice as bright as x_- . The sky-averaged escape fraction for K15 is 0.16. Recall that in these simulations SMC dust has been applied. However, as discussed in Sec. 8.3 using LMC dust does not alter the results significantly. Many factors regulate the probability of escaping, and stating f_{esc} for a single galaxy is not very elucidative. In the next section we investigate the correlation of f_{esc} with galaxy size.

11.5 General results

The results found in the previous sections turn out to be quite illustrative of the general outcome of $\text{Ly}\alpha$ RT in a dusty medium: photons are absorbed primarily in the dense, luminous regions, leading to a reduced luminosity in these parts of the galaxies and effectively smoothing out prominent features. Furthermore, the wings of the spectrum experience a strong cut-off.

11.5.1 Anisotropic escape of $\text{Ly}\alpha$

As found in Sec. 10.3, in general the radiation does *not* escape isotropically; the ratio of luminosities observed from different directions ranges from ~ 1.5 to ~ 4 . Without dust, these ratios were found to be somewhat higher, up to a factor of

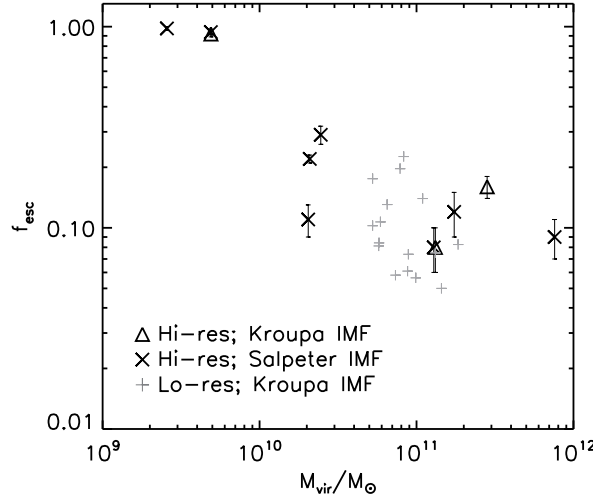


Figure 11.7: Escape fractions f_{esc} as a function of galactic virial mass M_{vir} . Errorbars denote the differences in f_{esc} in different directions. Although the plot exhibits a large scatter, there is a clear trend of f_{esc} decreasing with increasing M_{vir} .

~6. Although “bright directions” are affected more by the dust than less bright directions, the variation in f_{esc} as a function of direction is not large, and not very different from the sky-averaged f_{esc} .

11.5.2 Correlation of f_{esc} with galactic mass

Figure 11.7 shows the escape fractions of the galaxies as a function of the virial masses of the galaxies. Despite a large scatter, and although the sample is too small to say anything definite, the figure indicates that f_{esc} decreases with increasing mass of the host galaxy. In addition to the nine high-resolution galaxies (of which two appear in two “versions”; with a [Salpeter](#) and with a [Kroupa](#) IMF), 17 galaxies from the (Kroupa) cosmological simulation are shown. The mass resolution of these galaxies is thus $8\times$ lower. To ensure an acceptable resolution, the galaxies were chosen according to the criterion that the number of star particles is ≥ 1000 . Similar results are found for the escape of ionizing UV radiation ([Razoumov & Sommer-Larsen, 2009](#)). The reason is probably a combination of two mechanisms: small galaxies have a lower SFR and hence lower metallicity and less dust than large galaxies. Furthermore, due to their smaller gravitational potential the stellar feedback will “puff up” small galaxies relatively more and make them less ordered, thus reducing the column density of both dust and gas.

This effect might explain the results found by [Vijh et al. \(2003\)](#), who studied the effects of dust in a sample of > 900 LBGs at $2 > z > 4$: they found that the FUV continuum (at 1600 \AA) dust attenuation increases with the UV luminosity of the galaxies.

11.5.3 Narrowing of the spectrum

Figure 11.8 shows the emergent spectra of the studied galaxies, arranged according to virial mass. In general, the same trend as for K15 is seen for all galaxies: the dust primarily affects the wings of the profiles. As discussed in Sec. 11.3, the reason is that the wings of the Ly α profile are comprised by photons originating in the very dense regions of the galaxy having to diffuse far from the line center in order to escape, and since this is also where the most of the dust is residing, these photons have a larger probability of being absorbed. For the two least massive galaxies, S108sc and S115sc, the ISM is neither very dense nor very metal-rich, meaning that photons escape rather easily. Consequently, the line is not particularly broadened and most of the photons escape the galaxies.

An effective “escape fraction as a function of wavelength” can be defined as the ratio between the calculated, realistic spectrum and the spectrum that would be seen if there were no dust, i.e. “ $f_{\text{esc}}(\lambda) = I_{\text{dusty}}/I_{\text{dustless}}$ ”. Figure 11.9 shows this ratio for the nine galaxies.

Evidently, this is not a factor that can simply be multiplied on the intrinsically emitted spectrum. Nevertheless, it illustrates which wavelengths escape more easily. $f_{\text{esc}}(\lambda)$ resembles a Gaussian; for larger galaxies the maximum decreases, but the width does not change much. For a homogeneous mixture of gas and (gray) dust, $f_{\text{esc}}(\lambda)$ would be a flat line. Previous attempts to ascertain the impact of dust on Ly α spectra predicted a constant suppression of the spectrum with wavelength (e.g. Verhamme et al., 2006). The present results show the importance of treating the distribution of gas and dust properly.

11.5.4 Extended surface brightness profile

The fact that more photons are absorbed in the bright regions tend to “smooth out” the SB profiles of the galaxies. As found in Sec. 10.1, even without dust, resonant scattering itself may cause an extended Ly α SB profile. Including dust merely adds to this phenomenon, since steep parts of the profile are flattened. Figure 11.10 shows this effect for three of the galaxies.

11.6 Temporal fluctuations

Many factors play a role in determining the exact value of f_{esc} . Although the metallicity, and hence the state of maturity of the galaxy, as well as the size of the galaxy seem to be the most significant property regulating f_{esc} , less systematic factors like the specific configuration of gas and stars are also likely to have a large influence. The scatter in Fig. 11.7 is probably due to this effect. To get an idea of the fluctuations of f_{esc} with time, RT calculations was run for snapshots of K15 from 100 Myr before ($z = 3.8$) to 100 Myr after ($z = 3.5$) the one already explored at $z = 3.6$. In this relatively short time, neither Z nor M_{vir} should not evolve much, and thus any change should be due to stochastic scatter.

Figure 11.11 shows the variation of f_{esc} during this time interval, demonstrating that the temporal dispersion is of the order 10% on a 10 Myr scale. This suggests that the scatter seen in $f_{\text{esc}}(M_{\text{vir}})$ (Fig. 11.7) reflects galaxy-to-galaxy variations rather than f_{esc} of the individual galaxies fluctuating strongly with time.

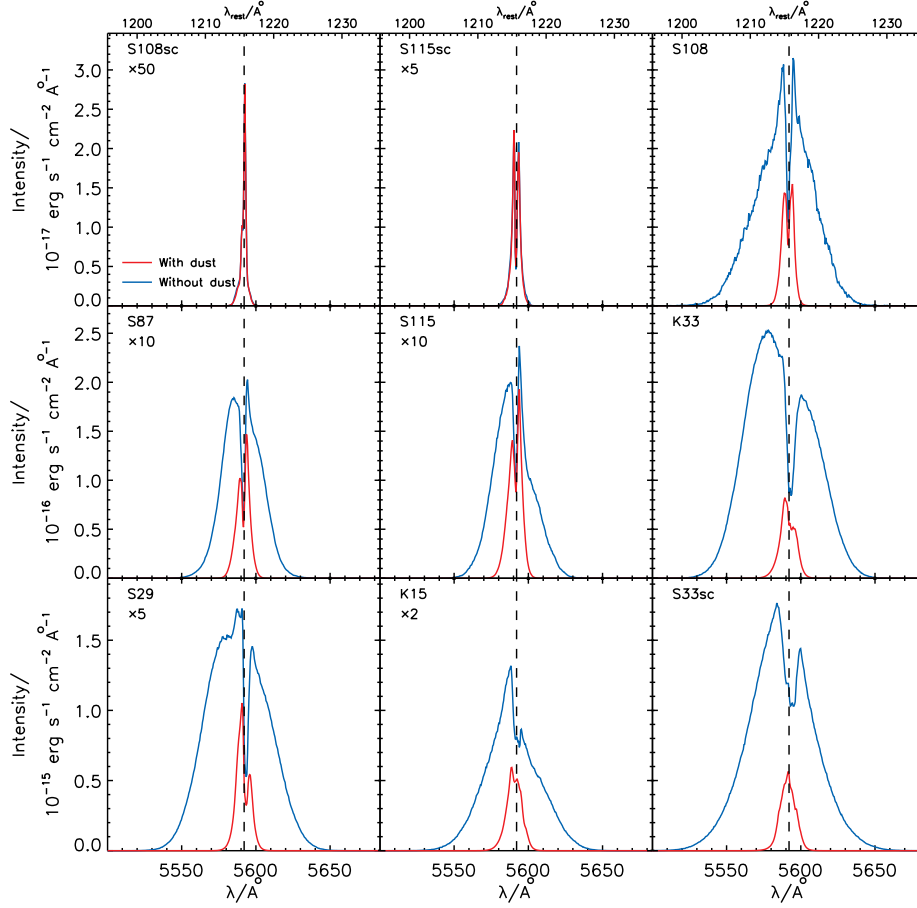


Figure 11.8: Emergent spectra of the studied galaxies, without (*blue*) and with dust (*red*), ordered after decreasing virial mass. In order to use the same ordinate axis for a given row, some intensities have been multiplied a factor indicated under the name of the galaxy. Generally, lines that are broadened by resonant scattering tend to be severely narrowed when including dust.

11.7 Discussion

The obtained results (f_{esc} , SB, spectra) seem to be quite insensitive to the assumed values of various parameters characterizing the dust, such as dust albedo, scattering asymmetry, dust cross section, extinction curve, etc. Of the studied input parameters, the only actual uncertainty comes from insufficient knowledge about the dust contents of ionized gas, but this probably *at most* introduces an error of $\sim 20\%$. This robustness against input parameters is convenient in the sense that we can rely on the results, but is also a nuisance since at least from Ly α observations, we should not expect to be able to learn much about the physical properties of the dust itself.

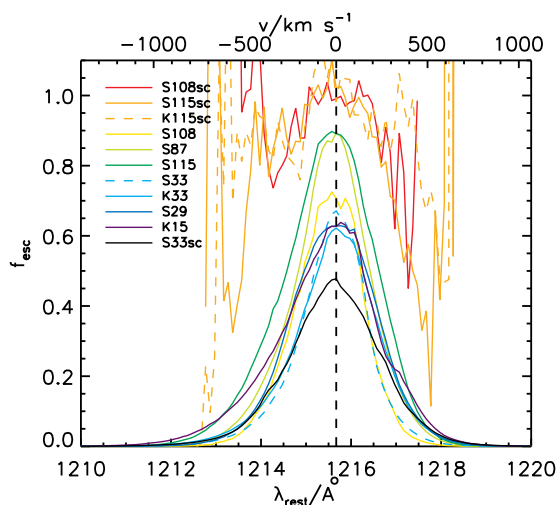


Figure 11.9: Escape fraction f_{esc} as a “function” of wavelength λ for the studied galaxies. The legend is ordered according to the virial mass of the galaxies, S33sc being the most massive. The vertical dashed line marks the Ly α line center. Although the dust cross section is close to being independent of the wavelength of the light, the absorption profile is highly λ -dependent.

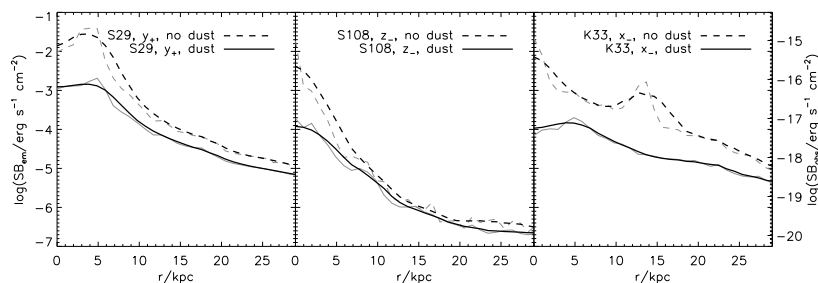


Figure 11.10: Ly α SB profiles of three of the simulated galaxies as observed from three arbitrary directions, with (*solid*) and without (*dashed*) dust. While the intrinsic SB profiles are shown in *gray*, the *black* lines show the profiles convolved with a Gaussian kernel corresponding to a seeing of $0''.5$. In general, the inclusion of dust tends to “smooth out” the profiles, effectively resulting in a more extended SB profile.

As discussed in the introduction, previous attempts to determine Ly α escape fractions have been quite divergent, ranging from a few percent to close to a hundred percent. In this work it was shown that f_{esc} may indeed vary rather much from galaxy to galaxy, and a tentative evidence for a negative correlation with galactic mass was proposed. Obviously, many factors play a role in regulating f_{esc} ; in particular the age of a given galaxy will be significant, since the dust accumulates over time.

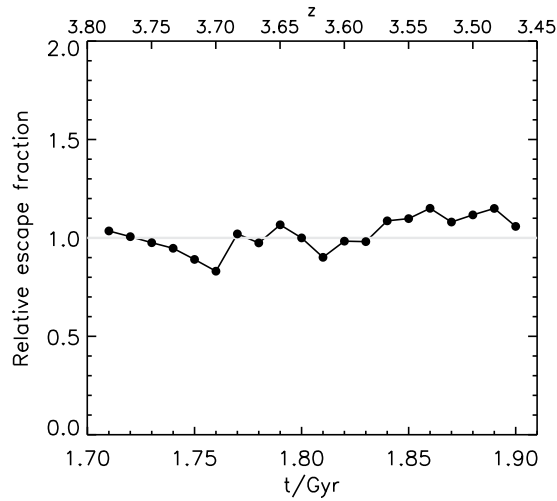


Figure 11.11: Escape fraction f_{esc} from the galaxy K15 as a function of time t over a period of 200 Myr, normalized to f_{esc} at $t = 1.8$ Gyr. The dispersion of f_{esc} over time is quite small, indicating that the dispersion in Fig. 11.7 is due to galaxy-to-galaxy variations rather than the escape fractions of the individual galaxies fluctuating.

Various authors have invoked different scenarios to explain their inferred escape fractions, e.g. galactic outflows, ionized paths, multi-phase medium, and viewing angle. In this work, no evidence was found that any single of these scenarios should be dominating entirely the magnitude of f_{esc} . Rather, a mixture of gas kinematics, ISM clumpiness and ionization state, as well as viewing angle will influence the total observed Ly α luminosity, and hence the deduced escape fraction, when comparing Ly α luminosity to UV luminosity. The investigated galaxies exhibit both outflows and infall, but not at exceptionally high velocities, and artificially setting all velocities to zero still allows plenty of radiation to escape (this was done for K15; the shape of the spectrum is altered, but f_{esc} remains of the same order). Artificially erasing the clumpiness of the ISM decreases f_{esc} as expected but also in this case much radiation still escapes.

Chapter 12

On the impact of the intergalactic medium¹



THE RESULTS PRESENTED in Chapters 10 and 11 ignore the effect of the IGM. At the studied redshift of $z = 3.6$, the IGM should be almost completely neutral, and thus the simulated spectra and SB profiles should be fairly accurate. To confirm this assertion, as well as to study the IGM at other redshift, the IGM RT has been conducted as described in Chap. 9.

However, this was not the only reason for this part of the project; an additional motivation was to inquire into the possibility of an alternative to the “outflow scenario” as an explanation of the many observed asymmetric Ly α spectra. As shown in Sec. 10.2, in general Ly α photons should escape a galaxy in a double-peaked spectrum. Although this has indeed been observed, apparently most Ly α profiles from high-redshift galaxies seem to be missing the blue peak. An immediate conclusion would be that high-redshift LAEs are in the process of massive star formation and thus exhibit strong outflows. In the reference frame of atoms moving away from the source, blue photons will be shifted into resonance and be scattered, whereas red photons will be shifted further from resonance and thus escape more easily (cf. the discussion in Sec. 8.1.5 and Fig. 8.8 on page 86). Indeed, this scenario has been invoked to explain a large number of LAE spectra, most convincingly by Verhamme et al. (2008) who — assuming a central source and thin surrounding shell of neutral gas, while varying its expansion velocity, temperature, and gas and dust column density — manage to produce nice fits to a number of observed spectra.

Although the thin expanding shell scenario hinges on a physically plausible mechanism, it is obviously rather idealized. Furthermore, since most observations show only the red peak of the profile, it seems to indicate that most (high-redshift) galaxies exhibit outflows. However, at high redshifts many galaxies are still forming, resulting in infall which would in turn imply an increased *blue* peak. Since this is rarely observed, it was investigated whether absorption in the IGM could serve as a explanation.

The present study complements other recent endeavors to achieve a comprehensive understanding of how the Ly α line is redistributed in frequency and real

¹This chapter is based on Paper III (App. D).

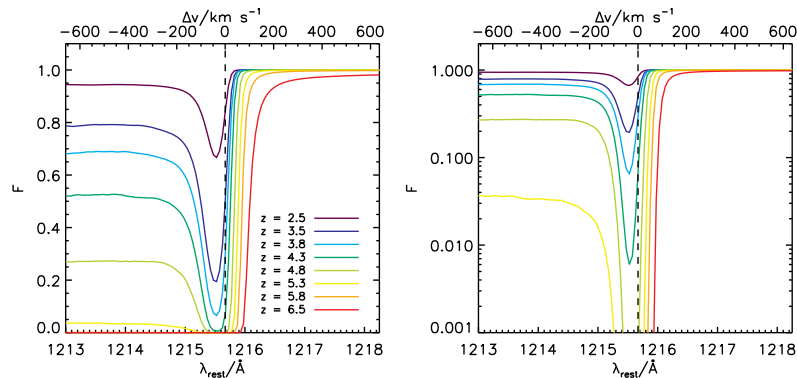


Figure 12.1: Normalized transmission $F(\lambda)$ at wavelengths around $\text{Ly}\alpha$, for different redshifts given by the color. In the *left* panel, the vertical axis is linear, while in the *right* it is logarithmic, emphasizing the transmission at high redshifts.

space *after* having escaped its host galaxy (Iliev et al., 2008; Barnes & Haehnelt, 2010; Faucher-Giguère et al., 2010; Zheng et al., 2010a,b,c). Our cosmological volume is not as large as most of these studies, and although gas dynamics are included in the simulations, the fact that the ionizing UV RT is calculated as a post-process rather than on the fly may mean a less accurate density field. The reward is a highly increased resolution, allowing us to study the circumgalactic environs in great detail. Moreover, we inquire into the temporal evolution of the IGM.

12.1 Results

In the following sections, Model 1 is taken to be the “benchmark” model, while the others are discussed in Sec. 12.3.5.

12.1.1 The $\text{Ly}\alpha$ transmission function

Figure 12.1 shows the calculated transmission functions $F(\lambda)$ as a function of redshift. Indeed, a dip just blueward of the line center is visible at all redshifts. The results in Fig. 12.1 were calculated as the median of sightlines emerging from all galaxies in the sample. Of course a large scatter exists, since each sightline goes through very different regions, even if emanating from the same galaxy. Fig. 12.2 shows the scatter associated with F for three different redshifts. The equivalent transmission functions for the $z_{\text{re}} = 6$ model are shown in Figure 12.3. While at high redshifts the $z_{\text{re}} = 6$ model clearly results in a much more opaque universe, at lower redshifts the transmission properties of the IGM in the different models are more similar, although at $z = 3.5$, the $z_{\text{re}} = 10$ model still transmits more light.

To see the difference in transmission around galaxies of different sizes, Fig. 12.4 shows transmission function for three size ranges (defined in Sec. 9.1.2). Since the distance from the galaxies at which the sightlines start is given in terms of virial radii, sightlines emerging from small galaxies start closer to their source

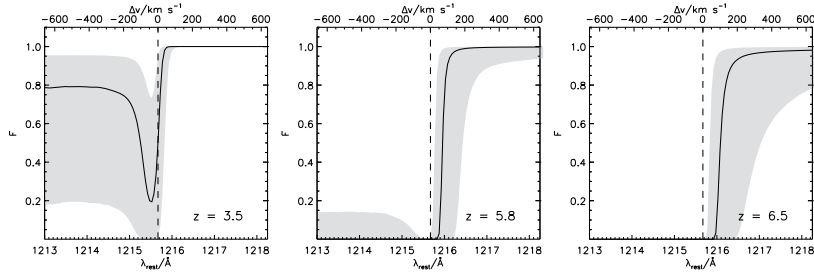


Figure 12.2: Transmission F for $z = 3.5$ (left), 5.8 (middle), and 6.5 (right). The shaded region indicated the range within which 68% of the individual calculated transmission functions fall.

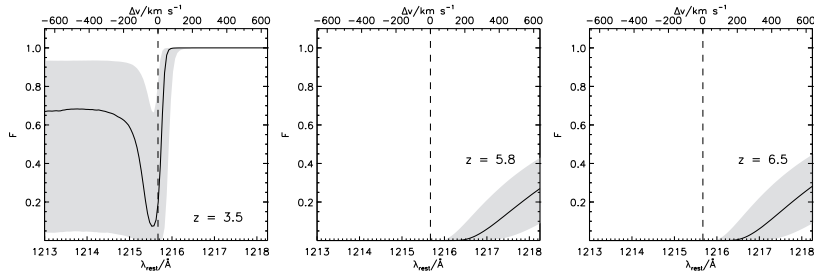


Figure 12.3: Same as Figure 12.2 for Model 3, i.e. with $z_{\text{re}} = 6$. While at high redshifts a much more neutral IGM than in the $z_{\text{re}} = 10$ model causes a severe suppression of the Ly α line, by $z = 3.5$ the state of the IGM is not very different.

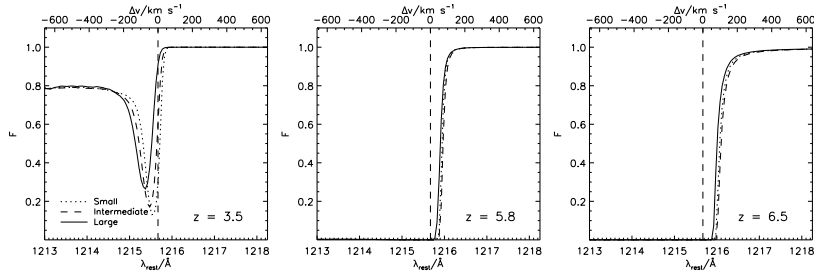


Figure 12.4: Transmission F for $z = 3.5$ (left), 5.8 (middle), and 6.5 (right), for three different size categories of galaxies; small (dotted), intermediate (dashed), and large (solid lines). Although slightly more absorption is seen in the vicinity of smaller galaxies, the transmission functions are quite similar for the three size ranges.

than for large galaxies, and since at lower redshifts they tend to be clustered together in the same overdensities as large galaxies, this results in slightly more absorption. However, the difference is not very significant.

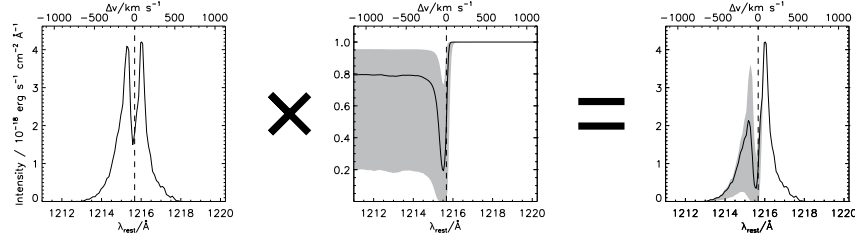


Figure 12.5: Illustration of the effect of the IGM on the observed Ly α profile emerging from a galaxy at $z \sim 3.5$. Without taking into account the IGM the two peaks are roughly equally high (*left panel*). However, when the spectrum is transmitted through the IGM characterized by the transmission function $F(\lambda)$ (*middle panel*), the blue peak is diminished, resulting in an observed spectrum with a higher red peak (*right panel*).

12.1.2 Effect on the spectrum and escape fraction

In Fig. 12.5 the “purpose” of the transmission function is illustrated: the left panel shows the spectrum emerging from a galaxy of $M_{\text{vir}} = 4.9 \times 10^9 M_{\odot}$ and Ly α luminosity $L_{\text{Ly}\alpha} = 4.9 \times 10^{40} \text{ erg s}^{-1}$ (“S115c”). According to the criterion stipulated in Sec. 9.1.2, its circular velocity of 42 km s^{-1} characterizes it as a small galaxy. The spectrum which is actually observed, after the light has been transferred through the IGM, is shown in the right panel. Although on average the effect of the IGM is not very large at this redshift, as seen by the solid line in the right panel, due to the large dispersion in transmission (visualized by the gray-shaded area) at least *some* such galaxies will be observed with a substantially diminished blue peak.

As seen in Fig. 11.8 on page 121, in general the larger a galaxy is the broader its emitted spectrum is, since Ly α photons have to diffuse farther from the line center for higher column densities of neutral gas. If dust is present, this will tend to narrow the line. Larger galaxies tend to have higher metallicities and hence more dust, but the lines will still be broader than the ones of small galaxies. The galaxy used in Fig. 12.5 is quite small. In Fig. 12.6 the impact of the IGM on the nine simulated spectra from the previous chapters is shown.

Besides altering the shape of the emitted spectrum, the IGM also has an effect on another quantity of much interest to observers, namely the observed fraction f_{obs} of the intrinsically emitted number of Ly α photons. The escape fractions f_{esc} shown in Fig. 11.7 on page 119 give the fraction of the intrinsically emitted photons that make it out of the galaxies. As already discussed in Sec. 4.1.1, since the bulk of the emitted Ly α photons is caused by young stars, the total Ly α luminosity of a galaxy may be used as a proxy for its SFR, one of the main quantities characterizing galaxies. Assuming case B recombination, $L_{\text{Ly}\alpha}$ can be converted to a total H α luminosity $L_{\text{H}\alpha}$ (through $L_{\text{H}\alpha} = L_{\text{Ly}\alpha}/8.7$), which in turn can be converted to an SFR using the Kennicutt relation.

The above conversion factors assumes that none of the emitted light is lost. If dust is present in the galaxy a fraction of the emitted photons will be absorbed (possibly making the LAE observable in FIR; see Dayal et al., 2010). This can be corrected for if the color excess $E(B - V)$ is measured, assuming some

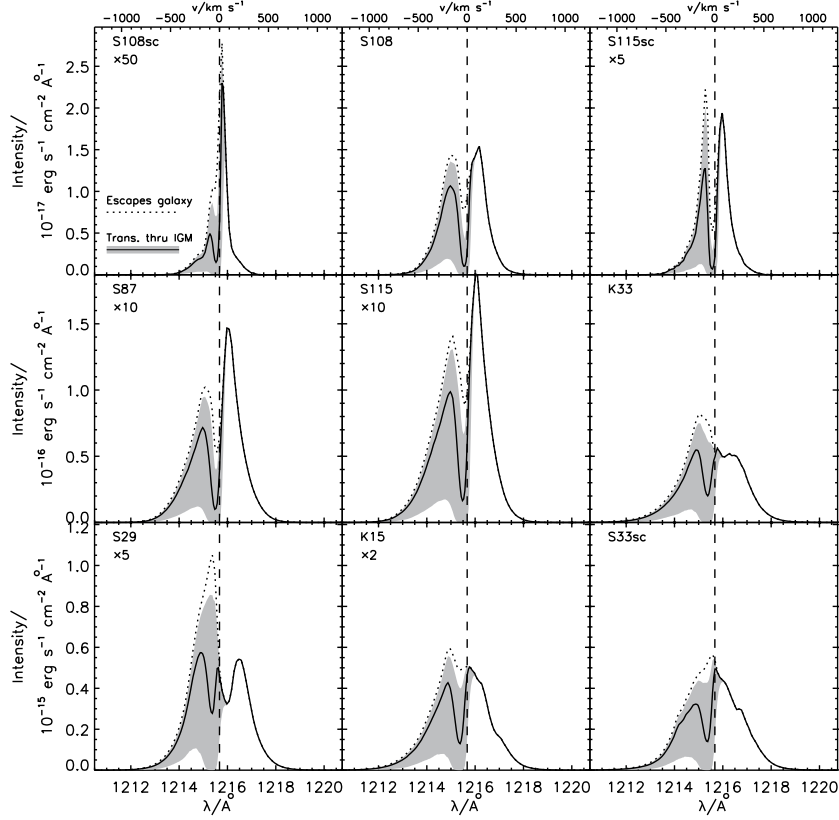


Figure 12.6: Spectra (*dotted lines*) emitted from nine different simulated galaxies at ~ 3.5 — ordered after increasing size — and the corresponding spectra after being transmitted through the IGM (*solid lines with gray regions denoting the 68% confidence intervals*). The transmission functions appropriate for the given galaxy sizes have been used. In order to use the same ordinate axis for a given row, some intensities have been multiplied a factor indicated under the name of the galaxy.

standard extinction curve. However, this assumes that both the $H\alpha$ and $Ly\alpha$ radiation is simply reduced by some factor corresponding to having traveled the same distance through the dusty medium. But since the path of $Ly\alpha$ photons is complicated by resonant scattering, this may be far from the truth. Comparing the $Ly\alpha$ -inferred SFR with that of $H\alpha$ (or UV continuum), the effect of scattering can be constrained, as the quantity $SFR(Ly\alpha)/SFR(H\alpha;UV)$ will be an estimate of f_{obs} . In this way values from a few percent (mostly in the nearby Universe; e.g. Hayes et al., 2007; Atek et al., 2008; Hayes et al., 2010b) to $\sim 1/3$ at high redshifts (Gronwall et al., 2007) have been found, as discussed in Sec. 4.1.1.

Once the radiation enters the IGM, it is also not affected in the same way, since the IGM is transparent to $H\alpha$, but not to $Ly\alpha$. Dijkstra et al. (2007)

TRANSMISSION FRACTIONS FOR NINE SIMULATED GALAXIES AT $z \sim 3.5$

Galaxy	V_c	f_{esc}	f_{IGM}	f_{obs}
S108sc	17	0.97 ± 0.02	$0.66^{+0.24}_{-0.36}$	$0.64^{+0.23}_{-0.35}$
S108	33	0.12 ± 0.02	$0.78^{+0.16}_{-0.35}$	$0.09^{+0.02}_{-0.04}$
S115sc	42	0.95 ± 0.03	$0.76^{+0.18}_{-0.34}$	$0.72^{+0.17}_{-0.32}$
S87	69	0.22 ± 0.01	$0.81^{+0.15}_{-0.32}$	$0.18^{+0.03}_{-0.07}$
S115	73	0.30 ± 0.05	$0.80^{+0.16}_{-0.34}$	$0.24^{+0.06}_{-0.11}$
K33	126	0.08 ± 0.02	$0.78^{+0.17}_{-0.34}$	$0.06^{+0.02}_{-0.03}$
S29	137	0.12 ± 0.03	$0.75^{+0.19}_{-0.35}$	$0.09^{+0.03}_{-0.05}$
K15	164	0.17 ± 0.02	$0.79^{+0.17}_{-0.37}$	$0.13^{+0.03}_{-0.07}$
S33sc	228	0.08 ± 0.02	$0.80^{+0.16}_{-0.33}$	$0.06^{+0.02}_{-0.03}$
Average			$0.77^{+0.17}_{-0.34}$	

Table 12.1: Columns are, from left to right: galaxy name, circular velocity V_c in km s^{-1} , fraction f_{esc} of emitted photons escaping the galaxy (i.e. not absorbed by dust), fraction f_{IGM} of these transmitted through the IGM, and resulting observed fraction $f_{\text{obs}} = f_{\text{esc}}f_{\text{IGM}}$. Uncertainties in f_{esc} represent varying escape fractions in different directions, while uncertainties in f_{IGM} represent variance in the IGM. Uncertainties in f_{obs} are calculated as $(\sigma_{\text{obs}}/f_{\text{obs}})^2 = (\sigma_{\text{esc}}/f_{\text{esc}})^2 + (\sigma_{\text{IGM}}/f_{\text{IGM}})^2$.

estimated analytically the fraction of Ly α photons that are scattered out of the line of sight by the IGM (at $z \sim 4.5$ – 6.5) and found a mean transmission of $f_{\text{IGM}} \sim 0.1$ – 0.3 , depending on various assumptions (note that in [Dijkstra et al. \(2007\)](#) this fraction is called “ \mathcal{T}_α ”). In that study, the intrinsic Ly α line profile is modeled as a Gaussian, the width of which is given by the circular velocity of the galaxies, in turn given by their mass, and assuming that no dust in the galaxies alters the shape of the line before the light enters the IGM.

Since the transmission function is a non-trivial function of wavelength, the exact shape and width of the Ly α line profile is important. With MOCALATA more realistic spectra has been modeled, and applying the transmission function found in [Sec. 12.1.1](#), f_{IGM} can be calculated for the sample of simulated galaxies. The transmitted fraction is not a strong function of galaxy size; on average, a fraction $f_{\text{IGM}} = 0.77^{+0.17}_{-0.34}$ of the photons escaping the galaxies is transmitted through the IGM, at the investigated redshift of $z \sim 3.5$. The results for the individual galaxies is given in [Tab. 12.1](#).

At higher redshifts the metallicity is generally lower, leading to less dust and hence larger values of f_{esc} . However, the increased neutral fraction of the IGM scatters a correspondingly higher number of photons out of the line of sight, resulting in a smaller total observed fraction. [Figure 12.7](#) and [Figure 12.8](#) shows the impact of the IGM on Ly α profiles at $z \sim 5.8$ and $z \sim 6.5$, respectively, and [Table 12.2](#) and [Table 12.3](#) summarizes the obtained fractions. At these redshifts, for the six galaxies for which the calculations have been carried out on average a fraction $f_{\text{IGM}}(z = 5.8) = 0.26^{+0.13}_{-0.18}$ and $f_{\text{IGM}}(z = 6.5) = 0.20^{+0.12}_{-0.18}$ of the

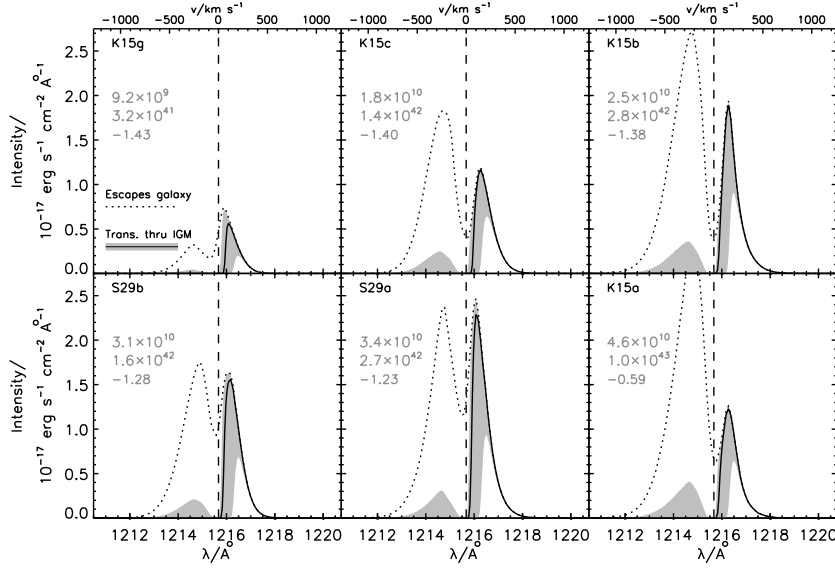


Figure 12.7: Same as Fig. 12.6, but for $z = 5.8$.

TRANSMISSION FRACTIONS FOR SIX SIMULATED GALAXIES AT $z \sim 5.8$

Galaxy	V_c	f_{esc}	f_{IGM}	f_{obs}
K15g	63	0.93 ± 0.02	$0.35^{+0.16}_{-0.24}$	$0.33^{+0.15}_{-0.23}$
K15c	78	0.82 ± 0.02	$0.25^{+0.11}_{-0.14}$	$0.21^{+0.09}_{-0.11}$
K15b	88	0.46 ± 0.02	$0.23^{+0.12}_{-0.14}$	$0.11^{+0.05}_{-0.06}$
S29b	94	0.85 ± 0.01	$0.27^{+0.14}_{-0.17}$	$0.23^{+0.12}_{-0.15}$
S29a	96	0.52 ± 0.08	$0.31^{+0.14}_{-0.22}$	$0.16^{+0.07}_{-0.12}$
K15a	108	0.17 ± 0.05	$0.16^{+0.11}_{-0.11}$	$0.03^{+0.02}_{-0.02}$
Average			$0.26^{+0.13}_{-0.18}$	

Table 12.2: Same as Tab. 12.1, but for $z = 5.8$.

photons is transmitted through the IGM, consistent with what was obtained by [Dijkstra et al. \(2007\)](#).

12.1.3 Probing the Epoch of Reionization

We now focus on a different topic, namely the RT in the IGM far from the emitting galaxies. Measuring for a sample of quasars or other bright sources the average transmission in a wavelength interval blueward of the Ly α line, the average transmission properties, and hence the physical state, of the IGM can be ascertained. The interval in which the transmission is calculated should be large enough to achieve good statistics, but short enough that the bluest

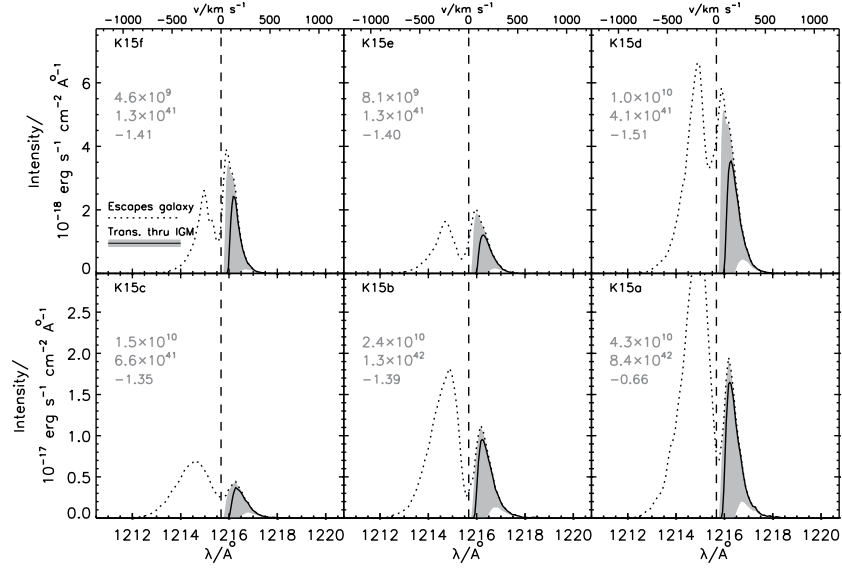


Figure 12.8: Same as Fig. 12.6, but for $z = 6.5$.

TRANSMISSION FRACTIONS FOR SIX SIMULATED GALAXIES AT $z \sim 6.5$

Galaxy	V_c	f_{esc}	f_{IGM}	f_{obs}
K15f	50	0.96 ± 0.03	$0.24^{+0.18}_{-0.22}$	$0.23^{+0.17}_{-0.22}$
K15e	62	0.91 ± 0.04	$0.24^{+0.14}_{-0.22}$	$0.22^{+0.13}_{-0.20}$
K15d	66	0.95 ± 0.02	$0.18^{+0.13}_{-0.16}$	$0.17^{+0.12}_{-0.16}$
K15c	76	0.88 ± 0.02	$0.16^{+0.07}_{-0.14}$	$0.14^{+0.06}_{-0.13}$
K15b	89	0.83 ± 0.03	$0.20^{+0.06}_{-0.17}$	$0.17^{+0.05}_{-0.14}$
K15a	108	0.26 ± 0.09	$0.18^{+0.06}_{-0.16}$	$0.05^{+0.02}_{-0.04}$
Average			$0.20^{+0.12}_{-0.18}$	

Table 12.3: Same as Tab. 12.1, but for $z = 6.5$.

wavelength does not correspond to a redshift epoch appreciably different from the reddest. Furthermore, in order to probe the real IGM and not the quasar’s neighborhood, the upper limit of the wavelength range should be taken to have a value somewhat below λ_0 .

Songaila (2004) measured the IGM transmission in the LAFs of a large sample of quasars with redshifts between 2 and 6.5, in the wavelength interval 1080–1185 Å. In Fig. 12.9 the simulated transmitted fractions is compared with her sample. As is evident from the figure, an “early” reionization, i.e. with $z_{\text{re}} = 10$ (Model 1 and 2), yields a slightly too transparent Universe, while a “late” reionization (Model 3) yields a too opaque Universe. Note that the log scale makes the $z_{\text{re}} = 6$ data seem much farther off than the $z_{\text{re}} = 10$ data.

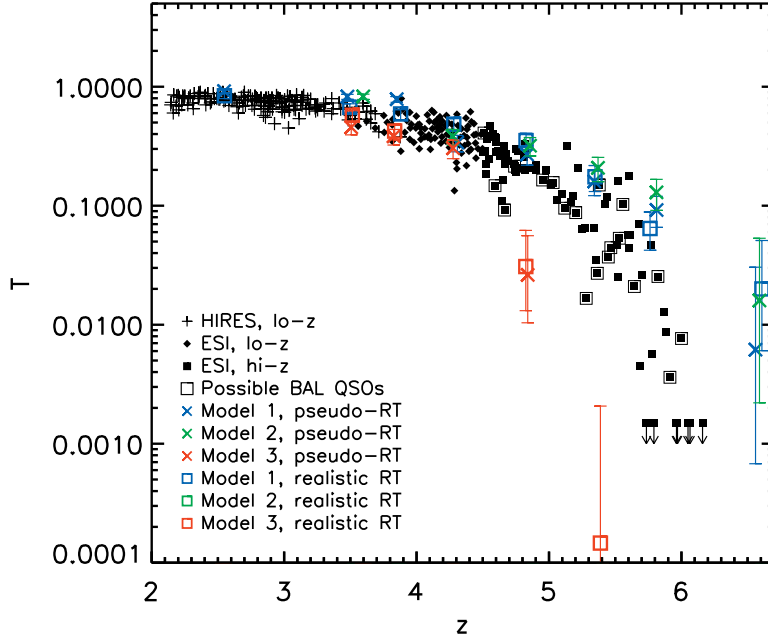


Figure 12.9: Comparison of observations (*black data points*) and simulations (*colored data points*) of the transmitted flux blueward of the Ly α line as a function of redshift; The three models are represented by the colors *blue*, *green*, and *red* for model 1, 2, and 3, respectively. To highlight the significance of the improved UV RT, we show both the transmission in the “original” simulation with the “pseudo”-RT (*crosses*) and with the improved UV RT (*squares*). For details on the observations see [Songaila \(2004\)](#), from where the data are kindly supplied.

12.2 Convergence test

In Sec. 9.2 it was stated that the sightlines should initiate at a distance from the centers of the galaxies given by their virial radius. Figure 12.10 displays the cumulative probability distributions of the distance of the last scattering from the galaxy center for different redshifts and mass ranges, demonstrating that in most cases a photon will have experienced its last scattering at the order of 1 r_{vir} from its host galaxy. For increasing redshift, the photons tend to escape the galaxies at larger distances due to the higher fraction of neutral hydrogen, but the change with redshift seems quite slow. Furthermore, at a given redshift the distinction between different galactic size ranges appear insignificant (as long as r_0 is measured in term of r_{vir}).

Also shown in Fig. 12.10 are the transmission curves for sightlines initiating at various distances r_0 from the centers of the galaxies. For very small values of r_0 , a significantly lower fraction is transmitted due to the high density of neutral gas. Around $r \sim r_{\text{vir}}$ the change in $F(\lambda)$ becomes slow, converging to $F(\lambda)$ exhibiting no dip for $r_0 \rightarrow \infty$.

In summary, scaling r_0 to the virial radius r_{vir} of the galaxies allows us to use

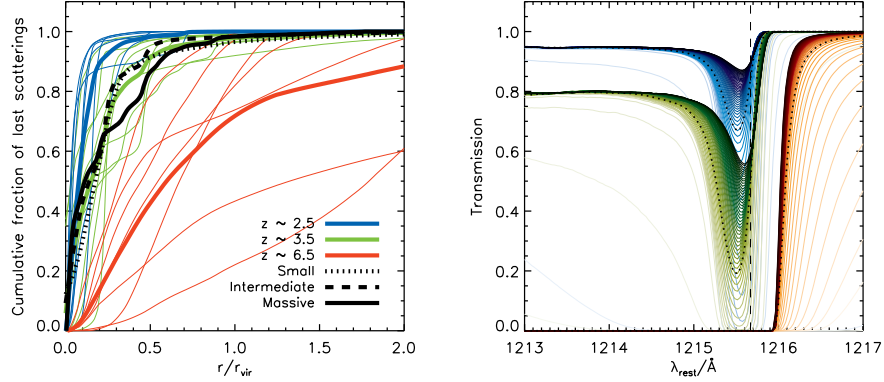


Figure 12.10: *Left:* Cumulative probability distribution of the distance r from the center of a galaxy at which the last scattering takes place. *Thin solid* lines represent individual galaxies at redshift 2.5 (*blue*), 3.5 (*green*), and 6.5 (*red*), while *thick solid colored* lines are the average of these. Also shown, in *black*, are the average of three different size ranges at $z = 3.5$; small (*dotted*), intermediate (*dashed*), and large galaxies (*solid*).

Right: Resulting transmission function $F(\lambda)$ for sightlines originating at various distances r_0/r_{vir} from galactic centres, increasing in steps of $0.1r_{\text{vir}}$ and ranging from $r_0 = 0.1r_{\text{vir}}$ to $r_0 = 5r_{\text{vir}}$. The three different redshifts are shown in shades of *blue*, *green*, and *red*, for $z = 2.5$, 3.5, and 6.5, respectively, and the lines go from light shades for low values of r_0 to dark shades for high values of r_0 . The transmission functions corresponding to $r_0 = 1.5r_{\text{vir}}$ are shown in *black dotted* lines. All results are for Model 1.

the same value of $r_0 = 1.5r_{\text{vir}}$ for all sightlines.

12.3 Discussion

12.3.1 The origin of the dip

In general, the effect of the IGM — *even at relatively low redshifts* — is to reduce the blue peak of the Ly α line profile. At $z \sim 3.5$, the effect is not strong enough to fully explain the observed asymmetry, but at $z \gtrsim 5$, almost all radiation blueward of the line center is lost in the IGM.

Figures 12.11 and 12.12 display for three different epochs the velocity field and the density of neutral hydrogen, respectively, of the IGM associated with the galaxies, taken as an average of all galaxies in the samples, and in all directions.

At all redshifts, on average the IGM close to the galaxies recedes at a somewhat slower rate than that given by the pure Hubble flow, slowly converging toward the average expansion rate of the Universe. At the higher redshifts, the IGM in the immediate proximity of the galaxies is characterized by higher velocities, due to outflows generated by starbursts. At $z = 3.5$, however, this effect is overcome by the accretion of gas.

Inspecting the dips in Fig. 12.1, the minima are seen to be located at roughly 50 km s^{-1} , almost independently of the redshift but becoming slightly broader with

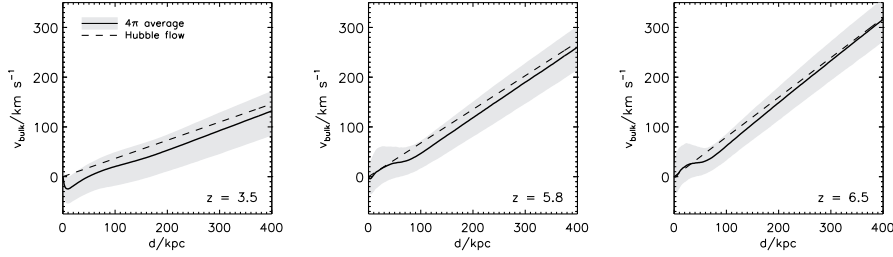


Figure 12.11: Average recession velocity v_{bulk} of the IGM as a function of proper distance d from the centers of the galaxies in Model 1 (solid black lines, with gray regions indicating the 68% confidence intervals). At all redshift, the expansion is retarded compared to the pure Hubble flow (dashed line) out to a distance of several comoving Mpc. At high redshifts, however, very close to the galaxies outflows generate higher recession velocities.

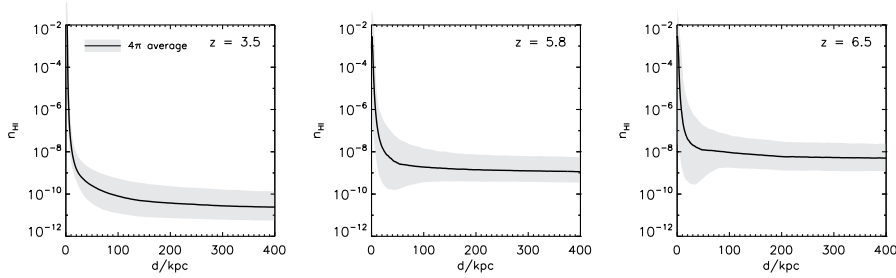


Figure 12.12: Average density n_{HI} of neutral hydrogen as a function of proper distance d from the centers of the galaxies in Model 1 (solid black lines, with gray regions indicating the 68% confidence intervals). While in general the density decreases with distance, at high redshifts ionizing radiation reduces n_{HI} in the immediate surroundings of at least some of the galaxies, as seen by the small dip at ~ 50 kpc in the lower part of the gray zone.

increasing z . At $z = 3.5$, the dip extends all the way out to $300\text{--}400 \text{ km s}^{-1}$. This corresponds to the central absorption being caused by the IGM within ~ 150 kpc, and the wings of the absorption by the IGM within ~ 1 Mpc. As shown in Fig. 12.12, at $z = 3.5$ the density of neutral hydrogen decreases monotonically with distance from the source, and within ~ 150 kpc n_{HI} is substantially higher than the cosmic mean. Further away, the density is close to the mean density of the Universe. However, as seen in Fig. 12.11 the recession velocity of the gas continues to lie below that of the average, Universal expansion rate, and in fact does so until approximately 1 Mpc from the source.²

Thus, the cause of the suppression of the blue wing of the Ly α line may, at wavelengths close to the line center ($\Delta\lambda \simeq 1/2 \text{ \AA}$), be attributed to an increased density of neutral hydrogen close to the galaxies, while farther away from the

²Since the cosmological volume is several Mpc across, except for the galaxies lying close to the edge the absorption takes place before the sightlines “bounce”, so in general there is no risk of a sightline going through the same region of space before having escaped the zone causing the dip.

line center ($\Delta\lambda \lesssim 1\text{--}1.5 \text{ \AA}$), to a retarded Hubble flow.

Zheng et al. (2010a) perform Ly α RT in the IGM at $z = 5.7$ through full Monte Carlo simulations, and make a detailed comparison with the observed line profile obtained from simply multiplying the intrinsic line by $e^{-\tau}$, as has been done in previous models (e.g. Iliev et al., 2008). They conclude that neglecting scattering effects severely underestimates the transmitted fraction. While it is certainly true that treating scattering processes as absorption inside the galaxies is only a crude approximation, once the probability of photons being scattered *into* the line of sight becomes sufficiently small, this approach is quite valid. In their analysis, Zheng et al. (2010a) start their photons in the center of the galaxies, which are resolved only by a few cells (their dx being ~ 28 kpc in physical coordinates and their fiducial galaxy having $r_{\text{vir}} = 26$ kpc). Since the side length of our smallest cells are more than 400 times smaller than the resolution of Zheng et al. (2010a), we are able to resolve the galaxies and their surroundings in great detail, and we are hence able to determine the distance at which the $e^{-\tau}$ model becomes realistic. Moreover, when coupling the IGM RT with Ly α profiles, we use the realistically calculated profile, whereas Zheng et al. (2010a) use a Gaussian set by the galaxies' halo masses. Their line widths $\sigma_{\text{init}} = 32M_{10}^{1/3} \text{ km s}^{-1}$, where M_{10} is the halo mass divided by $10^{10}h^{-1}M_{\odot}$, thus neglect broadening by scattering. This makes them much smaller than ours, which are typically several hundred km s^{-1} . Note, however, that our relatively small cosmological volume and the fact that ionizing UV RT is performed as a post-process rather than on the fly may make our density field less accurate than that of Zheng et al. (2010a).

The photons that are scattered out of the line of sight are of course not lost, but rather become part of a diffuse Ly α background. Since more scatterings take place in the vicinity of galaxies, this is the reason for the previously discussed low-surface brightness halo around the LAEs at $r \sim 10\text{--}100$ kpc scales. As argued above, part of the cause of the line suppression (mostly in the wings) is due to the IGM up to ~ 1 Mpc of the source. At this distance, the surface brightness is much lower than observational thresholds, but could be detected by stacking images of LAEs (Zheng et al., 2010c).

As seen in e.g. Figure 12.2, a large scatter between individual sightlines exists, reflecting the generally quite inhomogeneous IGM. Consequently, one cannot simply use the calculated transmission function for deconvolving observed Ly α lines to obtain the intrinsic line profiles, other than in a statistical sense. With a large sample, however, more accurate statistics on Ly α profiles could be obtained. Calculating the transmission functions as an average of all directions, as we have done in this work, assumes that observed galaxies are randomly oriented in space, i.e. that there is no selection effects making more or less luminous directions pointing toward the observer. For LAEs clustered in, e.g., filaments, the effect of the retarded Hubble flow may be enhanced perpendicular to the filament, making the galaxies more luminous if observed along a filament than perpendicular to it (see Figure 9 in Zheng et al., 2010b).

12.3.2 Galactic outflows

As discussed in the beginning of the chapter, at high redshifts many galaxies are still in the process of forming and are expected to be accreting gas. In principle, this should result in a blueshifted Ly α profile, but this is rarely seen. Evidently,

IGM absorption is unable to always be the cause of this missing blue peak. On larger scales, mass is observed to be conveyed through large streams of gas; the cosmic filaments. Although this has not been seen on galactic scales, galaxy formation may be expected to occur in a similar fashion. Indeed, numerical simulations confirm this scenario (e.g. Dekel et al., 2009; Goerdt et al., 2010)³. In contrast to gas accreting through a few narrow streams, outflows are more or less isotropic. Even bipolar outflows have a rather large opening angle, and thus the probability of a sightline towards a galaxy passing through outflowing gas is larger than passing through infalling gas. Thus, it may be expected that more observations are obtained of Ly α profiles lacking the blue peak than lacking the red peak.

The fact that starbursts are needed to generate large outflows also imposes a bias on the observations; even if outflows happen only during relatively short phases in the early life of a galaxy (for LBGs, Ferrara & Ricotti (2006) found that a typical starburst phase lasts only about 30 ± 5 Myr), such galaxies are more likely to appear in surveys, simply because they are more luminous than those with small SFRs.

12.3.3 Transmitted fraction of Ly α photons

Even though absorption in the IGM does not alter the line shape drastically at an intermediate redshift of 3.5, it reduces the intensity by roughly 25%, as seen from Tab. 12.1. This fraction is not a strong function of the size of a galaxy, but since the spectra emerging from larger galaxies tend to be broader than those of smaller galaxies, a comparatively larger part of the small galaxy spectra will fall in the wavelength region characterized by the dip in the transmission function. Hence, on average the IGM will transmit a larger fraction of the radiation escaping larger galaxies.

One-fourth is not a lot, but since it is preferentially blue photons which are lost, the spectrum may become rather skewed when traveling through the IGM. The lost fraction f_{IGM} is in addition to what is lost internally in the galaxies due to the presence of dust. As mentioned in Section 11.3, dust tends to make the line profile more narrow. For galaxies with no dust, the lines can be very broad. In this case, f_{IGM} will be slightly higher, since for broad lines a relatively smaller part of the spectrum falls on the dip seen in $F(\lambda)$.

As expected, at higher redshifts the IGM is more opaque to Ly α photon; at $z = 5.8$ and $z = 6.5$ the intensity was found to be reduced by approximately 75% and 80%, respectively. At $z = 6.5$ the blue wing is completely lost. In most cases this is true also at $z = 5.8$. However, as is seen from the gray area representing the 68% confidence interval, in some cases an appreciable fraction of the blue wing can make it through the IGM.

12.3.4 The significance of dust

The calculations performed in this work are all neglecting the effect of dust. However, as dust is mostly (although not completely) confined to the galaxies, especially the central parts, and since by far the greatest part of the distance

³Since the submission of this thesis, Cresci et al. (2010) reported on an “inverted” metallicity gradient in three $z \sim 3$ galaxies, which they interpret as being due to the central gas having been diluted by the accretion of primordial gas.

covered by a given sightline is in the hot and tenuous IGM, one may expect this to be a fair approximation.

This anticipation was confirmed including dust in the calculations. The factor $n_{\text{H}}\sigma(\lambda)$ in Eq. 9.2 is then replaced by $n_{\text{H}}\sigma(\lambda)+n_{\text{d}}\sigma_{\text{d}}(\lambda)$. The resulting decrease in transmission is at the 10^{-4} to 10^{-3} level.

12.3.5 “Early” vs. “late” reionization

As is evident from Fig. 12.9, although none of the models really *fit*, the early and late reionization bracket the observations. Model 1, with $\sigma_8 = 0.74$ provides a somewhat better fit to the observations than Model 2 with $\sigma_8 = 0.9$. Due to the more clumpy structure of the latter, galaxies tend to form earlier, rendering the IGM more free of gas and thus resulting in a slightly more transparent Universe. However, this should not be taken to mean that the lower value of σ_8 is more realistic, since a higher σ_8 could be accounted for by a (slightly) smaller z_{re} .

As discussed in Sec. 5.2.1, since the number density n_e of free electrons increases as the Universe gets reionized, a signature of the EoR can be obtained by measuring the total optical depth τ_e to Thomson scattering. In the present simulations, τ_e can be calculated by integrating Eq. 5.1 that gives $d\tau_e/dz$.

Figure 12.13 displays the average comoving number density n_e of electrons as a function of redshift, as well as the corresponding total optical depth τ_e of electrons. The results for Model 2 and Model 3 are shown; those for Model 1 lie very close to those of Model 2. Going from larger toward smaller redshifts, both models are seen to be characterized by a roughly constant and very low density of electrons before reionization, then a rapid increase not *at*, but shortly *after* z_{re} , and finally a slow decrease, due to subsequent gas cool-out and resulting galaxy formation. The rapid increase marking the EoR lasts approximately 100 Myr. The difference in ionization history for the pseudo- and the realistic UV RT schemes is not critical, although the creation of ionized bubbles around stellar sources causes a slightly earlier EoR in the realistic UV RT than the pseudo-RT is able to, especially in Model 3 ($z_{\text{re}} = 6$).

Also shown in Figure 12.13 is the corresponding τ_e history that would prevail in the hypothetical case of an *instant* reionization, where the Universe is fully neutral before, and fully ionized after, some redshift z_{reion} fixed to make the total τ_e match the value measured by WMAP. In this model, no gas is assumed to be locked up in stars, and n_e is thus given by

$$n_e(z) = \begin{cases} 0 & \text{for } z > z_{\text{reion}} \\ \frac{\psi\Omega_b\rho_c(1+z)^3}{m_{\text{H}}} & \text{for } z \leq z_{\text{reion}}, \end{cases} \quad (12.1)$$

where $\psi = 0.76$ is the mass fraction of hydrogen, $\Omega_b = 0.046$ is the baryonic energy density parameter (Jarosik et al., 2010), and ρ_c is the critical density of the Universe.

As seen from Fig. 12.13, not even the early reionization model is able to reproduce the optical depth probed by WMAP. However, for a model with an even earlier EoR, the transmission \mathcal{T} of the IGM would be even farther off the observational data, as seen in Fig. 12.9. In general, there seems to be a significant disagreement between the WMAP results and the QSO results concerning the redshift of the EoR. Many authors have tried to resolve this apparent dis-

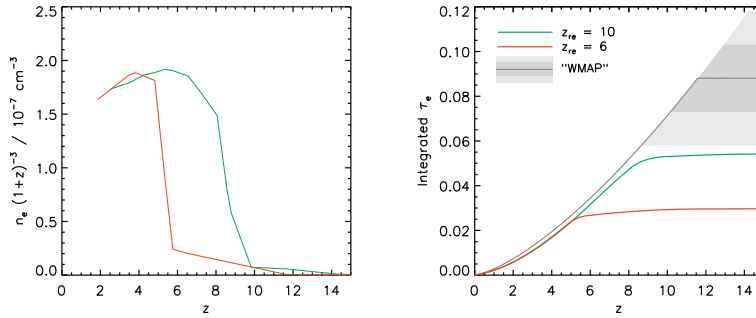


Figure 12.13: Volume-averaged, comoving electron density $n_e/(1+z)^3$ as a function of redshift z for Model 2 (green) and 3 (red) which have $z_{\text{re}} = 10$ and $z_{\text{re}} = 6$, respectively. Both models are characterized by a quite sharp increase in n_e shortly after the onset of UVB. For Model 2 the EoR is seen to take place around $z \sim 8.5$, while for Model the EoR lies at $z \sim 5.5$.

Right: Integrated optical depth τ_e of electrons as a function of redshift z for the two models. As expected, none of the models are able to reach the 0.088 ± 0.015 inferred from the WMAP results, although the $z_{\text{re}} = 10$ model is “only” $\sim 2\sigma$ away. Since the n_e data do not extend all the way to $z = 0$, a fiducial value of $n_e(z = 0) = 1.4 \times 10^{-7} \text{ cm}^{-3}$ has been used. The exact value is not very important, since the proper density at low redshift is very small. At low redshift, the model curves lie slightly below the theoretical curve. This is due to a combination of the models including helium ionization, releasing more electrons, and star formation and gas cool-out, removing free electrons.

crepancy, e.g. Wyithe & Loeb (2003) and Cen (2003) who considered a *double* reionization, first at $z \sim 15$ –16 and later at $z \sim 6$.

Notice nevertheless that the total τ_e of the $z_{\text{re}} = 10$ model is not entirely inconsistent with the WMAP-inferred value, being roughly 2σ away. Furthermore, since only the *total* optical depth is measured by WMAP, the exact history of the EoR is obviously less certain. Generally, either an instant reionization must be assumed, or perhaps a two-step function to make the EoR slightly extended, and possibly with an additional step at $z \sim 3$ to account for helium reionization.

The above results are at odds with the interpretation of the CMB EE polarization maps as showing that the reionization of the Universe was complete at $z = 10.5$ (Jarosik et al., 2010). However, many factors enter the conversion of the polarization maps into an optical depth, and the model of this EoR may be too simplistic. Compared to WMAP, the recently launched Planck⁴ satellite has a much higher resolution and sensitivity; when Planck data become available, these issues may be solved as much tighter constraints can be put on parameters like τ_e (Galli et al., 2010).

⁴<http://www.rssd.esa.int/Planck/>

Chapter 13

On the Ly α emission from damped Ly α absorbers¹



AS ALREADY CONSIDERED in Chap. 2, a prime goal of modern cosmology should be to unveil the relationship between the different populations of high-redshift galaxies. However, whereas the observational overlap of emission selected galaxies has been studied in reasonable detail, little is known about the connection between absorption and emission selected galaxies.

If DLAs are really cradles of star formation, they should also emit Ly α , which should be observable spectroscopically, i.e. as a small peak in the bottom of the DLA trough. However, of the >1000 DLAs found to date, in only a handful of cases associated Ly α has been detected (see Tab. 13.1), even though the search for DLA emission has been going on for more than two decades (e.g. Smith et al., 1989), and several tens of DLAs have been showed to have *no* emission (e.g. Charlot & Fall, 1991; Lowenthal et al., 1995; Colbert & Malkan, 2002; Kulkarni et al., 2006, these are in addition to many null-detections that have not been published).

Although the numerous null-detections may be largely due to the intrinsic difficulties associated with the detection of a galaxy in the projected proximity of the bright background source, the contrasting selection criteria also complicates matters. While LAEs and LBGs tend to probe the bright end of the LF, because they are flux limited, DLAs predominantly probe the faint end. The reason is that, at least in the local Universe, the area that a galaxy covers on the sky is proportional to its luminosity². If this is true also at higher redshifts, from the slope of the faint end of the LF it is expected that the majority of the DLAs must be selected from the faint end (Fynbo et al., 1999; Haehnelt et al., 2000; Schaye, 2001; Fynbo et al., 2008; Pontzen et al., 2008).

¹This chapter is partly based on unpublished observations by the author and collaborators, partly on Paper IV (App. E).

²According to the so-called Holmberg and Bosma relations; see, e.g., Wolfe et al. (1986) and Zwaan et al. (2005)

DLAs WITH ASSOCIATED LY α EMISSION

Background quasar	Reference
PKS0528-250	Møller & Warren (1993)
2233+131	Djorgovski et al. (1996)
Q0151+048	Møller et al. (1998)
Q2059-360	Leibundgut & Gorden (1999)
Q2206-19A	Møller et al. (2002)
PKS0458-02	Møller et al. (2004)
HS1549+1919	Adelberger et al. (2006)
Q2222-0946	Paper IV

Table 13.1: List of quasars, in the spectra of which Ly α emission has been detected (and published) in the trough of a DLA. Entries written in boldface are bona fide detections, i.e. “true” DLAs (as opposed to “sub-DLAs” with $N_{\text{HI}} < 10^{20.3} \text{ cm}^{-2}$), and at a redshift appreciably different from that of the quasar.

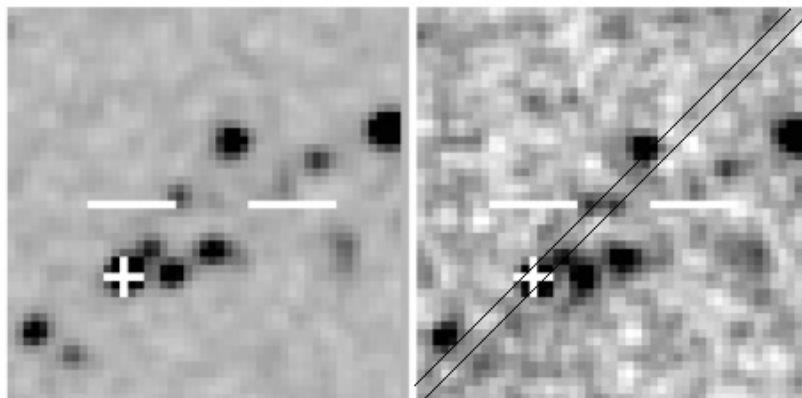


Figure 13.1: Broadband (*left*) and narrowband (*right*) images of the candidate (center of both images) 11'' from the quasar Q2348-011 (marked by the white cross). The dimension of each image is 40'' \times 40''. North is up and east is left. The image is taken from Mannucci et al. (1998), and the width and position angle of the slit used in this study are indicated by black lines.

13.1 Q2348-011

At an observing course at the Nordic Optical Telescope, Roque de los Muchachos, La Palma, in 2007, we — i.e. Johan Fynbo, Christa Gall, Giorgos Leloudas, and the author — performed observations of the quasar Q2348-011. This quasar, lying at a redshift of $z = 3.01$, features *two* DLAs along its line of sight, one at $z = 2.43$ and another at 2.61 (Abazajian et al., 2005), with evidence for an excess of UV flux associated with the former (Noterdaeme et al., 2007). However, as yet searches for a galaxy responsible for the absorption have proved fruitless. Several emitters have been identified in the immediate vicinity of the QSO. In particular, from the excess of H α narrowband to broadband, Mannucci et al. (1998) find an emitter located 11'' NW of the QSO (Fig. 13.1), at the same redshift as the first absorber.

OBSERVATIONAL DATA FOR THE THREE NIGHTS

Date	UT start	t_{exp}/s	Airmass	Seeing
08.18.2007	23 ⁰⁰	3×1800	1.48–2.05	2''0–2''4
08.19.2007	02 ⁰⁰	3×1800	1.15–1.19	0''8–2''4
08.21.2007	02 ³⁰	4×1800	1.15–1.20	0''6–1''0

Table 13.2:

In order to search for Ly α emission, deep, intermediate-resolution spectroscopy of Q2348-011 was carried out at the NOT, with the slit of spectrograph positioned at an angle such that also the spectrum of the emitter at 11'' distance should be obtained, thus enabling its redshift to be determined spectroscopically.

13.1.1 Observations

To acquire the spectra, the ALFOSC (Andalucia Faint Object Spectrograph and Camera) instrument together with the 2k×2k CCD on the NOT was applied. The two DLAs lie at redshifts $z = 2.43$ and $z = 2.61$, and their corresponding Ly α absorption troughs are thus located at wavelengths $\lambda = 4158 \text{ \AA}$ and $\lambda = 4389 \text{ \AA}$, respectively. Grism #16 of the ALFOSC was therefore used. The wavelength coverage of this grism is in the range 3500–5060 \AA and its absolute efficiency is around 50 percent at the according wavelengths. If used with a 0''5 slit it has a resolution of $R = 2000$. However, since high resolution was not the goal of these observations, a slit of width 1''3 was used, resulting in a resolution of $R \simeq 770$, with no second order light in the wavelength range.

Previous searches (Mannucci et al., 1998) have measured the narrowband magnitudes of the candidate objects at the H α line to be approximately 18.8. In order to obtain a satisfactory signal-to-noise ratio of such a faint object, an exposure time of at least five hours was needed. This was based on our calculations but also on previous experience of such detections reported in the literature (e.g., Møller et al., 2004). The total exposure time was divided in shorter exposures of 1800 seconds. Since for the chosen grism the dispersion is 0.77 \AA per pixel, the readout noise could be reduced by a binning of the CCD at 2×2 without any loss of information, providing final pixels of size 0''39 by 1.54 \AA .

In order to simultaneously acquire the spectrum of the H α emitter, the 1''3 long-slit was aligned at position angle $\text{PA} = 45^\circ$ with respect to the E-W direction (Fig. 13.1). The quasars were observed over three nights. During the first night the conditions were not optimal, with relatively high seeing and airmass. However, this improved radically during the last two nights (see Tab. 13.2). For the flux calibration, spectra of the standard star Feige 110 (SP2317059) was obtained, using the same grism and slit. This standard star was a perfect choice due its close alignment on the sky with Q2348-011. For the wavelength calibration and flat-fielding, a helium and a halogen lamp was used, respectively.

13.1.2 Data reduction

The data was reduced with IRAF³ through a standard image reduction procedure of overscan subtraction, bias subtraction, and flat-fielding. The uneven illumination of the halogen lamp was corrected for, using the tasks `response` and `illumination`.

False signals in the images were removed using the task `lacos_spec` (van Dokkum, 2001). The ten 1800 sec spectra were equally weighted and averaged (although there are alternative ways taking into account the different image variance, seeing, etc.), to obtain one final 2D spectrum.

Subsequently, the background was removed in the following way: two stripes of width ~ 10 –20 pixels to the left and right, respectively, of the spectrum and sufficiently close to it, were used to compute an average column. This average column, representing the average background per wavelength, was then subtracted from the original image. Due to the bending of the skylines, this way of background subtraction is only accurate in the center of the image, where the spectrum lies.

To obtain 1D spectra, the task `apall` was used. The 1D spectra were wavelength calibrated by use of the task `dispcor`. One wavelength calibrated 1D spectrum were obtained per night (assuming that the wavelength calibration did not change over the course of a single night) and the three 1D spectra are then combined with the help of `scombine` to obtain a final 1D spectrum (shown in Fig. 13.3).

13.1.3 Results

To determine the presence (and significance) of Ly α emission in the DLA trough, the two-dimensional, background corrected spectrum (Fig. 13.2) was used. A quick, visual inspection is enough to reveal that even if this emission is present, it is not as prominent as in Møller et al. (2004). However, there seems to be an excess of counts over the background. The significance of the detection was measured in the following way:

The corresponding image statistics were computed in IRAF with the use of `imexamine`, option `m`. This computes the statistics in an aperture centered at the position of the cursor. A square box covering an area of 25 pixels was used for this purpose. Measuring in this way the local background values close to the trough results in 0.61 ± 0.37 counts. Here the error is the standard deviation of the mean counts in the aperture averaged over 20 local regions. In the middle of the trough, the value is 1.91 counts, implying that the significance of the detection is at the 3.5σ level.

The effect of smoothing

The image in the left panel of Fig. 13.2 is rather noisy. Smoothing the image allows the detection to be seen more clearly. This was done with the task `boxcar` and a smoothing window 3×3 pixels. The resulting image can be seen in the right image of Fig. 13.2. Computing the corresponding statistics for this image,

³IRAF is distributed by the National Optical Astronomy Observatory (NOAO), which is operated by the Association of Universities for Research in Astronomy, Inc. (AURA) under cooperative agreement with the National Science Foundation.

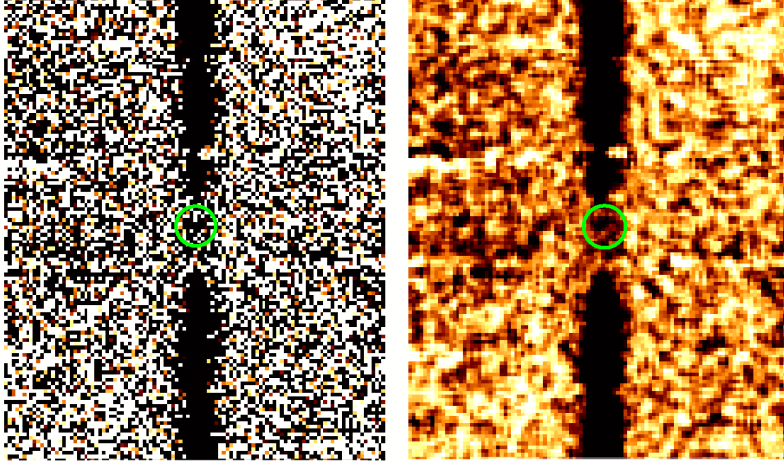


Figure 13.2: Two-dimensional spectrum of the quasar Q2348-011, non-smoothed (*left*) and smoothed (*right*). The emission in the trough of the DLA is marked by a *green* circle.

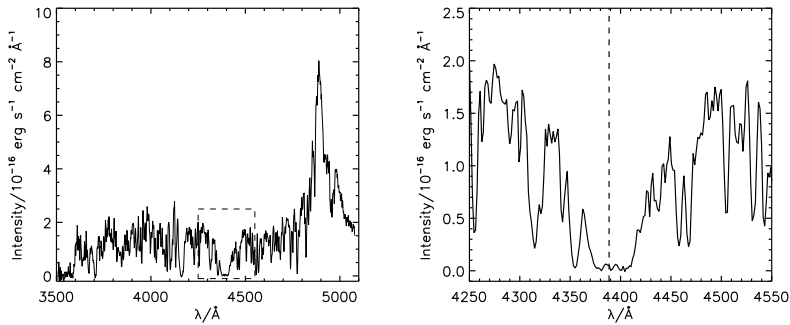


Figure 13.3: Full, one-dimensional spectra of the quasar Q2348-011 (*left*) and zoom-in on the region around the DLA situated at $z = 2.61$ (*right*). The possible Ly α emission is seen as two small bumps in the trough.

we get 0.41 ± 0.30 counts for the local background and 1.69 counts for the middle of the trough, implying a 4.2σ detection.

Emitted flux

The tentative detection of the Ly α emission line (even at this low significance) probably implies active star formation in the DLA. Using the tool `splot` on the final flux calibrated 1D spectrum (Fig. 13.3), a flux of 3.57×10^{-17} erg s $^{-1}$ cm $^{-2}$ Å $^{-1}$ at a wavelength of 4386 Å is deduced. There is also a second bump in the trough, with an excess over the background of 2.77×10^{-17} erg s $^{-1}$ cm $^{-2}$ Å $^{-1}$ at 4395 Å.

However, flux calibration of spectra might suffer from effects like slit losses, extraction choices, etc. For this reason, to measure the total emitted flux in

one more way, the counts level at the bottom of the trough was compared with another well calibrated line.

For this purpose, a spectrum of the quasar obtained by the Sloan Digitized Sky Survey (SDSS) was used. This spectrum, although it is not as deep as ours, has the advantage that it comes from a well known pipeline with standard, well understood and trustworthy calibrations. Surprisingly, the NOT spectrum has more flux than the SDSS spectrum. Since the results were very similar however, this correction was not applied.

13.1.4 Follow-up observations

Although 3.5σ implies a positive detection with 99.95% confidence, this is just not good enough for science! In order to secure an unambiguous detection, 15 more hours of observing time at the NOT were applied for, and granted (with the author as PI). Since originally the target was observed for five hours, this quadrupled the total exposure time, thus increasing the signal-to-noise ratio by a factor of two.

The observations were carried out during four nights, starting 9.14.2009. Due to unfavorable weather conditions, only 11.25 hours were obtained. The data were reduced and processed in a similar fashion as described below, and the spectra were then stacked with the 2007-spectra. Unfortunately, even with this total of more than 16 hours of integration, the detection confidence was not increased, and the project was not pursued further.

Of course, the fact that the emission was only detected at a fairly low significance does not necessarily imply that the absorber features no, or only very little, intrinsic Ly α emission. Previous identifications were all carried out on telescopes significantly larger, so the result may simply be a consequence of the relatively small mirror of the NOT. Moreover, as should be evident from the above numerical results, resonant scattering effects and dust may easily suppress the Ly α line below the detection limits.

13.2 Q2222-0946

As a more methodical way of probing Ly α emission from DLAs, one may specifically target candidate metal-rich DLAs. In the local Universe, the relation between the metallicity and the luminosity, as well as the metallicity and the line profile velocity width, of galaxies are fairly well-established. Similar slopes of these relations are expected to exist at high redshifts (Møller et al., 2004; Ledoux et al., 2006). Furthermore, despite a small sample the DLAs for which emission (in any wavelength) *has* been detected tend to have the highest metallicity among galaxies at the given redshifts (Møller et al., 2004; Weatherley et al., 2005).

To this end, a survey targeting 12 high-metallicity DLAs using the newly built echelle spectrograph X-shooter⁴, mounted on the European Southern Observatory (ESO) Very Large Telescope (VLT), Cerro Paranal, Chile, with Johan Fynbo as PI (and the author as co-I). X-shooter has the advantage that it covers the entire wavelength range from the atmospheric cut-off at ~ 3100 Å to the K-band at 2.5μ (in three different arms; the NIR, VIS, and UVB arm), thus

⁴<http://www.eso.org/sci/facilities/develop/instruments/xshooter/>

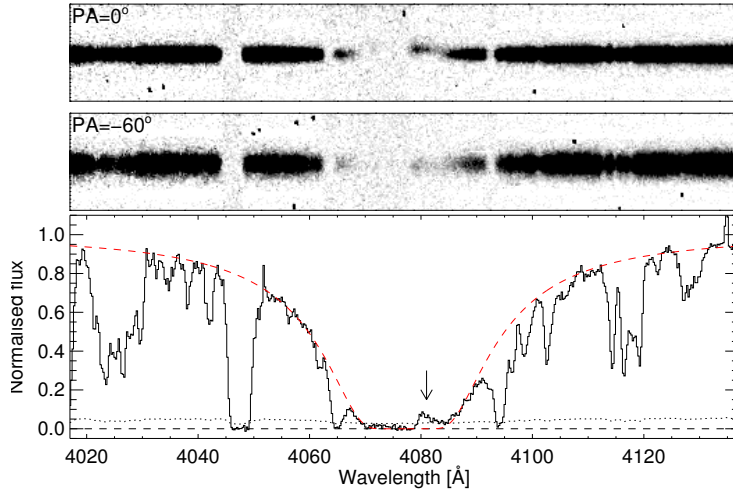


Figure 13.4: One- and two-dimensional spectra of the DLA toward Q2222-0946. The two 2D spectra correspond to the PA = 0° with the best seeing (*upper panel*) and the PA = -60° (*middle panel*). The 1D plot (*lower panel*) is extracted from the PA = 0° spectrum. In this plot the trace of the quasar spectrum is used, and since the Ly α emission line (marked by an arrow) is offset from the trace by $0''.57$, the line is not fully recovered. Also seen in the plot is the noise spectrum (*dotted line*) and the best fit Voigt profile (*red dashed line*).

allowing for simultaneous identification of many important lines. For this study, the intermediate spectral resolution is close to optimal, since near-IR sky lines will be resolved while it is sufficiently low not to be detector noise-limited.

The DLAs are selected from the SDSS DLA sample of [Noterdaeme et al. \(2009\)](#) according to the following criteria: First, the rest frame EW of SiII $\lambda 1526$ must be $>1 \text{ \AA}$. This should ensure that the metallicity is indeed high, i.e. $\gtrsim 0.1 Z_\odot$ (e.g. [Prochaska et al., 2008](#)). Second, the FeII $\lambda 2344$, $\lambda 2374$, $\lambda 2382$ must be well-detected. Finally, in order to be able to detect other emission than Ly α alone, only DLAs at a redshift of $z \sim 2.4$ are included in the final sample, since this implies that the H β , [OII], [OIII] and/or H α emission lines are in the NIR transmission windows.

To cover the field of view in the vicinity of the quasar and allow for a triangulation of a possible emitter, the observations are split up in three, with position angles (PAs) 60° , -60° , and 0° . The probability of missing the galaxy counterpart is then expected to be less than 10%, based on the model of [Fynbo et al. \(2008\)](#). The first target in the survey, the $z = 2.93$ quasar Q2222-0946, was observed on 10.21.2009, and turned out to exhibit a beautiful, unambiguous Ly α emission line in the trough of a DLA at $z_{\text{abs}} = 2.35$ (see Fig. 13.4). In this case, a $1''.3$ slit was used in the UVB arm, while a $1''.2$ slit was used in the VIS and NIR arms, resulting in a resolution of 4700 (UVB), 6700 (VIS), and 4400 (NIR). The intended exposure time was 1 hr per PA, but due to an error in the observing block the PA = 60° exposure was replaced by a second PA = 0° exposure.

The spectra were processed by means of a preliminary version of the X-shooter

data reduction pipeline (Goldoni et al., 2006).

13.2.1 Galaxy counterpart

Metallicity and dust

A plethora of absorption lines were detected at the redshift of the DLA, including various ionization and excitation states of carbon, oxygen, silicon, iron, and zinc. Since Si and Zn are thought not to deplete much to dust, these lines can be used to estimate the metallicity. Fitting Voigt profiles to the lines, metallicities of $[\text{Si}/\text{H}] = -0.51 \pm 0.06$ and $[\text{Zn}/\text{H}] = -0.46 \pm 0.07$ are found, indeed well above the expected threshold of 0.1 solar. For Ni, Fe, and Mn, metallicities lower by a factor of approximately 2, 3, and 6, respectively, are found, indicating notable dust depletion.

Star formation rate

Thanks to the spectacular wavelength range of X-shooter, it was possible simultaneously to obtain Ly α , [OIII], and H α emission lines. This has not been seen in DLA galaxies before and is rarely seen for other types of high- z galaxies.

The total flux in the Ly α line is $8.9 \times 10^{-17} \text{ erg s}^{-1} \text{ cm}^{-2}$, corresponding to a total Ly α luminosity of $L_{\text{Ly}\alpha} = 3.8 \times 10^{42} \text{ erg s}^{-1}$. Assuming standard case B recombination and the Kennicutt relation yields $\text{SFR} = 3\text{--}4 M_{\odot} \text{ yr}^{-1}$. For the H α line, a flux of $2.5 \times 10^{-17} \text{ erg s}^{-1} \text{ cm}^{-2}$ is measured, corresponding to a luminosity of $L_{\text{H}\alpha} = 1.1 \times 10^{42} \text{ erg s}^{-1}$, and an SFR of $8\text{--}9 M_{\odot} \text{ yr}^{-1}$.

The discrepancy between the two calculated SFRs suggests a loss of Ly α photons, either due to dust, anisotropic emission, or IGM absorption. According to case B recombination theory, the intrinsic ration between Ly α and H α luminosity is 8.7 (neglecting cooling radiation). But since in this case $L_{\text{Ly}\alpha}/L_{\text{H}\alpha} \simeq 3.5$, approximately $1 - 3.5/8.7 \simeq 60\%$ of the photons seem to have been lost.

Due to an unfortunate overlap with sky lines, oxygen can only be used to place an upper limit of the SFR of $40 M_{\odot} \text{ yr}^{-1}$.

Morphology and kinematics

Since only two PAs were obtained, an exact position is inaccessible, but in this case an approximate impact parameter of $\sim 0''.8$ could be estimated, corresponding to 6.5 kpc.

The spatial profiles of both the Ly α and the [OIII] line are consistent with the spectral PSF with a seeing of $0''.7$, meaning that the star-forming region of the galaxy is much more compact than the neutral gas. Comparing to the H α LF for $z \sim 2$ galaxies (Hayes et al., 2010a), the galaxy has an H α luminosity of $0.1 L^*$, corresponding to a dwarf galaxy.

Since [OIII] is created mainly in HII regions and does not resonant scatter, this line is expected to probe the systemic redshift of the galaxy. The width of this line is 80 km s^{-1} , while the width of both low- and high-ionization absorption lines are significantly broader and consist of two components. This could be a signature of galactic outflows, although of course the emission lines and the absorption lines probe two different regions. Still, however, the absorption redshifts are very similar to the systemic, as seen from Fig. 13.5.

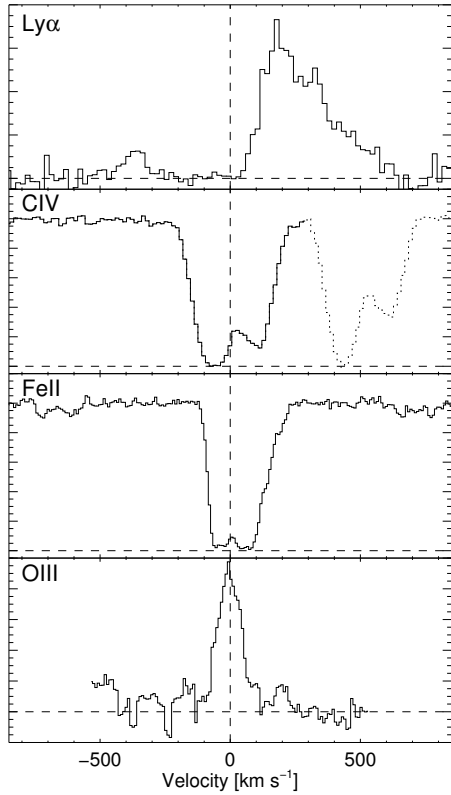


Figure 13.5: Emission and absorption lines associated with the DLA toward Q2222-0946. *Bottom* plot shows the [OIII] emission line, marking the systemic redshift of $z = 2.35406$ defining the velocity $v = 0$. The two *middle* plots show the low- and high-ionization emission lines, represented by FeII $\lambda 2600$ and CIV $\lambda 1548$, respectively, having a similar redshift as the absorption. *Top* plot shows the Ly α emission. The apparent shift in velocity can be explained by resonant scattering effects rather than by a different velocity component. The reminiscence of the blue peak is seen at $v \sim 400 \text{ km s}^{-1}$.

13.2.2 The Ly α emission line profile

The profile of the Ly α line shown in the top panel of Fig. 13.5 is clearly asymmetric. Remarkably the blue edge of the profile is close to the position of rest frame Ly α at the systemic redshift. Even more striking is the presence of a small peak on the blue side of the systemic redshift. This can be understood as a result of resonant scattering. As considered theoretically in Chap. 3 and numerically in Chap. 10, in general Ly α radiation should escape its host galaxy in with a double-peaked profile. Observationally, however, the blue peak is commonly found to be diminished or, more often, entirely suppressed. The cause of this suppression may be galactic winds, but could also be partly due to absorption in the IGM.

Considering the relatively high metallicity inferred for the system and the apparent depletion of refractory elements, the presence of dust is anticipated. Due to the path length of the Ly α radiation being increased by resonant scattering, dust may suppress the Ly α line more than other lines. Even for “gray” dust, the line is not affected uniformly, the wings being influenced more than the centre, as discussed in Sec. 11.3.

If we wish to understand the physical conditions responsible for the formation of the observed Ly α line, we must take all of these effects into account. Verhamme et al. (2008) successfully modeled a number of Ly α profiles by varying the temperature, column density, expansion velocity and dust contents of a thin shell. Analytical solutions exist only for homogeneous, isothermal, and static

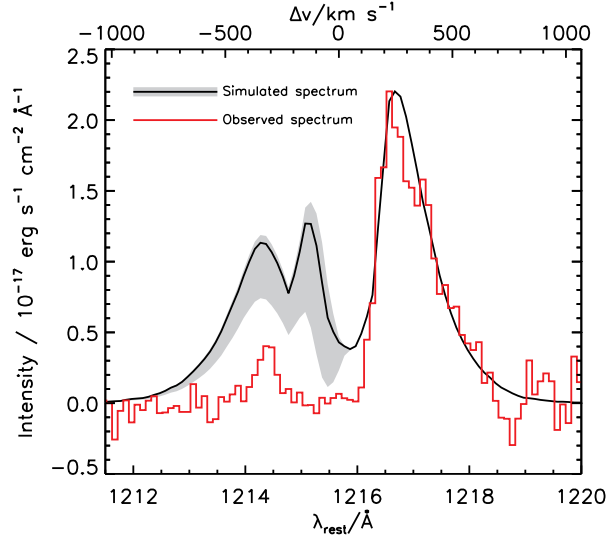


Figure 13.6: Observed Ly α spectrum (*red*) superimposed on a simulated spectrum (*black*), with 68% confidence interval (*gray*). The latter spectrum is produced by first performing Ly α RT in a galaxy that resembles the inferred properties of the observed galaxy, then multiplying by the transmission function $F(\lambda)$ (Sec. 12.1.1) to simulate the impact of the IGM, and finally normalizing such that the amplitude of the red peak matches that of the observed spectrum.

configurations of gas, with either a central or evenly distributed source of light. In the case of a homogeneous gas, each of the two peaks are fairly symmetric about their individual maxima, but taking into account the full range of densities, and the correlation of Ly α emission with these densities, often results in significantly more skewed peaks. This is the result of different parts of the spectrum originating in physically distinct regions. A realistic scenario of galactic outflows probably lies somewhere in between that of the homologously expanding sphere and that of a thin shell. From Fig. 8.8, which shows the spectra of a homologously expanding sphere of column density $N_{\text{HI}} = 10^{20.3} \text{ cm}^{-2}$, one sees that in the case of the expanding sphere with a maximum velocity v_{max} of 20 km s $^{-1}$, the red peak maximum is approximately twice as high as the blue peak maximum, while for $v_{\text{max}} = 200 \text{ km s}^{-1}$ the blue peak is missing completely. In the case of a shell, from Fig. 14 of Verhamme et al. (2006) slightly larger expansion velocities can occur while still allowing the blue peak to be seen.

Figure 13.6 shows the observed Ly α spectrum, together with a simulated spectrum taken from the (low-resolution) cosmological simulation with $z_{\text{re}} = 10$, $\sigma_8 = 0.74$, at a redshift of 2.5. The galaxy used for the Ly α RT has a metallicity of $[\text{O}/\text{H}] = -0.52$, a circular velocity of $V_c = 80 \text{ km s}^{-1}$, and a stellar mass of $1.1 \times 10^9 M_{\odot}$, and thus more or less resembles the above inferred properties of the observed galaxy counterpart.

Although hardly a fit, the similarity between the two spectra is quite remarkable, in particular the red peak. On average, the simulated galaxy is accreting gas at $\sim 50 \text{ km s}^{-1}$, but in the direction in which the fitted spectrum is “observed” (toward negative x -values), a stream of gas is flowing out at $\sim 10\text{--}20 \text{ km s}^{-1}$. If

this outflow were a bit higher, the blue peak would be further reduced, providing an even better fit.

The escape fraction of the simulated galaxy is $\sim 10\%$, somewhat lower than that inferred from comparing the $H\alpha$ and the $Ly\alpha$ luminosities. However, f_{esc} might increase to some extent if the galaxy were simulated at high resolution, matching more closely the $f_{\text{esc}} \sim 1/2$ of the observed galaxy.

Chapter 14

Postscript



NUMERICAL MONTE CARLO Ly α radiative transfer code has been presented and tested against various analytical solutions. The code is capable of propagating Ly α radiation on an adaptively refined mesh, with an arbitrary distribution of Ly α source emission, temperature and velocity field of the ISM, as well as density of neutral and ionized hydrogen, and dust. The abundance of, and the interaction probability with, dust was modeled by scaling known extinction curves to the (location-specific) metallicity of the galaxies, and destruction processes were modeled by reducing the dust density in regions where hydrogen is ionized. Applied to simulated galaxies emerging from fully cosmological simulations, a number of interesting characteristics of galaxies in the high-redshift Universe has been unveiled, many of which are not possible to ascertain in simplified model of galaxies.

To investigate the general effect of the RT in the IGM, these calculations were performed separately. Rather than continuing the Monte Carlo RT in the IGM, this was realized by calculating the average absorption of a large number of sight-lines starting just outside the galaxies. The high resolution of the cosmological simulations combined with the adaptive gridding for the RT allows us to probe the velocity field around the galaxies in great detail.

Additionally, as part of a more comprehensive survey with the aim of building a bridge between galaxies selected by their emission properties and those selected by their absorption properties, observations of DLAs were conducted, with the particular aim of finding their galaxy counterpart. One of these observations, performed with the X-shooter spectrograph mounted on the VLT proved successful, and the obtained spectrum was compared to a simulated spectrum, demonstrating the potential of the Ly α RT code as a tool for interpreting observations.

The main conclusions are summarized below.

14.1 Summary

14.1.1 Extended surface brightness

Although the bulk of the photons are produced in the central, star-forming regions, in general the scattering of Ly α photons in the neutral hydrogen encompassing young galaxies will make a significant fraction of the photons escape far from the center. In contrast to continuum radiation which escapes directly, this results in an extended SB. Comparing to observations of a LAE reveals not only qualitative but also quantitative agreement.

This effect is only amplified when dust is present in the galaxy. Because the bulk of the photons are produced in the vicinity of stars, which tend to be clustered in the central parts, in spite of scattering effects the SB profile will often exhibit a central bump. However, since dust is created from metals, which in turn are created by stars, these regions are also the most dusty, and since additionally most of the neutral gas resides here, greatly increasing the Ly α path length, the probability of being absorbed in regions that would otherwise appear most luminous is larger. Hence, the SB profiles of galaxies, when observed in Ly α , are “smoothed out”. In particular the central bump is reduced, giving rise to an even more “flat” SB profile, which can then be interpreted as an extended SB profile when comparing to continuum bands.

14.1.2 Anisotropic escape

Ly α photons tend to take the shortest way out. Thus, any deviation from spherical symmetry will make the photons escape anisotropically. In the sample of galaxies studied in this work it was found that the maximum observed SB on average varies by an order of magnitude, while the total observed Ly α flux varies somewhat less; a factor of 3–6. If dust is present in the galaxies, the effect is slightly reduced, but the difference is still a factor of 2–4. This effect introduces a larger scatter in the inferred luminosities and SFRs of LAEs than is prevalent inherently.

14.1.3 Narrowing of the Ly α line profile by dust

Although the cross section of the dust is nearly independent of the wavelength of light across the Ly α line, the spectrum is affected in a highly wavelength dependent fashion: close to the line center, the escape fraction is of the order 50%, while in the wings it quickly approaches zero. Consequently, the line is severely narrowed, although its width may still reach several hundreds and even ~ 1000 km s $^{-1}$.

The reason is that different parts of the spectrum originate in physically distinct environments of its host galaxy. The photons that are produced in the dense, central regions have to diffuse to either the blue or the red side of the line center, where the cross section of neutral hydrogen decreases rapidly. Hence, the wings of the spectrum emanate from the star-forming regions, whereas the central parts of the spectrum to a high degree stem from the regions less populated by stars, and from gravitational cooling of infalling gas. Since the dust originates from stars, by far most of the dust is found where the wings are produced, implying that this is the part of the spectrum that is affected the most by dust.

14.1.4 Correlation of Ly α escape fraction with galaxy size

The escape fraction of Ly α seems to decrease with increasing size of the host galaxy. This is indicated by Fig. 11.7, which show that f_{esc} is close to unity for galaxies of $M_{\text{vir}} \sim 10^9\text{--}10^{10} M_{\odot}$, while it falls off to a few % for $M_{\text{vir}} \sim 10^{11}\text{--}10^{12} M_{\odot}$. This effect could be caused partly by the fact that smaller galaxies experience less total star formation, so that the total amount of metals, and hence dust, is smaller than for massive galaxies. However, since the same trend is seen for the escape of ionizing UV radiation (Razoumov & Sommer-Larsen, 2009), for which dust is less important, the chief factor may be the feedback energy of the smaller galaxies being able to “puff up” and disorder its host to a larger degree than for massive galaxies, due to their gravitational potential being smaller.

14.1.5 Absorption in the intergalactic medium

With the scheme for the IGM RT it was calculated how Ly α line profiles emerging from high-redshift galaxies is reshaped by the surrounding IGM. While earlier studies (Zheng et al., 2010a) have shown that this approach of simply multiplying an $e^{-\tau}$ factor on the intrinsically emitted Ly α line is a poor approximation for the observed line profile and transmitted fraction, we have argued that when the circumgalactic environs are sufficiently resolved and combined with realistically calculated intrinsic Ly α lines, this approach should be valid. In general a larger fraction of the blue side of the line center λ_0 is lost as one moves toward higher redshifts. Special emphasis was put on how Ly α line profiles emerging from high-redshift galaxies are reshaped by the surrounding IGM. At $z \gtrsim 5$, almost all of the light blueward of λ_0 is lost, scattered out of the line of sight by the high neutral fraction of hydrogen. However, even at relatively low redshift more absorption takes place just blueward λ_0 . A transmission function $F(\lambda)$ was calculated, giving the fraction of light that is transmitted through the IGM at various epochs. At all redshifts where some of the light blueward of λ_0 is transmitted (i.e. at redshifts below ~ 5.5), a significant dip with a width of the order 1 Å is seen. The origin of this dip is a combination of an increased density of neutral hydrogen and a retarded Hubble flow in the vicinity of the galaxies.

This extra absorption may in some cases be the reason that the blue peak of an otherwise double-peaked Ly α profile is severely reduced, or lacking. Nevertheless, it is not sufficient to be the full explanation of the numerous observations of $z \sim 2\text{--}4$ Ly α profiles showing only the red peak. The outflow scenario still seems a credible interpretation.

Combining the inferred transmission functions with simulated line profiles, the fraction of Ly α photons that are transmitted through the IGM at $z \sim 3.5$, 5.8, and 6.5 was computed, and was found to be $f_{\text{IGM}}(z = 3.5) = 0.77^{+0.17}_{-0.34}$, $f_{\text{IGM}}(z = 5.8) = 0.26^{+0.13}_{-0.18}$, and $f_{\text{IGM}}(z = 6.5) = 0.20^{+0.12}_{-0.18}$, respectively. This is in addition to what is lost internally in the galaxies due to dust. The standard deviations were found to be dominated by sightline-to-sightline variations rather than galaxy-to-galaxy variations.

14.1.6 Constraints on the Epoch of Reionization

Considering the average fraction of light far from the line on the blue side transmitted through the IGM, and comparing to the comprehensive set of observations of the LAF by Songaila (2004), the EoR was constrained to have initiated between $z_{\text{re}} = 10$ and $z_{\text{re}} = 6$, corresponding to having ionized a significant fraction of the Universe around $z \sim 5.5$ and $z \sim 8.5$, respectively. Even though the “early” models of $z_{\text{re}} = 10$ produce a slightly too transparent Universe when comparing to the LAF, the optical depth of electrons is too low when comparing to the observations of the CMB by the WMAP satellite, possibly indicating a too simplistic interpretation of the CMB polarization.

14.1.7 Identification of a DLA galaxy counterpart

Two DLAs were searched for in emission; one with the Nordic Optical Telescope and one with the X-shooter spectrograph on the VLT. The former resulted only in a tentative detection, but the latter turned out to exhibit several emission lines, most notably Ly α emission in the bottom of the trough. Identifying on the basis of the inferred metallicity and velocity dispersion a similar simulated galaxy, the observed and simulated line profiles were compared. It was concluded that it was consistent with originating at the same redshift as the systemic (in spite of the most prominent feature being shifted by several hundred km s⁻¹), having a fair amount of its photons absorbed internally by dust, plus additionally some in the IGM, and possibly being surrounded by outflows at some tens of km s⁻¹.

14.2 Outlook

MOCALATA has proved a valuable tool, not only to predict various observables and physical properties of high-redshift galaxies, but also to interpret observations by modeling real data. Nonetheless, there is always room for improvement, as well as new fields to be explored. The following sections outline future prospects that are intended to be conducted.

14.2.1 Ly α radiative transfer in a multi-phase medium

As substantiated in Sec. 11.1, high resolution is very important to be able to calculate escape fractions realistically. Although convergence tests showed us that f_{esc} does not change with higher resolution, sub-grid physics could alter this picture. The smallest scales probed by the simulation is approximately 10 pc. This resolution is set not by MOCALATA, but by the underlying cosmological simulation. Since cooling below $\sim 10^4$ K is not implemented, the gas does not condense to cold clouds. If the dust is primarily locked up in such cold clouds of neutral hydrogen dispersed in an empty intercloud medium, the Ly α photon could in principle scatter off of the surface of the clouds, thus effectively confining their journey to the dustless medium. Continuum radiation, however, will penetrate the clouds and be subject to large attenuation, resulting in an enhanced Ly α EW (see Fig. 14.1).

This is the scenario described analytically and numerically by Neufeld (1991) and Hansen & Oh (2006), respectively. Numerous authors have relied on this

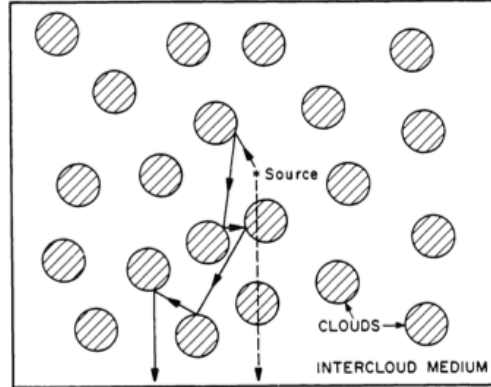


Figure 14.1: The “Neufeld scenario”: in a multi-phase medium, $\text{Ly}\alpha$ radiation (*solid line*) may escape more easily than continuum radiation (*dashed line*), effectively enhancing the equivalent width (from Neufeld (1991)).

to explain EWs larger than what their theories could account for, in the most extreme cases simply by tuning a “clumpiness parameter” to a convenient value. Although clumpiness of the ISM undoubtedly facilitates the escape, the “Neufeld scenario” *is* rather simplistic, in particular because the bulk of the photons are produced close to massive stars which predominantly are born *inside* giant molecular, and hence probably dusty, clouds.

To investigate the effect of sub-parsec resolution on f_{esc} , MOCALATA can be applied to small-scale simulations of star-forming regions. To calculate EWs, an RT scheme for continuum radiation needs to be implemented. Since the expressions for both the hydrogen and the dust cross sections are valid far from the $\text{Ly}\alpha$ line center, this should be rather straightforward, simply requiring knowledge about the ratio of emitted $\text{Ly}\alpha$ and continuum photons.

Simulating simultaneously galactic scales and realistic molecular clouds is still not feasible. Performing the RT in a large number of different regions, however, the general effect of the clumpiness of gas can be scrutinized. This, in turn, can be implemented in galactic RT simulations if in each cell a sub-grid clumping factor $C \equiv \langle n_{\text{HI}}^2 \rangle / \langle n_{\text{HI}} \rangle^2$ can be determined, based on the physical conditions in that cell.

14.2.2 $\text{Ly}\alpha$ polarization

When light is scattered it may be polarized, depending on the particular phase function governing the scattering process, as well as the direction into which it is scattered. For $\text{Ly}\alpha$ emitting galaxies, this has been investigated numerically only in idealized cases, with spherical, homogeneous, isothermal galaxies (e.g. Dijkstra & Loeb, 2008). Moreover, global magnetic fields has not been considered, which may or may not have a large impact on the polarization, through the Hanle effect, Zeeman effect, and/or Faraday rotation, as well as scattering on dust grains oriented in some preferred direction. Magnetic fields are known to appear on all scales, from planet formation to galaxy clusters.

With magnetohydrodynamical simulations, far more realistic configurations of

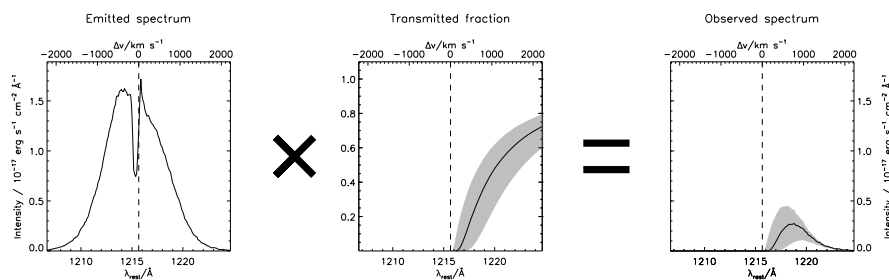


Figure 14.2: Effect of the IGM at $z = 8.8$. The spectrum escaping a galaxy (*right*) was taken from a dust-free version of a $z = 3.6$ -galaxy. The transmission function $F(\lambda)$ (*middle*) is calculated at $z = 8.8$ in a $z_{\text{re}} = 10$, $\sigma_8 = 0.9$ cosmological simulation. The observed spectrum (*left*) will appear significantly redshifted relative to the systemic redshift, and will be greatly, but not entirely suppressed.

gas and magnetic fields can be modeled. Since MOCALATA follows individual photons (or photon packets), the strategy would be to attach a Stokes' vector to each photon, and for each physical process determine the Müller matrix associated with the interaction. The results of these simulations may provide observables to bring new insight into the physical processes of structure formation.

14.2.3 Probing the very first galaxies

The Ultra-VISTA survey mentioned in Sec. 1.1 is a program that has been launched recently, utilizing the ESO VISTA telescope, located close to the VLT on a neighboring peak. In a single pointing, VISTA is capable of observing almost 1 deg^2 in the NIR wavelength region. One of the purposes of Ultra-VISTA is to secure ultra-deep imaging of LAEs at $z = 8.8$ in the COSMOS field (Scoville et al., 2001), with a total of 112 hours of integration (seven of which already have been secured at the time of writing). The most promising LAE candidates will probably followed up spectroscopically. At this redshift, the Ly α line falls in the NIR (the central wavelength of the filter is $1.19 \mu\text{m}$), a wavelength region where the sky is both transparent and relatively free of airglow emission lines.

The deepness and the large volume surveyed will allow to establish a census of the number and the properties of the very first (proto-)galaxies at a hitherto unprecedented early epoch, less than 600 million years after the Big Bang. With MOCALATA it is possible not only to predict what may be observed, but also to interpret these outstanding observations.

Figure 14.2 shows the tentative impact of the IGM on the observability of LAEs at $z = 8.8$. As is seen, the essentially completely neutral IGM hardly allows any of the light on the blue side of the Ly α line center to be transmitted, and the damping wing of the absorption even extends far into the red side. However, since little or no dust is present at such high redshifts, the spectrum of the light escaping the galaxies may be quite extended. As a toy model, the transmission function $F(\lambda)$ at $z = 8.8$ is applied to the simulated spectrum of a dust-free

LAE at $z = 3.6$ ¹. In this case the fraction transmitted through the IGM is $f_{\text{IGM}} = 0.09^{+0.07}_{-0.06}$. This is in agreement with the analytical results of [Dijkstra & Wyithe \(2010\)](#), who found that even in a completely neutral IGM, as much as $\gtrsim 5\%$ of the emitted radiation can be transmitted to the observer.

More simulations are of course needed to substantiate these preliminary calculations, along with simulations of SBs, but it is interesting to note that the observed profile in the left panel of [Fig. 14.2](#) appears redshifted relative to the systemic redshift by $\sim 3 \text{ \AA}$, or $\sim 700 \text{ km s}^{-1}$, thus resulting in the probed sample lying at a slightly lower redshift.

The prospects of applying MOCALATA to model individual observed Ly α spectra and SB profiles are promising. In contrast to previous attempts, with the adaptive gridding and the environment-dependent prescription of dust MOCALATA is capable of examining much more realistic scenarios. Obviously, the simulated galaxies are limited to a rather small number compared to model galaxies, where parameters can be tuned at will. A different approach could be a combination, e.g. to investigate the general effect of outflows by emitting realistically simulated spectra from a central source surrounded by shell of gas, where not only the column density and expansion velocity, but also anisotropy and clumpiness is varied.

Either way, a grid of simulated spectra and SB profiles can be constructed, providing a handy, comprehensive reference sample which, through least square fitting, may be employed to interpret observations of Ly α radiation from young, dusty galaxies.

¹Since unfortunately I don't have a hi-res galaxy at $z = 8.8$ at the moment.

Part IV

Appendix

Appendix A

Quantum mechanical derivation of the Ly α cross section

In this appendix a functional form for the cross section of neutral hydrogen is derived, i.e. the shape of the wavelength dependent line profile and the central wavelength. Also the oscillator strength and the lifetime of the excited state will be derived, and the validity of various approximations is discussed.

A.1 The Hamiltonian

A.1.1 Total Hamiltonian

Even in quite weak radiation fields, the density of photons is very high, implying that we can treat the field as continuous and the interaction between the photon and the atom as a perturbation to the Hamiltonian H of the atomic system. For an electron with position operator \mathbf{x} in a time varying electromagnetic field of scalar and vector potentials $\Phi(\mathbf{x}, t)$ and $\mathbf{A}(\mathbf{x}, t)$, the Hamiltonian is (e.g., Gasiorowicz, 1996)

$$H = \frac{1}{2m_e} \left| \mathbf{p} + \frac{e}{c} \mathbf{A} \right|^2 - e\Phi, \quad (\text{A.1})$$

where $\mathbf{p} = -i\hbar\nabla$ is the momentum operator and c is the speed of light. Interpreting operators as matrices, the nm 'th element of, say, \mathbf{x} is

$$\mathbf{x}_{nm} = \oint \psi_n^* \mathbf{x} \psi_m dV \quad (\text{A.2})$$

$$\equiv \langle n | \mathbf{x} | m \rangle, \quad (\text{A.3})$$

where $*$ denotes the complex conjugate and the integral is over some volume enclosing the wavefunction (in principle all space).

With a clever choice of gauge, viz. the Coulomb gauge defined by $\nabla \cdot \mathbf{A} = 0$,

Eq. A.1 can be expanded to

$$\begin{aligned} H &= \frac{1}{2m_e} |\mathbf{p}|^2 + e\Phi(\mathbf{x}) + \frac{e}{2mc} \mathbf{A} \cdot \mathbf{p} + \frac{e^2}{2mc^2} \mathbf{A} \cdot \mathbf{A} \\ &= H_0 + H_1 + H_2, \end{aligned} \quad (\text{A.4})$$

where $H_0 = |\mathbf{p}|^2/2m - e\Phi(\mathbf{x})$ represents the electrostatic field from the nucleus, and the two last terms the vacuum radiation field. Since $H_2 \ll H_1 \ll H_0$, H_1 can be treated as a small perturbation to H_0 , while the non-linear term H_2 can be neglected altogether. This approximation is valid in the weak field case which is satisfied under the conditions that we shall be dealing with.

Decomposing \mathbf{A} into its Fourier components,

$$\mathbf{A}(\mathbf{x}, t) = \sum_{\mathbf{k}} \left(\mathbf{a}(\mathbf{k}) e^{i(\mathbf{k} \cdot \mathbf{x} - \omega t)} + \mathbf{a}^*(\mathbf{k}) e^{-i(\mathbf{k} \cdot \mathbf{x} - \omega t)} \right), \quad (\text{A.5})$$

where \mathbf{k} is the wave (or propagation) vector and $\omega = 2\pi\nu$ is the angular frequency. Given the Coulomb gauge, Eq. A.5 implies that $\mathbf{k} \cdot \mathbf{a} = 0$. Thus \mathbf{a} has two components orthogonal to \mathbf{k} . These are the polarization states of the radiation field. A more complete description is then

$$\mathbf{A}(\mathbf{x}, t) = \sum_{\mathbf{k}, \varepsilon} \hat{\mathbf{e}}_\varepsilon(\mathbf{k}) \left(a_\varepsilon(\mathbf{k}) e^{i(\mathbf{k} \cdot \mathbf{x} - \omega t)} + a_\varepsilon^*(\mathbf{k}) e^{-i(\mathbf{k} \cdot \mathbf{x} - \omega t)} \right) \quad (\text{A.6})$$

where $\hat{\mathbf{e}}_\varepsilon \perp \mathbf{k}$, with $\varepsilon = 1, 2$.

A.1.2 The Hamiltonian of the perturbation

The Hamiltonian measures the total energy, which for a radiation field is (e.g., Jackson, 1999)

$$H_{\text{rad}} = \frac{1}{8\pi} \int (|\mathbf{E}|^2 + |\mathbf{B}|^2) dV, \quad (\text{A.7})$$

where \mathbf{E} and \mathbf{B} is the electric and magnetic field, respectively. Using the Maxwell's equations that relate \mathbf{E} and \mathbf{B} to \mathbf{A} ,

$$\mathbf{E} = -\frac{1}{c} \frac{\partial \mathbf{A}}{\partial t}, \quad \mathbf{B} = \nabla \times \mathbf{A}, \quad (\text{A.8})$$

together with Eq. A.6, Eq. A.7 is evaluated to

$$H_{\text{rad}} = \sum_{\mathbf{k}, \varepsilon} |a_\varepsilon(\mathbf{k})|^2 \frac{k^2 V}{2\pi}. \quad (\text{A.9})$$

In terms of the photon occupation number $N_\varepsilon(\mathbf{k})$ (the spectrum of the radiation field), $H_{\text{rad}} = \sum_{\mathbf{k}, \varepsilon} \hbar\omega N_\varepsilon(\mathbf{k})$, so that comparison with Eq. A.9 yields

$$|a_\varepsilon(\mathbf{k})| = c \left(\frac{\hbar N_\varepsilon(\mathbf{k})}{V\omega} \right)^{1/2}. \quad (\text{A.10})$$

From Eqs. A.4, A.6, and A.10 we get the perturbation Hamiltonian in the continuum limit

$$H_1 = \sum_{\varepsilon=1}^2 \frac{V}{(2\pi)^3} \int (H_\varepsilon^{\text{abs}}(\mathbf{k}) e^{-i\omega t} + H_\varepsilon^{\text{em}}(\mathbf{k}) e^{i\omega t}) d^3k, \quad (\text{A.11})$$

where

$$H_\varepsilon^{\text{abs}}(\mathbf{k}) = \frac{e}{m_e} \left[\frac{\hbar}{\omega V} N_\varepsilon(\mathbf{k}) \right]^{1/2} e^{i\mathbf{k}\cdot\mathbf{x}} \hat{\mathbf{e}}_\varepsilon(\mathbf{k}) \cdot \mathbf{p} \quad (\text{A.12})$$

and

$$H_\varepsilon^{\text{em}}(\mathbf{k}) = \frac{e}{m_e} \left[\frac{\hbar}{\omega V} (1 + N_\varepsilon(\mathbf{k})) \right]^{1/2} e^{-i\mathbf{k}\cdot\mathbf{x}} \hat{\mathbf{e}}_\varepsilon(\mathbf{k}) \cdot \mathbf{p}. \quad (\text{A.13})$$

The time evolution of the electron wave function is governed by the time-dependent Schrödinger equation

$$H\psi = i\hbar \frac{\partial \psi}{\partial t}. \quad (\text{A.14})$$

where $H = H_0 + H_1$. H_0 has eigenfunctions of the form

$$\psi_j(\mathbf{x}, t) = \phi_j(\mathbf{x}) e^{-iE_j t/\hbar}, \quad (\text{A.15})$$

where the energy E_j of the j 'th eigenstate ϕ_j is an eigenvalue of the time-independent Schrödinger equation $H_0\phi_j = E_j\phi_j$. Since for H_0 the set of all ϕ_j 's forms a basis for any possible wavefunction for stationary atomic systems, we can construct any perturbed wavefunction from

$$\psi(\mathbf{x}, t) = \sum_j c_j(t) \phi_j(\mathbf{x}) e^{-iE_j t/\hbar}, \quad (\text{A.16})$$

where $c_j(t)$ is the time-dependent amplitude of the j 'th eigenstate. With the initial conditions $\psi(\mathbf{x}, t \leq 0) = \phi_i(\mathbf{x})$, i.e. $c_j(t \leq 0) = \delta_{ij}$, using Eq. A.14 the $c_j(t)$'s are evaluated to first order in the perturbation H_1 to give

$$c_f(t) = -\frac{i}{\hbar} \int_0^t \langle f | H_1 | i \rangle e^{i\omega_{fi} t} dt. \quad (\text{A.17})$$

A.2 Absorption

To see how the absorption of photons happens, the transition probability for an electron absorbing a photon is now derived. Considering only the absorption part of Eq. A.11, integrating Eq. A.17 and squaring yields the probability of absorbing a photon of frequency $\omega = ck$:

$$|c_f(\mathbf{k}, t)|^2 = \frac{1}{\hbar^2} |\langle f | H_\varepsilon^{\text{abs}} | i \rangle|^2 \frac{\sin^2[(\omega - \omega_{fi})/2]}{[(\omega - \omega_{fi})/2]^2}. \quad (\text{A.18})$$

To get the total transition probability P_{if} , Eq. A.18 is summed over all \mathbf{k} and ε , so that with the relation $d^3k = k^2 dk d\Omega = (\omega^2/c^3) d\omega d\Omega$,

$$P_{if} = \left(\frac{e}{2\pi m_e} \right)^2 \sum_{\varepsilon=1}^2 \int \frac{N_\varepsilon(\mathbf{k})}{\hbar\omega} |\langle f | e^{i\mathbf{k}\cdot\mathbf{x}} \hat{\mathbf{e}}_\varepsilon(\mathbf{k}) \cdot \mathbf{p} | i \rangle|^2 \frac{\sin^2[(\omega - \omega_{fi})/2]}{[(\omega - \omega_{fi})/2]^2} \frac{\omega^2}{c^3} d\omega d\Omega. \quad (\text{A.19})$$

Note that the dependence on V disappeared, and that P_{if} is strongly peaked for $t \gg 2/\omega_{fi}$.

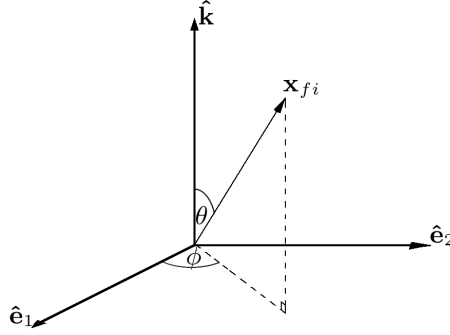


Figure A.1: Geometrical interpretation of the matrix element \mathbf{x}_{fi} in spherical coordinates r , θ and ϕ . The vector represents the orientation of the atomic charge distribution while $\hat{\mathbf{e}}_1$, $\hat{\mathbf{e}}_2$, and $\hat{\mathbf{k}}$ determine the orientation of the photon field and propagation vectors, respectively.

Eq. A.19 predicts that a transition will eventually occur. The interesting quantity is the transition probability *rate*

$$\frac{dP_{if}}{dt} = \sum_{\varepsilon=1}^2 \int \omega_{\varepsilon} d\Omega, \quad (\text{A.20})$$

where ω_{ε} is the constant probability rate per $d\Omega$ for the radiative transition $i \rightarrow f$. Thus, we must evaluate $|\langle f | e^{i\mathbf{k}\cdot\mathbf{x}} \hat{\mathbf{e}}_{\varepsilon}(\mathbf{k}) \cdot \mathbf{p} | i \rangle|^2$. In general, this is very difficult, but expanding in a multipole expansion greatly simplifies the problem. Because $\mathbf{k} \cdot \mathbf{x} \ll 1$, we can approximate $e^{i\mathbf{k}\cdot\mathbf{x}}$ with unity. This is the so-called *dipole approximation* and corresponds to neglecting retardation across the atom. This is a very good approximation for UV radiation, but becomes inadequate for X-ray transitions. From Eqs. A.12 and A.20, and the relation $\mathbf{p} = im_e[H_0, \mathbf{x}]/\hbar$, we then have

$$\frac{dP_{if}}{dt} = \frac{e^2}{\hbar c^3} \sum_{\varepsilon} \oint [N_{\varepsilon} \omega^3 |\hat{\mathbf{e}}_{\varepsilon} \cdot \mathbf{x}_{fi}|^2]_{fi} d\Omega. \quad (\text{A.21})$$

From Fig. A.1,

$$\hat{\mathbf{e}}_1 \cdot \mathbf{x}_{fi} = |\mathbf{x}_{fi}| \sin \theta \cos \phi; \quad (\text{A.22a})$$

$$\hat{\mathbf{e}}_2 \cdot \mathbf{x}_{fi} = |\mathbf{x}_{fi}| \sin \theta \sin \phi. \quad (\text{A.22b})$$

For an isotropic, unpolarized field, $N_1 = N_2 = N(\omega)/2$, so that Eq. A.21 becomes

$$\frac{dP_{if}}{dt} = \frac{4\pi}{3} \frac{e^2}{\hbar c^3} N(\omega_{fi}) \omega_{fi}^3 |\mathbf{x}_{fi}|. \quad (\text{A.23})$$

Conventionally, to translate the probability of absorption into a quantity with the dimensions of area, the bound-bound absorption cross section σ_{ω} is defined such that

$$\frac{dP_{if}}{dt} = \int_0^{\infty} \sigma_{\omega} c N(\omega) \frac{4\pi\omega^2}{(2\pi)^3 c^3} d\omega, \quad (\text{A.24})$$

so that, from Eq. A.23,

$$\sigma_{\omega} = \frac{4\pi^2}{3} \frac{e^2}{\hbar c} |\mathbf{x}_{fi}|^2 \omega \delta(\omega - \omega_{fi}). \quad (\text{A.25})$$

Comparison with Eq. 3.1 yields

$$\phi_{if}(\nu) = \omega\delta(\omega - \omega_{fi}) = 2\pi\nu\delta(\nu - \nu_{fi}), \quad (\text{A.26})$$

and

$$f_{if} = \frac{2m_e}{3\hbar}\omega_{fi}|\mathbf{x}_{fi}|^2. \quad (\text{A.27})$$

A.3 Natural broadening of the line profile

A quantum mechanical interpretation of the oscillator strength has now been derived. In the above calculation, however, the line profile was taken to be a delta function. But since emission processes compete with absorption processes, the absorption rate is affected by the transition rate for spontaneous emission, i.e. the atom decays to the ground state again. This, in fact, is the concept of the resonant scattering process. In principle, there is no fundamental difference between “absorbing and re-emitting” and “scattering” a photon, as long as the decay is to the same state as the initial state, since the energy of the photon is the same before and after the event in both cases (in the reference frame of the atom).

Before evaluating the oscillator strength, we will derive the proper line profile.

Let¹ $\Gamma \equiv dP_{fi}/dt$. Then the transition rate is

$$\begin{aligned} \frac{d}{dt} [\text{occupation of level } f] &= - [\text{probability of decay}] \times [\text{occupation of level } f] \\ \frac{d}{dt} |c_f|^2 &= -\Gamma |c_f|^2 \\ \dot{c}_f \Big|_{\text{spon.em.}} &= -\frac{1}{2}\Gamma c_f, \end{aligned} \quad (\text{A.28})$$

where dot denotes differentiation with respect to time. For spontaneous emission $N(\omega) = 1$, so with $|\mathbf{x}_{fi}| = |\mathbf{x}_{if}|$, adding the above result to the expression for $\dot{c}_f(t)$ yields

$$\sigma_\omega = \frac{4\pi^2}{3} \frac{e^2}{\hbar c} |\mathbf{x}_{fi}|^2 \omega_{fi} \mathcal{L}(\omega), \quad (\text{A.29})$$

where

$$\mathcal{L}(\omega) = \frac{1}{\pi} \frac{\Gamma/2}{(\omega - \omega_{fi})^2 + (\Gamma/2)^2} \quad (\text{A.30})$$

is the Lorentzian profile associated with the natural line profile. This profile is characterized by a sharp peak of width Γ centered at ω_{fi} , and broad wings.

A.4 Transition rate

To calculate the transition probability for the downward transition $(n', \ell', m') \rightarrow (n, \ell, m)$, where n , ℓ and m are the principal, orbital, and magnetic quantum numbers, respectively, we must evaluate the matrix element $\langle i | \mathbf{x} | f \rangle$. Since the wavefunction for the hydrogen atom is rotationally invariant, it can be separated as

$$|f\rangle = |n\ell m\rangle = R_{n\ell}(r) Y_\ell^m(\theta, \phi) \quad (\text{A.31})$$

¹This is the so-called *Einstein A coefficient*; sometimes written A_{fi} .

where $R_{n\ell}(r)$ and $Y_\ell^m(\theta, \phi)$ are the radial wavefunction and spherical harmonic, respectively (see, e.g., Sakurai, 1994). Writing \mathbf{x} as

$$\mathbf{x} = \frac{1}{2}[(x + iy)(\hat{\mathbf{e}}_y - i\hat{\mathbf{e}}_x) + (x - iy)(\hat{\mathbf{e}}_y + i\hat{\mathbf{e}}_x)] + z\hat{\mathbf{e}}_z, \quad (\text{A.32})$$

we see that $\hat{\mathbf{e}}_z \cdot \mathbf{x} = z$ represents interaction with a wave polarized in the z -direction, and hence traveling in the xy -plane, while $\hat{\mathbf{e}}_\pm \cdot \mathbf{x} \propto x \pm iy$ represents a wave traveling in the z -direction and having left or right circular polarization. These directions of polarization can be expressed in terms of spherical harmonics as

$$z = r \cos \theta = \left(\frac{4\pi}{3}\right)^{1/2} rY_1^0; \quad (\text{A.33})$$

$$x \pm iy = r \sin \theta e^{\pm i\phi} = \left(\frac{8\pi}{3}\right)^{1/2} rY_1^{\pm 1}. \quad (\text{A.34})$$

For the Ly α decay $|21m'\rangle \rightarrow |100\rangle$, there are three possible values of m' , and Y must be evaluated separately in each case. However, after a bit of algebra, it is found from Eqs. A.31–A.34 for all m' that

$$|\langle 21m' | \mathbf{x} | 100 \rangle|^2 = \frac{2^{15}}{3^{10}} a_0^2, \quad (\text{A.35})$$

where $a_0 = \hbar^2/m_e e^2$ is the Bohr radius. The transition rate is then evaluated to

$$\Gamma = 6.25 \times 10^8 \text{ s}^{-1}. \quad (\text{A.36})$$

This implies that the half-life $t_{1/2}$ of the excited state is

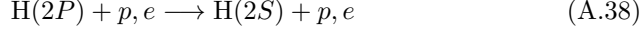
$$t_{1/2} = \frac{1}{\Gamma} = 1.60 \times 10^{-9} \text{ s}. \quad (\text{A.37})$$

By a coordinate transformation $\mathbf{x} \rightarrow -\mathbf{x}$, it can be shown that the scalar product $\hat{\mathbf{e}}_\varepsilon \cdot \mathbf{x}_{fi}$, and hence the transition probability, is non-vanishing only if $\ell + \ell'$ is odd, i.e. if the initial and final state have opposite parity. For this reason, the electron can be excited from the ground state $|100\rangle$ (the “1S” state) to $|21m'\rangle$ (the three “2P” states), but not to $|200\rangle$ (the “2S” state), since $\ell_{1S} = \ell_{2S}$. Expanding the term $e^{i\mathbf{k}\cdot\mathbf{x}}$ without making the dipole approximation yields a non-zero probability of this “forbidden” transition. The lifetime of the 2S is of the order of a second, i.e. ~ 8 orders of magnitude larger than that of the 2P states, and in fact the most probable decay is through an intermediate state of opposite parity, with the emission of two photons as result. Obviously, this would lead to the destruction of the Ly α photon. However, since the probability of being excited to the 2S state is then ~ 8 orders of magnitude smaller than to a 2P state, this effect can be safely neglected.

For the physical conditions governing the situations that we shall be dealing with, $t_{1/2}$ can effectively be regarded as instantaneous. Even in the very dense regions, the density n_{H} of neutral hydrogen rarely exceeds $\sim 10^4 \text{ cm}^{-3}$. In these regions, the temperature is $\sim 10^4 \text{ K}$, corresponding to a typical velocity of the order of 10 km s^{-1} . With a collisional cross section of the order of $n^2 a_0^2$ for hydrogen atoms, in one second the hydrogen atom sweeps out a volume of

$\sim 10^{-11} \text{ cm}^3$, so the probability of colliding with another atom is at most 10^{-6} s^{-1} . However, for high densities and temperatures, collisions may perturb the atom before de-excitation, in which case the above calculations are no longer valid.

The excited atom can also collide with free electrons and protons. For thermal protons and electrons at $T = 10^4 \text{ K}$, carrying out calculations similar to the above one finds that collisional cross sections q_p and q_e for the transitions



are $q_p = 4.74 \times 10^{-4} \text{ cm}^3 \text{ s}^{-1}$ and $q_e = 5.70 \times 10^{-5} \text{ cm}^3 \text{ s}^{-1}$, respectively (Osterbrock, 1989). For proton densities lower than $\sim 10^4 \text{ cm}^{-3}$, the $2P \rightarrow 2S$ transition can be relatively important, but for higher densities, the reverse transition $2S \rightarrow 2P$ cancels out the destruction effect (Osterbrock, 1989). The ratio between the transition rates gives the probability $P_{\text{destr.}}$ of photons being destroyed by two-photon processes:

$$P_{\text{destr.}} = \frac{P_{2P \rightarrow 2S}}{P_{2P \rightarrow 1S}} \quad (\text{A.39})$$

$$= \frac{q_p n_p + q_e n_e}{\Gamma} \quad (\text{A.40})$$

$$\simeq 8.5 \times 10^{-13} n_p, \quad (\text{A.41})$$

where the density n_p of protons is assumed to be approximately equal to the density n_e of electrons. Taking into account the temperature dependence of q_p and q_e introduces a factor of $(T/10^4 \text{ K})^{0.17}$ (Neufeld, 1990). Obviously, collisional transitions can be safely neglected.

The energy E_1 of the ground state is

$$E_1 = -\frac{e^2}{2a_0} = -13.6 \text{ eV}, \quad (\text{A.42})$$

so the energy of the $2P$ state is $E_2 = E_1/n^2 = -3.4 \text{ eV}$. The angular frequency of the Ly α transition is then

$$\omega_{21} = \frac{E_2 - E_1}{\hbar} = 1.55 \times 10^{16} \text{ s}^{-1}, \quad (\text{A.43})$$

so that the true *line center* frequency $\nu_0 \equiv \omega_{fi}/2\pi$ is

$$\boxed{\nu_0 = 2.466 \times 10^{15} \text{ s}^{-1}.} \quad (\text{A.44})$$

We are now ready to evaluate the oscillator strength and hence the absorption cross section. Due to the three-fold degeneracy of the $2P$, the effective oscillator strength of the upward transition is three times that of the downward transition. Thus, from Eqs. A.27 and A.43

$$\boxed{f_{12} = 0.4162.} \quad (\text{A.45})$$

By the uncertainty principle, the finite lifetime of the excited state translates into an uncertainty $\Delta E_2 = \hbar/t_{1/2}$ in the energy of the state. Expressed in terms of frequency this yields an uncertainty $\Delta \nu_L = \Delta E_2/h$, or

$$\boxed{\Delta \nu_L = 9.936 \times 10^7 \text{ s}^{-1}.} \quad (\text{A.46})$$

The absorption cross section σ_ν for the Ly α transition is then

$$\sigma_\nu = f_{12} \frac{\pi e^2}{m_e c} \frac{\Delta\nu_L/2\pi}{(\nu - \nu_0)^2 + (\Delta\nu_L/2)^2}. \quad (\text{A.47})$$

Appendix B

Paper I

The following page displays the abstract from the paper

Lyman α Radiative Transfer in Cosmological Simulations using Adaptive Mesh Refinement

by

Peter Laursen, Alexei O. Razoumov, & Jesper
Sommer-Larsen

published in The Astrophysical Journal, vol. 696, pp. 853–869, 2009 May 1
([Laursen et al., 2009a](#)).

A version of this thesis with the full papers in appendices can be downloaded
from the URL <http://www.dark-cosmology.dk/~pela/Phd/PhDthesis.pdf>.

Note that in the text following immediately after Eq. 17 in the published paper
a typographical error has sneaked in, misplacing inequality symbols “ \leq ” and
“ $>$ ” by “ \geq ” and “ $<$ ”, respectively. An erratum has been made ([Laursen et al.,
2009c](#)).

Ly α RADIATIVE TRANSFER IN COSMOLOGICAL SIMULATIONS USING ADAPTIVE MESH REFINEMENT

PETER LAURSEN¹, ALEXEI O. RAZOUMOV², AND JESPER SOMMER-LARSEN^{3,1}

¹Dark Cosmology Centre, Niels Bohr Institute, University of Copenhagen, Juliane Maries Vej 30, DK-2100, Copenhagen Ø, Denmark; pela@dark-cosmology.dk

²Institute for Computational Astrophysics, Department of Astronomy & Physics, Saint Mary's University, Halifax, NS, B3H3C3, Canada; razoumov@ap.smu.ca

³Excellence Cluster Universe, Technische Universität München, Boltzmannstraße 2, D-85748 Garching, Germany; jslarsen@astro.ku.dk

Received 2008 May 20; accepted 2009 February 6; published 2009 April 20

ABSTRACT

A numerical code for solving various Ly α radiative transfer (RT) problems is presented. The code is suitable for an arbitrary, three-dimensional distribution of Ly α emissivity, gas temperature, density, and velocity field. Capable of handling Ly α RT in an adaptively refined grid-based structure, it enables detailed investigation of the effects of clumpiness of the interstellar (or intergalactic) medium. The code is tested against various geometrically and physically idealized configurations for which analytical solutions exist, and subsequently applied to three different simulated high-resolution “Lyman-break galaxies,” extracted from high-resolution cosmological simulations at redshift $z = 3.6$. Proper treatment of the Ly α scattering reveals a diversity of surface brightness (SB) and line profiles. Specifically, for a given galaxy the maximum observed SB can vary by an order of magnitude, and the total flux by a factor of 3–6, depending on the viewing angle. This may provide an explanation for differences in observed properties of high-redshift galaxies, and in particular a possible physical link between Lyman-break galaxies and regular Ly α emitters.

Key words: galaxies: evolution – galaxies: formation – galaxies: fundamental parameters – line: formation – line: profiles – radiative transfer – scattering

Appendix C

Paper II

The following page displays the abstract from the paper

Lyman α Radiative Transfer with Dust: Escape Fractions from Simulated High-Redshift Galaxies

by

Peter Laursen, Jesper Sommer-Larsen, & Anja C.
Andersen

published in *The Astrophysical Journal*, vol. 704, pp. 1640–1656, 2009 October
20 ([Laursen et al., 2009b](#)).

Ly α RADIATIVE TRANSFER WITH DUST: ESCAPE FRACTIONS FROM SIMULATED HIGH-REDSHIFT GALAXIES

PETER LAURSEN¹, JESPER SOMMER-LARSEN^{1,2}, AND ANJA C. ANDERSEN¹

¹ Dark Cosmology Centre, Niels Bohr Institute, University of Copenhagen, Juliane Maries Vej 30, DK-2100, Copenhagen Ø, Denmark; pela@dark-cosmology.dk

² Excellence Cluster Universe, Technische Universität München, Boltzmannstraße 2, D-85748 Garching, Germany; jslarsen@astro.ku.dk

Received 2009 July 15; accepted 2009 September 10; published 2009 October 6

ABSTRACT

The Ly α emission line is an essential diagnostic tool for probing galaxy formation and evolution. Not only is it commonly the strongest observable line from high-redshift galaxies, but from its shape detailed information about its host galaxy can be revealed. However, due to the scattering nature of Ly α photons increasing their path length in a nontrivial way, if dust is present in the galaxy, the line may be severely suppressed and its shape altered. In order to interpret observations correctly, it is thus of crucial significance to know how much of the emitted light actually escapes the galaxy. In the present work, using a combination of high-resolution cosmological hydrosimulations and an adaptively refinable Monte Carlo Ly α radiative transfer code including an environment dependent model of dust, the escape fractions f_{esc} of Ly α radiation from high-redshift ($z = 3.6$) galaxies are calculated. In addition to the average escape fraction, the variation of f_{esc} in different directions and from different parts of the galaxies is investigated, as well as the effect on the emergent spectrum. Escape fractions from a sample of simulated galaxies of representative physical properties are found to decrease for increasing galaxy virial mass M_{vir} , from f_{esc} approaching unity for $M_{\text{vir}} \sim 10^9 M_{\odot}$ to f_{esc} less than 10% for $M_{\text{vir}} \sim 10^{12} M_{\odot}$. In spite of dust being almost gray, it is found that the emergent spectrum is affected nonuniformly, with the escape fraction of photons close to the line center being much higher than of those in the wings, thus effectively narrowing the Ly α line.

Key words: dust, extinction – galaxies: high-redshift – line: formation – line: profiles – radiative transfer – scattering

Appendix D

Paper III

The following page displays the abstract from the paper

Intergalactic Transmission and its Impact on the Ly α Line

by

Peter Laursen, Jesper Sommer-Larsen, & Alexei O.
Razoumov

accepted for publication in The Astrophysical Journal in January 2011
([Laursen et al., 2010a](#)).

2ND DRAFT
Preprint typeset using L^AT_EX style emulateapj v. 8/13/10

INTERGALACTIC TRANSMISSION AND ITS IMPACT ON THE LY α LINE

PETER LAURSEN^{1,2}, JESPER SOMMER-LARSEN^{1,3,4} AND ALEXEI O. RAZOUMOV⁵
2nd draft

ABSTRACT

We study the intergalactic transmission of radiation in the vicinity of the Ly α wavelength. Simulating sightlines through the intergalactic medium (IGM) in detailed cosmological hydrosimulations, the impact of the IGM on the shape of the line profile from Ly α emitting galaxies at redshifts 2.5 to 6.5 is investigated. In particular we show that taking into account the correlation of the density and velocity fields of the IGM with the galaxies, the blue part of the spectrum may be appreciably reduced, even at relatively low redshifts. This may in some cases provide an alternative to the often-invoked outflow scenario, although it is concluded that this model is still a plausible explanation of the many asymmetric Ly α profiles observed.

Applying the calculated wavelength dependent transmission to simulated spectra from Ly α emitting galaxies, we derive the fraction of photons that are lost in the IGM, in addition to what is absorbed internally in the galaxies due to dust.

Moreover, by comparing the calculated transmission of radiation blueward of the Ly α line with corresponding observations, we are able to constrain the epoch when the Universe was reionized to $z \lesssim 8.5$.

Subject headings: intergalactic medium — radiative transfer — scattering — line: profiles

Appendix E

Paper IV

The following page displays the abstract from the paper

Galaxy Counterparts of metal-rich Damped Lyman- α Absorbers – I: The case of the $z = 2.35$ DLA towards Q2222-0946

by

J. P. U. Fynbo, P. Laursen, C. Ledoux, P. Møller, P.
Goldoni, B. Gullberg, L. Kaper, J. R. Maund, P.
Noterdaeme, G. Östlin, M. L. Strandet, S. Toft, P. M.
Vreeswijk, & T. Zafar

published in Monthly Notices of the Royal Astronomical Society vol. 408,
pp. 2128–2136, November 2010 ([Fynbo et al., 2010](#)).

Galaxy counterparts of metal-rich damped Ly α absorbers – I. The case of the $z = 2.35$ DLA towards Q 2222–0946[★]

J. P. U. Fynbo,^{1†} P. Laursen,¹ C. Ledoux,² P. Møller,³ A. K. Durgapal,⁴ P. Goldoni,^{5,6} B. Gullberg,¹ L. Kaper,⁷ J. Maund,¹ P. Noterdaeme,⁸ G. Östlin,^{9,10} M. L. Strandet,¹ S. Toft,¹ P. M. Vreeswijk¹ and T. Zafar¹

¹Dark Cosmology Centre, Niels Bohr Institute, Copenhagen University, Juliane Maries Vej 30, 2100 Copenhagen O, Denmark

²European Southern Observatory, Alonso de Córdova 3107, Casilla 19001, Vitacura, Santiago 19, Chile

³European Southern Observatory, Karl-Schwarzschildstrasse 2, D-85748 Garching, Germany

⁴Department of Physics, DSB Campus, Kumaun University, Nainital 263001, Uttarakhand, India

⁵Laboratoire Astroparticule et Cosmologie, 10 rue A. Domon et L. Duquet, F-75205 Paris Cedex 13, France

⁶Service d'Astrophysique, DSM/DAPNIA/SAp, CEA-Saclay, F-91191 Gif-sur-Yvette, France

⁷Astronomical Institute 'Anton Pannekoek', University of Amsterdam, Kruislaan 403, 1098 SJ Amsterdam, the Netherlands

⁸Departamento de Astronomía, Universidad de Chile, Casilla 36-D, Santiago, Chile

⁹Department of Astronomy, Stockholm University, AlbaNova University Center, 10691 Stockholm, Sweden

¹⁰Oscar Klein Centre for Cosmoparticle Physics, Department of Astronomy, Stockholm University, SE-106 91 Stockholm, Sweden

Accepted 2010 July 2. Received 2010 July 2; in original form 2010 February 24

ABSTRACT

We have initiated a survey using the newly commissioned X-shooter spectrograph to target candidate relatively metal-rich damped Ly α absorbers (DLAs). Our rationale is that high-metallicity DLAs due to the luminosity–metallicity relation likely will have the most luminous galaxy counterparts. In addition, the spectral coverage of X-shooter allows us to search for not only Ly α emission, but also rest-frame optical emission lines. We have chosen DLAs where the strongest rest-frame optical lines ([O II], [O III], H β and H α) fall in the near-infrared atmospheric transmission bands. In this first paper resulting from the survey, we report on the discovery of the galaxy counterpart of the $z_{\text{abs}} = 2.354$ DLA towards the $z = 2.926$ quasar Q 2222–0946. This DLA is amongst the most metal-rich $z > 2$ DLAs studied so far at comparable redshifts and there is evidence for substantial depletion of refractory elements on to dust grains. We measure metallicities from Zn II, Si II, Ni II, Mn II and Fe II of -0.46 ± 0.07 , -0.51 ± 0.06 , -0.85 ± 0.06 , -1.23 ± 0.06 and -0.99 ± 0.06 , respectively. The galaxy is detected in the Ly α , [O III] $\lambda\lambda 4959, 5007$ and H α emission lines at an impact parameter of about 0.8 arcsec (6 kpc at $z_{\text{abs}} = 2.354$). Based on the H α line, we infer a star formation rate of $10 M_{\odot} \text{ yr}^{-1}$, which is a lower limit due to the possibility of slit loss. Compared to the recently determined H α luminosity function for $z = 2.2$ galaxies, the DLA-galaxy counterpart has a luminosity of $L \sim 0.1 L_{\text{H}\alpha}^*$. The emission-line ratios are 4.0 (Ly α /H α) and 1.2 ([O III]/H α). In particular, the Ly α line shows clear evidence for resonant scattering effects, namely an asymmetric, redshifted (relative to the systemic redshift) component and a much weaker blueshifted component. The fact that the blueshifted component is relatively weak indicates the presence of a galactic wind.

The properties of the galaxy counterpart of this DLA are consistent with the prediction that metal-rich DLAs are associated with the most luminous of the DLA-galaxy counterparts.

Key words: galaxies: formation – galaxies: high-redshift – galaxies: ISM – quasars: absorption lines – quasars: individual: Q 2222–0946 – cosmology: observations.

[★]Based on observations carried out at the European Organization for Astronomical Research in the Southern Hemisphere, Chile, under ESO programme 084.A-0303(A).

†E-mail: jfynbo@dark-cosmology.dk

Bibliography

- Aannestad, P. A. & Emery, R. J. 2001, *A&A*, 376, 1040
- Abazajian, K. et al. 2005, *AJ*, 129, 1755
- Adams, T. F. 1971, *ApJ*, 168, 575
- Adams, T. F. 1972, *ApJ*, 174, 439
- Adelberger, K., Steidel, C. C., Kollmeier, J. A., & Reddy, N. A. 2006, *ApJ*, 637, 74
- Aguirre, A., Hernquist, L., Schaye, J., Katz, N., Weinberg, D. H., Gardner, J. 2001, *ApJ*, 561, 521
- Ahn, S.-H., Lee, H.-W., & Lee, H. M. 2000, *JKAS*, 33, 29
- Ahn, S.-H., Lee, H.-W., & Lee, H. M. 2001, *ApJ*, 554, 604
- Ahn, S.-H., Lee, H.-W., & Lee, H. M. 2002, *ApJ*, 567, 922
- Ambarzumian, V. A. 1932, *MNRAS*, 93, 50
- Atek, H., Kunth, D., Hayes, M., Östlin, G., Mas-Hesse, J. M. 2008, *A&A*, 488, 491
- Atek, H., Kunth, D., Schaerer, D., Hayes, M., Deharveng, J. M., Östlin, G., Mas-Hesse, J. M. 2009, *A&A*, 506, 1L
- Auer, L. H. 1968, *ApJ*, 153, 783
- Avery, L. W. & House, L. L. 1968, *ApJ*, 152, 493
- Bardeen, J. M., Bond, J. R., Kaiser, N. & Szalay, A. S. 1986, *ApJ*, 304, 15
- Barnes, L. A. & Haehnelt, M. G. 2010, *MNRAS*, 403, 870
- Barnes, J. & Hut, P. 1986, *Nature*, 324, 446
- Barton, E. J., Davé, R., Smith, J.-D T., Papovich, C., Hernquist, L., Springel, V. 2004, *ApJ*, 604, 1
- Bechtold, J., Crotts, A. P. S., Duncan, R. C., & Fang, Y. 1994, *ApJL*, 437, L83
- Becker, R. H. et al. 2001, *AJ*, 122, 2850

- Bertoldi, F., Carilli, C. L., Cox, P., Fan, X., Strauss, M. A., Beelen, A., Omont, A., Zylka, R. 2003, *A&A*, 406, L55
- Bi, H. & Davidsen, A. F. 1997, *ApJ*, 479, 523
- Bianchi, L., Clayton, G. C., Bohlin, R. C., Hutchings, J. B., & Massey, P. 1996, *ApJ*, 471, 203
- Bisschop, S. E., Jørgensen, J. K., van Dishoeck, E. F., de Wachter, E. B. M. 2007, *A&A*, 465, 913
- Bohlin, R. C., Savage, B. D. & Drake, J. F. 1978, *ApJ*, 224, 132
- Bohren, C. F. & Huffman, D. R. 1983, *Absorption and scattering of light by small particles*, New York: Wiley
- Bonilha, J. R. M., Ferch, R., Salpeter, E. E., Slater, G., & Noerdlinger, P. D. 1979, *ApJ*, 233, 649
- Box, G. E. P. & Müller, M. E. 1958, *Ann. Math. Statist.*, 29, 610
- Bouchet, P. et al. 2006, *ApJ*, 650, 212
- Bouwens, R. J., et al. 2004, *ApJ*, 616, 79
- Brandt, J. C., Heap, S. R., Beaver, E. A., Boggess, E. A., Carpenter, K. G., & Ebbets, D. C. 1993, *AJ*, 105, 831
- Bransden, B. H. & Joachain, C. J. 2003, *Physics of Atoms and Molecules*, 2nd ed., Essex: Pearson Education Ltd.
- Bruscoli, M., Ferrara, A., Marri, S., Schneider, R., Maselli, A., Rollinde, E., & Aracil, B. 2003, *MNRAS*, 343, L41
- Bunker, A. J., Stanway, E. R., Ellis, R. S., & McMahon, R. G. 2004, *MNRAS*, 355, 374
- Burgh, E. B., McCandliss, S. R., & Feldman, P. D. 2002, *ApJ*, 575, 240
- Calzetti, D. 2001, *PASP*, 113, 1449
- Calzetti, D., Bohlin, R. C., Gordon, K. D., Witt, A. N., & Bianchi, L. 1995, *ApJ*, 446, 97
- Cantalupo, S., Porciani, C., Lilly, S. J., & Miniati, F. 2005, *ApJ*, 628, 61
- Caroff, L. J., Noerdlinger, P. D., & Scargle, J. D. 1972, *ApJ*, 176, 439
- Castro Cerón, J. M., Michałowski, M. J., Hjorth, J., Watson, D., Fynbo, J. P. U., & Gorosabel, J. 2006, *ApJ*, 653, L85
- Ceccarelli, C., Loinard, L., Castets, A., Tielens, A. G. G. M., Caux, E., Lefloch, B., & Vastel, C. 2001, *A&A*, 372, 998
- Cen, R. 2003, *ApJ*, 591, 12
- Chandrasekhar, S. 1935, *ZA*, 9, 266

- Chandrasekhar, S. 1955, *Radiative Transfer*, Oxford: Clarendon Press
- Charlot, S. & Fall, S. M. 1991, *ApJ*, 378, 471
- Chelouche, D., Koester, B. P., Bowen, D. V. 2007, *ApJ*, 671, 97
- Chini, R., Krügel, E., & Kreysa, E. 1986, *A&A*, 167, 315
- Choudhury, T. R. & Ferrara, A. 2006 ([arXiv:0603149](https://arxiv.org/abs/0603149))
- Colbert, J. W. & Malkan, M. A. 2002, *ApJ*, 566, 51
- Contini, M. 2004, *A&A*, 422, 591
- Contini, M. & Contini, T. 2003, *MNRAS*, 342, 299
- Coppin, K., et al. 2009, *MNRAS*, 395, 1905
- Couchman, H. M. P. 1991, *ApJ*, 368, 23
- Cowie, L. L., & Hu, E. M., 1998, *AJ*, 115, 1319
- Cresci, G., Mannucci, F., Maiolino, R., Marconi, A., Gnerucci, A., & Magrini, L. 2010 ([arXiv:1010.2534](https://arxiv.org/abs/1010.2534))
- Croft, R. A., Weinberg, D. H., Katz, N., & Hernquist L. 1998, *ApJ*, 495, 44
- Davé, R., Finlator, K., & Oppenheimer, B. D. 2006, *MNRAS*, 370, 273
- Dayal, P., Ferrara, A., Saro, A., Salvaterra, R., Borgani, S., & Tornatore, L. 2009, *MNRAS*, 400, 2000
- Dayal, P., Hirashita, H., & Ferrara, A. 2010, *MNRAS*, 403, 620
- Deharveng, J.-M. et al. 2008, *ApJ*, 680, 1072
- Dekel, A., Birnboim, Y., Engel, G., Freundlich, J., Goerdt, T., Mumcuoglu, M., Neistein, E., Pichon, C., Teyssier, R., & Zinger, E. 2009, *Nature*, 457, 451
- Dijkstra, M., Haiman, Z., & Spaans, M. 2006, *ApJ*, 649, 14
- Dijkstra, M., Haiman, Z., & Spaans, M. 2006, *ApJ*, 649, 37
- Dijkstra, M., Lidz, A., & Wyithe, J. S. B. 2007, *MNRAS*, 377, 1175
- Dijkstra, M. & Loeb, A. 2008, *MNRAS*, 386, 492
- Dijkstra, M. & Loeb, A. 2009, *MNRAS*, 396, 377
- Dijkstra, M., & Wyithe, J. S. B. 2010 ([arXiv:1004.2490](https://arxiv.org/abs/1004.2490))
- Dinshaw, N., Impey, C. D., Foltz, C. B., Weymann, R. J., & Chaffee, F. H. 1994, *ApJL*, 437, L87
- Djorgovski, S. G., Castro, S. M., Stern, D., & Mahabel, A. A. 2001, *ApJ*, 560, L5
- Djorgovski, S. G., Pahre, M. A., Bechtold, J., & Elston, R. 1996, *Nature*, 382, 234

- Djorgovski, S. & Thompson, D. J. 1992, *IAUS*, 149, 337
- Draine, B. T. 1988, *AJ*, 333, 848
- Draine, B. T. & Salpeter, E. E. 1979, *ApJ*, 231, 438
- Draine, B. T. & Salpeter, E. E. 1979, *ApJ*, 231, 77
- Efstathiou, G., Davis, M., Frenk, C. S., White, S. D. M. 1985, *ApJS*, 57, 241
- Eisenstein et al. 2005, *ApJ*, 633, 560
- Elíasdóttir, Á. et al. 200, *ApJ*, 697, 1725
- Ellison, S. L. 2006, *MNRAS*, 372, 38
- Emerson, D. 1996, *Interpreting Astronomical Spectra*, New York: John Wiley & Sons
- Fabian, A. C 1994, *ARA&A*, 32, 277
- Fan, X., Carilli, C. L., & Keating, B. 2006, *ARA&A*, 44, 415
- Fang, Y., Duncan, R. C., Crofts, A. P. S., & Bechtold, J. 1996, *ApJ*, 462, 77
- Fardal, M. A., Katz, N., Gardner, J. P., Hernquist, L., Weinberg, D. H., & Davé, R. 2001, *ApJ*, 562, 605
- Faucher-Giguère, C.-A., Keres, D., Dijkstra, M., Hernquist, L., & Zaldarriaga, M. 2010 ([arXiv:1005.3041](https://arxiv.org/abs/1005.3041))
- Faucher-Giguère, C.-A., Prochaska, J. X., Lidz, A., Hernquist, L., & Zaldarriaga, M. 2008, *ApJ*, 681, 831
- Feautrier, P. 1964, *CR*, 258, 3189
- Ferrara, A. 2003, *Mem. S. A. It. Suppl.*, 3, 198
- Ferrara, A. & Ricotti, M. 2006, *MNRAS*, 373, 571
- Ferrière, K. M. 2001, *Rev. Mod. Phys.*, 73, 1031
- Field, G. 1958, *ApJ*, 46, 240
- Field, G. 1959, *ApJ*, 129, 551
- Finkelstein, S. L., Rhoads, J. E., Malhotra, S., Grogin, N., Wang, J. 2000, *ApJ*, 678, 655
- Finkelstein, S. L., Rhoads, J. E., Malhotra, S., Pirzkal, N., Wang, J. 2007, *ApJ*, 660, 1023
- Fitzpatrick, E. L. & Massa, D. 2007, *ApJ*, 663, 320
- Fleck, J. A., Jr. 1963, *Methods in Computational Physics*, Vol. I, ed. B. Alder, S. Fernbach, & M. Rotenberg, New York: Academic Press
- Furlanetto, S. R., Schaye, J., Springel, V., Hernquist, L. 2003, *ApJ*, 599, 1

- Furlanetto, S. R., Schaye, J., Springel, V., Hernquist, L. 2005, *ApJ*, 622, 7
- Fynbo, J. P. U., Laursen, P., Ledoux, C., Møller, P., Goldoni, P., Gullberg, B., Kaper, L., Maund, J., Noterdaeme, P., Östlin, G., L. Strandet, M., Toft, S., M. Vreeswijk, P., Zafar, T. 2010 ([arXiv:1002.4626](https://arxiv.org/abs/1002.4626))
- Fynbo, J. P. U., Ledoux, C., Møller, P., Thomsen, B. & Burud, I. 2003, *A&A*, 407, 147
- Fynbo, J. P. U., Møller, P., & Thomsen, B. 2001, *A&A*, 374, 443
- Fynbo, J. P. U., Møller, P., & Warren, S. J. 1999, *MNRAS*, 305, 849
- Fynbo, J. P. U., Prochaska, J. X., Sommer-Larsen, J., Dessauges-Zavadsky, M., & Møller, P. 2008, *ApJ*, 683, 321
- Gail, H. P. 2009, *EAS*, 35, 173
- Galli, S., Martinelli, M., Melchiorri, A., Pagano, L., Sherwin, B. D., Spergel, D. N. 2010 ([arXiv:1005.3808](https://arxiv.org/abs/1005.3808))
- Gardner, J. P. 2006, *IAUSS*, 1, 16
- Gasiorowicz, S. 1996, *Quantum Mechanics*, 2nd ed., New York: John Wiley & Sons
- Gawiser et al. 2006, *ApJ*, 642, L13
- Gawiser et al. 2006, *ApJS*, 162, 1
- Gawiser et al. 2007, *ApJ*, 671, 278
- Giard, M., Montier, L., Pointecouteau, E., & Simmat, E. 2008, *A&A*, 490, 547
- Giavalisco, M., Steidel, C. C., Adelberger, K. L., Dickinson, M. E., Pettini, M., & Kellogg, M. 1998, *ApJ*, 503, 543
- Giavalisco, M. et al. 2004, *ApJL*, 600, L93
- Gingold, R. A. & Monaghan, J. J. 1977, *MNRAS*, 181, 375
- Gnedin, N. Y. 2000, *ApJ*, 542, 535
- Gnedin, N. Y. Kravtsov, A. V., & Chien, H.-W. 2008, *ApJ*, 672, 765
- Gnedin, N. Y. & Prada, F. 2004, *ApJ*, 608, 77
- Goerdt, T., Dekel, A., Sternberg, A., Ceverino, D., Teyssier, R., & Primack, J. R. 2010, *MNRAS*, 407, 613
- Goldoni, P., Royer, F., François, P., Horrobin, M., Blanc, G., Vernet, J., Modigliani, A., Larsen, J. 2006, *SPIE*, 6269, 80
- Gordon, K. D., Clayton, G. C., Misselt, K. A., Landolt, A. U., & Wolff, M. J. 2003, *ApJ*, 94, 279
- Gould, R. J., & Salpeter, E. E. 1963, *ApJ*, 138, 393

- Goto, T 2006, *MNRAS*, 371, 769
- Greenberg, J. M. 1976, *Ap&AA*, 39, 9
- Gronwall et al. 2007, *ApJ*, 667, 79
- Grove, L. F., Fynbo, J. P. U., Ledoux, C., Limousin, M., Møller, P., Nilsson, K. K., & Thomsen, B. 2009, *A&A*, 497, 689
- Guaita, L. et al. 2010, *ApJ*, 714, 255
- Guhathakurta, P., Tyson, J. A., & Majewski, S. R. 1990, *ApJL*, 357, L9
- Gunn, J. E. & Peterson, B. A. 1965, *ApJ*, 142, 1633
- Haardt, F. & Madau, P. 1996, *ApJ*, 461, 20
- Haehnelt, M. G., Steinmetz, M., & Rauch, M. 2000, *ApJ*, 534, 594
- Haiman, Z. & Rees, M. 2001, *ApJ*, 556, 87
- Haiman, Z., Spaans, M., & Quataert, E. 2000, *ApJ*, 537, L5
- Hamilton, D. R. 1940, *Phys. Rev*, 58, 122
- Hansen, M. & Oh, S. P. 2006, *MNRAS*, 367, 979
- Harper, D. A. & Low, F. J. 1971, *ApJ*, 165, 9
- Harrington, J. P. 1973, *MNRAS*, 162, 43
- Hartmann, L. W., Huchra, J. P., Geller, M. J., O'Brien, P., & Wilson, R. 1988, *ApJ*, 326, 101
- Hayes, M., Östlin, G., Atek, H., Kunth, D., Mas-Hesse, J. M., Leitherer, C., Jiménez-Bailón, E., Adamo, A. 2007, *MNRAS*, 382, 1465
- Hayes, M., Schaerer, D., & Östlin, G. 2010a, *A&A*, 509, L5
- Hayes, M., Östlin, G., Schaerer, D., Mas-Hesse, J. M., Leitherer, C., Atek, H., Kunth, D., Verhamme, A., de Barros, S., & Melinder, J. 2010b, *Nature*, 464, 562
- Heneyey, L. G. 1940, *PNAS*, 26, 50
- Heneyey L. G. & Greenstein J. L. 1941, *AJ*, 93, 70
- Hernquist, L. & Katz, N. 1989, *ApJS*, 70, 419
- Hernquist, L., Katz, N., Weinberg, D. H., & Miralda-Escudé, J. 1996, *ApJL*, 457, L51
- Hibon, P., Cuby, J.-G., Willis, J., Clément, B., Lidman, C., Arnouts, S., Kneib, J.-P., Willott, C. J., Marmo, C., McCracken, H. 2010, *A&A*, 515, 97
- Hogan C. J. & Rees M. J. 1979, *MNRAS*, 188, 791

- Hopkins, P. F., Strauss, M. A., Hall, P. B., Richards, G. T., Cooper, A. S., Schneider, D. P., Vanden Berk, D. E., Jester, S., Brinkmann, J., & Szokoly, G. P. 2004, *AJ*, 128, 1112
- Hu, E.M., Cowie, L. L., & McMahon, R. G. 1998, *ApJ*, 502, L99
- Hu, E. M., Cowie, L. L., McMahon, R. G., Capak, P., Iwamuro, F., Kneib, J.-P., Maihara, T., & Motohara, K. 2002, *ApJ*, 568, 75
- Hu, E. M., Cowie, L. L., McMahon, R. G., Capak, P., Iwamuro, F., Kneib, J.-P., Maihara, T., & Motohara, K. 2002, *ApJ*, 577, 99
- Hui, L., Gnedin, N. Y., & Zhang, Y. 1997, *ApJ*, 486, 599
- Hummer, D. G. 1962, *MNRAS*, 125, 21
- Höfner, S. 2009 ([arXiv:0903.5280](https://arxiv.org/abs/0903.5280))
- Höfner, S. & Andersen, A. C. 2007, *A&A*, 465, 39
- Iliev, I. T., Shapiro, P. R., McDonald, P., Mellema, G., & Pen, U.-L. 2010, *MNRAS*, 391, 63
- Iye, M., Ota, K., Kashikawa, N., Furusawa, H., Hashimoto, T., Hattori, T., Matsuda, Y., Morokuma, T., Ouchi, M., Shimasaku, K. 2006, *Nature*, 443, 186
- Jackson, J. D. 1999, *Classical Electrodynamics*, 3rd ed., New York: Wiley & Sons
- Jakobsson, P. et al. 2004, *A&A*, 427, 785
- Jarosik, N. et al. 2010 ([arXiv:1001.4744](https://arxiv.org/abs/1001.4744))
- Jefferies, J. T. & White, O. R. 1960, *ApJ*, 132, 767
- Junkkarinen, V. T., Cohen, Ross D., Beaver, E. A., Burbidge, E. M., Lyons, R. W., & Madejski, G. 2004, *ApJ*, 614, 658
- Kahn, F. D. 1962, *The Distribution and Motion of Interstellar Matter in Galaxies*, ed. L. Woltjer, New York: W. A. Benjamin, Inc.
- Kaiser, N. 1984, *ApJ*, 284, 9
- Kashikawa, N. et al 2006, *ApJ*, 648, 7
- Kelvin, W. T., 1st Baron 1901, *Nineteenth Century Clouds over the Dynamical Theory of Heat and Light*, The London, Edinburgh and Dublin Philosophical Magazine and Journal of Science, Series 6, 2:1-40
- Kennicutt, R. C., Jr. 1998, *ARA&A*, 36, 189
- Kobayashi, M. A. R., Totani, T., & Nagashima, M. 2007, *ApJ*, 670, 919
- Kodaira, K. et al. 2003, *PASJ*, 55, 17
- Koelbloed, D. 1956, *BAN*, 12, 341

- Kollmeier, J. A., Zheng, Z., Davé, R., Gould, A., Katz, N., Miralda-Escudé, J., Weinberg, D.H. 2010, *ApJ*, 708, 1048
- Kotak et al. 2009, *ApJ*, 704, 306
- Kravtsov, A. V., Klypin, A. A., & Khokhlov, A. M. 1997, *ApJS*, 111, 73
- Kroupa, P. 1998, *MNRAS*, 298, 231
- Kulkarni, V. P., Woodgate, B. E., York, D. G., Thatte, D. G., Meiring, J., Palunas, P., & Wassell, E., 2006, *ApJ*, 636, 30
- Kunth, D., Mas-Hesse, J. M., Terlevich, E., Terlevich, R., Lequeux, J., & Fall, S. M. 1998, *A&A*, 334, 11
- Lai, K., Huang, J., Fazio, G., Cowie, L. L., Hu, E. M., & Kakazu, Y. 2007, *ApJ*, 655, 704
- Lai, K. et al. 2008, *ApJ*, 674, 70
- Laursen, P. & Sommer-Larsen, J. 2007, *ApJL*, 657, L69
- Laursen, P., Razoumov, A. O., & Sommer-Larsen, J. 2009a, *ApJ*, 696, 853
- Laursen, P., Razoumov, A. O., & Sommer-Larsen, J. 2009c, *ApJ*, 702, 824
- Laursen, P., Sommer-Larsen, J., & Andersen, A. C. 2009b, *ApJ*, 704, 1640
- Laursen, P., Sommer-Larsen, J., & Razoumov, A. O. 2010a (arXiv:1009.1384)
- Laursen, P. 2010b, *subm. to arXiv yesterday*
- Le Delliou, M., Lacey, C. Baugh, C. M., Guiderdoni, B., Bacon, R., Courtois, H., Sousbie, T., & Morris, S. L. 2005, *MNRAS*, 357, 11
- Le Delliou, M.; Lacey, C. G., Baugh, C. M., & Morris, S. L. 2006, *MNRAS*, 365, 712
- Ledoux, C., Petitjean, P., Fynbo, J. P. U., Møller, P., & Srianand, R., *A&A*, 457, 71
- Lehnert, M. D., Nesvadba, N. P. H., Cuby, J.-G., Swinbank, A. M., Morris, S., Clément, B., Evans, C. J., Bremer, M. N., & Basa, S. 2010, *Nature*, 467, 940
- Leclerc, G.-L., Comte de Buffon 1733, *Mémoire sur le Jeu de Franc-Carreau*
- Leibundgut, B., Robertson, J. G. 1999, *MNRAS*, 303, 711
- Li, A. & Draine, B. T. 2001, *ApJ*, 554, 778
- Lia, C., Portinari, L., & Carraro, G. 2002, *MNRAS*, 330, 821
- Lia, C., Portinari, L., & Carraro, G. 2002, *MNRAS*, 335, 864
- Lillie, C. F. & Witt, A. N. 1976, *ApJ*, 208, 64
- Loeb, R. & Rybicki, G. B. 1999, *ApJ*, 524, 527

- Lowenthal, J. D., Hogan, C. J., Green, R. F., Woodgate, B., Caulet, A., Brown, L., & Bechtold, J. 1995, *ApJ*, 451, 484
- Lucy, L. 1977, *AJ*, 82, 1013
- Lynds, R. 1971, *ApJL*, 164, L73
- Madau, P., Ferguson, H. C., Dickinson, M. E., Giavalisco, M., Steidel, C. C., & Fruchter, A. 1996, *MNRAS*, 283, 1388
- Madau P., Meiksin A., & Rees M. 1997, *ApJ*, 475, 429
- Mannucci, F., Thompson, D., Beckwith, S. V. W., Williger, G. M. 1998, *ApJ*, 501, 11
- Maier, C., Meisenheimer, K., Thommes, E., Hippelein, H., Röser, H. J., Fried, J., von Kuhlmann, B., Phleps, S., & Wolf, C. 2003, *A&A*, 402, 79
- Malhotra, S. & Rhoads, J. 2004, *ApJL*, 617, L5
- Mas-Hesse, J. M., Kunth, D., Tenorio-Tagle, G., Leitherer, C., Terlevich, R. J., & Terlevich, E. 2003, *ApJ*, 598, 858
- Mathis, J. S., Rumpl, W., & Nordsieck, K. H. 1977, *ApJ*, 217, 425
- Matsuda et al. 2004, *AJ*, 128, 569
- Mattsson, L., Wahlin, R., Höfner, S., & Eriksson, K. 2008, *A&A*, 484, 5
- Meier, D. L. 1976, *ApJ*, 207, 343
- Meier, D. L. & Terlevich, R. 1981, *ApJ*, 246, 109
- Mellema, G., Arthur, S. J., Henney, W. J., Iliev, I. T., & Shapiro, P. R. 2006, *ApJ*, 647, 397
- Metropolis, N. & Ulam, S. 1949, *Journ. of the Am. Stat. Assoc.*, 44, 335
- Malhotra, S. & Rhoads, J. E. 2002, *ApJ*, 565, 71
- Meiksin, A. 2005, *MNRAS*, 356, 596
- Mie, G. 1908, *Ann. Phys.* 330, 377
- Miralda-Escudé, J., Cen, R., Ostriker, J. P., & Rauch, M. 1996, *ApJ*, 471, 582
- Mori, M., Umemura, M., & Ferrara, A. 2004, *ApJ*, 613, L97
- Møller, P., Fynbo, J. P. U., & Fall, S. M. 2004, *A&A*, 422, 33
- Møller, P., Warren, S. J., Fall, S. M., Fynbo, J. P. U., & Jakobsen, P. 2002, *ApJ*, 574, 51
- Morton, T. D., Slane, P., Borkowski, K. J., Reynolds, S. P., Helfand, D. J., Gaensler, B. M., Hughes, J. P. 2007, *ApJ*, 667, 219
- Møller, P. & Warren, S. J. 1993, *A&A*, 270, 43
- Møller, P. & Warren, S. J. 1998, *MNRAS*, 299, 611

- Møller, P., Warren, S. J., & Fynbo, J. P. U. 1998, *A&A*, 330, 19
- Nagamine, K., Ouchi, M., Springel, V., Hernquist, L. 2008 ([arXiv:0802.0228](https://arxiv.org/abs/0802.0228))
- Nandy, K., Morgan, D. H., Willis, A. J., Wilson, R., & Gondhalekar, P. M. 1981, *MNRAS*, 196, 955
- Natta, A. & Beckwith, S. 1986, *A&A*, 158, 310
- Neufeld, D. 1990, *ApJ*, 350, 216
- Neufeld, D. 1991, *ApJL*, 370, L85
- Nilsson, K. K., Fynbo, J. P. U., Møller, P., Sommer-Larsen, J. & Ledoux, C. 2006, *A&A*, 452, 23
- Nilsson, K. K., Møller, P., Möller, O., Fynbo, J. P. U., Michałowski, M. J., Watson, D., Ledoux, C., Rosati, P., Pedersen, K., & Grove, L. F. 2007, *A&A*, 471, 71
- Nilsson, K. K., Tapken, C., Møller, P., Freudling, W., Fynbo, J. P. U., Meisenheimer, K., Laursen, P., Östlin, G. 2009, *A&A*, 498, 13
- Noterdaeme, P., Petitjean, P., Ledoux, C., & Srianand, R. 2009, *A&A*, 505, 1087
- Noterdaeme, P., Petitjean, P., Srianand, R., Ledoux, C., Le Petit, F. 2007, *A&A*, 469, 425
- Orsi, A., Lacey, C. G., Baugh, C. M., & Infante, L., 2008, *MNRAS*, 391, 1589
- O’Meara, J. M., Prochaska, J. X., Burles, S., Prochter, G., Bernstein, R. A., & Burgess, K. M. 2007, *ApJ*, 656, 666
- O’Shea, B., Bryan, G., Bordner, J., Norman, M. L., Abel, T., Harkness, R., & Kritsuk, A. 2004, *Adaptive Mesh Refinement — Theory and Applications*, Eds. T. Plewa, T. Linde, & V. G. Weirs, Springer
- Osterbrock, D. E. 1962, *ApJ*, 135, 195
- Osterbrock, D. E. 1989, *Astrophysics of Gaseous Nebulae and Active Galactic Nuclei* Sausalito: University Science Books
- Ouchi, M., et al. 2003, *ApJ*, 582, 60
- Ouchi, M. et al. 2004, *ApJ*, 611, 660
- Ouchi, M., t al. 2004, *ApJ*, 611, 685
- Ouchi, M. et al. 2008, *ApJS*, 176, 301
- Ouchi, M. et al. 2010, *ApJ*, 723, 869
- Panangia, N. & Ranieri, M. 1973, *A&A*, 24, 219
- Papovich, C., Dickinson, M., & Ferguson, H. C. 2001, *ApJ*, 559, 620
- Partridge, R. B. & Peebles, P. J. E. 1967, *ApJ*, 147, 868

- Pei, Y. C. 1992, *ApJ*, 395, 130
- Pei, Y., Fall, M. & Hauser, M. 1999, *ApJ*, 522, 604
- Pettini, M., Ellison, S. L., Steidel, C. C., & Bowen, D. V. 1999, *ApJ*, 510, 576
- Pettini, M., King, D., Smith, L., & Hunstead, R. 1997, *ApJ*, 478, 536
- Pettini, M., Shapley, A. E., Steidel, C. C., Cuby, J., Dickinson, M., Moorwood, A. F. M., Adelberger, K. L., & Giavalisco, M. 2001, *ApJ*, 554, 981
- Phillips, K. C. & Mészáros, P. 1986, *ApJ*, 310, 284
- Pirzkal, N., Malhotra, S., Rhoads, J. E., & Xu, C. 2007, *ApJ*, 667, 49
- Pontzen, A., Governato, F., Pettini, M., Booth, C. M., Stinson, G., Wadsley, J., Brooks, A., Quinn, T., & Haehnelt, M. 2008, *MNRAS*, 390, 1349
- Press, W. H., Teukolsky, S. A., Vetterling, W. T., & Flannery, B. P. 1992, *Numerical Recipes in FORTRAN — The Art of Scientific Computing*, 2nd ed., New York: Cambridge University Press
- Prevot, M. L., Lequeux, J., Prevot, L., Maurice, E., & Rocca-Volmerange, B. 1984, *A&A*, 132, 389
- Prochaska, J. X., Chen, H.-W., Wolfe, A. M., Dessauges-Zavadsky, M., & Bloom, J. S. 2008, *ApJ*, 672, 59
- Prochaska, J. X., Herbert-Fort, S., & Wolfe, A. M. 2005, *ApJ*, 635, 123
- Purcell, E. M. & Pennypacker, C. R. 1973, *AJ*, 186, 705
- Rauch, M. 1998, *ARA&A*, 36, 267
- Rauch, M. & Haehnelt, M. G. 1995, *MNRAS*, 275, 76
- Razoumov, A. O. & Cardall, C. Y.
- Razoumov, A. O. & Sommer-Larsen, J. 2006, *ApJ*, 651, 81
- Razoumov, A. O. & Sommer-Larsen, J. 2007, *ApJ*, 668, 674
- Razoumov, A. O. & Sommer-Larsen, J. 2010, *ApJ*, 710, 1239
- Rhoads, J. E., Malhotra, S., Dey, A., Stern, D., Spinrad, H., & Jannuzi, B. T. 2000, *ApJ*, 545, 85
- Rhoads, J. E., et al. 2003, *AJ*, 125, 1006
- Reichard, T. A., Richards, G. T., Hall, P. B., Schneider, D. P., Vanden Berk, D. E., Fan, X., York, D. G., Knapp, G. R., & Brinkmann, J. 2003, *AJ*, 126, 2594
- Rigopoulou, D., et al. 2006, *ApJ*, 648, 81
- Robitaille, T. P. & Whitney, B. A. 2010, *ApJL*, 710, L1
- Roth, K. C., & Blades, J. C. 1995, *ApJL*, 445, L95

- Russell, S. C. & Dopita, M. A. 199, *ApJ*, 384, 508
- Rykoff et al. 2009, *ApJ*, 702, 489
- Saito, T., Shimasaku, K., Okamura, S., Ouchi, M., Akiyama, M., & Yoshida, M. 2006, *ApJ*, 648, 54
- Sakurai, J. J. 1994, *Modern Quantum Mechanics*, Rev. ed., Boston: Addison-Wesley Publishing Company, Inc.
- Salpeter, E. 1955, *ApJ*, 121, 161
- Sandage, A. R. 1961, *The Hubble Atlas of Galaxies*, Washington D. C.: Carnegie Institution
- Santos, M. R., Ellis, R. S., Kneib, J.-P., Richard, J., & Kuijken, K. 2004, *ApJ*, 606, 683
- Sargent, W. L. W., Young, P. J., Boksenberg, A., & Tytler, D. 1980, *ApJS*, 42, 41
- Savaglio, S., Fall, M. S. & Fiore, F. 2003, *ApJ*, 585, 638
- Savaglio, S., Panagia, N., & Stiavelli, M. 2000, *ASP Conf. Proc.*, 215, 65
- Sawicki, M & Yee, H. K. C 1998, *AJ*, 115, 1329
- Schaye, J. 2001, *ApJL*, 559, L1
- Schiminovich, D., Friedman, P. G., Martin, C., & Morrissey, P. F. 2001, *ApJ*, 563, 161
- Scoville, N. et al 2007, *ApJS*, 172, 1
- Scott D. & Rees M. J. 1990, *MNRAS*, 247, 510
- Shimasaku, K., et al. 2006, *PASJ*, 58, 313
- Shapley, A. E., Steidel, C. C., Adelberger, K. L., Dickinson, M., Giavalisco, M., & Pettini, M. 2001, *ApJ*, 562, 95
- Smail, I., Ivison, R. J. & Blain, A. W. 1997, *ApJ*, 90, L5
- Smith, H. E., Cohen, R. D., Burns, J. E., Moore, D. J., & Uchida, B. A. 1989, *ApJ*, 347, 87
- Smith, C. H., Bourke, T. L., Wright, C. M., Spoon, H. W. W., Aitken, D. K., Robinson, G., Storey, J. W. V., Fujiyoshi, T., Roche, P. F., & Lehmann, T. 1999, *MNRAS*, 303, 367
- Sommer-Larsen, J., Götz, M., & Portinari, L. 2003, *ApJ*, 596, 47
- Sommer-Larsen, J., Romeo, A. D., & Portinari, L. 2005, *MNRAS*, 357, 478
- Sommer-Larsen, J. 2006, *ApJL*, 644, L1
- Songaila, A. 2004, *AJ*, 127, 2598

- Songaila, A., Cowie, L. L., & Lilly, S. J. 1990, *ApJ*, 348, 371
- Spitzer, L. 1944, *ApJ*, 99, 1
- Spitzer, L. 1978, *Physical Processes in the Interstellar Medium*, New York: John Wiley & Sons
- Springel, V. & Hernquist, L. 2002, *MNRAS*, 333, 649
- Springel, V. 2005, *MNRAS*, 364, 1105
- Srianand, R., Gupta, N., Petitjean, P., Noterdaeme, P., & Saikia, D. J. 2008, *MNRAS*, 391, 69
- Stanway, E. R., Bunker, A. J., McMahon, R. G., Ellis, R. S., Treu, Tammaso, & McCarthy, P. J. 2004, *ApJ*, 607, 704
- Steidel, C. C., Adelberger, K. L., Dickinson, M., Giavalisco, M., Pettini, M., 1998, *ApJ*, 492, 428
- Steidel, C. C., Adelberger, K. L., Shapley, A. E., Pettini, M., Dickinson, M., & Giavalisco, M. 2000, *ApJ*, 532, 170
- Steidel, C. C., Adelberger, K. L., Shapley, A. E., Pettini, M., Dickinson, M., & Giavalisco, M. 2003, *ApJ*, 592, 728
- Steidel, C. C. & Hamilton, D. 1993, *AJ*, 105, 2017
- Stenflo, J. O. 1980, *A&A*, 84, 68
- Stickel, M., Klaas, U., Lemke, D., & Mattila, K. 2002, *A&A*, 383, 367
- Stratta, G., Maiolino, R., Fiore, F., & D'Elia, V. 2007, *ApJ*, 661, 9
- Takeuchi, T. T. & Ishii, T. T. 2004, *A&A*, 426, 425
- Taniguchi, Y. & Shioya, Y. 2000, *ApJL*, 532, L13
- Taniguchi, Y., Shioya, Y., & Yuko, K. 2001, *ApJ*, 562, 15
- Taniguchi, et al. 2005, *PASJ*, 57, 165
- Tapken, C., Appenzeller, I., Noll, S., Richling, S., Heidt, J., Meinköhn, E., Mehlert, D. 2007, *A&A*, 467, 63
- Tasitsiomi, A. 2006, *ApJ*, 645, 792
- Tasitsiomi, A. 2006, *ApJ*, 648, 762
- Tenorio-Tagle, G., Silich, S. A., Kunth, D., Terlevich, E., & Terlevich, R. 1999, *MNRAS*, 309, 332
- Terlevich, E., Diaz, A. I., Terlevich, R., & Vargas, M. L. G. 1993, *MNRAS*, 26, 3
- Tilvi, V. et al. 2010, *ApJ*, 721, 1853
- Turner, B. E. , *ApJL*, 362, L29

- Ulam, S. M. 1991, *Adventures of a Mathematician*, Berkeley: The University of California Press
- Unno, W. 1952, *PASJ*, 3, 158
- Unno, W. 1952, *PASJ*, 4, 100
- Unno, W. 1955, *PASJ*, 7, 81
- Valls-Gabaud, D. 1993, *ApJ*, 419, 7
- van de Hulst, H.C. 1957, *Light Scattering by Small Particles*, New York: Wiley
- van Dokkum, P. G. 2001, *PASP*, 113, 1420
- van Breukelen, C., Jarvis, M. J., & Venemans, B. P. 2005, *MNRAS*, 359, 895
- Venemans, B., et al. 2005, *A&A*, 431, 793
- Verhamme, A., Schaerer, D., & Maselli, A. 2006, *A&A*, 460, 397
- Verhamme, A., Schaerer, D., Atek, H., & Tapken, C. 2008, *A&A*, 491, 89
- Verma, A., Lehnert, M. D., Schreiber, N. M. F., Bremer, M. N., & Douglas, L. 2007, *MNRAS*, 377, 1024
- Vijh, U. P., Witt, Adolf N., & Gordon, K. D. 2003, *ApJ*, 587, 533
- Vladilo, G. 2002, *A&A*, 391, 407
- Vladilo, G. 1999, *ASP Conf. Proc.*, 187, 323
- Wadadekar. Y., Casertano, S., & de Mellao, D. 2006, *AJ*, 132, 1023
- Wang, J.-X., Malhotra, S., Rhoads, J. E., Zhang, H.-T., & Finkelstein, S. L. 2009, *ApJ*, 706, 762
- Weatherley, S. J., Warren, S. J., Møller, Fall, M, Fynbo, J. P. U., & Croom, S. M. 2005, *MNRAS*, 358, 985
- Weidinger, M., Møller, P., & Fynbo, J. P. U. 2004, *Nature*, 430, 999
- Weidinger, M., Møller, P., Fynbo, J. P. U., & Thomsen, B. 2005, *A&A*, 436, 825
- Weinberg, D. H., Davé, R., Katz, N., Kollmeier, J. A. 2003, *AIP Conf. Proc.*, 666, 157
- Weinberg, S. 1972 *Gravitation and Cosmology: Principles and Applications of the General Theory of Relativity*, New York: John Wiley & Sons
- Weingartner, J. C. & Draine, B. T. 2001, *ApJ*, 548, 296
- Welty, D. E., Frisch, P. C., Sonneborn, G., & York, D. G. 1999, *ApJ*, 512, 636
- Welty, D. E., Lauroesch, J. T., Blades, J. C., Hobbs, L. M., & York, D. G. 1997, *ApJ*, 489, 672

- Wilman, R. J., Gerssen, J., Bower, R. G., Morris, S. L., Bacon, R., de Zeeuw, P. T., & Davies, R. L. 2005, *Nature*, 436, 227
- Witt, A. N. & Oliveri, M. V. 1990, *AJ*, 99, 888
- Wolfe, A. M., Prochaska, J. X., & Gawiser, E. 2003, *ApJ*, 593, 215
- Wolf, C., Wisotzki, L., Borch, A., Dye, S., Kleinheinrich, M. & Meisenheimer, K. 2003, *A&A*, 408, 499
- Wolfe, A. M., Turnshek, D. A., Smith, H. E., & Cohen, R. D. 1986, *ApJS*, 61, 249
- Wouthuysen S. 1952, *AJ*, 57, 31
- Wyithe, J. S. B. & Loeb, A. 2003, *ApJ*, 586, 693
- Xilouris, E., Alton, P., Alikakos, J., Xilouris, K., Boumis, P., & Goudis, C. 2006, *ApJ*, 651, 107
- Yee, H. K. C. & De Robertis, M. M. 1991, *ApJ*, 381, 386
- Yusuf-Sadeh, F. & Morris, M. 1984, *ApJ*, 278, 186
- Zhang, Y., Anninos, P., & Norman, M. L. 1995, *ApJL*, 453, L57
- Zanstra, H. 1949, *BAN*, 11, 401
- Zanstra, H. 1951, *BAN*, 11, 359
- Zheng, Z. & Miralda-Escudé, J. 2002, *ApJ*, 578, 33
- Zheng, Z., Cen, R., Trac, H., & Miralda-Escudé, J. 2010a, *ApJ*, 716, 574
- Zheng, Z., Cen, R., Trac, H., & Miralda-Escudé, J. 2010b 2010b (arXiv:1003.4990)
- Zheng, Z., Cen, R., Weinberg, D., Trac, H., & Miralda-Escudé, J. 2010c (arXiv:1010.3017)
- Zwaan, M. A., van der Hulst, J. M., Briggs, F. H., Verheijen, M. A. W., & Ryan-Weber, E. V 2005, *MNRAS*, 364, 1467
- Östlin, G., Hayes, M., Kunth, D., Mas-Hesse, J. M., Leitherer, C., Petrosian, A., & Atek, H. 2009, *AJ*, 138, 923

Index

- 21 cm line, 48
- 2175 Å feature, 34, 37, 38
- α , 21
- Absorption
 - By dust, 4, 34, 87
 - Quantum mechanically, 165
- Albedo, 42
- Asymptotic giant branch, 34
- Atom velocity, 25, 66

- Collisions, 168
- Complete redistribution, 28
- Cooling radiation, 12
- Core/wing transition, 25
- Cosmic microwave background, 48
- Cosmological simulations, 56
- COSMOS, 14, 158
- Cross section, 22, 63
 - Absorption, 170
 - Collisional, 168
 - Conventional definition, 166
 - Derivation, 163
 - Dust, 37
 - Hydrogen, 20
 - In the line center, 22

- Damped Ly α absorbers, 12, 16
 - In emission, 141
- Damping parameter, 21
- Dark Ages, 9
- Dark matter, 9, 14
- Destruction of photons, 168, 169
- Dipole approximation, 166
- Dipole distribution, 25
- Double-peaks, 6, 107
- Dust, 33
 - Cross section, 37
 - Destruction, 41
 - Dust-to-gas ratio, 41
 - Dust-to-metal ratio, 40
 - Formation, 34
 - Properties, 36

- Epoch of Reionization, 9, 46
- Escape fractions
 - Ly α , 35
- η , 75
- Exact redistribution, 28
- Extinction curve, 34

- Frequency shift, 22, 26

- Galaxy formation, 9
- GALEX, 11
- GOODS, 36
- Gravitational cooling, 12
- Gravity softening length, 56

- Half-life
 - Collisional, 20
 - Natural, 168
- HII regions, 41
- HST, 11

- Intergalactic medium, 45
 - Radiative transfer, 98
- Interstellar medium, 45
- IUE, 11

- JWST, 5

- LALA, 4
- Large Magellanic Cloud, 34
- Line profile
 - Delta function, 167
 - Natural, 167
 - Thermal, 20
 - Total (Voigt), 21
- Line width
 - Natural, 169
- LOFAR, 49
- Lorentz transformation, 20, 65

- Lorentzian, 21, 167
 Ly α , 4
 Emission, 11
 Escape, 35
 Ly α emitters, 11
 Extendedness, 5
 Physical characteristics, 13
 Ly α blobs, 12
 Ly α forest, 45
 Lyman limit systems, 12
 Lyman-break galaxies, 15

 Metallicity, 17
 Monte Carlo, 53
 Multi-phase medium, 35, 113, 156
 MUSYC, 36

 Natural line width, 169
 Neufeld solution, 30

 Optical depth, 27, 63
 In the line center, 27
 Oscillator strength, 19, 167, 169
 Outflows, 35, 83, 125, 136

 PaST, 49
 Phase function, 23
 Core scatterings, 24
 Dust, 42
 Wing scatterings, 25
 Polarization, 23, 157, 164, 168
 Pop III stars, 9, 47

 Quasars, 12, 47

 Radiative transfer, 27, 64
 Rayleigh scattering, 25
 Recoil effect, 25
 Reionization, 46, 57
 Rejection method, 66
 Resonant scattering, 19, 167

 σ_8 , 57
 Scattering
 In code, 66
 Rayleigh, 25
 Theory, 22
 σ_x , 22
 SKA, 49
 Small Magellanic Cloud, 34
 Smoothed particle hydrodynamics, 55

 Spontaneous emission, 167
 Star formation rate
 Ly α emitters, 13
 Star formation rates
 From H α , 36
 Stars
 AGB, 34
 Pop III, 9, 47
 Strömgren spheres, 41
 Subaru, 4
 Supernovae, 34
 Superwinds, 12

 τ_0 , 27
 Thermal broadening, 20
 Thomson optical depth, 48
 Two-photon process, 169

 Ultra-VISTA, 5, 158
 UV background, 12, 57
 UV radiative transfer, 58

 Voigt function, 22
 Approximation, 63
 Voigt profile, 21

 Wing scattering, 24
 WMAP, 48

 x , 21
 z_{re} , 57